

CHARACTERIZATION OF ELECTRON CYCLOTRON RESONANCE ION SOURCE  
INSTABILITIES BY CHARGED PARTICLE DIAGNOSTICS

By

Bryan Isherwood

A DISSERTATION

Submitted to  
Michigan State University  
in partial fulfillment of the requirements  
for the degree of

Physics – Doctor of Philosophy

2020

## ABSTRACT

### CHARACTERIZATION OF ELECTRON CYCLOTRON RESONANCE ION SOURCE INSTABILITIES BY CHARGED PARTICLE DIAGNOSTICS

By

Bryan Isherwood

Ion sources are invaluable tools for producing charge particles for scientific, industrial, and medical applications. In particular, Electron Cyclotron Resonance (ECR) ion sources (ECRIS) are high power sources capable of producing high intensity, high charge state beams of heavy ions. The system uses microwaves to resonantly heat electrons within an inhomogeneous magnetic trap. However, the internal dynamics of the resulting plasma are complex and poorly understood. In particular, the excitation of kinetic instabilities within the plasma can make operating these ion sources difficult and unpredictable. This thesis focuses on studying these instabilities to determine ways to optimize ECRIS performance by minimizing their impact on the extracted beam current.

This study focuses on two measurements that look at the steady-state and time-resolved measurements of charged particle currents escaping the ion source during stable and unstable operations. The first measurement is a novel diagnostic of electrons escaping confinement from the plasma chamber. The second was a measurement of high charge state ions ( $\text{Ar}^{8+}$ ) extracted from the plasma chamber over a broad set of parameter spaces. These measurements provide insight into the ideal operating conditions for an ECR ion source and the dynamics of the ion and electron populations within its plasma.

Copyright by  
BRYAN ISHERWOOD  
2020

*I produced a detailed tribute to my wrongness.*  
Nathan Pyle



## ACKNOWLEDGEMENTS

This thesis, and large amounts of the work presented, were made possible only through the time and patience of Guillaume Machicoane, who helped see this projected through to its completion. I would also like to acknowledge Eduard Pozdeyev and Yoshi Yamazaki for their support throughout this study. This research was made possible by the National Science Foundation under NSF Grant 1632761, the U.S. Department of Energy Award Number DE-SC0018362, the National Superconducting Cyclotron Laboratory (NSCL), the Facility for Rare Isotope Beams (FRIB), and Michigan State University.

I would also like to thank my committee Yoshishige Yamazaki, Guillaume Machicoane, Kirsten Tollefson, Steven Lidia, and John Verboncoeur for their support and advice throughout this project. Finally, I would like to thank all of those who have provided help, insight, and expertise, without whom this project would not have been possible: Jeffrey Stetson, Larry Tobos, Jesse Fogleman, Shane Renteria, Derek Neben, Andreas Stoltz, Dirk Weisshaar, John Brandon, the entire FRIB and NSCL Diagnostic, Electronics, and RF Groups, the NSCL operations group, Cody Norat, Steven Lund, Olli Tarvainen, and Ivan Izotov.

## TABLE OF CONTENTS

LIST OF TABLES . . . . .	viii
LIST OF FIGURES . . . . .	x
CHAPTER 1 INTRODUCTION . . . . .	1
CHAPTER 2 ELECTRON CYCLOTRON RESONANCE ION SOURCES . . . . .	3
2.1 Plasma Physics . . . . .	3
2.1.1 Magnetic Confinement . . . . .	4
2.1.2 Oscillations and Collisions . . . . .	6
2.1.3 Plasma Diffusion . . . . .	8
2.1.4 Electronic Properties of the Plasma . . . . .	10
2.1.5 Plasma Waves . . . . .	12
2.2 Electron Cyclotron Resonance Ion Sources and their Plasmas . . . . .	15
2.2.1 Resonant Heating of Electrons Within ECR Ion Sources . . . . .	15
2.2.2 Ionization Processes . . . . .	20
2.2.3 Characteristics of the Electron Population . . . . .	23
2.2.4 Characteristics of the Ion Population . . . . .	25
2.3 Operational Principles for ECR Ion Sources . . . . .	26
2.3.1 Electron Confinement and the Minimum-B Magnetic Field Topology . . . . .	27
2.3.2 Ion Confinement . . . . .	30
2.3.3 Afterglow . . . . .	32
2.3.4 Scaling Laws . . . . .	35
2.4 Kinetic Instabilities . . . . .	38
2.4.1 Diagnostic Observations . . . . .	39
2.4.2 Role of Hot Electrons . . . . .	42
2.4.3 Theory: Quasi-linear Diffusion and Kinetic-Cyclotron Masers . . . . .	44
CHAPTER 3 EXPERIMENTAL APPARATUS . . . . .	49
3.1 Superconducting Source for Ions (SuSI) . . . . .	49
3.2 Diagnostics . . . . .	54
3.2.1 Microwave Power Diode . . . . .	55
3.2.2 Beam Spectrometer . . . . .	55
3.2.3 4-Jaw Collimator . . . . .	57
3.2.4 Beam Current . . . . .	58
3.2.5 X-Ray Spectrometer . . . . .	60
CHAPTER 4 DISTRIBUTION OF ESCAPING ELECTRONS . . . . .	70
4.1 Experimental Goals . . . . .	70
4.2 Considerations for the Electron Current Measurement . . . . .	71
4.3 Parameter Space . . . . .	80
4.4 Results . . . . .	84

4.4.1	Varying Power . . . . .	85
4.4.2	Effect of a Variable Pressure . . . . .	89
4.4.3	Effect of a Variable Hexapole . . . . .	92
4.4.4	Effect of Varying the Injection Side Magnetic Maximum . . . . .	95
4.4.5	Effect of Varying the Extraction Side Magnetic Maximum . . . . .	99
4.4.6	Effect of Varying the Magnetic Minimum . . . . .	102
4.5	Concluding Thoughts . . . . .	108
CHAPTER 5 PARAMETER SWEEP . . . . .		114
5.1	Goals . . . . .	114
5.2	Parameter Space . . . . .	114
5.3	Results . . . . .	115
5.3.1	Beam Current Transient Profiles . . . . .	117
5.3.2	Stability Maps . . . . .	128
5.3.3	Varying the Hexapolar Field Maximum . . . . .	137
5.3.4	Effect of the Injection Side Magnetic Field upon Plasma Stability . . . . .	142
5.3.5	Varying the Extraction Field Maximum . . . . .	146
5.3.6	Source stability for a varying magnetic minimum . . . . .	153
5.3.7	Understanding the 'over-extraction' transient profiles . . . . .	161
5.4	Concluding Thoughts . . . . .	163
CHAPTER 6 CONCLUSION . . . . .		169
APPENDICES . . . . .		172
APPENDIX A	MATLAB CODES . . . . .	173
APPENDIX B	LONGITUDINAL FIELD PROFILES FOR THE MEASUREMENT OF THE DISTRIBUTION OF ESCAPING ELECTRONS . . . . .	177
APPENDIX C	EXTRA DATA FROM THE MEASUREMENT OF THE DISTRI- BUTION OF ESCAPING ELECTRONS . . . . .	179
APPENDIX D	LONGITUDINAL FIELD PROFILES FOR THE PARAMETER SWEEP MEASUREMENT OF ION STABILITY . . . . .	187
BIBLIOGRAPHY . . . . .		189

## LIST OF TABLES

Table 2.1: A comparison of electron Debye lengths for the different electron populations. In accordance with the qualitative trends estimated in Mironov et al., it is assumed that $n_{e,cold} \sim 1 \times 10^{11} \text{ cm}^{-3}$ and $n_{e,warm/hot} \sim 5 \times 10^{11} \text{ cm}^{-3}$ [58]. . . . .	24
Table 2.2: A comparison of electron collision and gyration frequencies in a region where $B = 1 \text{ T}$ , $n_e = 5 \times 10^{11} \text{ cm}^{-3}$ , $\ln \Lambda = 10$ assuming the energy distribution fo electrons follows a Maxwell-Boltzmann distribution. $f_{ce}$ decreases due to the $\gamma^{-1}$ term in equation 2.5. . . . .	25
Table 2.3: The collision frequencies for $\text{Ar}^{1+}$ and $\text{Ar}^{8+}$ with $n_e = 5 \times 10^{11} \text{ cm}^{-3}$ , $\bar{q} = 8$ , $\ln \Lambda = 10$ assuming that the energy distribution of ions follows a Maxwell-Boltzmann distribution. The right hand side of the plot compares the different collision frequencies against the gyration frequencies for both of these charge states assuming $B = 1 \text{ T}$ . . . . .	26
Table 3.1: The measurable range could be set by the BCM controller. While there is an upper limit of current that each range can measure, the actual value of the range (first column) does not determine the maximum value. That is to say, the first column is more of an order of magnitude reference. Increasing the BCM measurable current range, generally, decreased the relative error of each measurement. The variance increased along side the measurable range, but did not have a significant effect upon each measurement. . . . .	59
Table 3.2: Information of the calibration source used. $A_0$ is the initial soruce activity, measured on November 1st, 1988. $A$ is the theoretical activity at the time of the measurement. Calibration data was taken on February 15th, 2018. . . . .	63
Table 4.1: Closing the vertical gap from 38 to 5 mm decreased the observable current by about an order of magnitude. The relative current variance was calculated use values similar to those in table 3.1. . . . .	80
Table 4.2: Comparison between the longitudinal field extrema of the NSCL standard operating point for facility operations, and the control field used for this measurement.	81
Table 4.3: The set of operating points used where chosen to measure the coupling between the magnetic minimum and maximum at injection and other measured parameters. $\langle B \rangle$ is the average magnetic field between the injection and extraction maxima. The extraction side maxima was held constant at 1.100 T for all operating points. . . . .	83

Table 5.1: The field maxima used were scaled to either be on average larger or smaller than the scaling laws prescribe. The values above are there to demonstrate the relative range of values used as the magnetic minimum was varied. As calculated, the fields in each of the four ranges corresponds to  $B_{\min}/B_{RF} = 0.725$ . The standard facility operating point uses  $B_{\min}/B_{RF} = 0.711$ . . . . . 115

Table 5.2: Each of the different transient profiles has been assigned a different color. Generally speaking each of the different profiles exists over a different repetition frequency range, with ion bust dominated events occurring over the smallest time scale and over-extraction events occurring over the longest. . . . . 128

## LIST OF FIGURES

Figure 2.1: The series of solenoids generates a semi-uniform magnetic field. The field strength reaches a minimum at some point between the centers of the coils, represented by the less dense field lines (top). The bottom left plot shows an example field profile from the center of the above configuration to the center of the last coil. The bottom right plot shows an example loss cone. . . . .	5
Figure 2.2: The dispersion relation for an under dense plasma ( $\omega_{ce} > \omega_{pe}$ ). . . . .	14
Figure 2.3: A 2D projection of the typical operational magnetic field across the central axis of the SuSI ECR ion source at the NSCL. This data was generated using the program POISSON/Superfish. . . . .	17
Figure 2.4: A 3D projection of the magnetic field magnitude within an ECR ion source. This particular profile was generated by using CST model of the SuSI ion source at the NSCL. The black lines represent iso-B surfaces within the volume of the magnetic trap. . . . .	18
Figure 2.5: A contour projection of the minimum-B magnetic field configuration seen in figure 2.4. The black rings indicate the position of iso-B surfaces within the field structure. The red ring represent the ECR surface over which the heating of cold electrons occurs. . . . .	19
Figure 2.6: A calculation of the Electron Impact Ionization cross section, given in [103]. . . . .	22
Figure 2.7: Golovanivsky's plot which shows the criteria for producing high charge state ions in an ECRIS plasma. The circles represent the atomic species which is fully ionized for the given density and ion confinement time. Those in parenthesis to the right show the highest charge state achievable for other atomic species. Reproduced from [17], with permission from AIP Publishing. . . . .	28
Figure 2.8: Comparison of the radial component of the magnetic field generated by the solenoids alone (left) and the hexapole alone (right). . . . .	29
Figure 2.9: The three different decay modes are dependent upon the degree of turbulence of the plasma. The three curves show the typical decay forms of afterglow pulses: a) Turbulent, b) Quiescent, c) Non-linear particle diffusion. Figure originally printed in [18] and has been re-published with permission of Taylor & Francis Group LLC. . . . .	34

Figure 2.10: By pulsing RF power again after the initial afterglow burst, an instability can be ignited which forces hot electrons out of the plasma. This results in a second burst of ions. This method will work so long as the hot electrons have not diffused out of the plasma by other means. Figure originally printed in [18] and has been re-published with permission of Taylor & Francis Group LLC. . . . . 35

Figure 2.11: A demonstration of the magnetic scaling laws for intermediate to high charge state argon ions. The measurement was taken using SuSI at the NSCL.  $B_{\min} = 0.4$  T,  $P^{\mu} = 350$  W,  $p_{\text{Ar}} = 214$  nTorr. . . . . 37

Figure 2.12: Beam current losses for  $\text{Ar}^{8+}$ , normalized by the largest measured value. . . . . 40

Figure 2.13: Spectrogram of an unstable microwave emission in open space (no waveguide) for a 14.056 GHz ECR ion source, 400 W microwave power,  $B_{\min}/B_{\text{RF}} = 0.83$ . The solid line above 14.056 GHz results from the heating RF that leaked out of the system. The microwave emission was so powerful that it was possible to detect the emission in free space. Experimentally, this means that frequencies above and below the waveguide cutoffs could be measured. This plot has not been adjusted for transmission efficiency of the microwaves. Reproduced from [25], with permission from AIP Publishing. . . . . 41

Figure 2.14: Dispersion relationship of the extraordinary wave in an ECRIS plasma.  $f_p = 6$  GHz,  $f_{ce} = 14$  GHz,  $\theta = 5^\circ$ ,  $f_z = 2.22$  GHz,  $f_{ZI} = 14.1$ . The 'slow' and 'fast' qualifiers signify whether the phase velocity of the wave is less than or greater than the speed of light in vacuum, respectively. The slow Z-mode propagates between the plasma frequency and Z-Infinity (Blue). The fast Z-mode propagates in the orange region below the plasma frequency. The X-mode propagates in the orange region above  $f_x$ . . . . . 42

Figure 2.15: Phase velocity of the extraordinary wave in an ECRIS plasma.  $f_p = 6.00$  GHz,  $f_{ce} = 14.00$  GHz,  $\theta = 5^\circ$ ,  $f_z = 2.22$  GHz,  $f_{ZI} = 14.01$ , and  $f_x = 16.22$ . The horizontal dashed line represents  $v_{\theta} = c$ . The 'slow' and 'fast' qualifiers signify whether the phase velocity of the wave is less than or greater than the speed of light in vacuum, respectively. The slow Z-mode propagates between the plasma frequency and Z-Infinity (Blue). The fast Z-mode propagates in the orange region below the plasma frequency. The X-mode propagates in the orange region above  $f_x$ . The region above  $f_{ZI}$  but below  $v_{\theta} = c$  is a forbidden region with imaginary propagation. . . . . 43

Figure 3.1: A schematic of the source-beamline configuration used for this research. . . . . 50

Figure 3.2: A 3D model showing the cross-section of SuSI. Gas and microwave are injected on the left and the ion beam is extracted to the right. Arrows on the bottom point to the four active solenoid coils that surround the hexapole and plasma chamber. . . . . 51

Figure 3.3: An example of the on axis longitudinal field profile for SuSI. The three curves were generated by POISSON/Superfish. The vertical dashed line represents the position of the ion source’s extraction aperture. The horizontal dashed line represents the resonance field for 18 GHz microwaves with cold electrons. . . . . 52

Figure 3.4: An example of SuSI’s radial field as a function of distance from the center axis, with 375 A going through each hexapole coil. The curve was generated by a CST model of SuSI’s coil and yoke configuration. The horizontal dashed line represents the resonance field for 18 GHz microwaves with cold electrons. . . . . 52

Figure 3.5: (Top) The full geometry of the source and beamline model used in this study. All models were taken from pre-rendered SolidWorks files created by NSCL mechanical engineers. Those files were imported into CST studio suite, where they were used to perform magnetic field and beam trajectory calculations. The model includes a yoke (in blue), plasma chamber, extraction geometry, einzel lens, transport lines, dipole, and Faraday cup geometry. The cup housing geometry has been simplified in order to improve simulation speed. (Bottom) Coil geometry and current direction. On the left are the dipole coils and on the right the source coils. The white arrows represent current direction. In this picture the dipole is set to analyze electrons. . . . . 53

Figure 3.6: The blue lines show the results of a trace simulation of  $Ar^{8+}$  ions traveling through SuSI’s beamline up to the first Faraday cup. Data from a charge state distribution measurement was input into the program to calculate the magnetic field of the the ion source and analyzing dipole:  $E_{beam} = 160$  keV ( $V_{ext} = 20$  kV),  $V_{einzel} = -20$  kV,  $V_{puller} = 0$  V,  $I_{dip} = 102.671$  A. The beam energy was predefined, rather than relying upon the electrostatics simulator. The simulation does slightly over approximate the field in the dipole as it was necessary to increase the beam’s energy by 4 keV (or extraction potential by 0.5 kV) in order to make the beam hit the center of the cup. The simulation was performed using CST particle studio. . . . . 54

Figure 3.7: Examples of the measured microwave signals coming from the ion source, as recorded from an oscilloscope trace. Data was recorded in ‘AC’ mode, ignoring the steady state offset. Each plot has been normalized such that their largest value is 1. a) The instability shows a large burst of microwave energy. The ‘hump’ after the large peak is believed to be a result of a changing reflection coefficient. b) A moderate burst in microwave power which decays back to a steady state value. c) A small burst in microwave power but possible a much longer change in the reflection coefficient of the plasma. . . . . 56

Figure 3.8: The 4-jaw collimator (red and blue) in front of the first Faraday cup (gray) limited the current by closing a gap in the horizontal (dipole bending plane) and vertical directions. . . . . 57



Figure 3.9: The Faraday cup-to-oscilloscope transmission line consists of the cup, a twinax cable, a twinax-to-coax converter box, and the oscilloscope (top). The dashed lines on the attenuation curve show the -3 dB point of the transmission line (bottom). The attenuation plot was generated using LTspice. . . . . 59

Figure 3.10: Two lead blocks (grey) were used to collimate the x-rays coming from the source. The tungsten slug (red) was only present in the block closest to the dipole (see figure 3.1). Picture has been supplied by the courtesy of Derek Neben. 61

Figure 3.11: The acceptance area of the collimation system (red dashed line) falls on all three electrodes of the extraction system. . . . . 61

Figure 3.12: An example Eu-152 emission spectrum as measured by the germanium detector used in this study. . . . . 62

Figure 3.13: Channel-to-energy calibration for the germanium detector used in this study. . . 63

Figure 3.14: The program known as TV, written by Andreas Fitzler from the university of Köln, was used to integrate the observed peaks of the spectra. The program uses the region surrounding the peak to subtract background counts. It then fits a Gaussian distribution to the background subtracted peak and then integrates that Gaussian in order to determine the total number of photons observed. . . . 65

Figure 3.15: Repeating the efficiency calibration three times helps confirm the solid angle calculation. Measurements were taken at 30, 60, and 100 cm distances away from the radial edge of the detector (assuming cylindrical geometry). . . . . 66

Figure 3.16: The two/three measurements were averaged together and a the resulting data set was fit with a 6th order polynomial. The fit was generated by MATLAB's curve fitting tool. . . . . 66

Figure 3.17: Natural log of the bremsstrahlung intensity. The smaller plot show the fit of the linear region of the distribution. The domain was manually chosen to be  $130 \text{ keV} < E_\gamma < 320 \text{ keV}$ . The line is described by  $\ln I_\gamma = -0.01629 \times E_\gamma + 6.261$ , giving a spectral temperature of  $61.39 \text{ keV} \pm 0.599 \text{ keV}$ . . . . . 67

Figure 3.18: Choosing the fitting region algorithmically, rather than blindly fitting over a region which worked for a different operating point, dramatically improves the overall fit. Properly using this method can result in improved analytical results when applied across multiple operating points. . . . . 69

Figure 4.1: A varying extraction voltage has little effect on the hot-electron bremsstrahlung distribution. The spectral temperature seems to fluctuate at low voltages and then decreases higher extraction voltages. This low order deviation is likely an effect of a changing background between measurements due to changing facility operational conditions (compare to figure C.1). Plasma parameters are  $B_{\min} = 0.397$  T,  $P = 350$  W,  $T_{\text{live}} = 600$  s, pressure = 212 nTorr. . . . . 72

Figure 4.2: The transient profiles of the extracted ion currents were measured for each operating point used in Figure 4.1. While ions do escape confinement at lower voltages (< 2kV), it is difficult to distinguish one charge state from another.  $B_{\min} = 0.397$  T,  $P = 350$  W, pressure = 212 nTorr. . . . . 73

Figure 4.3: The residual magnetic flux parallel and perpendicular to the beamline transverse axis. Measurements were taken while all beamline elements were turned off. 74

Figure 4.4: Argon charge state distributions from SuSI for 20 kV, 10 kV, and 5 kV extraction voltages measured at the first Faraday cup after the ion source in figure 3.1. Ion charge state increases from right to left, starting at  $Q = 1$ . Once again, we see that the extracted current decreases with decreasing voltage. Compared to figure 4.2, however, the purpose here is simply to increase the domain over which the system’s magnetic rigidity has been measured. . . . . 75

Figure 4.5: Measurements of the integral form of the magnetic rigidity between the ion source and the first Faraday cup. The (red) dashed line shows the linear best fit  $\int B(I_{dip}) \cdot dl = mI_{dip} + b$ , where  $m = 6.98624 \times 10^{-4}$  ( $6.98909 \times 10^{-4}$ ,  $7.01300 \times 10^{-4}$ ) and  $b = 2.47924 \times 10^{-4}$  ( $0.77833 \times 10^{-4}$ ,  $5.73681 \times 10^{-4}$ ). 76

Figure 4.6: The electron simulation under approximates the energy calibration created by measuring the magnetic rigidity of the ions. This is likely due to the presence of ambient and residual magnetic fields, as seen in figure 4.3. . . . . 76

Figure 4.7: The largest differences between the ion rigidity and electron simulation energy calibrations occur at lower energies. This is likely due to the presence of ambient magnetic fields and interparticle interactions, which the simulation did not take into account. . . . . 77

Figure 4.8: The yellow lines represent electron trajectories along the beamline within the model ion source. Trajectories begin at a 5 mm radius extraction aperture and end at the first Faraday cup in figure 3.2. All electrons are emitted in a direction perpendicular to the extraction aperture opening, with no angular divergence. The color of the lines represent their energy. The sudden change to blue at Faraday results from the -149 V potential on the cup’s electron suppressor ring. . . . . 78

Figure 4.9: The relative efficiency data (blue dots) approach a linear relationship with energy as the energy of electrons increases. Each data point was calculated by dividing the number of electrons emitted from the 6 mm extraction aperture by the number of electrons which reached the Faraday cup. All electrons in a given simulation/calculation were assumed to have escaped parallel to the center axis of the ion source, with no divergence and at a single energy. As such, these results best represent the effect of the ion source's and dipole's magnetic field on the transmission of electrons of a given energy. The fit was performed with MATLAB's CFit module and used a 'Robust' Least Absolute Residual fitting option. The largest contributor to transmissions losses were the fringe fields of the ion source. The charges are deflected away from the beamline center by the locally diverging field lines. This effect can be seen in figure 4.8. . . . . . 79

Figure 4.10: The magnetic field maximum at injection and extraction were chosen to be 2.3 T and 1.1 T, respectively. These values roughly follow the scaling laws with  $B_{Inj}/B_{RF} \approx 3.59$  and  $B_{Ext}/B_{RF} \approx 1.72$ . Throughout this measurement the plasma volume and gradient at resonance are allowed to vary. The resonance field is given by the black dashed line. The extraction aperture is represented by the vertical dashed line at  $x = 0$  cm. . . . . . 81

Figure 4.11: Values of the extraction side loss cone pitch angle used while varying the magnetic minimum while holding the extraction maximum constant. . . . . . 82

Figure 4.12: Values of the injection side loss cone pitch angle used, here the magnetic minimum is held constant. . . . . . 82

Figure 4.13: Values of the extraction side loss cone pitch angle used while varying the extraction side maximum while holding the magnetic minimum constant. . . . . . 83

Figure 4.14: Values of the radial loss cone pitch angle used while varying the hexapole with the longitudinal solenoid fields held constant. . . . . . 84

Figure 4.15: Measured electron distribution for the measurements 'control' operating point. The 50 keV reliability threshold is shown by the dashed line.  $B_{min} = 0.4$  T,  $B_{Inj,max} = 2.367$  T,  $B_{Ext,max} = 1.100$  T,  $P_{\mu} = 350$  W, Pressure = 212 nTorr,  $B_{Rad,wall} = 1.217$  T. . . . . . 85

Figure 4.16: By applying the efficiency calibration described in the previous section, the total current observed increases by several orders of magnitude, from  $10^{-1} - 1$  nA to  $10^3$  nA. The changing vertical gap distance had little effect upon the distribution once it was corrected for beamline and gap area transmission.  $B_{min} = 0.4$  T,  $B_{Inj,max} = 2.367$  T,  $B_{Ext,max} = 1.100$  T,  $P_{\mu} = 350$  W, Pressure = 212 nTorr,  $B_{Rad,wall} = 1.217$  T. . . . . . 86

Figure 4.17: The total measured current was found to vary linearly with a varying square acceptance area (equal horizontal and vertical gap widths). The red dashed line demonstrates the linear fit of the data points (blue). . . . .	87
Figure 4.18: Increasing the injected microwave power increased the measured electron current uniformly across the entire energy range. The central energy of the peak was largely unaffected by the changing microwave power. . . . .	87
Figure 4.19: The trend in the measured electron distribution is reflected in the bremsstrahlung spectrum as the total number of photons increases while the energy spread remains largely the same. . . . .	88
Figure 4.20: The similarities between the measured electron and bremsstrahlung distributions is most easy seen in the comparison between the systems' energy content and measured particle numbers. Overall, the effect of increasing power leads to a more dense electron population, but not a more energetic one. All sets shown have been normalized by the largest values in their sets: $E_{\text{peak,max}} = 565$ keV, $T_{\text{s,max}} = 39.7$ keV, $X_{T_{\text{s,max}}} = 278$ keV, $I_{\text{peak,max}} = -1383$ nA, and $N_{\gamma} = 5.0$ Mcounts. . . . .	89
Figure 4.21: The changing electron distribution suggests that increased pressure leads to a cooler, higher density plasma. . . . .	90
Figure 4.22: As the pressure increases, the measured bremsstrahlung distribution sees a trend towards lower energy photons. . . . .	91
Figure 4.23: While the energy content of both measurements agree to an increased pressure resulting in a cooler plasma, the trend total particles observed are inversely proportional to one another. Both top and bottom plots are normalized by the largest values in their sets: $E_{\text{peak,max}} = 592$ keV, $T_{\text{s,max}} = 42.1$ keV, $X_{T_{\text{s,max}}} = 297$ keV, $I_{\text{peak,max}} = -1224$ nA, and $N_{\gamma} = 5.8$ Mcounts. . . . .	92
Figure 4.24: The increasing radial field causes the overall current of the distribution to increase, although this effect is minimal compared to varying the microwave power. The central energy of the peak is also, largely, unaffected by the changing radial field. . . . .	93
Figure 4.25: The bremsstrahlung distribution was largely unaffected by the changing radial field, however, as the radial field at the wall increases there is a preference for the emission of lower energy photons. . . . .	94

Figure 4.26: The energy content of the distributions were largely unaffected by a changing radial field strength. The increasing radial field causes an increase in the both the height of the electron peak and total number of photons observed.  $E_{\text{peak,max}} = 669$  keV,  $T_{\text{s,max}} = 46.7$  keV,  $X_{T_{\text{s,max}}} = 315$  keV,  $I_{\text{peak,max}} = -1061$  nA, and  $N_{\gamma} = 6.3$  Mcounts. . . . . 95

Figure 4.27: The varying injection side magnetic maximum mostly affected the lower energy distribution of electrons, having minimum effect on the high energy peak. 96

Figure 4.28: The bremsstrahlung distribution was largely unaffected by a varying injection side magnetic maximum. . . . . 97

Figure 4.29: All operating points were nearly identical to one another. The inverse relationship between the electron peak amplitude and the total number of observed photons can be seen, however, the largest effect is likely on the lower energy side of the distribution, as the electron measurement suggests.  $E_{\text{peak,max}} = 568$  keV,  $T_{\text{s,max}} = 38.6$  keV,  $X_{T_{\text{s,max}}} = 281$  keV,  $I_{\text{peak,max}} = -1357$  nA, and  $N_{\gamma} = 4.9$  Mcounts. . . . . 98

Figure 4.30: The bias disk current decreased as the injection side magnetic field increased,  $|I_{\text{BD,max}}| = 730$  mA. . . . . 98

Figure 4.31: Increasing the extraction maximum slowly decreases the amplitude of the high energy peak. Between 1.2 T and 1.23 T the change in peak amplitude increases and results in a dramatic decrease in peaks height. These distributions have not been corrected for changes in the transmission coefficient due to a changing extraction field maximum. . . . . 100

Figure 4.32: The bremsstrahlung distribution remains largely unchanged as a result of a changing extraction field maximum, up to a point. Between 1.2 T and 1.23 T the number of intermediate to low energy photons observed decreases dramatically. These spectra have not been corrected for changes in the beamline transmission coefficient which result from a varying field maximum at extraction. 101

Figure 4.33: While the total number of photons observed decreases only slightly as the extraction maximum is increased, the sudden sudden drop-off in extracted beam current reduces the number of photons observed by more than 50%. No appreciable change in the system's energy content is observed.  $E_{\text{peak,max}} = 585$  keV,  $T_{\text{s,max}} = 38.6$  keV,  $X_{T_{\text{s,max}}} = 270$  keV,  $I_{\text{peak,max}} = -1756$  nA, and  $N_{\gamma} = 4.9$  Mcounts. Each data set has been normalized by the largest value in their respective sets. The normalized electron peak amplitude has been corrected for changes in the beamline transmission coefficient which result from a varying extraction maximum. . . . . 102

Figure 4.34: There is an obvious change in the energy content of the measured electron distribution resulting from a changing magnetic minimum. While the central energy of the peak increased, the height of the peak decreased. . . . . 103

Figure 4.35: Just as in figure 4.34, an increasing magnetic minimum pushes the photon distribution to higher energies. The total number of counts, however, increases where the electron peak's height decreases. This suggests that overall electron density increases, even if the measured electron current decreases. . . . . 104

Figure 4.36: Both the electron and bremsstrahlung distributions agree to a near linear increased in the energy content of the plasma. The spectral temperature lags behind due to the influence of lower energy electrons.  $E_{\text{peak,max}} = 742$  keV,  $T_{\text{s,max}} = 56.47$  keV,  $X_{T_{\text{s,max}}} = 359$  keV,  $I_{\text{peak,max}} = -1916$  nA, and  $N_{\gamma} = 6.7$  Mcounts. Each data set has been normalized by the largest value in their respective sets. . . . . 105

Figure 4.37: Maximum and minimum energy limits for fitting the spectral temperature as the magnetic field is varied. . . . . 105

Figure 4.38: There is a linear correlation between the decreasing trend of the height of the high energy peak and the reciprocal square of the central energy of that peak.  $I_{\gamma}/I_{\gamma,max} = 4.897 \times \gamma^{-2} - 0.4523$ ,  $R^2 = 0.9938$ . . . . . 106

Figure 4.39: The magnetic field lines (blue arrows), within the acceptance area of the extraction aperture (red dashed lines), are primarily parallel to the longitudinal axis of the plasma chamber. . . . . 107

Figure 4.40: There is a near-perfect inverse correlation between the trends of the decreasing height of the high energy peak and the increasing number of photons observed  $I_e/I_{e,max} = -0.9998 \times N_{\gamma}/N_{\gamma,max} - 1.37$ ,  $R^2 = 0.9888$  . . . . . 108

Figure 4.41: Bremsstrahlung distributions analyzed using the algorithm described in section 3.2.5 show much better agreement with the electron distribution data than those where an arbitrary energy domain was blindly applied to all operating points. In this case, the disagreement is larger for operating points with lower magnetic fields. Top plot:  $B_{\text{min}} = 0.337$  T. Bottom plot:  $B_{\text{min}} = 0.468$  T. . . . . 112

Figure 5.1: Example  $\text{Ar}_{8+}$  current (orange) and microwave power (purple) diagnostics while operating a stable ECR ion source plasma. The signals have been normalized to their maximum value over a 400 ms period. The extracted  $\text{Ar}_{8+}$  beam varies up to several percent even under stable conditions, in this case  $\delta I_{\text{Ar}_{8+}} \sim 7\%$ . The 60 Hz noise, and its harmonics, in the microwave signal results from the facility power source and is persistent throughout the lab. 117

- Figure 5.2: Multiple measurements of the transient current of escaping electrons, at different energies, were taken using an oscilloscope. The energy of electrons was selected by varying the energy in the dipole. The traces were then averaged 128 using the oscilloscopes averaging function. Those traces were put together, side-by-side, to plot the transient electron energy distribution. The peak current is 8460 nA at an electron energy of 62.88 keV, almost twice the central energy of the 'low energy peaks' seen in chapter 4. Higher energy electrons are minimally effected by the instability and the high energy peak is unaffected by the instability. . . . . 118
- Figure 5.3: The general semi-quantitative model of the transient ion current during the unstable operation of an ECR ion source.  $A_1$ ,  $A_2$ , and  $A_3$  represent the amplitudes of the three predominant period of beam current variations that result from an instability event. The time scales are meant to represent general ranges over which the variation occurs. Not every instability event will result in all three and, under most circumstances, there is one predominant feature which best describes the beam. However, under rare circumstances, all three can occur simultaneously. . . . . 119
- Figure 5.4: An example of the observed time resolved beam current (orange) and microwave power (purple) diagnostics seen during a transient profile dominate by the 'ion burst' effect. Notice how there is a large but short-lived burst in ions immediately after the burst of microwave energy. While present, the 'ion loss' profile is not dominant. The majority of the microwave power is emitted over a several milliseconds.  $\text{Ar}^{8+}$ ,  $B_{\min} = 0.39 \text{ T}$ ,  $B_{\text{Hex,wall}} = 1.2 \text{ T}$ ,  $P_{\mu} = 150 \text{ W}$ ,  $p_{\text{Ar}} = 131 \text{ nTorr}$ . . . . . 121
- Figure 5.5: An example of the observed time resolved beam current (orange) and microwave power (purple) diagnostics seen during a transient profile dominate by the 'ion loss' effect. Notice that almost 50% of the steady state current is lost following the microwave burst. While present, the 'ion burst' profile is not dominant, and can only be seen by focusing on the 100's  $\mu\text{s}$  time scale (bottom plot). The majority of the microwave power is emitted over 10's  $\mu\text{s}$  and very rapidly decays. The 'hump' in the emitted power is believed to result from a changing reflection coefficient within the plasma chamber.  $\text{Ar}^{8+}$ ,  $B_{\min} = 0.48 \text{ T}$ ,  $B_{\text{Hex,wall}} = 1.2 \text{ T}$ ,  $P_{\mu} = 250 \text{ W}$ ,  $p_{\text{Ar}} = 131 \text{ nTorr}$ . . . . . 122

- Figure 5.6: An example of the observed time resolved beam current (orange) and microwave power (purple) diagnostics seen during a transient profile dominated by the 'over-extraction' effect. Extracted Notice the almost 30% increase in extracted beam current following the exceptionally small burst of microwave power from the system. While present, the 'ion loss' profile is not dominant. Most importantly, this repetition frequency of this transient profile is on the order of 10's Hz, compared to figures 5.4 and 5.5 which are on the order of 100's Hz (top plot). The emitted microwave power is exceptionally small compared to the previous two cases (bottom plot). The 'hump' in the emitted power is believed to result from a changing reflection coefficient within the plasma chamber.  $Ar^{8+}$ ,  $B_{min} = 0.48$  T,  $B_{Hex,wall} = 1.32$  T,  $P_{\mu} = 350$  W,  $p_{Ar} = 131$  nTorr. . . . . 123
- Figure 5.7: 'Ion burst' dominated transient profiles are characterized by an increase in the average extracted current at low charge states ( $Ar^{2+}$ , blue, top trace) and a decreased in the average extracted current for high charge states ( $Ar^{8+}$ , orange, bottom trace). Both current traces have been normalized to the largest value in their respective scope traces.  $B_{min} = 0.45$  T,  $B_{Hex,wall} = 1.2$  T,  $P_{mu} = 50$  W,  $p_{Ar} = 141$  nTorr,  $V_{BD} = -17$  V. . . . . 124
- Figure 5.8: 'Ion loss' dominated transient profiles are characterized by an increase in the average extracted current at low charge states ( $Ar^{2+}$ , Blue, bottom trace) and a decreased in the average extracted current for high charge states ( $Ar^{8+}$ , orange, top trace). The plasma is also perturbed to a greater degree, compared to the 'ion burst' case. High charge state ion losses can be upwards of 80 - 100% of steady state beam currents, with much larger bursts in current for low charge states. Both current traces have been normalized to the largest value in their respective scope traces.  $B_{min} = 0.52$  T,  $B_{Hex,wall} = 1.2$  T,  $P_{mu} = 350$  W,  $p_{Ar} = 123$  nTorr,  $V_{BD} = -17$  V. . . . . 125
- Figure 5.9: Unlike the other two cases, 'over-extraction' dominated transient profiles are characterized by a decrease in the average extracted current at low charge states ( $Ar^{2+}$ , blue, top trace) and an increase in the average extracted current for high charge states ( $Ar^{8+}$ , orange, top trace). Both current traces have been normalized to the largest value in their respective scope traces.  $B_{min} = 0.42$  T,  $B_{Hex,wall} = 1.2$  T,  $P_{mu} = 250$  W,  $p_{Ar} = 131$  nTorr,  $V_{BD} = 20$  V. . . . . 126
- Figure 5.10:  $B_{min} = 0.42$  T,  $B_{Hex,wall} = 1.2$  T,  $P_{\mu} = 350$  W,  $p_{Ar} = 131$  nTorr,  $V_{BD} = +20$  V. . 126
- Figure 5.11:  $B_{min} = 0.42$  T,  $B_{Hex,wall} = 1.2$  T,  $P_{\mu} = 350$  W,  $p_{Ar} = 131$  nTorr.  $V_{BD} = +20$  V . 127
- Figure 5.12: Increasing the neutral gas pressure often changes the dominant transient mode of the extracted beam current during unstable operating.  $B_{min} = 0.515$  T,  $B_{Hex,wall} = 1.2$  T,  $P_{mu} = 350$  W. (Top)  $p_{Ar} = 96$  nTorr, (Middle)  $p_{Ar} = 123$  nTorr, (Bottom)  $p_{Ar} = 159$  nTorr. . . . . 127



Figure 5.13: Field maps for operating points where the average injection and extraction maxima were above the limits described by the scaling laws:  $\bar{B}_{Inj,max}/B_{RF} \approx 4.09$ ,  $\bar{B}_{Ext,max}/B_{RF} \approx 2.02$ . . . . . 129

Figure 5.14: Field maps for operating points where the average injection and extraction maxima were above the limits described by the scaling laws:  $\bar{B}_{Inj,max}/B_{RF} \approx 3.71$ ,  $\bar{B}_{Ext,max}/B_{RF} \approx 1.78$ . . . . . 129

Figure 5.15: Field maps for operating points where the average injection and extraction maxima were above the limits described by the scaling laws:  $\bar{B}_{Inj,max}/B_{RF} \approx 3.43$ ,  $\bar{B}_{Ext,max}/B_{RF} \approx 1.95$ . . . . . 130

Figure 5.16: Field maps for operating points where the average injection maximum was larger than and extraction maxima small than the limits described by the scaling laws:  $\bar{B}_{Inj,max}/B_{RF} \approx 4.11$ ,  $\bar{B}_{Ext,max}/B_{RF} \approx 1.61$ . . . . . 130

Figure 5.17: Percentage of measured operating points with average currents greater than  $60\mu A$ . 132

Figure 5.18: Percentage of measured operating points with average currents greater than  $80\mu A$ . 132

Figure 5.19: Percentage of measured operating points with average currents greater than  $100\mu A$ . . . . . 133

Figure 5.20: Percentage of measured operating points where beam loss was greater than 30%. 133

Figure 5.21: Percentage of measured operating points where beam loss was greater than 60%. 134

Figure 5.22: Percentage of measured operating points where beam loss was greater than 80%. 134

Figure 5.23: Percentage of measured operating points with peak currents greater than  $60\mu A$ . 135

Figure 5.24: Percentage of measured operating points with peak currents greater than  $80\mu A$ . 136

Figure 5.25: Percentage of measured operating points with peak currents greater than  $100\mu A$ . 136

Figure 5.26: Ar<sup>8+</sup> beam current for a varying hexapole field maxima: (Top left)  $B_{Hex,wall} = 1.12$  T, (Top right)  $B_{Hex,wall} = 1.18$  T, (Bottom left)  $B_{Hex,wall} = 1.22$  T, (Bottom right)  $B_{Hex,wall} = 1.28$  T.  $B_{min} = 0.4$  T,  $P_{\mu} = 350$  W,  $p_{Ar} = 213$  nTorr. Signals have been treated with a digital low pass filter using the Matlab signal processing toolkit, with a cutoff frequency of 333 kHz. . . . . 138

Figure 5.27: Average, maximum, and minimum beam current measurements of extracted Ar<sup>8+</sup> beam current for varying hexapole field maxima:  $B_{min} = 0.4$  T,  $P_{\mu} = 350$  W,  $p_{Ar} = 213$  nTorr. . . . . 138

Figure 5.28: Microwave power signals for a varying hexapole field: (Top left)  $B_{\text{Hex,wall}} = 1.12$  T, (Top right)  $B_{\text{Hex,wall}} = 1.18$  T, (Bottom left)  $B_{\text{Hex,wall}} = 1.22$  T, (Bottom right)  $B_{\text{Hex,wall}} = 1.28$  T.  $B_{\text{min}} = 0.4$  T,  $B_{\text{Ext,max}} = 1.1$  T,  $P_{\mu} = 350$  W,  $p_{\text{Ar}} = 213$  nTorr. Microwave power has been offset by its minimum value, over the entire 100 ms measurement period, to account for the AC coupling of the oscilloscope. Signals have been treated with a digital low pass filter using the Matlab signal processing toolkit, with a cutoff frequency of 333 kHz. . . . . 140

Figure 5.29: Fourier transform of the microwave power signals emitted from the ion source for a varying hexapolar field: (Top left)  $B_{\text{Hex,wall}} = 1.12$  T, (Top right)  $B_{\text{Hex,wall}} = 1.18$  T, (Bottom left)  $B_{\text{hex,max}} = 1.22$  T, (Bottom right)  $B_{\text{hex,max}} = 1.28$  T.  $B_{\text{min}} = 0.4$  T,  $B_{\text{Ext,max}} = 1.1$  T,  $P_{\mu} = 350$  W,  $p_{\text{Ar}} = 213$  nTorr. . . . . 141

Figure 5.30: Average and maximum peak microwave power for a varying hexapole field maxima:  $B_{\text{min}} = 0.4$  T,  $B_{\text{Ext,max}} = 1.1$  T,  $P_{\mu} = 350$  W,  $p_{\text{Ar}} = 213$  nTorr. . . . . 141

Figure 5.31:  $\text{Ar}^{8+}$  beam current for a varying injection field maxima: (Top Left)  $B_{\text{Inj,max}} = 2.20$  T, (Top Right)  $B_{\text{Inj,max}} = 2.33$  T, (Bottom Left)  $B_{\text{Inj,max}} = 2.45$  T, (Bottom Right)  $B_{\text{Inj,max}} = 2.58$  T.  $B_{\text{min}} = 0.4$  T,  $P_{\mu} = 350$  W,  $p_{\text{Ar}} = 213$  nTorr. Signals have been treated with a digital low pass filter using the Matlab signal processing toolkit, with a cutoff frequency of 333 kHz. . . . . 143

Figure 5.32: Average, maximum, and minimum  $\text{Ar}^{8+}$  beam currents, measured over a 100 ms period, for a varying injection field maxima:  $B_{\text{min}} = 0.4$  T,  $P_{\mu} = 350$  W,  $p_{\text{Ar}} = 213$  nTorr. . . . . 143

Figure 5.33: Microwave power signals for a varying injection field maxima: (Top Left)  $B_{\text{Inj,max}} = 2.20$  T, (Top Right)  $B_{\text{Inj,max}} = 2.33$  T, (Bottom Left)  $B_{\text{Inj,max}} = 2.45$  T, (Bottom Right)  $B_{\text{Inj,max}} = 2.58$  T.  $B_{\text{min}} = 0.4$  T,  $P_{\mu} = 350$  W,  $p_{\text{Ar}} = 213$  nTorr. Microwave power has been offset by its minimum value, over the entire 100 ms measurement period, to account for the AC coupling of the oscilloscope. Signals have been treated with a digital low pass filter using the Matlab signal processing toolkit, with a cutoff frequency of 333 kHz. . . . . 144

Figure 5.34: Fourier transform of the microwave power signals emitted from the ion source for a varying injection field maximum: (Top Left)  $B_{\text{Inj,max}} = 2.20$  T, (Top Right)  $B_{\text{Inj,max}} = 2.33$  T, (Bottom Left)  $B_{\text{Inj,max}} = 2.45$  T, (Bottom Right)  $B_{\text{Inj,max}} = 2.58$  T.  $B_{\text{min}} = 0.4$  T,  $P_{\mu} = 350$  W,  $p_{\text{Ar}} = 213$  nTorr. . . . . 145

Figure 5.35: Average and maximum output microwave power, measured over a 100 ms period, for a varying injection side field maximum:  $B_{\text{min}} = 0.4$  T,  $P_{\mu} = 350$  W,  $p_{\text{Ar}} = 213$  nTorr. . . . . 145

Figure 5.36: Ar<sup>8+</sup> beam current for a varying extraction field maxima: (Top Left)  $B_{Ext,max} = 0.99$  T, (Top Right)  $B_{Ext,max} = 1.07$  T, (Bottom Left)  $B_{Ext,max} = 1.15$  T, (Bottom Right)  $B_{Inj,max} = 1.23$  T.  $B_{min} = 0.4$  T,  $P_{\mu} = 350$  W,  $p_{Ar} = 213$  nTorr. Signals have been treated with a digital low pass filter using the Matlab signal processing toolkit, with a cutoff frequency of 333 kHz. . . . . 147

Figure 5.37: Average, maximum, and minimum Ar<sup>8+</sup> beam currents, measured over a 100 ms period, for a varying extraction field maxima:  $B_{min} = 0.4$  T,  $P_{\mu} = 350$  W,  $p_{Ar} = 213$  nTorr. The dashed vertical line show where  $B_{Ext,max}/B_{RF} = 1.8$ . . . . 148

Figure 5.38: Trends of the average and standard deviations of the average extracted Ar<sup>8+</sup> beam current as the extraction field maximum is varied, normalized to the largest values in their respective sets:  $B_{min} = 0.4$  T,  $P_{\mu} = 350$  W,  $p_{Ar} = 213$  nTorr. The vertical dashed line shows where  $B_{Ext,max}/B_{RF} = 1.8$ . . . . . 149

Figure 5.39: Microwave power signals for a varying extraction field maxima: (Top Left)  $B_{Ext,max} = 0.99$  T, (Top Right)  $B_{Ext,max} = 1.07$  T, (Bottom Left)  $B_{Ext,max} = 1.15$  T, (Bottom Right)  $B_{Inj,max} = 1.23$  T.  $B_{min} = 0.4$  T,  $P_{\mu} = 350$  W,  $p_{Ar} = 213$  nTorr. Microwave power has been offset by it's minimum value, over the entire 100 ms measurement period, to account for the AC coupling of the oscilloscope. Signals have been treated with a digital low pass filter using the Matlab signal processing toolkit, with a cutoff frequency of 333 kHz. . . . . 150

Figure 5.40: Fourier transform of the microwave power signals emitted from the ion source for a varying extraction field maxima: (Top Left)  $B_{Ext,max} = 0.99$  T, (Top Right)  $B_{Ext,max} = 1.07$  T, (Bottom Left)  $B_{Ext,max} = 1.15$  T, (Bottom Right)  $B_{Inj,max} = 1.23$  T.  $B_{min} = 0.4$  T,  $P_{\mu} = 350$  W,  $p_{Ar} = 213$  nTorr. . . . . 151

Figure 5.41: Maximum output microwave power for a varying extraction field maxima:  $B_{min} = 0.4$  T,  $P_{\mu} = 350$  W,  $p_{Ar} = 213$  nTorr. The dashed vertical line shows where  $B_{Ext}/B_{RF} = 1.8$ . . . . . 151

Figure 5.42: Average and maximum output microwave power, measured over a 100 ms period, for a varying extraction field maxima:  $B_{min} = 0.4$  T,  $P_{\mu} = 350$  W,  $p_{Ar} = 213$  nTorr. The dashed vertical line shows where  $B_{Ext}/B_{RF} = 1.8$ . . . . . 152

Figure 5.43: Ar<sup>8+</sup> beam current for varying magnetic minimums (Top left)  $B_{min} = 0.34$  T, (Top right)  $B_{min} = 0.35$  T, (Bottom left)  $B_{min} = 0.37$  T, (Bottom Right)  $B_{min} = 0.4$  T.  $P_{\mu} = 350$  W,  $p_{Ar} = 213$  nTorr. Signals have been treated with a digital low pass filter using the Matlab signal processing toolkit, with a cutoff frequency of 333 kHz. . . . . 154

Figure 5.44: Ar<sup>8+</sup> beam current for varying magnetic minimums (Top left) B<sub>min</sub> = 0.43 T, (Top right) B<sub>min</sub> = 0.44 T, (Bottom left) B<sub>min</sub> = 0.46 T, (Bottom Right) B<sub>min</sub> = 0.47 T. P<sub>μ</sub> = 350 W, p<sub>Ar</sub> = 213 nTorr. Signals have been treated with a digital low pass filter using the Matlab signal processing toolkit, with a cutoff frequency of 333 kHz. . . . . 155

Figure 5.45: Average, maximum, and minimum Ar<sup>8+</sup> beam currents, measured over a 100 ms period, for a varying magnetic minimum. . . . . 156

Figure 5.46: Ar<sup>8+</sup> beam current for varying magnetic minimums (Top left) B<sub>min</sub> = 0.34 T, (Top right) B<sub>min</sub> = 0.35 T, (Bottom left) B<sub>min</sub> = 0.37 T, (Bottom Right) B<sub>min</sub> = 0.4 T. P<sub>μ</sub> = 350 W, p<sub>Ar</sub> = 213 nTorr. Microwave power has been offset by it's minimum value, over the entire 100 ms measurement period, to account for the AC coupling of the oscilloscope. Signals have been treated with a digital low pass filter using the Matlab signal processing toolkit, with a cutoff frequency of 333 kHz. . . . . 157

Figure 5.47: Ar<sup>8+</sup> beam current for varying magnetic minimums (Top left) B<sub>min</sub> = 0.43 T, (Top right) B<sub>min</sub> = 0.44 T, (Bottom left) B<sub>min</sub> = 0.46 T, (Bottom Right) B<sub>min</sub> = 0.47 T. P<sub>μ</sub> = 350 W, p<sub>Ar</sub> = 213 nTorr. Microwave power has been offset by it's minimum value, over the entire 100 ms measurement period, to account for the AC coupling of the oscilloscope. Signals have been treated with a digital low pass filter using the Matlab signal processing toolkit, with a cutoff frequency of 333 kHz. . . . . 158

Figure 5.48: Fourier transform of the microwave power signals emitted from the ion source for a varying magnetic minimums (Top left) B<sub>min</sub> = 0.34 T, (Top right) B<sub>min</sub> = 0.35 T, (Bottom left) B<sub>min</sub> = 0.37 T, (Bottom Right) B<sub>min</sub> = 0.4 T. P<sub>μ</sub> = 350 W, p<sub>Ar</sub> = 213 nTorr. . . . . 159

Figure 5.49: Fourier transform of the microwave power signals emitted from the ion source for a varying magnetic minimums (Top left) B<sub>min</sub> = 0.43 T, (Top right) B<sub>min</sub> = 0.44 T, (Bottom left) B<sub>min</sub> = 0.46 T, (Bottom Right) B<sub>min</sub> = 0.47 T. P<sub>μ</sub> = 350 W, p<sub>Ar</sub> = 213 nTorr . . . . . 159

Figure 5.50: Average and maximum output microwave power, measured over a 100 ms period, for a varying magnetic minimum. . . . . 160

Figure 5.51: The exponential decay time of the 'over-extracted' current scales roughly as q<sup>-2</sup>. The deviation can result from non-linear effects in the plasma, such as continuous heating, charge exchange, and ionizing collisions. B<sub>Hex,wall</sub> = 1.2 T, p<sub>Ar</sub> = 131 nTorr, For the red curve: P<sub>μ</sub> = 350 W. For the green curve: P<sub>μ</sub> = 250 W. . . . . 164

Figure B.1: Measured electron distribution for the measurements 'control' operating point. The 50 keV reliability threshold is shown by the dashed line.  $B_{\min} = 0.4$  T,  $B_{\text{Inj,max}} = 2.367$  T,  $B_{\text{Ext,max}} = 1.100$  T. . . . . 177

Figure B.2: Measured electron distribution for the measurements 'control' operating point. The 50 keV reliability threshold is shown by the dashed line.  $B_{\min} = 0.4$  T,  $B_{\text{Inj,max}} = 2.367$  T,  $B_{\text{Ext,max}} = 1.100$  T. . . . . 178

Figure B.3: Measured electron distribution for the measurements 'control' operating point. The 50 keV reliability threshold is shown by the dashed line.  $B_{\min} = 0.4$  T,  $B_{\text{Inj,max}} = 2.367$  T,  $B_{\text{Ext,max}} = 1.100$  T. . . . . 178

Figure C.1: A varying extraction voltage has little effect on the hot-electron bremsstrahlung distribution. The count rate and bremsstrahlung are much more stable than in figure 4.1 due to the much more consistent background during the measurement. The stability of the nuclear peak at 510 keV demonstrates this most clearly. Plasma parameters are  $B_{\min} = 0.397$  T,  $P = 350$  W,  $T_{\text{live}} = 600$  s, pressure = 212 nTorr. . . . . 179

Figure C.2: A varying magnetic field does not appreciably change how the injected microwave power affects the measured electron distributions. . . . . 180

Figure C.3: Similar to figure C.2, a varying magnetic field does not appreciably change how the injected microwave power affects the measured bremsstrahlung distributions. . . . . 180

Figure C.4: All field distributions agree to a linear increase in the number of measured particles with respect to the microwave power. Although a small change in the spectral temperature is seen as the injection side magnetic field is varied, the overall trend indicates an insensitivity of electron energy to microwave power. 181

Figure C.5: All field distributions agree to a close to linear increase in the number of measured particles with respect to the microwave power. Although a small change in the spectral temperature is seen as the injection side magnetic field is varied, the overall trend indicates an insensitivity of electron energy to microwave power. . . . . 181

Figure C.6: The dependence of the high energy electron distribution on pressure was not appreciably affected by a varying longitudinal field profile. Although out of the scope of this study, it should be recognized that low energy portion of the distribution ( $E_{\text{kin}} < 70\text{keV}$ ) is affected by the both the pressure and the average magnetic field within the source chamber. . . . . 182

Figure C.7: The dependence of the bremsstrahlung distribution on pressure was not appreciably affected by a varying longitudinal field profile. . . . . 183

Figure C.8: All measurements agreed to the same overall trend, regardless of longitudinal field profile. . . . .	183
Figure C.9: All measurements agreed to the same overall trend, regardless of longitudinal field profile. . . . .	184
Figure C.10: There was a greater effect upon the measured electron distribution's height as a function of the radial magnetic field maximum as the magnetic minimum increased. . . . .	184
Figure C.11: The longitudinal magnetic field had no effect on the measured bremsstrahlung distribution for high energy photons. . . . .	185
Figure C.12: Comparison between the electron peak energy/intensity and bremsstrahlung spectral temperature/total photon counts for across multiple ion source longitudinal magnetic field profiles with varying radial field maximum. . . . .	185
Figure C.13: Comparison between the electron peak energy/intensity and bremsstrahlung spectral temperature/total photon counts for across multiple ion source longitudinal magnetic field profiles with varying radial field maximum. . . . .	186
Figure D.1: Measured electron distribution for the measurements 'control' operating point. The 50 keV reliability threshold is shown by the dashed line. $B_{\min} = 0.4$ T, $B_{\text{Inj,max}} = 2.367$ T, $B_{\text{Ext,max}} = 1.100$ T. . . . .	187
Figure D.2: Measured electron distribution for the measurements 'control' operating point. The 50 keV reliability threshold is shown by the dashed line. $B_{\min} = 0.4$ T, $B_{\text{Inj,max}} = 2.367$ T, $B_{\text{Ext,max}} = 1.100$ T. . . . .	187
Figure D.3: Measured electron distribution for the measurements 'control' operating point. The 50 keV reliability threshold is shown by the dashed line. $B_{\min} = 0.4$ T, $B_{\text{Inj,max}} = 2.367$ T, $B_{\text{Ext,max}} = 1.100$ T. . . . .	188
Figure D.4: Measured electron distribution for the measurements 'control' operating point. The 50 keV reliability threshold is shown by the dashed line. $B_{\min} = 0.4$ T, $B_{\text{Inj,max}} = 2.367$ T, $B_{\text{Ext,max}} = 1.100$ T. . . . .	188

# CHAPTER 1

## INTRODUCTION

The ability to produce and accelerate charged particles has become an invaluable tool in many industries worldwide. Nuclear and particle physics research facilities, medical treatment facilities (such as proton and carbon therapy facilities), and semiconductor fabricators all use energetic electrons and ions throughout their day to day operations [7]. As such, the research and development of ion sources are essential for many scientific and engineering applications.

Many nuclear and particle physics research facilities rely upon producing high intensity, high charge state ions for their operations. Accelerating highly charged ion beams is overall more efficient, as the electric force that a particle feels is directly proportional to its charge. Furthermore, the production of large currents increases the probability of producing and meaningfully observing rare isotopes. In many cases, scientists and engineers will turn to the Electron Cyclotron Resonance Ion Source (ECRIS) for their facility's needs. Invented in 1974 by Richard Geller, the devices quickly proved themselves to be powerful and reliable sources of highly charged ions [7]. The most modern and advanced of these sources can produce 100's  $e\mu\text{A}$  of uranium ion beams for use in accelerator facilities. For example, the VENUS and SECRA ion sources can produce up to 320  $e\mu\text{A}$  of  $\text{Xe}^{20+}$  [42] and 360  $e\mu\text{A}$  of  $\text{Xe}^{30+}$  [101], respectively.

The guiding principle of the ECRIS is rather straightforward: ignite and heat a magnetized plasma and then extract ions produced therein. Microwaves heat the plasma's electrons through the process of Electron Cyclotron Resonance (ECR). This process occurs as electromagnetic radiation interacts with electrons gyrating about magnetic field lines. The transferred energy is, principally, stored in the electrons' gyromotion. With stronger magnetic fields, the maximum stored energy increases. The heated electrons can then inelastically collide with atoms and low charge state ions to bring about electron impact ionization. Through this mechanism, and with large enough magnetic fields, it is possible to strip even the heaviest of ions of most, if not all, of their orbital electrons.

Nevertheless, behind this straight forward approach lie complications capable of crippling ion source, and facility, operations. Under large enough magnetic fields, the electrons within the system can suddenly release all the energy stored within their rotational motion. These kinetic instabilities, caused by imbalances in the temperature distributions of electrons throughout the plasma, cause sudden losses of extracted ion currents [81]. Overall, the instabilities limit the performance of ECR ion sources.

As beam current stability is of vital importance for many ion source applications, these plasma instabilities create limitations on ECR ion sources' performance. This study seeks to better understand these limiting plasma instabilities by studying the ion source plasma's response to various ranges of source parameters. Plasma and beam current diagnostics gathered data across a series of measurements of both stable and unstable plasmas. This data provided insight into the diffusion mechanisms of plasma electrons and ways to optimize the ion source's performance.

This discussion in this thesis is broken down across five chapters. It begins in chapter 2 with a discussion of ECR ion source plasmas, including the underlying plasma physics, operating principles, and microinstabilities that cause losses of high energy electrons. Chapter 3 discusses the experimental apparatuses and procedures used throughout this study. Chapters 4 and 5 discuss the results of these measurements. Chapter 6 concludes this thesis by briefly discussing the ramifications of the results of these measurements on our understanding of ECRIS operations.



## CHAPTER 2

### ELECTRON CYCLOTRON RESONANCE ION SOURCES

#### 2.1 Plasma Physics

Before entering the heart of this study (or even just its introduction), it is important to understand some underlying concepts from plasma physics. Many authors have described and derived the critical aspects of plasma physics on a fundamental level (see [5], [44]). Others have followed in Geller's [18] footsteps and have written specifically on aspects of plasma physics relevant to ECR ion sources [88] or ECR heating in general (see [22, 29, 43, 59]). As such, the good work of others is referenced for in-depth discussions of plasma effects and interactions in ECR heating environments, and in general. The focus of this section is to reduce down their work to the material most relevant for the discussion at hand.

A plasma is the so-called fourth state of matter. It is a state where, as most simply described by Lieberman [44], is "a collection of free charged particles moving in random directions that is, on average, electrically neutral." As a gaseous substance gains energy, it can eventually break apart into a collection of electrons and ions. Although broken up into individual charges, the material as a whole remains neutral. Magnetic fields can ensure that the system stays confined to one region of space. However, the individual charges remain unbounded within the plasma. As such, they oscillate about field lines and undergo multiple collisions. The collisions can lead to diffusion along and across magnetic field lines. The high mobility of the unbound charges gives the plasma unique electronic characteristics; along its surface and through its volume. These unique characteristics give rise to a variety of wave-plasma interactions, both globally and for individual particles.

The remainder of this section focused on the building blocks of plasma physics, which underline ECR ion sources' operation. We will begin by discussing magnetic confinement, oscillations and collisions, and then diffusion. The last two sections focus specifically on plasma field interactions; through discussions of plasma permittivity and then plasma wave propagation.

### 2.1.1 Magnetic Confinement

Electrostatics do not provide stable confinement of charged particles; proper confinement requires a magnetic field. In particular, the magnetic mirror is a simple and straightforward method of confining charged particles within a region of space. A charged particle acquires a magnetic moment,  $|\vec{M}| = IA$ , as it gyrates about a magnetic field line. The magnetic moment is an invariant of motion and is conserved [5]. As such:

$$\vec{M} = -\frac{W_{\perp}}{B^2}\vec{B} = \text{const}, \quad (2.1)$$

where  $W_{\perp} = \frac{1}{2}mv_{\perp}^2$  is the energy of the perpendicular motion of the charge and  $B$  is the local magnetic field strength.

As the charged particle moves through space, towards increasing magnetic fields, it will see its transverse energy increase to keep its magnetic moment and total energy constant. It does this by decreasing its energy parallel to the magnetic field lines,  $W_{\parallel}$ . A large enough magnetic field can convert all the particle's longitudinal energy to rotational energy. At this point, the electron will reverse direction and move along the external magnetic field lines towards a region with lower magnetic flux. That field maximum causes the electron to "reflect" backward into regions with lower magnetic fields. We call that magnetic field  $B_{\text{mirr}}$ . This, of course, does require there to be a magnetic field maximum capable of causing the mirroring effect. If the longitudinal momentum of the charge is too large, then the particle can penetrate through the magnetic maximum.

Now suppose we co-axially align two magnetic mirrors with some spatial separation, as seen in figure 2.1. By combining the requirements of conservation of energy and magnetic moment, it can be shown that a charged particle will remain confined if:

$$\frac{B_{\text{min}}}{B_{\text{max}}} = \frac{1}{R} > \frac{v_{\perp}^2}{v^2} = \sin^2 \alpha_0 \quad (2.2)$$

where,  $B_{\text{min}}$  is the minimum magnetic field the particle interacts with,  $B_{\text{max}}$  is the maximum magnetic field strength in the system (representing the last place where the particle can reverse direction before escaping),  $R$  is the so-called mirror ratio, and  $\alpha_0$  is the pitch angle defining the

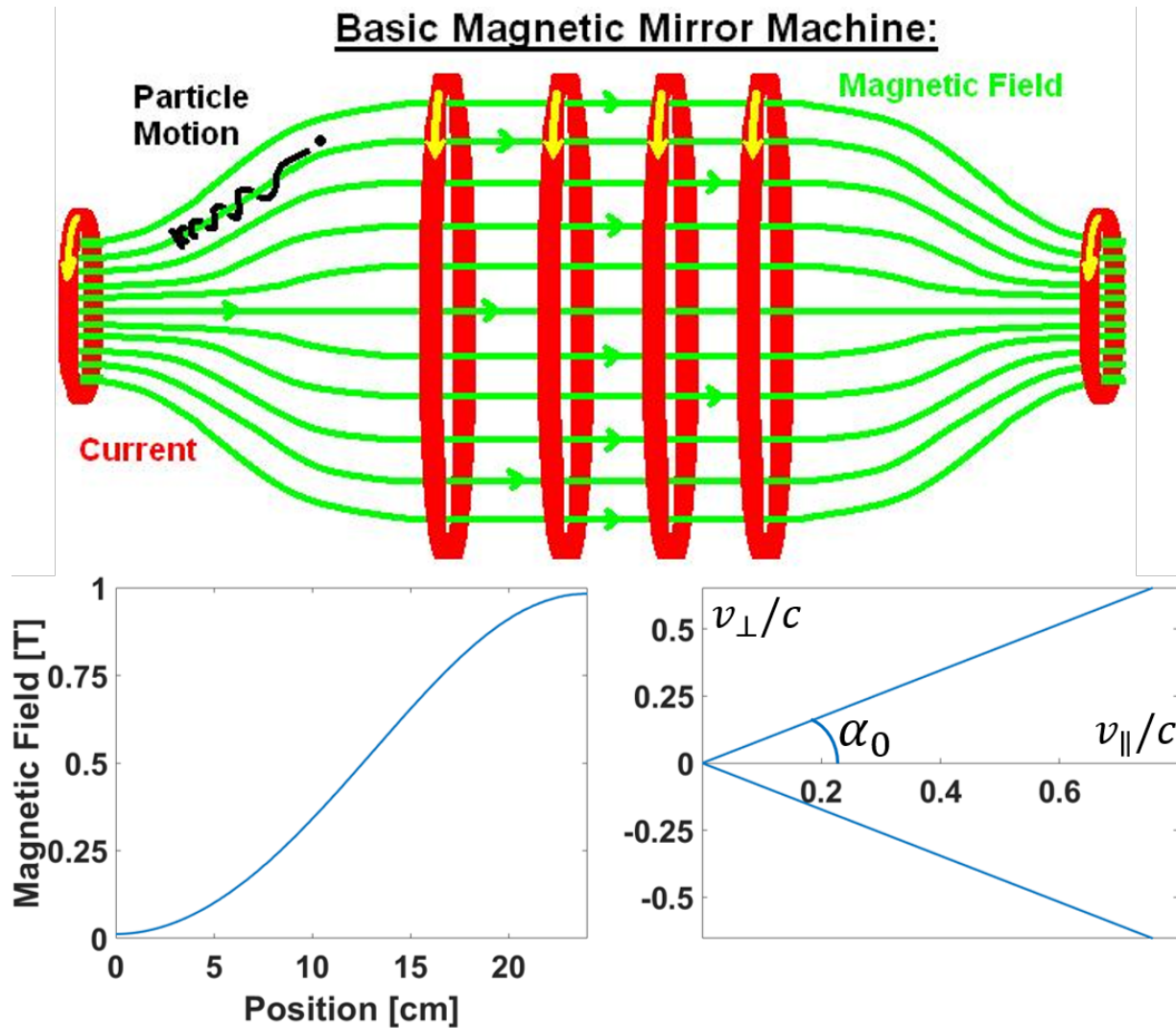


Figure 2.1: The series of solenoids generates a semi-uniform magnetic field. The field strength reaches a minimum at some point between the centers of the coils, represented by the less dense field lines (top). The bottom left plot shows an example field profile from the center of the above configuration to the center of the last coil. The bottom right plot shows an example loss cone.

system's loss cone. If the particle exists within the cone, then it is capable of escaping from the plasma. However, any particles outside of the loss cone will remain confined until they are scattered into the loss cone [68]. This confinement configuration is known as the magnetic bottle.

The formalism for the magnetic bottle does a good job describing confinement on a particle-by-particle basis. Although it is sometimes useful to think about confinement from the thermodynamic

perspective. To that end, we can describe the macroscopic stability of the plasma by [5]:

$$\beta = \frac{n_e k_B T_e}{\frac{B_0^2}{2\mu_0}} \quad (2.3)$$

where,  $k_B$  is Boltzmann's constant,  $T_e$  is the electron distribution temperature, and  $B_0$  is the field strength at the plasma boundary. The parameter  $\beta$  is the ratio of plasma kinetic pressure to the magnetic pressure at the boundary of the plasma. So long as  $\beta \ll 1$  the plasma will be confined. At higher values, the kinetic pressure overtakes the magnetic pressure, and the plasma becomes macroscopically unstable. This method of analyzing confinement does not provide insight into the particle-field interaction. It is, however, very useful from a global perspective. Particularly when it is difficult to ascertain details about the individual particles in a system.

### 2.1.2 Oscillations and Collisions

Small electrostatic perturbations within the plasma bring about spatial oscillations of charges. The charged particles oscillate with what is called the plasma frequency:

$$\omega_p = \sqrt{\frac{nq^2}{m\epsilon_0}} \quad (2.4)$$

where  $n$  is the charged particle density,  $q$  and  $m$  are the particle's charge and mass, respectively, and  $\epsilon_0$  is the permittivity of free space. In most cases, it is the lighter electrons which oscillate around the heavier ions ( $m_p/m_e \sim 2000$ ). As such, the electron-plasma frequency,  $\omega_{pe}$  is often used as the plasma frequency.

As described by Lorentz's force law, charged particles moving perpendicular to magnetic field lines will feel a force that causes oscillation around the field lines. The frequency of oscillation about the magnetic lines of force is known as the particle's cyclotron frequency:

$$\omega_c = 2\pi f_c = \frac{qB}{\gamma m} = \frac{\Omega_c}{\gamma} \quad (2.5)$$

where  $B$  is the local magnetic field strength,  $\gamma$  is the Lorentz factor:  $(1 - v^2/c^2)^{-\frac{1}{2}}$ , where  $c$  is the speed of light in vacuum, and  $\Omega_c$  is the classical gyro frequency (sometimes called the 'cold' gyro

frequency). It is handy to know that the classical electron gyro frequency is well approximated by the relation:

$$f_{ce}(GHz) \approx 28B.$$

where B is the magnetic field in T. Likewise, the classical ion cyclotron frequency can be approximated by:

$$f_{ci}(MHz) \approx \frac{3.8qB}{A}$$

where q and A are the charge state and mass number, respectively.

The collision frequency describes how often, on average, a single particle will collide with another particle. In general it is given by [64]:

$$\nu_c = n_a \langle \sigma v_b \rangle = \frac{n_a}{n_b} \int v_b f_b(v_b) \sigma d^3v \quad (2.6)$$

where  $n_a$  is the target particle density,  $n_b$  is the incoming particle density,  $\sigma$  is the cross-section of interaction for a particular type of collision or interaction,  $f_b$  is the velocity distribution function of the incoming particles, and  $v_b$  is the incoming particle velocity. The rate of collisions per unit volume is then given by:

$$R_c = n_b \nu_c = n_b n_a \langle \sigma v_b \rangle. \quad (2.7)$$

We can apply equation 2.6 to various different types of collisions. These include electron-electron (ee) collisions, electron-ion (ei) collisions, ion-ion (ii), and neutral-electron (ne) or neutral-ion (ni) collisions. For the moment, I will discuss electron-electron and ion-ion collisions. A discussion on electron-ion and ion-neutral collisions is saved for section 2.2.2. Electron-electron and ion-ion collisions are both elastic collisions dictated by the coulomb interaction.

For electrons, this interaction can be approximated by the frequency of collisions which cause the electrons to deflect at a 90° angle [21]:

$$\langle \nu_{ee}^{90} \rangle \approx \frac{n_e e^4 \ln \Lambda}{\epsilon_0 m_e^{1/2} T_e^{3/2}} \quad (2.8)$$

where  $T_e$  is the electron temperature in eV and  $\ln \Lambda$  is the so-called coulomb logarithm. It can be shown that  $\Lambda \sim n_e \lambda_D$  [21]. It is usually assumed that  $\ln \Lambda \approx 10 - 12$  in ECRIS plasmas. The

ion-ion collision rate can be similarly calculated by [53]:

$$\langle v_{ij} \rangle \approx \frac{6.8 \times 10^{-8} \ln \Lambda_{ij} q_i^2}{T_i^{3/2}} \sum_j \sqrt{A_j} \sum_q n_j^q q_j^2$$

where the 'ij' indices indicate the collisions of the moving ion 'i' on the target ion of species 'j'.

By assuming a single species, quasi-neutral plasma we can write the collision frequency as:

$$\langle v_{ii} \rangle \approx \frac{6.8 \times 10^{-8} \ln \Lambda_{ij} * q^2 n_e \bar{q}}{T_i^{3/2} \sqrt{A_i}} \quad (2.9)$$

where the quasi-nutrality allows us to define  $n_e \bar{q} = \sum_q n_j^q q_j^2$ , which is the mean-effective charge of the plasma.

The three quantities above, the plasma, cyclotron, and collision frequencies, dictate the movement of an electron or ion within a plasma. The mechanism which dominates the time scales of a plasma is dependent upon its density, degree of ionization, and temperature. In the case of a magnetized plasma, the constraints of the externally applied magnetic field or internal charge currents will also help govern the kinematics of individual charges. The effect which produces the highest overall frequency will be the one which determines the equation of motion for a given charge species. The dominant timescales for the electron and ion populations are estimated in sections 2.2.3 and 2.2.4.

### 2.1.3 Plasma Diffusion

The previous section showed a selection of the various types of collisions that can affect charged particles. These collisions are responsible for determining how particles move throughout the plasma. In general, collisions are largely responsible for the ways that electrons diffuse out of the plasma.

Plasma pressure gradients and collisions can lead to diffusion of charges out of the plasma. For example, the rate of change of the electron density can be described through Fick's Law as:

$$\frac{\partial n_e}{\partial t} \approx D_e \nabla^2 n_e \quad (2.10)$$

where

$$D_e = \frac{k_B T_e}{m_e \nu_c} \quad (2.11)$$

is the electron free-diffusion coefficient [5]. The presence of a magnetic field changes the situation, of course, primarily by making the diffusion anisotropic. If there is a uniform magnetic field  $\vec{B} = B_0 \hat{z}$  within the plasma, then the diffusion coefficients perpendicular and parallel to the magnetic field lines go as:

$$D_{\perp} = \frac{\nu_c^2}{\nu_c^2 + \Omega_{ce}^2} D_e \quad (2.12)$$

$$D_{\parallel} = D_e,$$

where  $\nu_c$  is the effective electron collision frequency and  $\Omega_{ce}$  is the cold (non-relativistic) electron cyclotron frequency. Using these diffusion coefficients, it can be shown that:

$$\frac{\partial n_e}{\partial t} = D_{\perp} \left( \frac{\partial^2 n_e}{\partial x^2} + \frac{\partial^2 n_e}{\partial y^2} \right) + D_e \frac{\partial^2 n_e}{\partial z^2}.$$

The diffusion coefficients in equations 2.11 and 2.12 further demonstrate the confining characteristics of the magnetic fields.  $D_{\perp}$  decreases as  $B_0^{-2}$ , compared to  $D_e$ , which is not directly affected by the magnetic field. As a result, systems with large magnetic field strengths favor diffusion along magnetic field lines rather than across them.

Equation 2.11 is equally valid for ions as it is for electrons, exchanging the electron mass, temperature, and collision frequency for those of ions. It is often the case that  $D_e > D_i$  due to the mass difference between electrons and ions. This, of course, means that electrons will diffuse out of the plasma faster than ions. The electric imbalance that results from the species diffusion imbalance causes ambipolar diffusion [5]. The electric field, which is generated by the charge imbalance, couples the ion and electron diffusion equations. The resulting diffusion coefficient is:

$$D_a = \frac{k_B(T_e + T_i)}{m_e \nu_e + m_i \nu_i}. \quad (2.13)$$

In the case of a fully ionized plasma, the diffusion across magnetic field lines goes as [5]:

$$D_{\perp} = \frac{nk_B(T_e + T_i)}{e^2 B_0^2} \nu_c. \quad (2.14)$$

Once again, we predict that  $D \sim B^{-2}$ . However, experiments show that the diffusion coefficient will more often go as  $B^{-1}$ . To compensate for this, Bohm determined the semiempirical formula [5]:

$$D_{\perp} = D_B = \frac{k_B T_e}{16eB}. \quad (2.15)$$

This particular type of diffusion is known as Bohm diffusion.

Lastly, this leads to a discussion on the topic of mobility. Here, mobility is defined as the ratio of a particles drift velocity to the force which causes the drift:

$$\mu_d = \frac{|v_d|}{|F|}$$

It is related to the diffusion coefficient through Einsteins relation, which states [64]:

$$D = \mu_d k_B T \quad (2.16)$$

Through this, we can rewrite the mobility to take the form:

$$\mu_d = \frac{1}{m\nu_{eff}} \quad (2.17)$$

where  $\nu_{eff}$  is the effective particle collision frequency. The mobility is valuable qualitatively as a way to compare the movements of different plasma species to one another. For example, electrons will generally have a higher mobility than ions, due to the factor of 2000 difference in mass between nucleons and electrons.

#### 2.1.4 Electronic Properties of the Plasma

One of the more interesting properties of plasmas is their ability to act as either a conductor or a dielectric medium. These are both due to the electrons' ability to move throughout the plasma volume freely. Generally speaking, plasma electrons are attracted to and attempt to surround the positively charged ions. If an external electric field is present, the electrons will move around the ion to compensate for the electric perturbation. This effectively creates an electronic shield around the ion, which will screen incoming electric field lines. This well-known phenomenon is



known as Debye Shielding [5, 21, 96]. If we assume the area around the ion follows the Boltzmann distribution,  $n_e(r) = n_{e0} \exp(e\Phi(r)/k_B T_e)$ , it can be shown that:

$$\Phi(r) = \frac{q}{r} e^{-\frac{r}{\lambda_D}}$$

where  $\Phi$  is the local electric potential,  $q$  is the ion charge, and  $\lambda_D$  is Debye's length, given by:

$$\lambda_D = \sqrt{\frac{\epsilon_0 k_B T_e}{e^2 n_e}}. \quad (2.18)$$

Qualitatively, Debye's length describes the distance over which electrostatic perturbations will penetrate through the plasma [5].

In the absence of a magnetic field a plasma will act like an isotropic conductor and dielectric with their respective constants being [5, 80]:

$$\sigma_0 = \frac{n_e e^2}{m_e (\nu_c - i\omega)}$$

and

$$\epsilon = \epsilon_0 - \frac{\sigma_0}{i\omega} = \epsilon_0 \left( 1 - \frac{i}{\omega} \frac{\omega_{pe}^2}{(\nu_c - i\omega)} \right)$$

where  $\omega$  is the frequency of some propagating electromagnetic wave, should it exist. The presence of magnetic fields changes this, principally by giving the plasma anisotropic conductive and dielectric properties. As a result, we must generalize the conductive and dielectric constants in the form of tensors [5, 80]. Here, we will focus on the dielectric tensor, as it is the overwhelmingly more important quantity for this study. For simplicity assume a cold (non-relativistic) plasma in the presence of a static magnetic field  $\vec{B} = B_0 \hat{z}$ . Ignoring ion motion, it can be shown that:

$$\epsilon = \epsilon_0 \begin{pmatrix} \epsilon_1 & -\epsilon_2 & 0 \\ \epsilon_2 & \epsilon_1 & 0 \\ 0 & 0 & \epsilon_3 \end{pmatrix} \quad (2.19)$$

where

$$\epsilon_1 = 1 + \frac{i}{\omega} \frac{\omega_{pe}^2 (\nu_c - i\omega)}{(\nu_c - i\omega)^2 + \Omega_{ce}^2}$$

$$\epsilon_2 = \frac{i}{\omega} \frac{\omega_{pe}^2 \omega_{ce}}{(\nu_c - i\omega)^2 + \Omega_{ce}^2}$$

$$\epsilon_3 = 1 + \frac{i}{\omega} \frac{\omega_{pe}^2}{(\nu_c - i\omega)}.$$

### 2.1.5 Plasma Waves

The wave equation for propagating electromagnetic waves can be derived from Maxwell's equation, assuming an isotropic dielectric constant [80]. However, the presence of a magnetic field causes the dielectric properties of the plasma to become anisotropic [5]. As a result, the wave propagation will be directly affected by its relationship to the external magnetic field.

There are two ways that a wave's relationship with the plasma can be determined. The first method involves solving Maxwell's equations while considering the plasma to be either a dielectric or conductive material. This method explicitly solves the wave equation for the plasma. The second method is to solve Maxwell's equations with a fluid model of the plasma [5]. The latter case does not provide an explicit solution to the wave equation. However, both methods provide the dispersion relationship for the plasma,  $\omega(\vec{k})$ .

The dispersion relationship is the more useful relationship for this study. The exact wave interactions for ECRIS plasmas are unknown, as the medium has a complicated, inhomogeneous magnetic field. On the other hand, the range of possible electron cyclotron frequencies is well known, and the system's plasma frequency can be estimated [56]. Together these make the fluid description of the plasma more useful as the dispersion relationship determines the frequency and polarization of propagating waves [39].

The dispersion of electromagnetic waves in a plasma is governed by the Altar-Appleton equation which determines the index of refraction for a plasma [5, 39]:

$$N_{\pm}^2 = k^2 c^2 / \omega^2 = 1 - \frac{2X(U - X)}{2U(U - X) - Y^2 \sin^2 \theta \pm \Delta} \quad (2.20)$$

where

$$\Delta = \sqrt{Y^4 \sin^4 \theta + 4Y^2(U - X)^2 \cos^2 \theta}$$

and  $X = (\omega_{pe}/\omega)^2$ ,  $Y = \Omega_{ce}/\omega$ ,  $U = 1 + i\nu_e/\omega$ ,  $\omega$  is the angular frequency of the propagating electromagnetic mode,  $\nu_e$  is the effective electron collision frequency, and  $\theta$  is the angle at which it propagates relative to the external magnetic field. This equation is valid in the cold plasma approximation, where charges are assumed to be stationary within a homogeneous plasma [5]. While the ECRIS plasma is neither cold nor homogeneous (due to the magnetic field), the equation can approximate the wave relationship in local areas within the plasma.

Individually,  $\omega$  and  $\vec{k}$  describe how a wave propagates through time and space, respectively. More precisely, assuming a plane wave,  $\vec{E} \sim \exp\left(i\left(\vec{k} \cdot \vec{x} - \omega t\right)\right)$ , where  $i = \sqrt{-1}$ . However, there is nothing that demands that either  $\omega$  or  $\vec{k}$  be real valued. In general form of either quantity is  $\omega = \omega_r + i\omega_i$  and  $\vec{k} = \vec{k}_r + i\vec{k}_i$ , where the subscripts  $r$  and  $i$  denote the real and imaginary components of either quantity [8]. The imaginary components add a new dynamic to the propagating wave by allowing it to grow or decay in time or space. Generally speaking, a wave is unstable if it grows exponentially either temporally or spatially. However, since both  $\omega$  and  $\vec{k}$  may be complex simultaneously, determining if a particular wave is unstable is not always a straightforward process [80]. For simplicity, we will assume that  $\vec{k}_i = 0$  within the ECR plasma. Thus, all instabilities are time-like and occur only when  $\omega_i > 0$ .

The propagation direction of a wave determines many of its properties as well. In the case of a longitudinally propagating wave ( $\theta = 0$ ), the plus and minus sign in equation 2.20 denote left-handed (L) and right-handed (R) circularly polarized waves, respectively. For transversely propagating waves ( $\theta = \pi/2$ ), the plus sign denotes ordinary waves (O) and the minus sign extraordinary waves (X). The extraordinary wave has an upper and lower branch as well. Traditionally, the upper branch of the extraordinary mode is called the X-mode with the lower branch called the Z-mode [37]. The distinction is most common among space plasma physicists but will also be used here [80]. Figure 2.2 shows an example calculation of the dispersion relationship for O-, X-, and Z-mode waves.

Using equation 2.20 we find various cutoffs ( $N = 0$ ) and resonances ( $N = \text{inf}$ ) that result from the plasma dispersion. Ignoring ion motion, for propagation parallel to magnetic field lines  $\theta = 0$  we find that the R wave resonates at  $\omega = \Omega_{ce}$  and is cutoff at  $\omega = \omega_{pe}$  [5, 37]. This phenomena

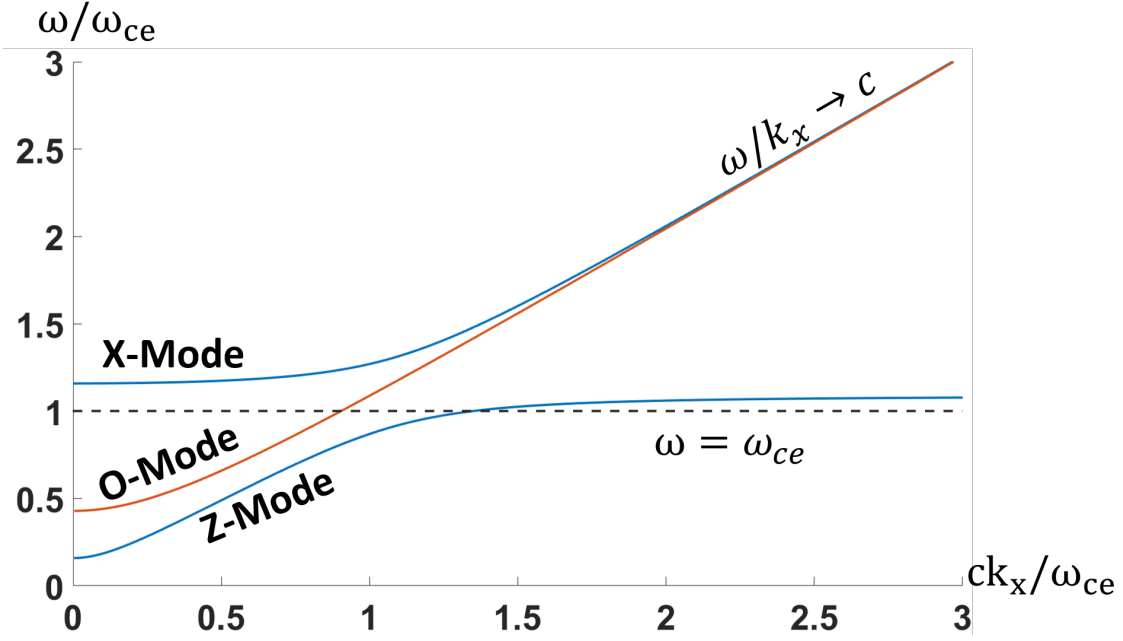


Figure 2.2: The dispersion relation for an under dense plasma ( $\omega_{ce} > \omega_{pe}$ ).

is known as electron cyclotron resonance and will be discussed further in section 2.2.1. For perpendicular propagation, resonance for the Z-mode occurs at the upper hybrid frequency,  $f_{uh}$ . The Z-mode has a lower cutoff at  $f_z$ . The X-mode propagates above its lower cutoff frequency  $f_x$ . For propagation at angles  $0 < \theta < \frac{\pi}{2}$ , the Z-mode resonance changes to be the so-called Z-infinity, denoted by  $f_{ZI}$  [37]. The Z-infinity, in truth, is a generalization of the upper hybrid frequency for oblique propagation. Those cutoffs and resonances are given in equation 2.21.

$$\begin{aligned}
 f_{uh} &= \sqrt{f_{pe}^2 + f_{ce}^2} \\
 f_z &= \frac{f_{ce}}{2} \left( -1 + \sqrt{1 + 4 \frac{f_{pe}^2}{f_{ce}^2}} \right) \\
 f_x &= \frac{f_{ce}}{2} \left( 1 + \sqrt{1 + 4 \frac{f_{pe}^2}{f_{ce}^2}} \right) = f_z + f_{ce} \\
 f_{ZI} &= \frac{1}{\sqrt{2}} \sqrt{f_{uh}^2 + \sqrt{f_{uh}^4 - 4 f_{ce}^2 f_{pe}^2} \cos^2 \theta}
 \end{aligned} \tag{2.21}$$

## 2.2 Electron Cyclotron Resonance Ion Sources and their Plasmas

The electron cyclotron resonance ion source is an open ended mirror machine designed for the purpose of producing beams of high charge state ions. It does this by creating magnetic field structure that allows for cyclotron resonance heating of electrons within the plasma chamber [18]. The most powerful of these sources are capable of producing milliamperes of high charge state currents for a range of ion mass species [79]. The most advanced sources rely upon cutting edge advances in electrical, mechanical, microwave, and cryogenic engineering. The bare minimum requirements to produce an ECRIS plasma, however, are rather minimal:

- Confining Magnetic Field
- Microwave Power
- Adequate Neutral Gas or Vapor Pressure

The magnetic field allows for resonant heating, which produces a wide, non-Maxwellian distribution of electrons. A part of this distribution collides with low charge state ions and atomic species to produce highly charged ions through electron impact ionization. Finally, an extraction system accelerates ions away from the plasma and produces a beam. This next section will focus on how electron heating and the ionization of atomic species produce the plasma properties of the ECRIS plasma. Chapter 3 discusses specific confinement and extraction details.

### 2.2.1 Resonant Heating of Electrons Within ECR Ion Sources

ECR ion sources rely upon the process of electron cyclotron resonance in order to stochastically heat electrons. This process occurs as electromagnetic radiation propagating through the plasma collides with electrons gyrating along magnetic field lines. The electrons will resonate with and gain energy from the EM radiation if [28, 97]:

$$\omega_{RF} = \omega_{ce}(1 \pm N_{\parallel}\beta_{\parallel}) \quad (2.22)$$

where  $N_{\parallel}$  is the longitudinal index of refraction and  $\beta_{\parallel} = v_{\parallel}/c$  is the electron's velocity, parallel to the external magnetic field, normalized by the speed of light. The resonance interaction, principally, heats the electrons transversely. This being due to the acceleration coming from the right handed polarized component of the incoming wave. However, the electron will see an increase in its longitudinal velocity due to the wave's magnetic field [20]. At very high energies this interaction converts perpendicular energy into longitudinal energy; resulting in pitch angle scattering.

The ECR ion source uses a combination of a series of co-linear solenoids and a hexapole magnet in order to produce a magnetic field. This superposition of fields serves two purposes: heating and confinement of electrons. Section 2.3.1 discusses the confinement properties of this magnetic field geometry.

In general, the solenoids create a two peak magnetic field distribution; a non-zero minimum exists between the two peaks (Fig. 2.3). The three extrema must have values such that there is a magnetic field between them that will allow electrons to resonate with the incoming microwave radiation.  $B_{RF}$  denotes the field strength where this interaction occurs.<sup>1</sup> It is often the case that the heating frequency used to heat the electrons acts as a constraint upon the confining magnetic field. As a consequence of this, ECRIS plasmas are often compared to one another by the ratio  $B_{min}/B_{RF}$  used during operation.<sup>2</sup> The addition of the hexapole causes the magnetic field to increase away from the longitudinal axis of the plasma chamber. Together, these coils create what is known as the Minimum-B field structure (Min-B, Fig. 2.4). This 3D field creates a closed surface for heating the electrons (Fig. 2.5).<sup>3</sup>

---

<sup>1</sup>It is more common to use the symbol  $B_{ECR}$  to denote the magnetic field where resonance occurs. The resonance condition is velocity/energy-dependent, however, and what authors *really* mean when they say  $B_{ECR}$  is 'the magnetic field where non-relativistic resonance occurs'. As such, this discussion uses  $B_{RF}$  as it is more representative of what authors mean in the literature: 'the field strength for classical electron resonance between the plasma and the microwave power I injected into the system'.

<sup>2</sup>The relative height of each extremum to one another is also important but this discussion is outside the scope of the current topic. See Sec. 2.3.4 for more details.

<sup>3</sup>For more details on the specific ion source which created these fields, see section 3.1.

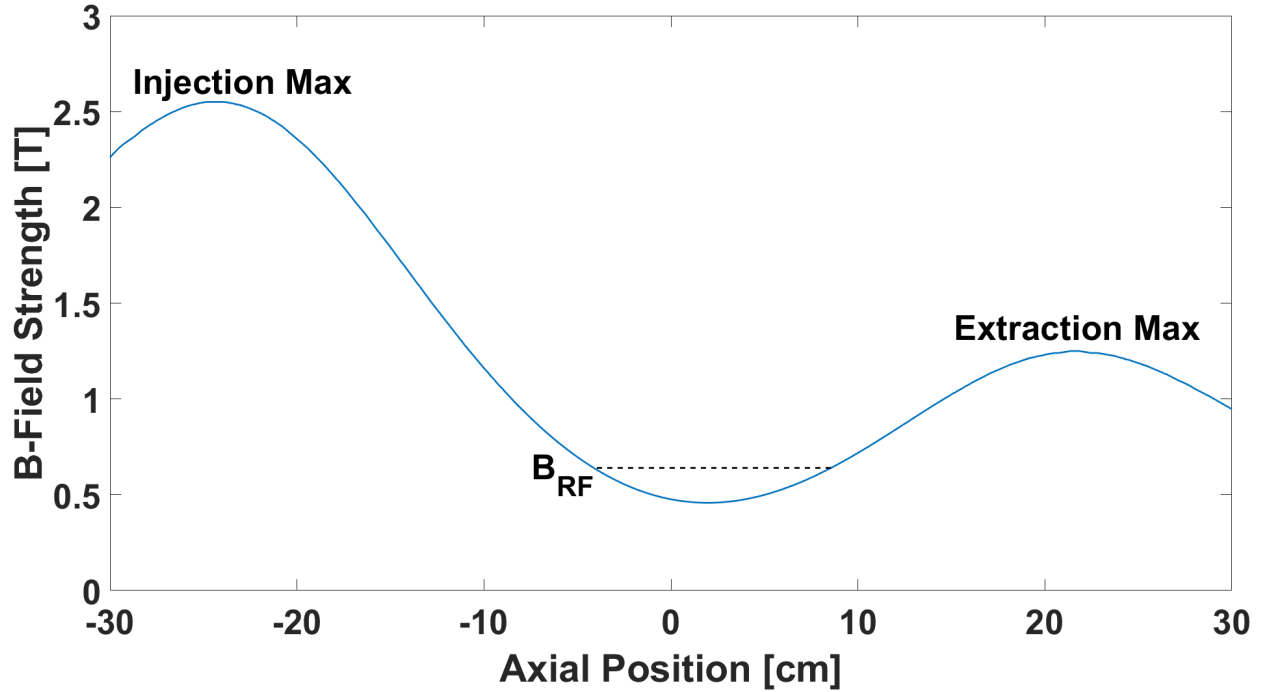


Figure 2.3: A 2D projection of the typical operational magnetic field across the central axis of the SuSI ECR ion source at the NSCL. This data was generated using the program POISSON/Superfish.

The Min-B field structure is a complicated, inhomogeneous field topology that makes many properties of the plasma difficult to calculate, or even describe. Part of that complication manifests in the stochastic heating of electrons. For our purposes, a stochastic system is a system that evolves in time through random interactions [12]. The energy of electrons within the ECR plasma is a good example of this. Ideally, electrons will undergo numerous random collisions during their 'life-time' in the plasma, the period over which the electron is first confined to when it escapes confinement. We want this to happen for two reasons. First, the electrons need to impact atomic species to produce ions. Secondly, collisions make the global heating process more efficient [59] by randomizing the gyration phase of electrons with respect to the incoming RF. As a result, the heating process occurs over multiple passes through the ECR region.

Mathematically, relativistic effects make it possible to heat electrons when  $B_{min} > B_{RF}$ . In practice, however, the energy of these electrons is too high to sustain the plasma. While relativistic heating is impractical, it is important to remember that the electron cyclotron frequency does change

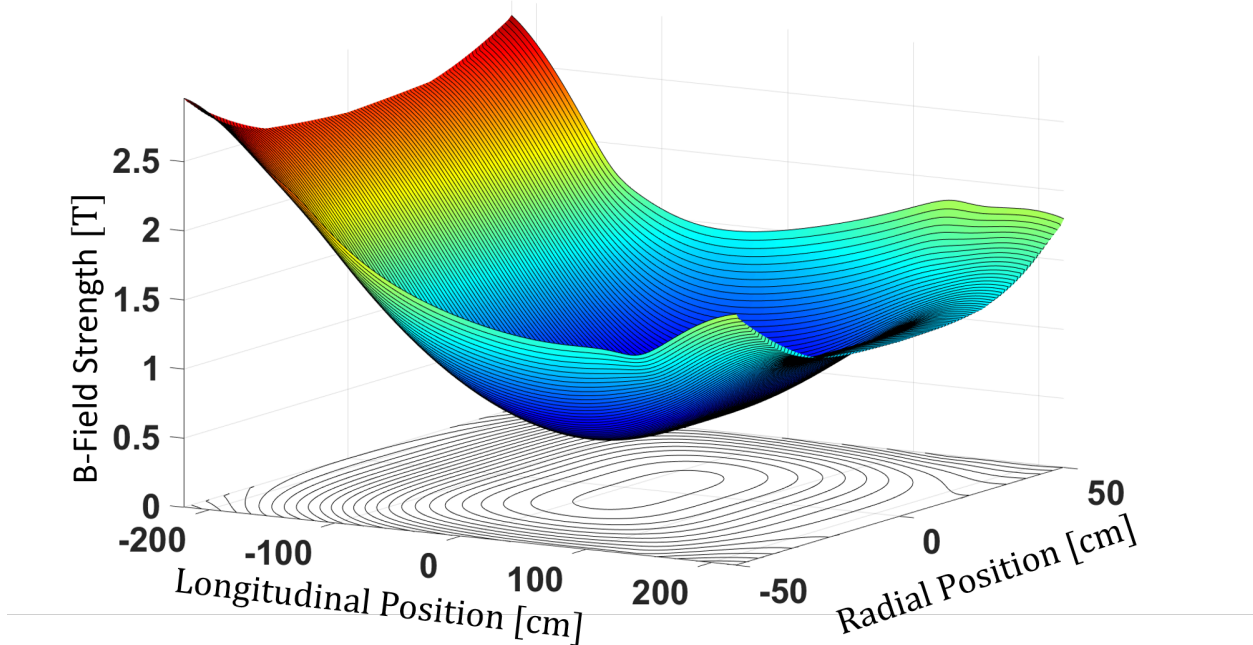


Figure 2.4: A 3D projection of the magnetic field magnitude within an ECR ion source. This particular profile was generated by using CST model of the SuSI ion source at the NSCL. The black lines represent iso-B surfaces within the volume of the magnetic trap.

with large velocities, see 2.5. The relativistic factor qualitatively changes the resonant interaction [97]. In particular, it changes the resonance from occurring along a line in momentum or velocity phase space to being an ellipse. This can be shown by re-writing the resonance condition in terms of velocity:

$$\omega - \Omega_e * (1 - v^2/c^2)^{1/2} - \omega N \cos\theta \frac{v_{\parallel}}{c} = 0$$

and then further rewriting this to be in the form of an ellipse whose in velocity phase space:

$$\frac{v_{\perp}^2}{a^2} + \frac{(v_{\parallel} - v_0)^2}{b^2} = 1 \quad (2.23)$$



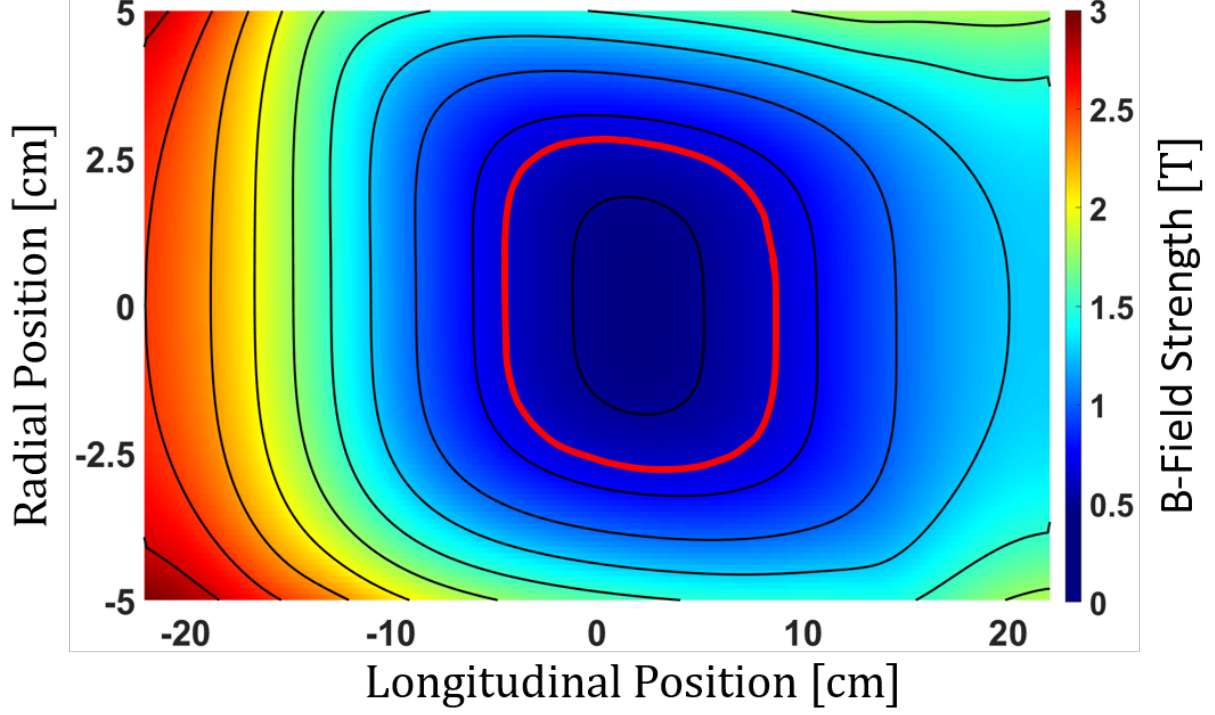


Figure 2.5: A contour projection of the minimum-B magnetic field configuration seen in figure 2.4. The black rings indicate the position of iso-B surfaces within the field structure. The red ring represent the ECR surface over which the heating of cold electrons occurs.

where

$$v_0 = \frac{w_r^2}{\Omega_e^2} \frac{cN \cos \theta}{1 + \frac{w_r^2}{\Omega_e^2} N^2 \cos^2 \theta}$$

$$a^2 = c^2 \left( \frac{w_r^2}{\Omega_e^2} (N^2 \cos^2 \theta - 1) + 1 \right) \left( 1 + \frac{w_r^2}{\Omega_e^2} N^2 \cos^2 \theta \right)^{-1}$$

$$b^2 = a^2 \left( 1 + \frac{w_r^2}{\Omega_e^2} N^2 \cos^2 \theta \right)^{-1}$$

There are several consequences to looking at resonance in an elliptical form. Even to the lowest order approximation, the relativistic effect results in qualitative changes to the resonance condition [97]. Secondly, it allows the majority of electrons which satisfy the resonance condition to exist in a region where  $\partial f_e / \partial v_\perp > 0$  [54]. Here,  $f_e = f_e(\vec{v})$  is the electron velocity distribution function. Under this condition, the resonant wave feels a net increase in energy at the expense of the electrons [5, 10]. In other words,  $\omega_i > 0$  for resonant ordinary and extraordinary waves. The

opposite case,  $\partial f_e / \partial v_{\perp} < 0$  where  $\omega_i < 0$  increases the energy of electrons on average. This effect is commonly referred to as Landau damping, in the case of longitudinally propagating waves, or Cyclotron damping, in the case of transversely propagating waves [5]. Further qualitative and quantitative effects reveal themselves as other non-linear effects are introduced into the resonance framework [54, 94, 97]. The ability for relativist electrons to produce unstable electromagnetic modes is the most crucial point, at least for this study. Instabilities that result from the highly anisotropic electron distributions that the resonant heating mechanism creates are detrimental to ion source operation [18, 82]. Of course, the appearance of such instabilities is a significant focus of this study, and they will be discussed further in section 2.4.

### 2.2.2 Ionization Processes

The production of highly charged ions within an ECR ion source takes place in progressive steps. As the system consists of many mutually interacting particles ( $\sim 10^{11} \text{ cm}^{-3}$ ), the exact growth rate for a single charge state population is rather complicated. A single plasma species will undergo many collisions of varying types before finally escaping the plasma. For simplicity this discussion will focus on the dominant ionizing interactions: single electron-ion/neutral impact and charge exchange [17, 88]. Electron Impact (EI) ionization is an inelastic scattering process where an electron with a high enough energy removes an electron bound to an atomic shell. Charge exchange (CX) occurs when an ion captures as an electron from a neutral species. The neutral is then ionized, and the higher charge state ion's ionization level decreases by one. Together, EI and CX interactions increase and decrease the system's average charge state, respectively. The sum of collision rates describes the growth or decay of a given charge state population. The plasma only reaches a steady-state once the EI ionization rate is equal to the sum of CX and confinement loss rates.

The EI cross-section, and thereby collision rate, can be approximated by Lotz's formula [45] where:

$$\sigma_{q-1 \rightarrow q}^{EI} \propto \frac{\ln E_e / I_{qk}}{E_e / I_{qk}} \quad (2.24)$$

$$R_{EI} = n_e n_{q-1} \langle \sigma_{q-1 \rightarrow q}^{EI} v_e \rangle$$

Here  $\sigma_{q-1 \rightarrow q}^{EI}$  is the collision cross-section going from charge state  $q-1$  to  $q$ ,  $R_{EI}$  is the ionization rate,  $E_e$  is the impacting electron's energy,  $I_{qk}$  represents the binding energy of the electron to be removed,  $n_e$  is the electron density of the plasma,  $n_{q-1}$  is the density of ions in charge state  $q-1$ , and  $v_e$  is the velocity of electrons. While only an approximation, the formula has been shown to work quite well for high charge states [4]. Most importantly, equation 2.24 is heavily dependent on the impacting electron's energy and bound electron's binding energy. As a result, the increasing binding energies associated with more tightly bound electrons cause the optimal energy for ionization to increase. Simultaneously, the optimal cross-section associated with that energy decreases. As seen in figure 2.6, the maximum cross-section of interaction for argon 40 decreases by five orders of magnitude between initial ionization and the removal of the final electron.

Alongside EI ionizing collisions are charge exchange collisions. As mentioned above, these collisions act to reduce the average charge state of the plasma by the exchange of electrons between neutral species and ions. The CX cross-section and collision rate are given by:

$$\sigma_{q+1 \rightarrow q}^{CX} \propto q \left( \frac{I_0}{I} \right)^{3/2} \quad (2.25)$$

$$R_{CX} = n_0 n_{q+1} \langle \sigma_{q+1 \rightarrow q}^{CX} v_{q+1} \rangle$$

where  $\sigma_{q+1 \rightarrow q}^{CX}$  is the cross section for an ion reducing its charge from  $q+1$  to  $q$ ,  $I_0$  is the Bohr energy,  $I$  is the ionization potential of the neutral species,  $n_0$  is the density of neutral species,  $n_{q+1}$  is the density of ions of charge  $q+1$ , and  $v_{q+1}$  is their velocity. Importantly, the cross-section of interaction is independent of either the ion or neutral atom's motion.

The characteristics of the steady-state population can be well approximated through single-electron impact ionization, charge exchange, and diffusion:

$$\frac{\partial n_i}{\partial t} = R_{EI, i-1 \rightarrow i} + R_{CX, i+1 \rightarrow i} - R_{EI, i \rightarrow i+1} - R_{CX, i \rightarrow i-1} - \frac{n_i}{\tau_i} \quad (2.26)$$

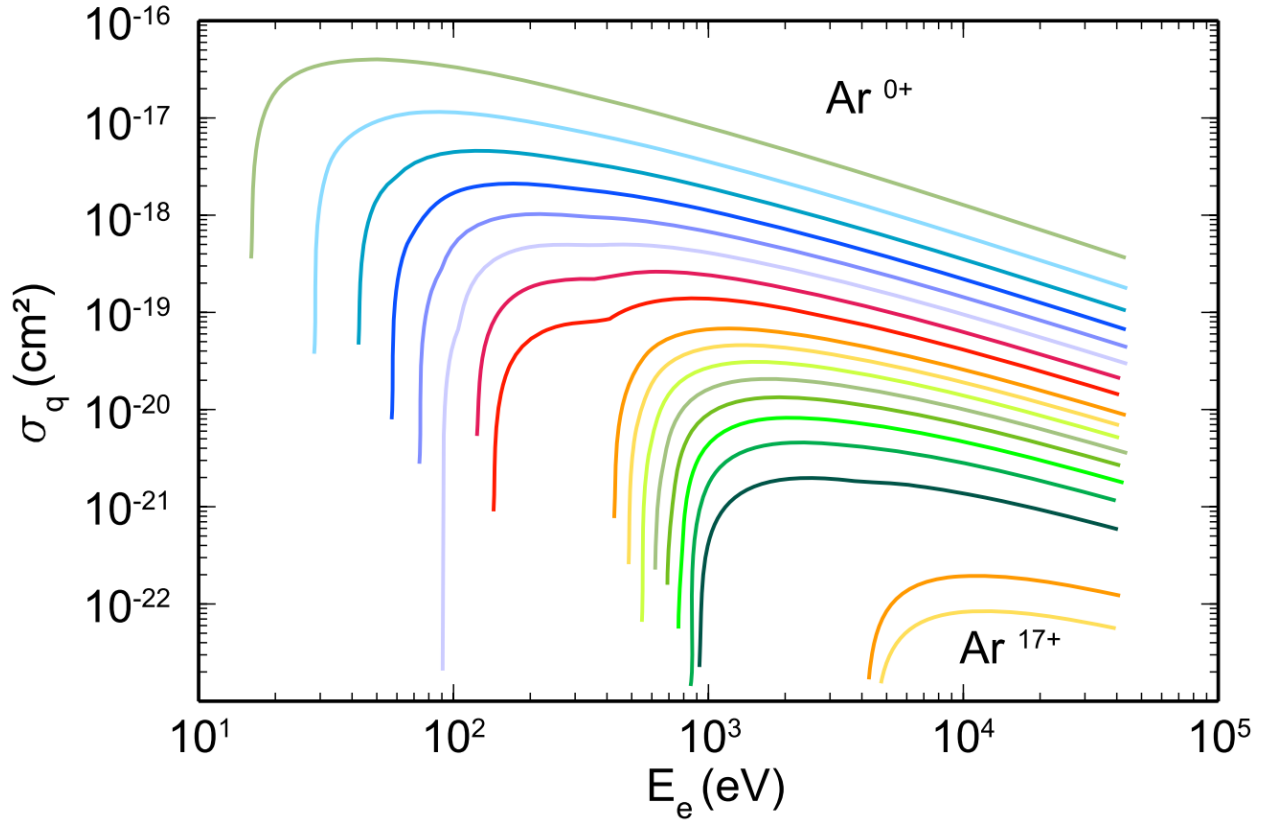


Figure 2.6: A calculation of the Electron Impact Ionization cross section, given in [103].

where  $n_i$  is the density of ions of charge state  $i$  and  $\tau_i$  is the confinement time of ions. The last term is an extension of Fick's law (equation 2.10) where we assume that  $D\nabla^2 n_i \sim n_i/\tau_i$ , where  $\tau_i \sim L^2/D$ , where  $L$  is some characteristic length of the plasma. The first two terms on the right-hand side act as source terms, increasing the population of the charge state of interest. The second two terms act as sinks, taking ions from the population of interest to a different one, reducing the population of interest. The last term is a loss term that removes a particular species from the plasma altogether. The second two terms do not have to be considered as losses, as the individual ions themselves remain in the plasma, but exist in different charge populations. An ion can be ionized from state  $i \rightarrow i + 1$  through EI and then reduced back,  $i + 1 \rightarrow i$ , through charge exchange. Once the ion has diffused out of the plasma, however, it is lost forever.

Comparing equations 2.24 and 2.25 shows an obvious difference between how the two reactions respond to higher charge state ions. The EI reaction rapidly becomes less probable from one charge

state to the next. Charge exchange interactions, on the other hand, favor higher charge state ions. The CX cross-section of interaction increases linearly with higher charge states ions. As a result, having a higher neutral gas density becomes detrimental to the production of high charge states.

These two interactions alone define the core set of goals for producing highly charged ions of a particular atomic species:

1. Increase Electron Energy to reach the EI cross section maximum.
2. Increase Electron Density in order to increase the probability of interaction.
3. Increase the ion confinement time in order to increase the probability of colliding with an electron.
4. Minimize the density of neutral atomic species within the plasma region.

### 2.2.3 Characteristics of the Electron Population

The typical ECRIS plasma is estimated to have electron densities in the range of  $10^{11} - 10^{13} \text{ cm}^{-3}$  [56, 58]. This corresponds to a GHz range plasma frequency ( $\omega_{pe} \approx 6.34 \text{ GHz}$  for  $n_e = 5 \times 10^{11} \text{ cm}^{-3}$ ). Experiments and simulations show that the electrons in an ECRIS plasma exist over a large range of energies  $10 - 10^6 \text{ eV}$  [1, 2, 41, 56]. The distribution of these electrons is also non-Maxwellian; the exact form of the distribution is unknown. Typically, the electron energy distribution function (EEDF) is qualitatively approximated as a sum of three Maxwell-Boltzman distributions. Each distribution is responsible for a different property or mechanism within the plasma. A cold population ( $T_e \sim 10 - 100' \text{ eV}$ ) determines the dielectric properties of the plasma. It is also believed to be responsible for conserving the plasma neutrality. A warm population ( $T_e \sim 1 - 10' \text{ keV}$ ) is principally responsible for ionization of atomic species (see Fig. 2.6). A hot population ( $T_e \sim 100 - 1000' \text{ keV}$ ) is principally believed to aid in electron confinement while storing the majority of the free energy within the system [1]. The spread in temperature also comes with a spread in the Debye length for the different populations of electrons. Simulations of the

$T_e$ [eV]	10	$10^3$	$10^5$
$\lambda_D$ [mm]	0.24	0.33	3.33

Table 2.1: A comparison of electron Debye lengths for the different electron populations. In accordance with the qualitative trends estimated in Mironov et al., it is assumed that  $n_{e,cold} \sim 1 \times 10^{11} \text{ cm}^{-3}$  and  $n_{e,warm/hot} \sim 5 \times 10^{11} \text{ cm}^{-3}$  [58].

plasma, performed by Mironov et al., suggest that the density of the different electron populations are roughly on the same order of magnitude [58]. Following their estimates, we will assume  $n_e \sim 1 \times 10^{11} \text{ cm}^{-3}$  for cold electrons and  $n_e \sim 5 \times 10^{11} \text{ cm}^{-3}$  for warm and hot electrons [58]. Table 2.1 shows a comparison between the Debye lengths for different electron population (eq. 2.18).

It is worth pointing out the importance of the  $T_e^{-3/2}$  term in equation 2.8, which makes the collision frequency highly dependent on the electron temperature. However, the magnetic field does the most to govern the motion of electrons within the plasma. Table 2.2 compares the electron gyrofrequency to the electron-electron collision frequency using plasma parameters typically associated with ECR ion sources. The physical mechanism (collisions, Lorentz force, Coulomb force) acting over the smallest timescale determines the motion of electron, and ion, within the plasma. For electrons, this is the static magnetic field. In practice, however, the magnetic confinement of electrons relies upon resonant heating. Section 2.1.1 explores the topic of electron confinement in greater detail. For now, it is sufficient to recognize that magnetic field effects dominate the hierarchy of electron time scales. It is important to note that the plasma frequency for this model of the plasma is quite close to the gyro frequency. If the plasma becomes overdense ( $\omega_{pe} > \omega_{ce}$ ), then the injected microwaves would be incapable of propagating through the medium. This condition effectively creates an upper limit on the density of electrons within the plasma. See section 2.3.4 for more details.

$T_e$ [eV]	10	$10^3$	$10^5$
$f_{ce}$	27.99 GHz	27.95 GHz	23.42 GHz
$\langle \nu_{ee} \rangle$	21.7 MHz	21.7 kHz	21.7 Hz

Table 2.2: A comparison of electron collision and gyration frequencies in a region where  $B = 1$  T,  $n_e = 5 \times 10^{11} \text{ cm}^{-3}$ ,  $\ln \Lambda = 10$  assuming the energy distribution fo electrons follows a Maxwell-Boltzmann distribution.  $f_{ce}$  decreases due to the  $\gamma^{-1}$  term in equation 2.5.

## 2.2.4 Characteristics of the Ion Population

To preserve charge neutrality, the total density of ions needs to be on the order of the electron density. However, since ions can be multiply charged, the density of a single ion species is approximately an order of magnitude lower than the electron density ( $n_i \sim 10^{10}$ ) [56]. The energy distribution of ions is also very different to that of the electrons. ECRIS ions are believed to exist in a thermal distribution at relatively low temperatures (1- 10's eV). Traditionally, maximum ion temperatures of 1 eV have been assumed. These values result from measurements of the extracted beam current, such as those seen in [53]. However, several recently developed measurement techniques suggest the ion temperature can be as high as 30 eV [36, 49]. Despite the small range of temperatures, these results cannot be overlooked. An increase in temperature to even 5 eV dramatically changes the collision characteristics of the plasma ions. Table 2.2.4 demonstrates this point by comparing the effects on an increasing ion temperature on Argon 1+ and 8+ by using equation 2.9. While the collision frequency is exceptionally high for lower temperatures, easily breaking the gyromotion of ions. As the temperature of ions increases, the ion gyro frequency can quickly overtake the collision frequency. This could potentially indicate that the low charge state ions are magnetically confined. Section 2.3.2 discusses ion confinement mechanisms in ECRIS plasmas in greater detail. As a measure of completeness, equations 2.4 determines that the ion plasma frequency is on the order of 10's kHz.<sup>4</sup>

<sup>4</sup>This can be seen using eq. 2.4 for every charge state or by defining an effective ion plasma frequency  $f_{pi,eff} = \sqrt{n_e \bar{q} e^2 / 4\pi^2 m_i \epsilon_0}$ .

$T_e$ [eV]	1	5	30	$f_{ci}$
$\langle v_{ii}^{1+} \rangle$ [kHz]	430	38.5	2.62	96.2
$\langle v_{ii}^{8+} \rangle$ [MHz]	2.75	2.46	0.168	0.769

Table 2.3: The collision frequencies for  $\text{Ar}^{1+}$  and  $\text{Ar}^{8+}$  with  $n_e = 5 \times 10^{11} \text{ cm}^{-3}$ ,  $\bar{q} = 8$ ,  $\ln \Lambda = 10$  assuming that the energy distribution of ions follows a Maxwell-Boltzmann distribution. The right hand side of the plot compares the different collision frequencies against the gyration frequencies for both of these charge states assuming  $B = 1 \text{ T}$ .

## 2.3 Operational Principles for ECR Ion Sources

The previous section discussed the plasma parameters resulting from the heating and ionization processes that naturally occur in an ECRIS plasma. Ion source scientists and engineers seek to optimize these values to produce the most beam possible.<sup>5</sup> A simple calculation can demonstrate which parameters most appreciably affect source performance. First, consider that, eventually, each ion will leave the plasma. Each ion also must undergo multiple collisions in order to reach a high charge state. We can maximize the number of electron-ion collisions by minimizing the time between each collision. Let us consider the time it takes for a species to undergo  $q$  ionizing collisions:

$$\tau_q \geq \sum_{i=1}^q \tau_{i-1 \rightarrow i} = \sum_{i=1}^q \frac{1}{\nu_{i-1 \rightarrow i}} = \sum_{i=1}^q \frac{1}{n_e \langle v_e \sigma_{i-1 \rightarrow i} \rangle}$$

We can further simplify this by assuming a Maxwell-Boltzmann distribution to get:

$$n_e \tau_q \geq 5 \times 10^4 T_{e,opt}^{3/2} \quad (2.27)$$

where  $T_{e,opt}$  is the optimal electron energy for ionization. Equation 2.27 defines the criteria for high charge state production in ECR ion source:

- Large electron densities
- Long ion lifetimes
- Sufficient electron energies

---

<sup>5</sup>The emittance of the beam is also important, but a full discussion of extraction is outside the scope of this study.



Golovanivsky's plot, Fig. 2.7, visualizes these criteria [17]. This plot compares the product of the electron density and ion lifetime necessary,  $n_e \cdot \tau_i$  to achieve full ionization against the optimal electron temperature,  $T_e$ , for ionization. As the optimal electron density increases, so too must the electron density and ion confinement time.

Ultimately, the production of high charge state ions is a balancing act. It requires satisfying the demands of atomic physics, electrodynamics, and thermal physics without overindulging in any direction. As mentioned by Geller [17], many natural processes within the plasma can hamper the production of higher charge state ions. For example, increasing the electron density promotes high charge state production, while also increasing  $\beta$  (Sec. 2.1.1) and promoting a macroscopically unstable plasma. This section focuses on how ECR ion sources meet Golvavanski's criteria. Furthermore, we will discuss operational techniques to enhance and optimize the ion source's performance by exploiting the physical properties of the plasma.

### **2.3.1 Electron Confinement and the Minimum-B Magnetic Field Topology**

The confining magnetic field is generated through the superposition of a series of solenoid coils and a hexapole magnet. The solenoids provide two, lopsided magnetic mirrors, on either side of the plasma chamber, that provide longitudinal confinement (Fig. 2.3). The magnetic hexapole provides a third mirror in the radial direction of the plasma chamber. Early ECRIS devices relied upon a set of two-room temperature solenoids and a permanent magnet hexapole to fulfill these requirements. More modern devices have built upon this model, adding more solenoids to gain more control over the magnetic field and variable magnet hexapole to control the radial field. Sources such as SuSI [99], VENUS [42], and SECRA [101] use fully superconducting coil designs in order to achieve the largest magnetic field possible.

The superposition of all three mirrors is important as they provide both macroscopic stability and a surface over which to heat the plasma. Together, these three fields create what is known as the Min-B field profile. Beyond creating a closed resonance surface, the Min-B field also improves the confinement and macroscopic stability characteristics of the plasma. The solenoids

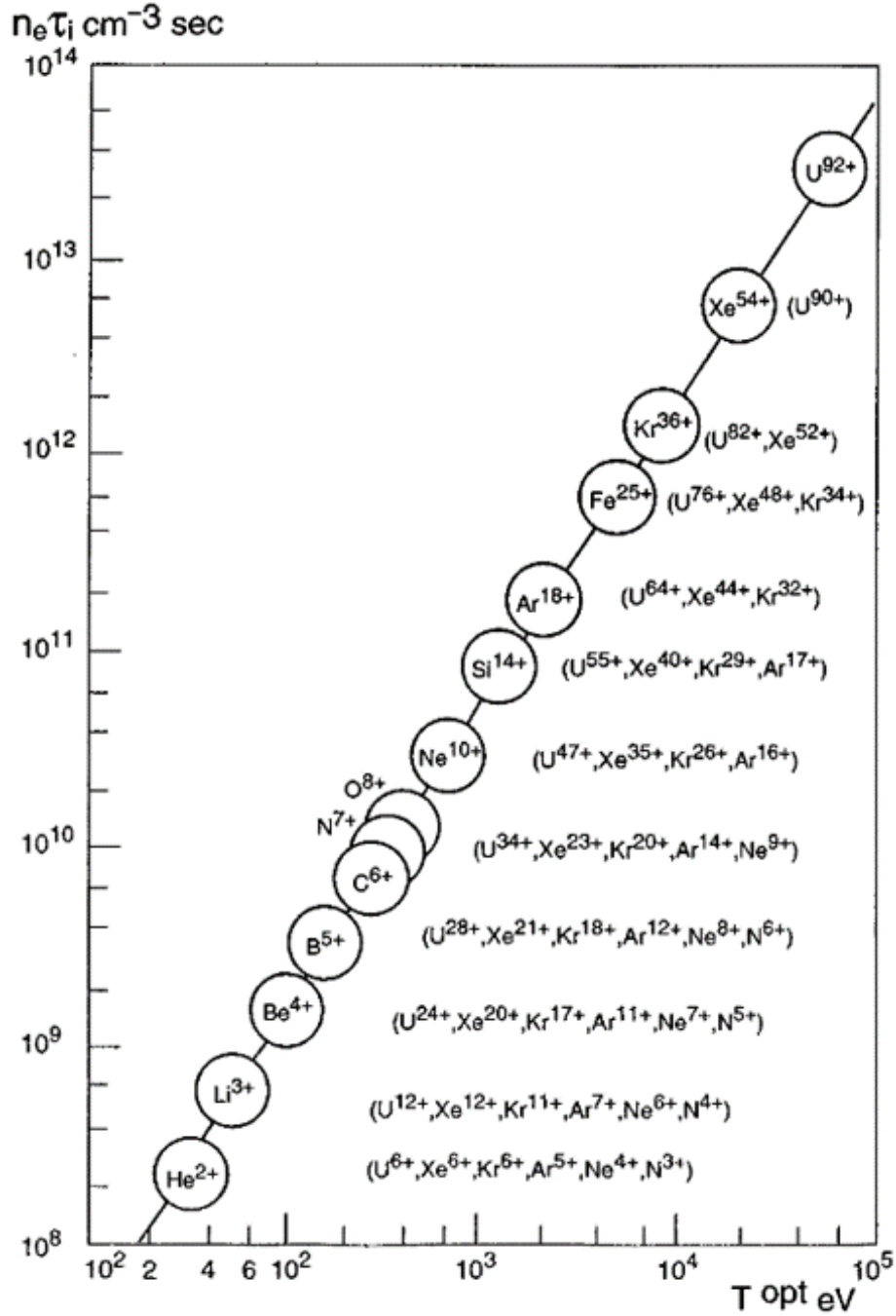


Figure 2.7: Golovanivsky's plot which shows the criteria for producing high charge state ions in an ECRIS plasma. The circles represent the atomic species which is fully ionized for the given density and ion confinement time. Those in parenthesis to the right show the highest charge state achievable for other atomic species. Reproduced from [17], with permission from AIP Publishing.

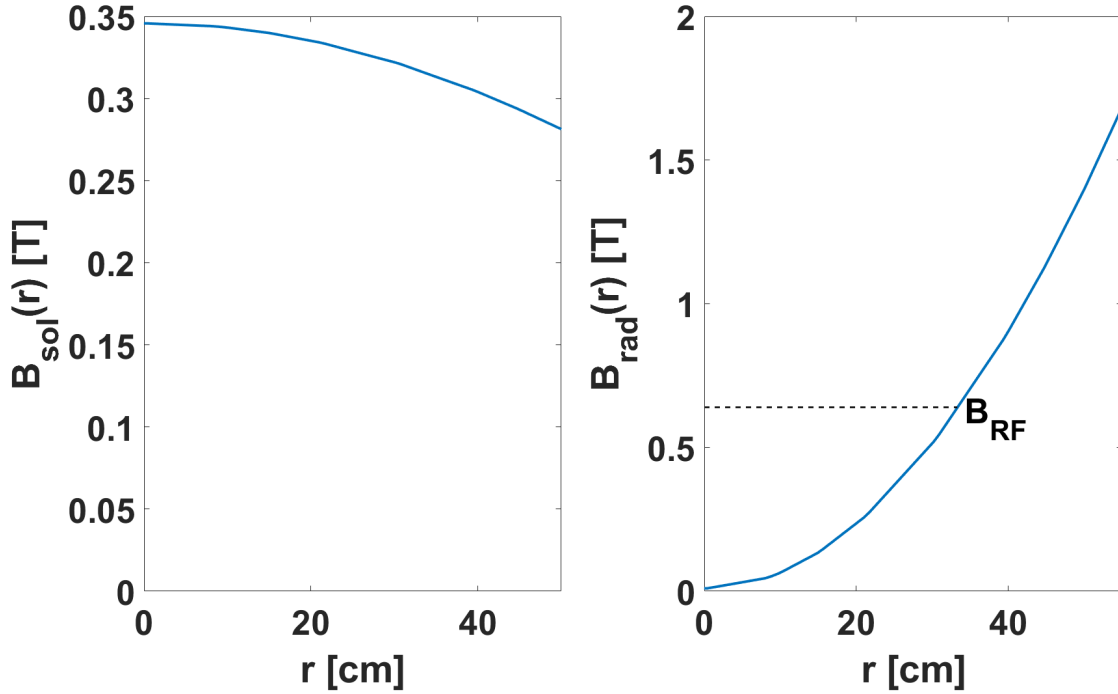


Figure 2.8: Comparison of the radial component of the magnetic field generated by the solenoids alone (left) and the hexapole alone (right).

alone have difficulty confining the plasma radially. An electron or ion moving radially outward from the center of the trap would see a decreasing field magnitude, causing the ratio of kinetic to magnetic pressures,  $\beta$ , to increase. An increasing value of  $\beta$  corresponds to lower confinement and increased diffusion of charged particles out of the plasma. The axially centered hexapole solves this problem by introducing a radially *increasing* component of the magnetic field. This configuration ensures that the system is macroscopically stable. Figure 2.8 compares the radial field distributions produced by a set of solenoid coils, alone, and a magnetic hexapole.

Simulations of the plasma provide a way to understand the plasma without the need for perturbative diagnostics [84]. The NAM-ECRIS program does an excellent job of simulating the charge state distributions of extracted ions [56]. Despite the advances of such programs, the spatial distribution of electrons is still mostly unknown. However, these calculations suggest that electrons' energy distribution affects their spatial distribution throughout the ECRIS volume. Low energy cold electrons distribute uniformly throughout the plasma, while warm and hot electrons concentrate,

to varying degrees, at the center and turning points of the confining magnetic field [58]. They also show that microwave heating is essential for electron confinement, as it pushes the cold electrons out of the loss cone. As a result, losses of electrons increase or decrease by turning the microwave power off or on [57].

Perfect confinement is not ideal for an ECRIS plasma, otherwise there would be no beam. It is also exceptionally difficult to perfectly confine charged particles within a plasma. In one way or another, the plasma species will find a way to escape the plasma. Electrons escape the plasma by entering the magnetic loss cone, such as collisional and pitch angle scattering trap[11]. Pitch angle scattering plays an essential role in preventing the buildup of hot electrons within the plasma. At high velocities, the resonant interaction causes transverse energy to convert to longitudinal energy [20]. This mechanism becomes vital for limiting the density of hot, non-collisional electrons within the plasma. However, experiments suggest new non-linear mechanisms for the diffusion of electrons, as will be discussed in section 2.4.3.

### **2.3.2 Ion Confinement**

Confinement in the case of ions is much different. While electrons become better confined over time, ions will become more diffusive the longer they stay in the plasma. This is partially due to the ion gyro-frequency increasing as  $q$  and ion collision frequency as  $q^2$  (see tab. 2.2.4). This creates an interesting problem. Ion collisions are necessary in order to produce more highly charged ions. Those collisions can also cause ions to diffuse out of the plasma before they are fully ionized. However, if no ions diffuse out of the plasma, then there is no beam. While impressive in its own right, a perfectly confined ion plasma would be useless for accelerator operation. We then need to understand how to balance the useful ion diffusive effects with the useful non-diffusive collision effects.

While the exact diffusion constant is unknown, it has been shown to depend on the magnetic field strength as  $B^{-k}$ , where  $1 \leq k \leq 2$  [86].  $k = 1$  would indicate a more turbulent Bohm diffusion while  $k = 2$  would indicate more traditional ambipolar diffusion, as discussed in section 2.1.3.

Similar to electrons, the ion diffusion constant generally decreases with larger magnetic fields. However, their low mobility causes them to leave the plasma at a lower rate. The imbalance of positive and negative charge flow produces a small positive potential over the surface of the plasma. This plasma potential pushes ions out of the system while retarding the diffusion of electrons. The potential, however, is rather small with  $\Phi_p \sim 20$  V.

The confinement properties of ions may change as a function of their charge state. Some evidence suggests that ions could be confined magnetostatically at low charge states and electrostatically at high charge states [36, 49]. High charge state confinement, on the other hand, may require electrostatic confinement. These ions rely upon high density, hot electron populations to improve their lifetime in the plasma. The well-confined electrons exist in the center of plasma and create an electric field pointed into the center of the plasma [56]. This field creates a potential barrier,  $\Delta\Phi$ , that ions must overcome before they can escape the plasma [49]. This type of phenomenon is called a 'Potential Dip'. High charge state ions that have kinetic energies less than  $Q\Delta\Phi$  are unable to escape from the plasma. The diffusion time for an ion of charge  $q$  within this plasma model goes as [36]:

$$\tau_i^q = \frac{\sqrt{\pi}Rl}{v_T} \exp \frac{|qe\Delta\Phi|}{T_i^q} \quad (2.28)$$

for a plasma of characteristic length  $l$ , mirror ratio  $R$ , and thermal velocity  $v_T$ . The value of the dip can be described as [18]:

$$\Delta\Phi = \frac{\pi}{2}er^2 \left(1 + 2 \ln \frac{l}{r}\right) \left(\sum_i in_i - n_{e,hot}\right) \quad (2.29)$$

where the last term is the electrical balance of the local ion and electron density in a cylindrical plasma of length  $l$  and radius  $r$ . What is important about equation 2.29 is that the potential is directly proportional to the density of hot electrons. A large hot electron population creates a larger potential dip, up to a point. Large densities of hot electrons can produce a wide variety of plasma microinstabilities [9]. Particularly, once the total number of hot electrons,  $N_{hot}$ , is greater than the number of cold electrons  $N_{cold}$  [92]. These instabilities are detrimental to the production of high charge state ions, even as large hot-electron populations improve the confinement of ions.

Unfortunately, the potential dip has never been measured. Simulations and estimates of the ECRIS plasma suggest a small potential on the order of 0.01 - 1 V [13, 57]. These estimates result in an overall lower ion temperature. However, measuring the Doppler broadening of spectral emission lines from atomically excited ions suggests much higher ion temperatures than previously suggested [36]. Ion temperatures up to 30 V were measured by analyzing the Doppler broadening of atomic emissions lines coming from the source. If this is the case, then the potential dip must also be on the order of 5 - 20 V; otherwise, it would be incapable of confining those higher energy ions. This increase in the depth of the potential also dramatically increases the lifetime of ions in the plasma.

Simulations of the plasma demonstrate how ion confinement is also affected by the spatial distribution of different charge states [56]. Those calculations suggest that low-charge state ions concentrate in the high field region on the periphery of the plasma. The highest charge states appear in the center of the plasma, where a large number of hot electrons are also present. The described simulation does *not* include a potential dip, which would help draw high-charge state ions into the central part of the plasma. The NAM-ECRIS simulation does a good job describing ion dynamics within the plasma; however, it suggests that the depth of the potential dip is on the order of 0.01-0.05 V [58]. This result is contradicted by the Doppler broadening measurements described above, which suggest the existence of 30 V dips. However, it does not mean that the simulation results are incorrect but instead limited by our present understanding of the physics of the source plasma. As such, the simulation may give accurate results in the limit of collisions dominating interparticle interactions.

### **2.3.3 Afterglow**

While providing strong plasma confinement is necessary for ECR ion source operations, manipulating the confinement of electrons and ions can enhance the system's performance. One way of doing so is by operating in the so-called afterglow mode. Afterglow, or plasma afterglow, is the emission of radiation from a cooling plasma, once the driving power has been turned off. As the

emission of ions is a desirable effect for ECR ion source, operating a plasma in an afterglow state allows for the extraction of much higher beam currents than can be offered in continuous wave (CW) operation [86]. This is achieved in ECRIS devices by turning off the injected microwave power after a period of CW operation [52, 90]. The technique was initially used at CERN and later tested or adopted at other facilities, such as GSI [6, 40, 51, 76, 77].

Presently, there is no formal, analytical description of the phenomena in ECR ion sources. Our current understanding suggests that the enhancement is a result of the loss of confinement characteristics immediately after the RF turnoff [18, 86]. In the absence of power, electron losses rapidly increase, as the heating mechanism was necessary for driving cold electrons out of the loss cone [57]. Warm electrons will continue to undergo ionizing collisions, further increasing losses by exchanging the energy, which keeps them confined in the magnetic trap, to produce more poorly confined cold electrons. Consequently, the increased electron diffusion rate results in an increase in the emission of x-rays from the plasma chamber [89]. The sudden loss of the cold electron population breaks the plasma's quasi-neutral state. As the plasma potential increases, the ions are accelerated out of the ion source, creating a short term ( $\sim$  ms) burst of ions from the plasma. This peak current decays exponentially, reflecting the exponential decrease in ion density resulting from the diffusion process [40, 86].

Without a heating mechanism we can reduce equation 2.26 to:

$$\frac{\partial n_i}{\partial t} \approx -\frac{n_i}{\tau_i}$$

which can be solved as  $n_i(t) = n_0 \exp(-t/\tau_i)$  [18]. This results in the characteristic exponential decay seen in many studies of the afterglow effect [40, 89]. The diffusion coefficient for these ions is largely dominated by collision effects. Consequently, the decay time of ions in the afterglow phase scales with charge states as ( $\tau \sim q^{-2}$ ), reflecting the charge dependence of the ion collision frequency (eq. 2.9). Geller pointed out that there are a couple of different afterglow decay modes depending on the operation of the plasma (figure 2.9). Case a) demonstrates a turbulent Bohm-like diffusion processes which scale as  $B^{-1}$  [87]. Case b) shows more quiescent decays that are heavily dominated by collisional and RF diffusion effects, resulting in more slowly decaying peaks. Geller

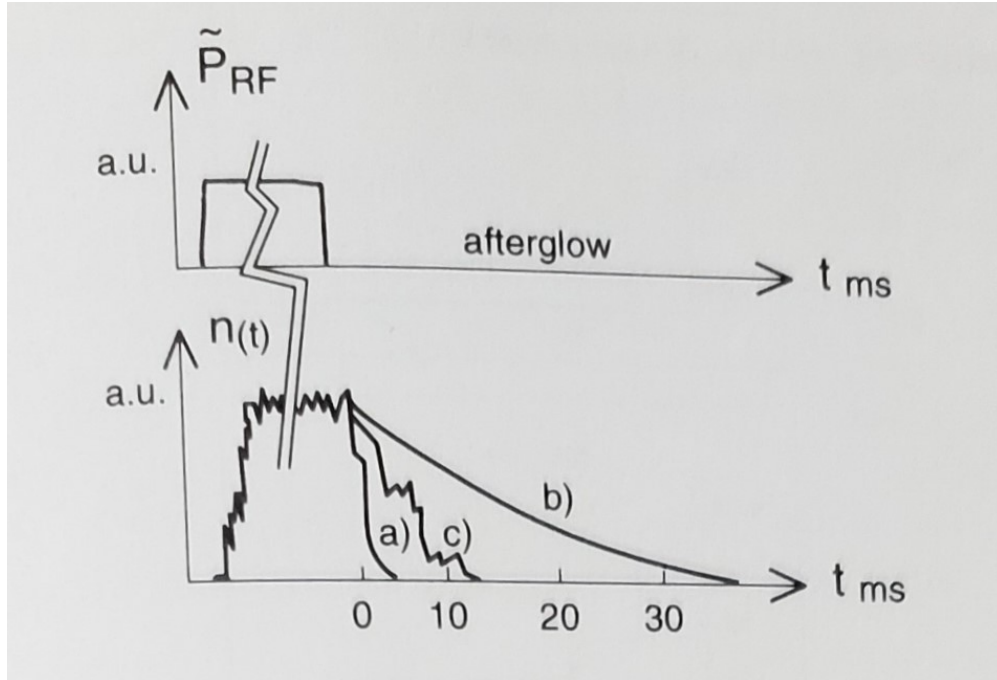


Figure 2.9: The three different decay modes are dependent upon the degree of turbulence of the plasma. The three curves show the typical decay forms of afterglow pulses: a) Turbulent, b) Quiescent, c) Non-linear particle diffusion. Figure originally printed in [18] and has been re-published with permission of Taylor & Francis Group LLC.

notes that hot electron plasmas would exhibit this kind of decay. Case c) involves the ignition of non-linear processes, such as plasma instabilities, which cause rapid particle loss on time scales much slower than the decay of the ion population. Such instabilities have been seen in afterglow plasmas before [52, 76].

While many authors have written on and described this phenomenon, as of writing this dissertation, there is no formal definition for the afterglow mode of operation (at least none that is known to this author). For our present purpose, let us use the following definition:

**Definition 2.3.1. (Afterglow Mode)** A mode of operation of ECR Ion Sources that temporarily enhances extracted beam current from the plasma chamber by means of electrostatic imbalance due to loss of electrons from confinement.

This definition is purposefully left broad to avoid specifying any singular underlying mechanism for electron exodus. It is also purposefully vague in regard to the temperature of the electrons lost



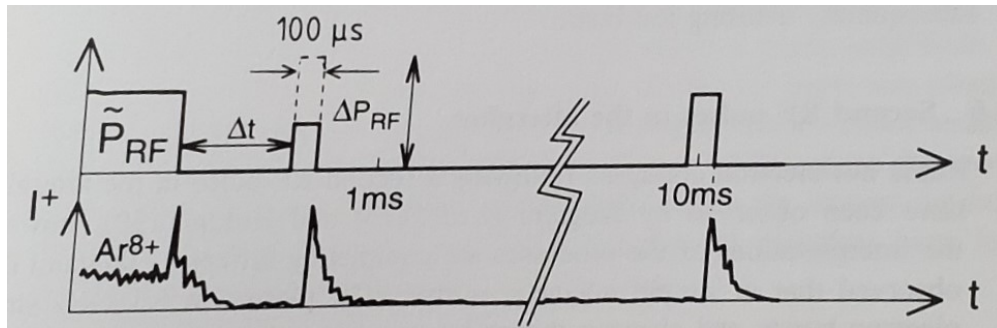


Figure 2.10: By pulsing RF power again after the initial afterglow burst, an instability can be ignited which forces hot electrons out of the plasma. This results in a second burst of ions. This method will work so long as the hot electrons have not diffused out of the plasma by other means. Figure originally printed in [18] and has been re-published with permission of Taylor & Francis Group LLC.

from confinement. Despite the literature's focus on the effect of cold electrons losses, a second *hot* electron afterglow burst can occur by pulsing the RF power for a short period after the initial burst [18]. The RF pulse perturbs the confinement of hot electrons, causing the diffusion of high-charge state ions, which were electrostatically trapped by the very well-confined hot electron population. Importantly, this effect can occur up to 10's of milliseconds after the microwave turn off, as the hot electron population remains well confined in the absence of heating. Time-resolved x-ray measurements reinforce this perspective by demonstrating how the hot electron population's decay can occur over minutes [33]. Figure 2.10 shows an example of this type of burst. This second method of producing afterglow has been successfully used in ion sources like MINIMAFIOS at CERN in Switzerland and CAPRICE at GSI in Germany.

### 2.3.4 Scaling Laws

While there is no formal analytical description of the ECRIS plasma, many have developed empirical and quasi-analytical scaling laws to guide source development. Equation 2.27, for example, describes the scaling of confinement time with electron density and energy. Geller et al. [15, 16] and Gammino and Ciavola [14] determined laws which described how the optimal charge state and current extracted from the ion source scaled with various ion source parameters. Hitz et al. [24] and

Lyneis [46] discovered that specific magnetic field typologies also optimized ECRIs performance.

The nature of cyclotron heating puts an upper limit on the electron density within the plasma. As mentioned in 2.1.5, right hand circularly polarized EM waves cannot propagate in regions where  $\omega_{pe} = \omega_{ce}$ . The cut off condition defines a critical density of the plasma above which incoming RF waves will not propagate:

$$n_{crit} = \frac{4\pi^2 \epsilon_0 m_e f_{RF}^2}{e^2} = \frac{\epsilon_0 B_{ECR}^2}{m_e}. \quad (2.30)$$

For example, this limit occurs at  $4.48 \times 10^{11} \text{ cm}^{-3}$  for 6 GHz and  $97.5 \times 10^{11} \text{ cm}^{-3}$  for 28 GHz microwaves. The plasma will become turbulent above  $n_{crit}$  leading to poor charged particle confinement [16]. Increasing the average magnetic field, and thereby  $\omega_{ce}$ , allows for higher heating frequencies and subsequently larger electron densities. If we assume that ions diffuse in an ambipolar manner, then the ion lifetime increases with the average magnetic field,  $B_{avg}$ , as  $\tau_i \propto B_{avg}^{1.5}$  [15].

The minimum energy necessary for producing a given charge state goes as the ionization potential, which goes as  $q^2$  for a given ion. For low to moderate microwave power, the average electron energy goes as  $P_{RF}$ . At high energies, the power conversion becomes non-linear and goes as  $P_{RF}^{0.5}$  [16]. Thus, to fulfill the criteria for high charge state production, the ion source must be run with high power, magnetic fields, and microwave frequencies.

Gammino et al., Hitz et al., and Lyneis discovered adjusting the magnetic field's topology could optimize the extracted beam current [14, 24, 46]. To begin with, we know from equation 2.3 that the magnetic pressure must be larger than the kinetic plasma pressure in order to have good confinement. Using equations 2.3 and 2.30:

$$n_e k_B T_e < n_{crit} k_B T_e = \frac{\epsilon_0 k_B T_e B_{ECR}^2}{m_e} = \beta \frac{B_{max}^2}{2\mu_0}$$

which can be rewritten as:

$$\frac{B_{max}}{B_{RF}} = \left( \frac{2k_B T_e}{\beta m_e c^2} \right)^{\frac{1}{2}} \quad (2.31)$$

Let us assume that a 'good' ECR plasma has  $\beta = 0.01$  and  $k_B T_e \sim 10 \text{ keV}$  to get [14]:

$$\frac{B_{max}}{B_{RF}} \approx 2. \quad (2.32)$$

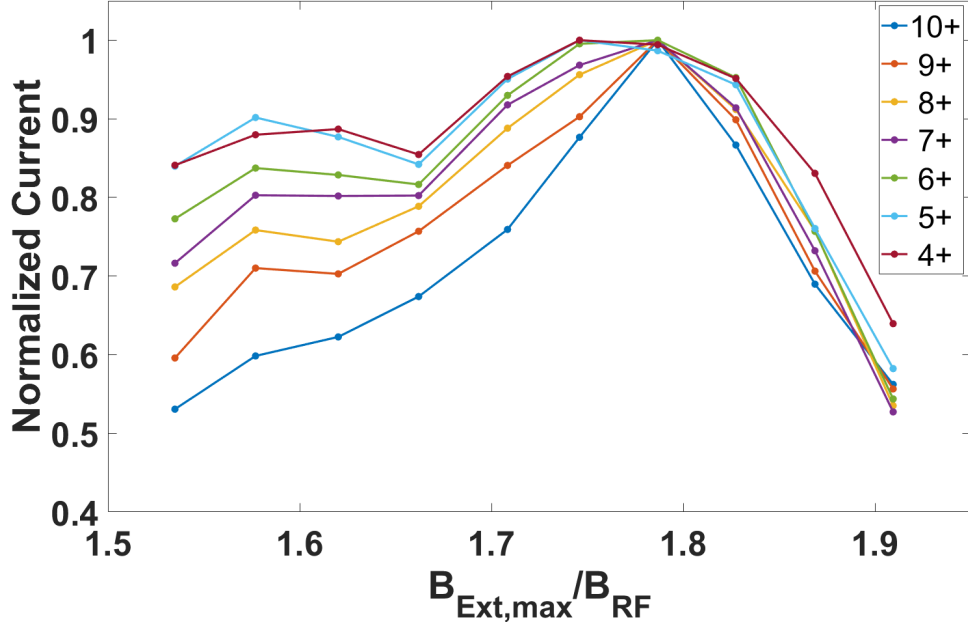


Figure 2.11: A demonstration of the magnetic scaling laws for intermediate to high charge state argon ions. The measurement was taken using SuSI at the NSCL.  $B_{min} = 0.4$  T,  $P^\mu = 350$  W,  $p_{Ar} = 214$  nTorr.

Measurements from various ion sources found that the extracted beam is maximized when [24, 46]:

$$\begin{aligned}
 B_{Rad,max} &= 2B_{RF} \\
 B_{Inj,max} &= 3 - 4B_{RF} \\
 B_{Ext} &\approx 0.9 - 1B_{Rad} = 1.8 - 2B_{RF} \\
 B_{Min} &\approx 0.4B_{Rad} = 0.8B_{RF}.
 \end{aligned}
 \tag{2.33}$$

An example of these relations can be seen in figure 2.11.

While the magnetic field scaling laws do a good job describing the source performance, they are not well understood. Consequently, they act more like guidelines rather than rules. For example, equation 2.32 sets a minimum lower limit on the last iso-B field surface within the plasma chamber, ensuring  $\beta = 0.01$ . A larger magnetic field at the plasma chamber's injection side and radial wall maximizes the ion source's performance by minimizing electron and ion diffusion rates towards these boundaries. However, a lower extraction side field maximum improves the performance of the ion source. A higher value of  $\beta$  at extraction encourages the diffusion of electrons and ions through the extraction aperture. It is difficult to predict how all the ion source parameters will affect

ECRIS performance, and the ideal operating points for one ion source may differ from another.

Advancing our understanding of the scaling laws require more direct investigations of the source's performance. A better understanding of how the plasma parameters affect the plasma will allow scientists and engineers to improve the ion source's overall capabilities. Not only that, but further investigations can also reveal when and how those relations fail. To that end, this study focuses on an experimental investigation of one of the possible mechanisms limiting the application of the laws: kinetic plasma instabilities.

## 2.4 Kinetic Instabilities

Extracted high charge state currents typically reach a maximum when  $B_{min}/B_{RF} = 0.7 - 0.8$ , as suggested by the scaling laws of equation 2.33 [83]. Directly observing the extracted current, on the high field side of the ion source's operating parameter space, will often demonstrate quasi-periodic  $\mu s$  range losses of extracted ion currents [81]. Experimental investigations determined that these losses result from micro-instabilities, in the form of kinetic cyclotron maser instabilities, occurring within the plasma. These instabilities result from the unstable amplification of electromagnetic wave modes within the plasma, which themselves result from large electron temperature anisotropies,  $T_{\perp} \gg T_{\parallel}$  [54, 67, 71, 92].

The minimum-B field configuration prevents macroscopic instabilities from occurring. These instabilities occur due to an imbalance between the outward thermal pressure of electrons and the inward, confining magnetic pressure. However, the field structure cannot prevent micro-instabilities from occurring. On the contrary, the large magnetic fields actively cause the instabilities to occur [81, 83]. The resonant heating and loss cone confinement scheme create large temperature anisotropies,  $T_{\perp} \gg T_{\parallel}$ , in the electron population.<sup>6</sup> The hot, non-collisional electrons store large amounts of free energy, which results in the excitation and amplification of electromagnetic plasma

---

<sup>6</sup>This is a natural result of the loss cone and resonant heating combination. The energy in the transverse motion of electrons, perpendicular to the magnetic field lines, is increased through the ECR process. Moreover, eq. 2.2 shows that electrons with large longitudinal velocities (or energies) will enter the loss cone and escape confinement. Together, these effects create a temperature anisotropy.

modes [47, 92]. Through this amplification process, the electrons drive themselves into the loss cone, breaking the confinement of ions while also suppressing their production rate [26, 83]. If the operating conditions are not changed, then the instabilities will repeat with a frequency range of 10 Hz - 10 kHz, depending upon source parameters. This next section discusses the operational ramifications of these instabilities in detail. Beginning with the diagnostic observations made during unstable operation and leading into a discussion about the role of hot electrons and possible mechanisms of suppressing the instability.

### 2.4.1 Diagnostic Observations

Three principal diagnostic signals characterize the kinetic instabilities within an ECRIS plasma: emission of microwave power, bursts of bremsstrahlung radiation, and periodic variations of extracted beam currents. The beam current variations provided the initial observation of the instabilities [38, 81]. Further investigation revealed bursts of microwave power and bremsstrahlung radiation preceding the current variations [26, 81]. The microwave radiation signals the beginning of the instability and lasts for several  $\mu\text{s}$ . A burst of bremsstrahlung radiation, lasting for 10's - 100's  $\mu\text{s}$ , immediately follows the microwave emission and result from the sudden loss of electrons from confinement. The absence of electrons in the system breaks quasi-neutrality and reduces the production rate of ions. Eventually, the plasma will settle and the normal heating process will begin again, leading to a recovery of the extracted ion currents, on the order of the electron heating time (1-10's ms). If none of the ion source parameters have changed, then the instability will ignite once again and repeat in a quasi-periodic manner. Figure 2.12 shows an example of the beam current losses for an extracted  $\text{Ar}^{8+}$  beam at the NSCL.

Figure 2.13 shows a spectrogram of the microwave emission from the JYFL 14 GHz source during unstable operation [25]. Izotov et al. found that the emitted frequencies spanned from 6 GHz - 11 GHz (first harmonic), with a second band in the 12 - 22 GHz range (second harmonic). Increasing the ion sources average magnetic field causes the plasma to emit electromagnetic radiation, predominately, at lower microwave frequencies [25, 26]. However, the total range of emitted

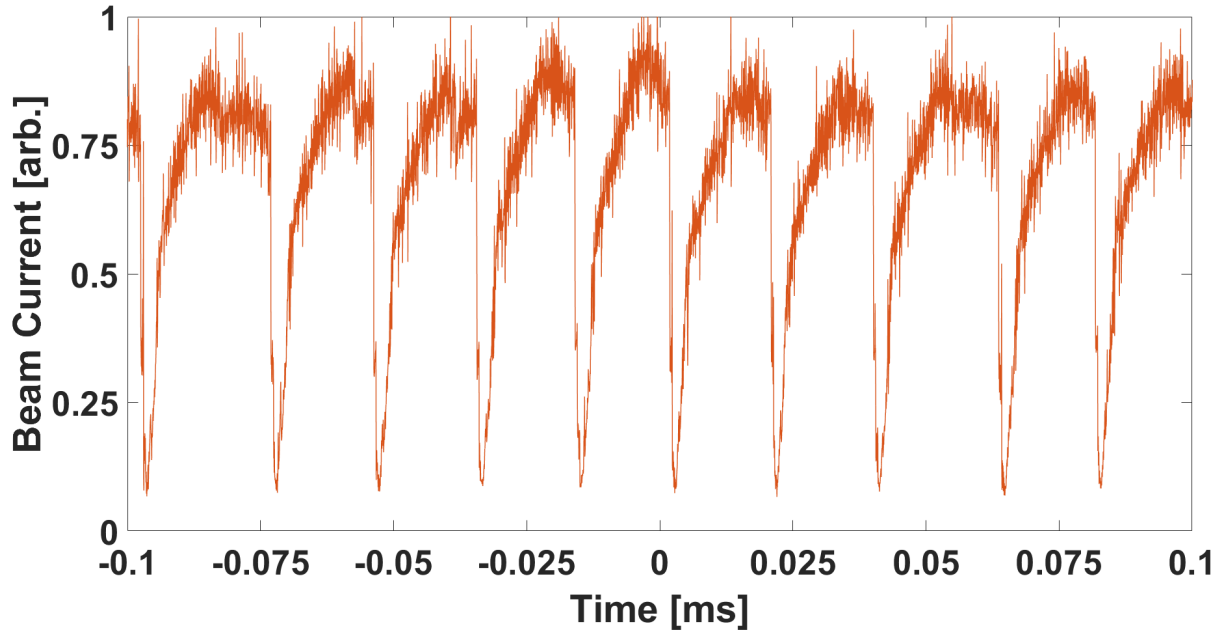


Figure 2.12: Beam current losses for  $\text{Ar}^{8+}$ , normalized by the largest measured value.

frequencies does not change. Despite this, the emission always appears to begin with higher frequency microwaves and progress with the falling tones.

Mansfeld et al. [47] thoroughly discussed why the Z-mode best fits the observed dynamic microwave spectrum. The mode most likely propagates quasi-longitudinally with respect to the magnetic field lines, that is to say,  $\theta \leq 1$  Rad (see eq. 2.20). The excitation results from electron temperature anisotropies,  $T_{\perp} \gg T_{\parallel}$ , a natural consequence of the loss-cone confinement and resonant heating process [26, 47, 73]. The interested reader should take a moment to look at the arguments put forth by Mansfeld et al. [47] as to why the Z-mode tentatively explains the observed frequencies. For our purposes, however, we will only focus on the range of frequencies emitted from the plasma chamber. Figures 2.14 and 2.15 shows the dispersion relation and phase velocity for the extraordinary wave, respectively, for a plasma similar to the ECRIS plasma described in Izotov et al. [26]. The domain labeled 'Slow Z-mode' almost perfectly encapsulates the range of observed microwave frequencies emitted from the plasma chamber during an instability event. Furthermore, the subliminal ( $v_{\phi} < c$ ) propagation of this mode makes the unstable resonant process

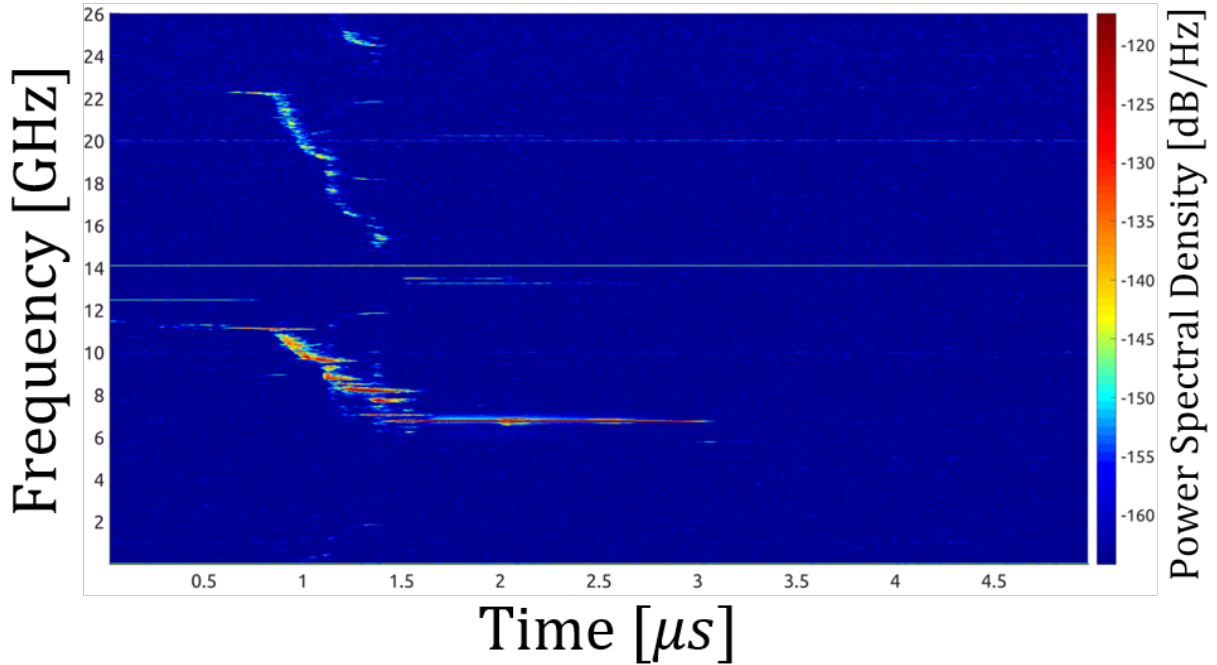


Figure 2.13: Spectrogram of an unstable microwave emission in open space (no waveguide) for a 14.056 GHz ECR ion source, 400 W microwave power,  $B_{min}/B_{RF} = 0.83$ . The solid line above 14.056 GHz results from the heating RF that leaked out of the system. The microwave emission was so powerful that it was possible to detect the emission in free space. Experimentally, this means that frequencies above and below the waveguide cutoffs could be measured. This plot has not been adjusted for transmission efficiency of the microwaves. Reproduced from [25], with permission from AIP Publishing.

more efficient.

At this time, there are no reported measurements of the spectroscopic decomposition of the x-ray burst that follows the microwave emissions. The brief timescale of the burst makes time-resolved measurements difficult, due to the small measurement window ( $\sim 100\mu\text{s}/\text{event}$ ).<sup>7</sup> However, measurements of electrons escaping confinement due to the instability demonstrate losses of electrons over a wide range of energies [28]. The energy distribution of electrons escaping confinement will be discussed further in chapter 4.

---

<sup>7</sup>Multiple x-ray detectors could compensate for this, but doing so presents other practical issues, such as space constraints, equipment costs, shielding, etc.

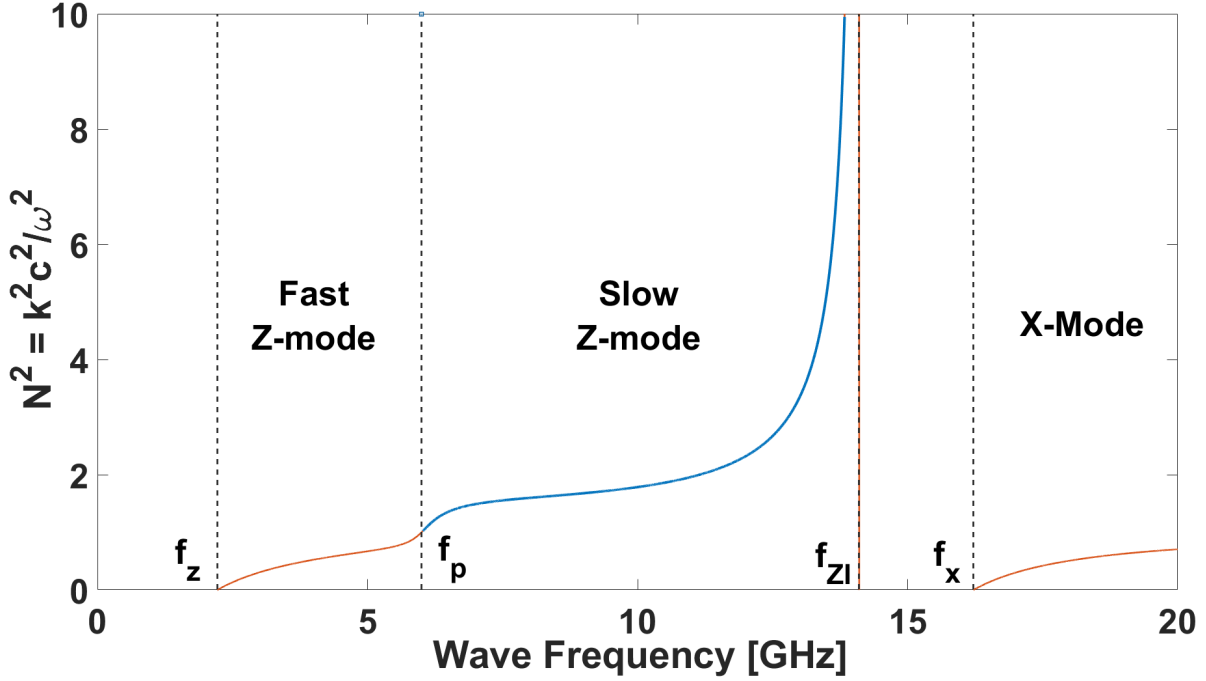


Figure 2.14: Dispersion relationship of the extraordinary wave in an ECRIS plasma.  $f_p = 6$  GHz,  $f_{ce} = 14$  GHz,  $\theta = 5^\circ$ ,  $f_z = 2.22$  GHz,  $f_{ZI} = 14.1$ . The 'slow' and 'fast' qualifiers signify whether the phase velocity of the wave is less than or greater than the speed of light in vacuum, respectively. The slow Z-mode propagates between the plasma frequency and Z-Infinity (Blue). The fast Z-mode propagates in the orange region below the plasma frequency. The X-mode propagates in the orange region above  $f_x$ .

## 2.4.2 Role of Hot Electrons

The instability is the result of large temperature anisotropies,  $T_{\perp} \gg T_{\parallel}$ , within a magnetized plasma. In particular, slow Z-mode emission can occur when  $N_{\text{hot}} \geq N_{\text{cold}}$ , that is when the number of hot electrons is greater than or on the order of cold electrons [92]. Measurements show that instabilities only appear after several 10's ms, corresponding to the time it takes to develop hot electrons [65, 66, 81]. Instabilities in the afterglow regime demonstrate the role of hot electrons in producing instability events. The lack of heating drives increases the diffusion of cold electrons, increasing the ratio of hot to cold electrons [33, 57]. Even if the CW plasma is stable, the decaying plasma will go through a series of instability events until the plasma fully decays [47].

The central role that hot electrons play can also explain one of the more interesting experimental discoveries in the literature: the suppression of the instabilities by two frequency heating of the



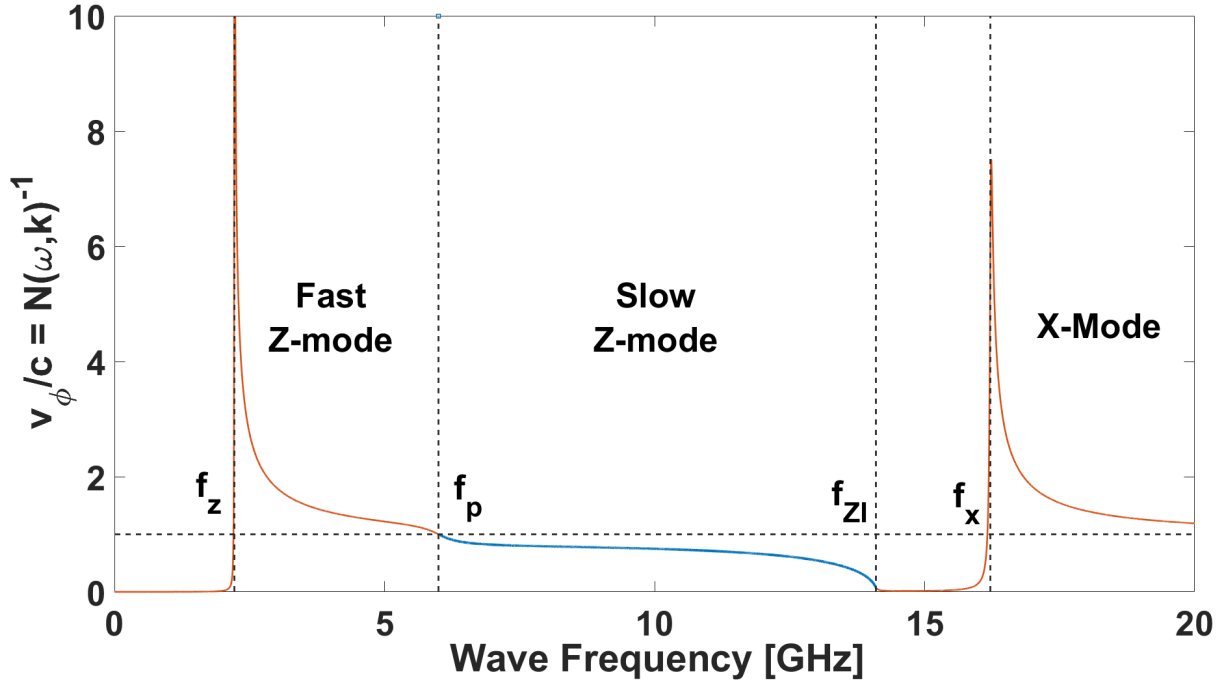


Figure 2.15: Phase velocity of the extraordinary wave in an ECRIS plasma.  $f_p = 6.00$  GHz,  $f_{ce} = 14.00$  GHz,  $\theta = 5^\circ$ ,  $f_z = 2.22$  GHz,  $f_{ZI} = 14.01$ , and  $f_x = 16.22$ . The horizontal dashed line represents  $v_\theta = c$ . The 'slow' and 'fast' qualifiers signify whether the phase velocity of the wave is less than or greater than the speed of light in vacuum, respectively. The slow Z-mode propagates between the plasma frequency and Z-Infinity (Blue). The fast Z-mode propagates in the orange region below the plasma frequency. The X-mode propagates in the orange region above  $f_x$ . The region above  $f_{ZI}$  but below  $v_\theta = c$  is a forbidden region with imaginary propagation.

source plasma. Injecting a second, lower microwave frequency into the plasma can suppress the instabilities, depending on the power of injected microwaves. The amount of power necessary to suppress the instabilities increases with the system's magnetic field and, generally speaking, the secondary microwave frequency [75]. In the most interesting case, the microwave frequency was lower than the minimum cold electron gyrofrequency within the plasma. The only way that the lower frequency microwaves could interact with the plasma is if they were interacting with very high energy, relativistic, electrons. The stabilization may be a result of increased diffusion of hot electrons that interact with the injected microwaves.

We can quantify the effect of hot electrons by linearizing the excited microwave energy density

growth rate [47, 75, 92]:

$$\frac{dE_\mu}{dt} \approx (\gamma_\mu - \delta_\mu)E_\mu \quad (2.34)$$

where  $E_\mu$  is the energy density of unstable electromagnetic modes of growth rate  $\gamma_\mu$  and decay rate  $\delta_\mu$ . The growth rate,  $\gamma_\mu$ , is proportional to the gradient of the electron distribution function, but can be seen to go as  $N_{\text{hot}}/N_{\text{cold}}$  [75, 92]. The decay rate,  $\delta_\mu$ , is proportional to the electron collision frequency. Once the growth rate overtakes the decay rate in equation 2.34, the excited electromagnetic mode becomes unstable, and the microwave energy density increases exponentially. The microwave energy begins resonantly interacting with electrons within the system and drives them into the loss cone. More details on the theoretical description of this phenomenon are discussed in the next section. What is important for the moment is that the onset of the instability is highly dependent on the plasma's ability to prevent the buildup of free energy within the hot electron population of the system. One major goal in preventing the instabilities is to find ways to diffuse hot electrons out of the system quickly.

### 2.4.3 Theory: Quasi-linear Diffusion and Kinetic-Cyclotron Masers

A theoretical description of the instability phenomena is well outside the scope of this study. A rigorous analysis would easily fulfill the requirements of a separate thesis. The framework is also actively under construction, with minimal examples of its application to experimental systems. However, it does exist, and Shalashov et al. [73] recently presented a shallow description of the phenomenon. This section covers an even more brief, qualitative description of Shalashov, Gospodchikov, and Izotov's heroic effort.

The instability is formally known as the Kinetic-Cyclotron Maser (KCM) instability. This unfortunate naming convention finds its roots in space plasma physics, where the phenomena contribute to type I solar radio bursts, decametric radio emission from Jupiter, and auroral Z-mode radiation from the Earth's ionosphere. As Wu mentions, this phenomenon shares the same name as the also-unfortunately named cyclotron maser instability, which is responsible for the emission of coherent microwaves from *gyrotron* devices [97, 98]. The phenomenon that occurs with ECR

ion sources is *NOT* the same as the one which occurs within gyrotron devices. A comparison between these instabilities has been discussed at length by Winglee [94]. Gyrotron amplification results from fluid processes within the plasma, where KCM instabilities cannot be entirely *kinetic* phenomena. Discussions of the theory of this instability, as it is applied to space plasmas, can be found in these references [54, 55, 63, 91, 97].

There are distinct differences in how the instability manifests in space and laboratory plasmas, however, requiring a new approach to the build-up of free energy within the system [73]. While space plasmas gain their free energy through naturally occurring accelerating mechanisms, ion source electrons gain their energy through the externally injected microwave radiation. As a result, the ECRIS plasma is ignited and sustained by the energy source that actively drives the instability.

Before beginning the discussion of KCM interactions within ECR ion source plasmas, we must first discuss a second phenomenon known as quasilinear diffusion. This framework is a perturbative approach to analyzing electron phase-space diffusion caused by wave-particle resonance events. We can define a phase space for electrons, characterized by their transverse adiabatic invariant,  $I_{\perp} = p_{\perp}^2/2m_e\omega_{ce}(z)$  and kinetic energy  $E_{kin} = (\gamma - 1)mc^2$ . If we assume an electron distribution governed by these values,  $\tilde{f}$ , we can discuss the Fokker-Planck interactions of the electrons with monochromatic electromagnetic radiation, of frequency  $\omega$  and harmonic number  $s$ . The theory is simplified if we perform a coordinate rotation by defining:

$$\xi = (sE_{kin} + \omega I_{\perp})/2 \quad (2.35)$$

$$\kappa = (sE_{kin} - \omega I_{\perp})/2 \quad (2.36)$$

which transforms our distribution:  $\tilde{f}(\xi, \kappa) = f(E_{kin}, I_{\perp})$ . Under this transformation, the Fokker-Planck equation takes the form:

$$\frac{\partial \tilde{f}}{\partial t} = \frac{\partial}{\partial \xi} \left( D_{ql} \frac{\partial \tilde{f}}{\partial \xi} \right) \quad (2.37)$$

where  $D_{ql}$  is the quasilinear diffusion coefficient, given by:

$$D_{ql} = \frac{\langle (\Delta \xi)^2 \rangle}{2\tau} \quad (2.38)$$

where  $\tau$  is the time between consecutive 'kicks' with dispersion  $\langle(\Delta\xi)^2\rangle$ . To a good approximation,  $\tau$  is given by the bounce time between mirror points  $\tau_b$ . It is also shown that:

$$D_{ql} = \frac{\pi e^2}{m} \frac{I_{\perp}}{\gamma^2 \tau_b} |E_{\omega}|^2 \sum_{z_r} \left| \frac{\omega_{ce}}{\omega'_{ce} (v_z - k_z I_{\perp}/m)} \right|_{z_r}, \quad (2.39)$$

where  $\omega'_{ce} = \partial\omega_{ce}/\partial z$ ,  $E_{\omega}$  is the spectral intensity of the wave's electric field, and  $z_r$  is the exact location where the resonance condition is met. As electrons that interact with the monochromatic radiation accelerate along lines of constant  $\kappa$ . Taking the time rate of change of the line integral of the distribution along those curves allows us to determine that the electron will absorb power equivalent to:

$$\tilde{P}_{RF} = \int_{\xi_1}^{\xi_2} D_{ql} \frac{\partial \tilde{f}}{\partial \xi} d\xi. \quad (2.40)$$

The transfer of power from the electrons to the EM wave occurs by moving in the opposite direction along the line of constant  $\kappa$ , such that:

$$\tilde{P}_{RF,absorb} = -\tilde{P}_{RF,emit}. \quad (2.41)$$

This is the case during unstable operation. Of course, as the authors note, a full interaction require the integration over all lines of  $\kappa$ . The resulting total power of the interaction is then:

$$P_{RF} = \frac{1}{s^2 \omega} \int D_{ql} \frac{\partial \tilde{f}}{\partial \xi} d\xi d\kappa.$$

We can now discuss resonant heating mechanism, as it pertains to an electron's interaction with a monochromatic electromagnetic wave. To simplify things, Shalashov describes the electron energy in relation to the loss cone. In this case, the  $(I_{\perp}, E_{kin})$  phase space boundaries exist between particles that have *only* transverse energy at the system's magnetic minimum and those that have *only* transverse energy at the system's magnetic maximum. The upper bound is the maximum kinetic energy that a particle can have while still existing in the loss cone. Analytically, these boundaries take the form:

$$E_{kin,(min,max)} = \sqrt{m^2 c^4 + 2mc^2 \omega_{(min,max)} I_{\perp}} - mc^2. \quad (2.42)$$

If an electron interacts with a particle anywhere between these phase-space boundaries, then it is heated until the quasilinear diffusion process pushes it into the loss cone at an energy of:

$$E_{kin}^* = 2mc^2(\omega_{ce,max}/\omega - 1). \quad (2.43)$$

where  $\omega_{ce,max}$  is the maximum angular gyration frequency along a magnetic field line within the trap,  $\omega_{ce}(B_{max})$ .

The ECR ion source KCM, as we know it, is not the result of monochromatic heating. As described in section 2.4.1, the instability occurs as a result of a second-excited frequency within the plasma, possibly more. To that end, we must discuss two-frequency heating. Suppose the electron interacts resonantly with two frequencies  $\omega_1$  and  $\omega_2$ . Extending the framework written above, using equations 2.35, 2.36, and 2.37 we can write:

$$\frac{\partial \tilde{f}}{\partial t} = \frac{\partial}{\partial \xi_1} \left( D_{ql,1} \frac{\partial \tilde{f}}{\partial \xi_1} \right)_{\kappa_1=const} + \frac{\partial}{\partial \xi_2} \left( D_{ql,2} \frac{\partial \tilde{f}}{\partial \xi_2} \right)_{\kappa_2=const} + S, \quad (2.44)$$

where S is a source of electrons into the distribution. The lines of diffusion interact and interfere with one another, allowing the electron to take multiple paths to the loss cone in  $(I_{\perp}, E_{kin})$  phase space [73]. In principle, any number of different frequencies, external or excited, can create a path to diffusion for electrons. This mechanism may also explain how two frequency heating of the ECRIS plasma improves the system's overall stability [75].

The quasilinear diffusion framework sets up the kinetic instability theory known as the cyclotron maser paradigm. This theory has been in development for quite some time as a model for stability of mirror plasmas in laboratory settings [48, 47, 71, 72, 93, 92]. It has successfully described some phenomena within the source plasma such as the so-called 'continuous wave mode' of the kinetic instability [70, 69]. Despite this, the theory is difficult to apply due to the complexity of the inhomogeneous nature of the plasmas in which they occur.<sup>8</sup> Here, it will provide a qualitative context to the underlying mechanism of the instability. As mentioned previously, Shalashov et al. discussed the phenomenon more thoroughly [73].

---

<sup>8</sup>ECRIS plasmas are inhomogeneous in their energy, magnetic field, constituent species, and charge densities.

For this problem, our second frequency  $\omega_2$  is unstable, that is to say,  $\text{Im}(\omega_s) > 0$  [54, 97]. The second frequency is excited by the electrons being heating along quasilinear diffusion lines. Consequently, the electrons can interact with the wave which they have excited and use it as a second path into the loss cone. Thus,  $D_{ql,1}$  is determined by the externally injected microwaves and  $D_{ql,2}$  by those excited internally (see eq. 2.39). The growth rate of the unstable mode goes as  $\pm \left| \partial \tilde{f} / \partial \kappa \right|$ , where the plus or minus sign correspond to emission or absorption of the unstable wave energy, respectively. This mechanism is also known as inverse Landau damping.

The development of the cyclotron maser paradigm for ECR ion sources has provided a much needed analytical understanding of the observed kinetic instabilities within the source plasma. There is still much work to do, however, as new diagnostic techniques are currently under development [25, 27, 36, 49, 84, 85]. The remainder of this study focuses on direct measurements of the electrons which diffuse out of the plasma and measurements of the ion beam under stable and unstable operation. Through these measurements, we can find trends that suggest how the plasma responds to different plasma parameters and how the instabilities may be suppressed or even utilized to enhance source performance.

## CHAPTER 3

### EXPERIMENTAL APPARATUS

All measurements were taken using the Superconducting Source for Ions (SuSI) at the National Superconducting Cyclotron Laboratory (NSCL)[99, 100]. Figure 3.1 shows the beamline configuration, which includes a series of corrector magnets, a dipole analyzing magnet, and a series of focusing solenoids. Beam diagnostics consisted of two Faraday cups, which measured the current coming from the ECR ion source. Microwave power detectors and a High Purity Germanium Detector (HPGe) measured the electromagnetic radiation emitted from the ion source plasma chamber.

This chapter will focus on these different experimental apparatuses. The first section of this chapter will focus on the ion source itself, how to use the ion source to study plasma instabilities, and the different operational configurations used through this study. The latter section will focus on the use and calibration of plasma and beamline diagnostics.

#### 3.1 Superconducting Source for Ions (SuSI)

SuSI is an incredibly powerful ion source for both ion production as well as research. Its fully superconducting magnet design gives its magnetic field an unparalleled degree of flexibility, making it the ideal ion source for studying source-based kinetic instabilities. Six coaxial solenoids generate the system's longitudinal magnetic field, although only four coils are active at any one time. This magnet design allows for the generation of longitudinal magnetic field maxima in the range of 2-3 T. A superconducting hexapole coil surrounds the plasma chamber to generate the field for radial confinement [99]. Figure 3.2 shows a diagram of SuSI's internal components.

The system's principal advantage is the flexibility of its magnetic field. With four longitudinal coils, it is possible to observe how different aspects of the magnetic field affect the plasma. For example, it is possible to vary the magnetic minimum while keeping the injection and extraction side field maxima constant (see fig. 3.3). In general, it is possible to control the value of one of the

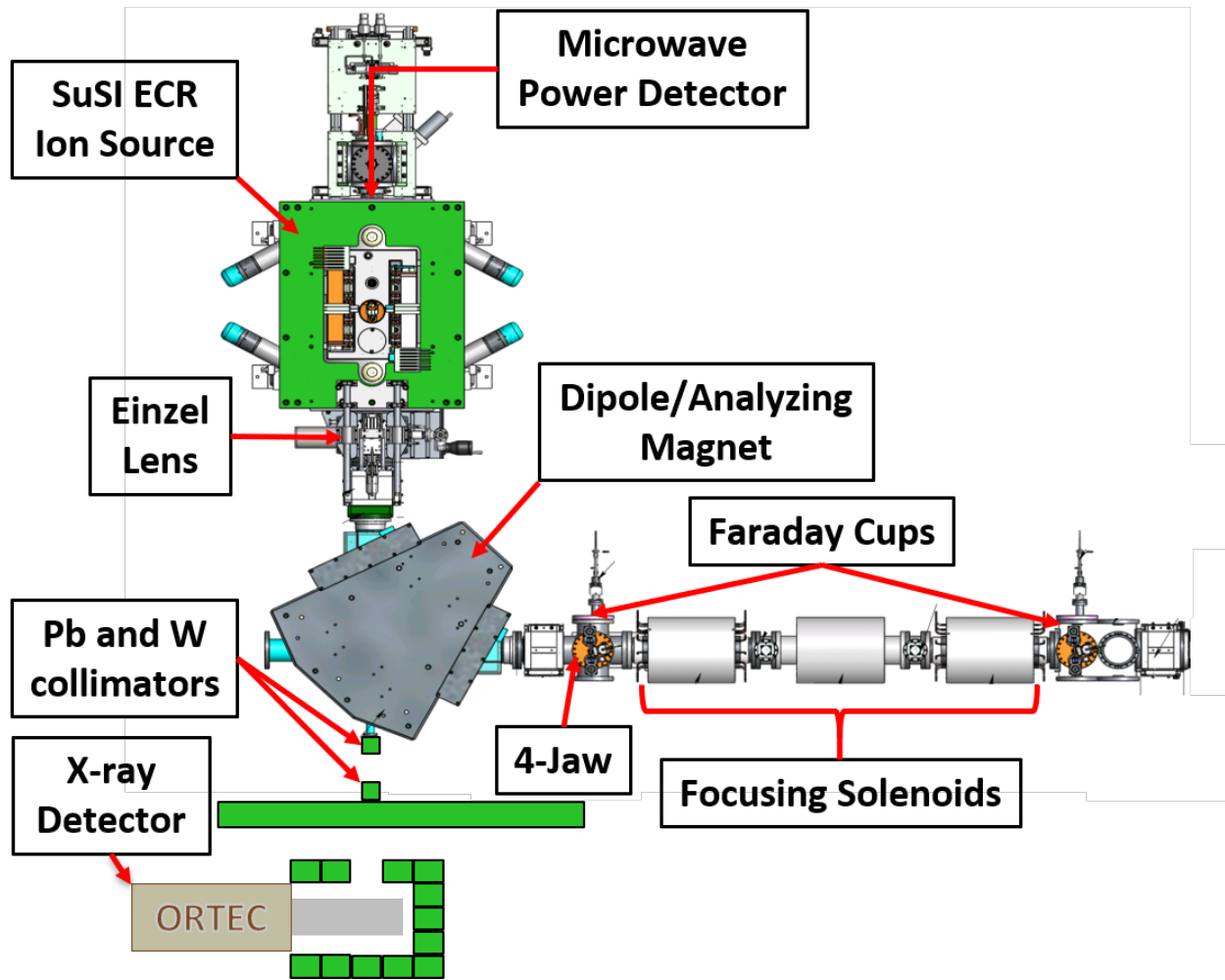


Figure 3.1: A schematic of the source-beamline configuration used for this research.

field extrema within the source chamber while leaving the other two extrema constant. However, the system cannot control the gradient at resonance while also controlling two extrema. Thus, the field gradients were allowed to vary freely. Of course, the hexapole coils allow for a variable radial confinement scheme. Figure 3.4 shows an example calculation of the magnetic field created by the hexapole, in the absence of the solenoids.

A CST simulation model of SuSI performed magnetic field and particle trajectory calculations in the ion source and throughout its beamline (fig. 3.5). The radial field distribution in figure 3.4 is an example of one such magnetic field calculation. Some simplifications were necessary to minimize the computational time of each simulation. These include ignoring the steel frames that



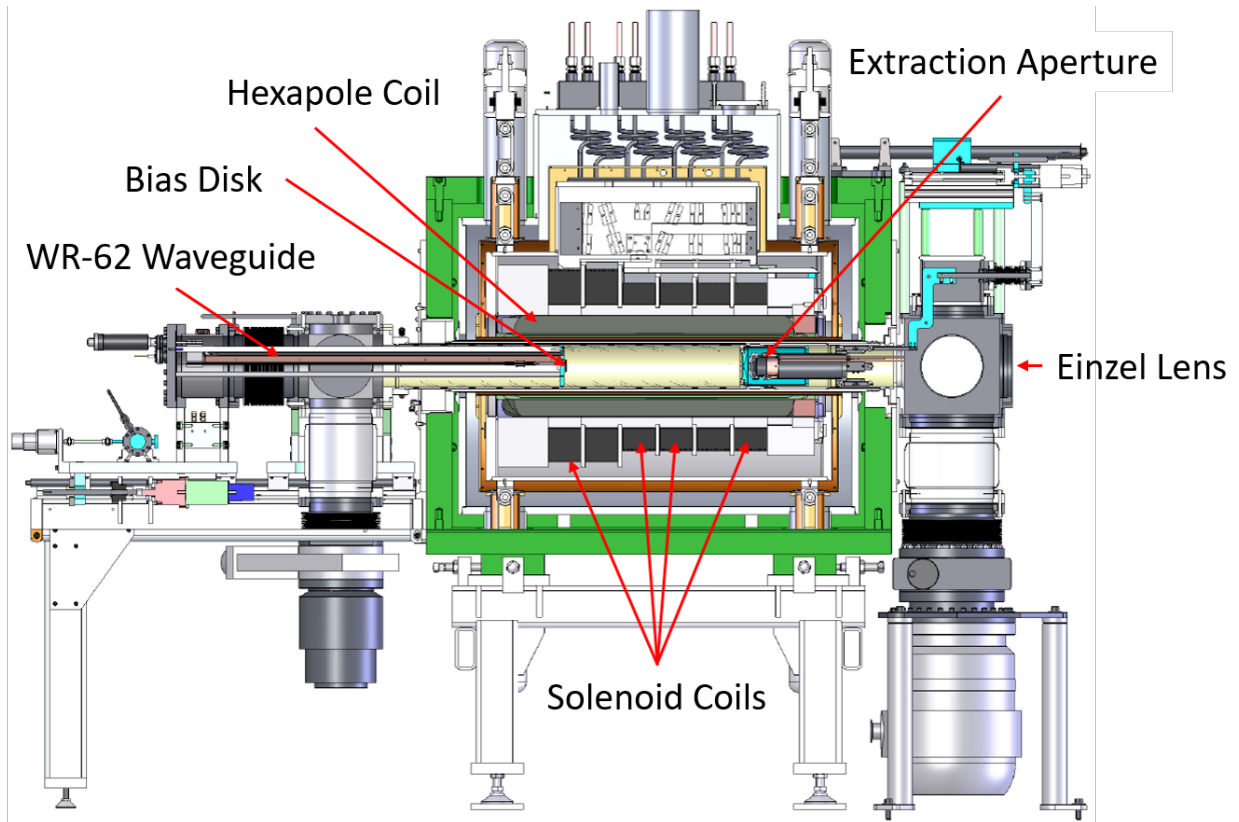


Figure 3.2: A 3D model showing the cross-section of SuSI. Gas and microwave are injected on the left and the ion beam is extracted to the right. Arrows on the bottom point to the four active solenoid coils that surround the hexapole and plasma chamber.

support the ion source and analyzing dipole. Despite this, the simulation reliably reproduced the trajectories of ions extracted from the ion source, within a reasonable error (see fig. 3.6).

A klystron set to 18 GHz ( $B_{RF} \approx 0.64$  T) propagates microwaves, via WR-62 waveguide, into the plasma chamber in order to ignite and heat the plasma. A ULV 150 precision leak gas valve, open and closed by a motor, controls the gas flow rate into the ion source chamber. A bias disk, an electrostatic probe affixed to the injection baffle, acted as both a diagnostic and tuning probe in the plasma chamber. An EPICS controller set the voltage on the disk while measuring the ion current deposited onto it.

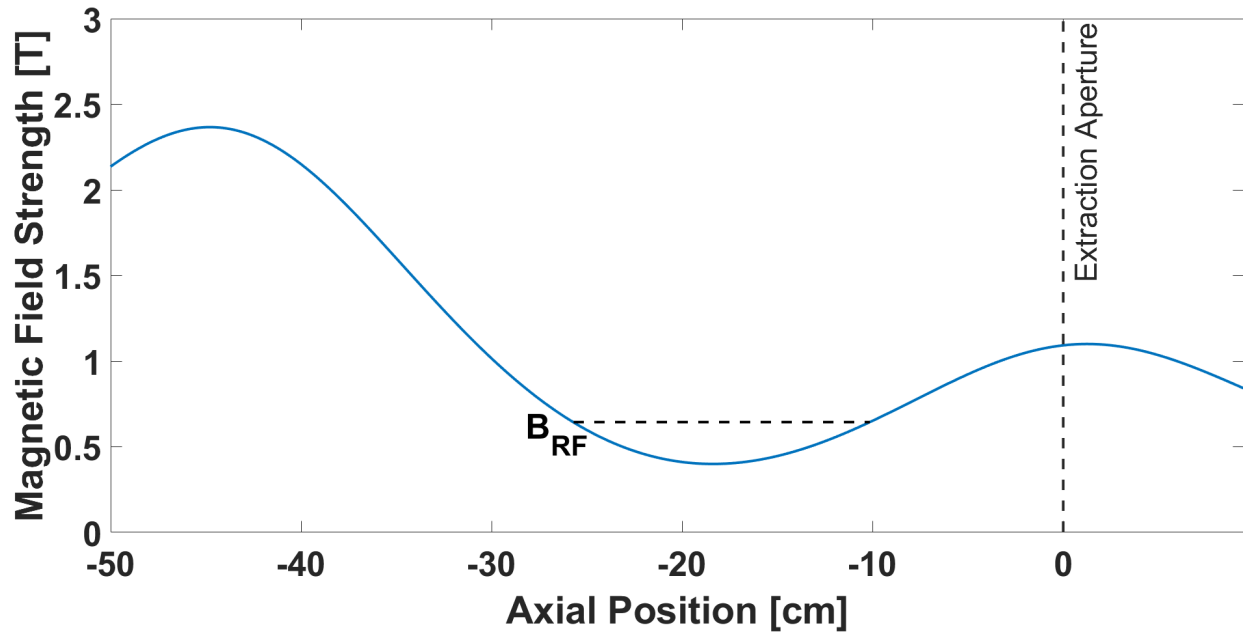


Figure 3.3: An example of the on axis longitudinal field profile for SuSI. The three curves were generated by POISSON/Superfish. The vertical dashed line represents the position of the ion source’s extraction aperture. The horizontal dashed line represents the resonance field for 18 GHz microwaves with cold electrons.

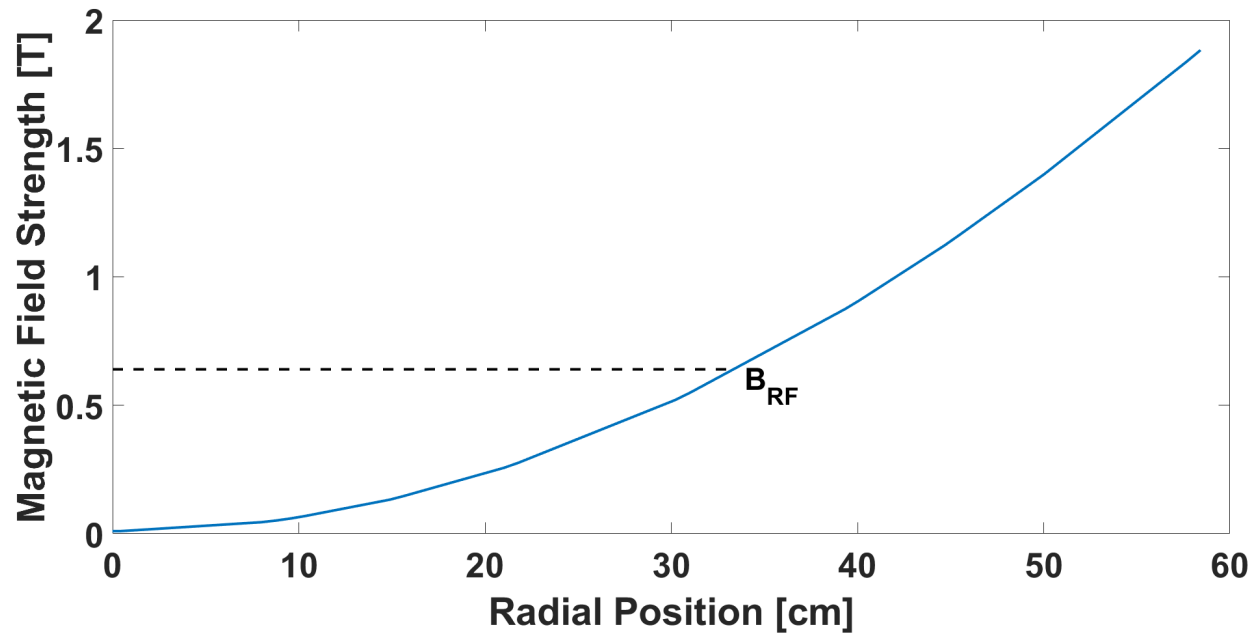


Figure 3.4: An example of SuSI’s radial field as a function of distance from the center axis, with 375 A going through each hexapole coil. The curve was generated by a CST model of SuSI’s coil and yoke configuration. The horizontal dashed line represents the resonance field for 18 GHz microwaves with cold electrons.

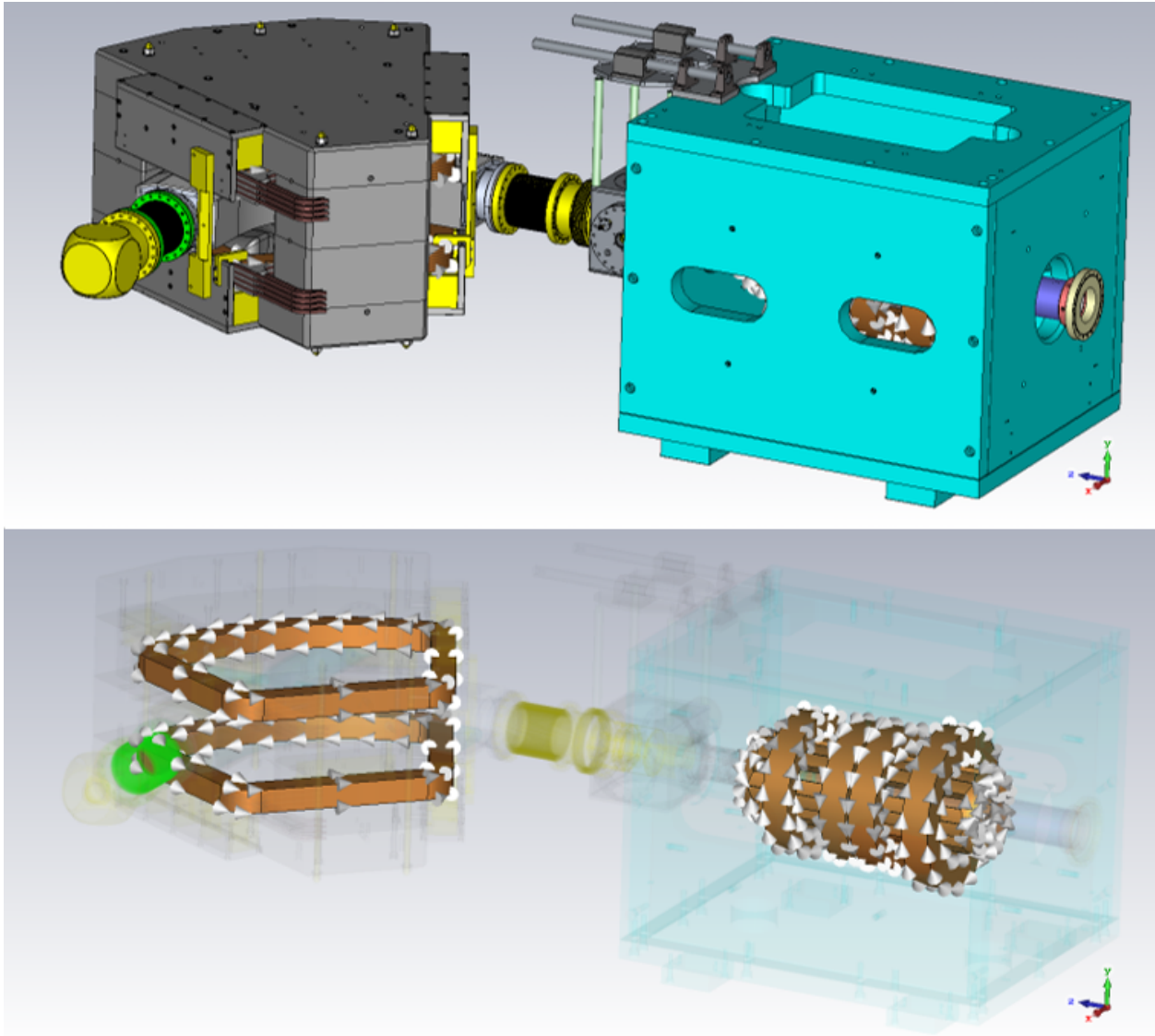


Figure 3.5: (Top) The full geometry of the source and beamline model used in this study. All models were taken from pre-rendered SolidWorks files created by NSCL mechanical engineers. Those files were imported into CST studio suite, where they were used to perform magnetic field and beam trajectory calculations. The model includes a yoke (in blue), plasma chamber, extraction geometry, einzel lens, transport lines, dipole, and Faraday cup geometry. The cup housing geometry has been simplified in order to improve simulation speed. (Bottom) Coil geometry and current direction. On the left are the dipole coils and on the right the source coils. The white arrows represent current direction. In this picture the dipole is set to analyze electrons.

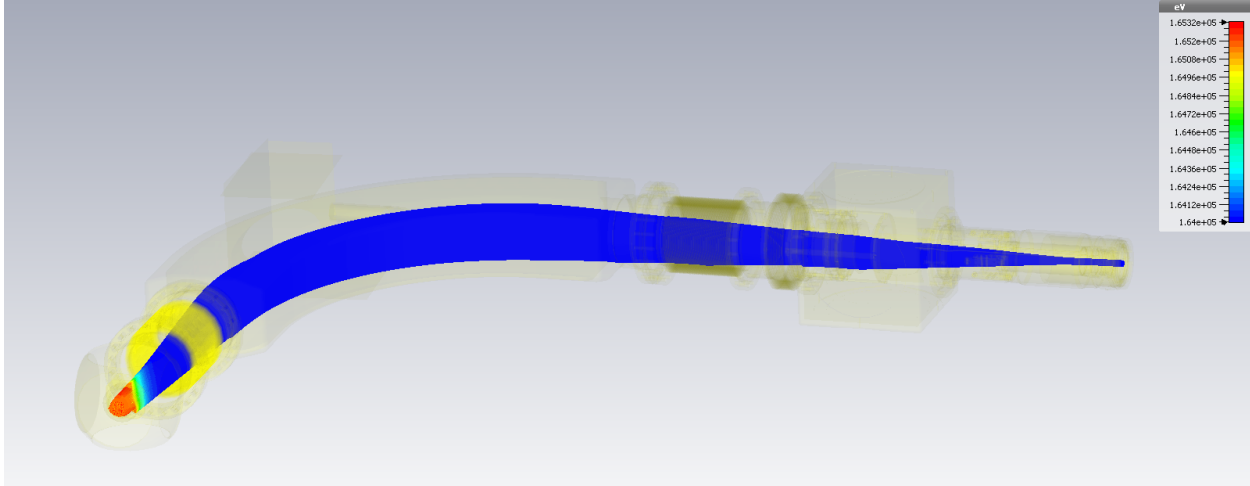


Figure 3.6: The blue lines show the results of a trace simulation of  $\text{Ar}^{8+}$  ions traveling through SuSI's beamline up to the first Faraday cup. Data from a charge state distribution measurement was input into the program to calculate the magnetic field of the the ion source and analyzing dipole:  $E_{beam} = 160$  keV ( $V_{ext} = 20$  kV),  $V_{einzel} = -20$  kV,  $V_{puller} = 0$  V,  $I_{dip} = 102.671$  A. The beam energy was predefined, rather than relying upon the electrostatics simulator. The simulation does slightly over approximate the field in the dipole as it was necessary to increase the beam's energy by 4 keV (or extraction potential by 0.5 kV) in order to make the beam hit the center of the cup. The simulation was performed using CST particle studio.

## 3.2 Diagnostics

To understand how varying ion source parameters affect different plasma parameters, we must first have a way of measuring those parameters. This brings about one of the most challenging aspects of ECRIS research: the diagnostics. The plasma can only be reliably studied by non-invasive diagnostics, such as extracted particle currents or emitted electromagnetic radiation [84]. Invasive methods, such as Langmuir probes, perturb the plasma and change the electron and ion distributions [32, 57]. Any diagnostic used must perturb the plasma as little as possible.

The use of non-invasive diagnostics produces its other issues as well. Only observing particles or energy that escapes the system provides a limited look into the internal interactions occurring within the source plasma. They also tend to be coupled with non-plasma related effects. For example, ion source bremsstrahlung is a reliable method of determining the effect of varying

plasma parameters. However, it is very difficult to separate plasma produced x-rays from wall produced x-rays. It is also effectively impossible to deconvolute the multiple electron scattering and photon scattering events from the measured spectra. At best, this method provides qualitative information on the condition of the source plasma. Tarvainen et al. [84] and Girard et al. [19] have provided detailed reviews of the different diagnostics typically used to study the ECRIS plasma.

This study used three plasma diagnostics to understand the ion source plasma's condition and the instabilities affecting its performance. Those are the beam current, ion source bremsstrahlung, and a novel measurement of electrons that escape confinement through the extraction aperture. This section will discuss the strengths, weaknesses, and steps for analysis for each diagnostic method.

### **3.2.1 Microwave Power Diode**

An HP 8473C Low Barrier Schottky Diode connected to a bi-directional coupler detected the microwave power emitted from the plasma chamber. The diode has a frequency range of 0.01 - 26.5 GHz and has a maximum detectable rise time of 8 - 12 ns. The coupler attenuates power coming from the plasma chamber by -40 dB and any power coming from the klystron by -65 dB. It is impossible to estimate the waveguide's attenuation coefficient, as we do not know the frequency content of the emitted microwaves. The diode allows us to determine when an instability event occurs by measuring variations in the microwave power directed out of the plasma chamber. Those fluctuations could result from a sudden burst of microwave power, emitted from the plasma chamber, or a change in the reflected power due to changing ion and electron densities. Figure 3.7 shows several examples of microwave power signals, measured on an oscilloscope. Both the microwave power and ion beam current diagnostics could be measured simultaneously on the same oscilloscope, allowing for coincidence measurements.

### **3.2.2 Beam Spectrometer**

SuSI's injection beamline comes equipped with a 90° sector magnet that acts as a mass-to-charge selector for injection into the CCF. However, when transmitting electrons through the dipole, the

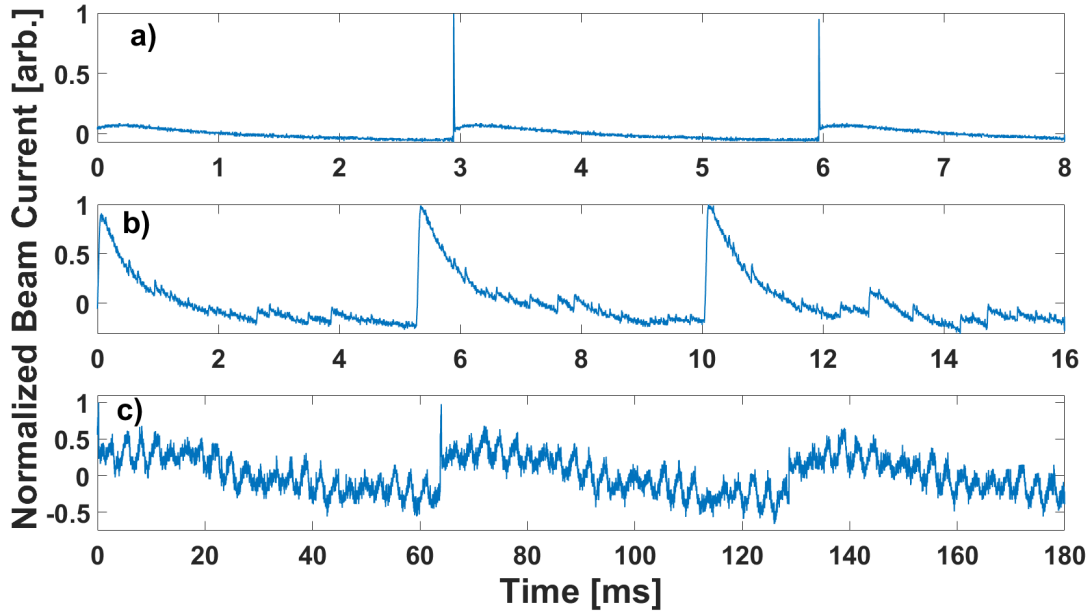


Figure 3.7: Examples of the measured microwave signals coming from the ion source, as recorded from an oscilloscope trace. Data was recorded in 'AC' mode, ignoring the steady state offset. Each plot has been normalized such that their largest value is 1. a) The instability shows a large burst of microwave energy. The 'hump' after the large peak is believed to be a result of a changing reflection coefficient. b) A moderate burst in microwave power which decays back to a steady state value. c) A small burst in microwave power but possible a much longer change in the reflection coefficient of the plasma.

system becomes an energy spectrometer. In general, we can say that the momentum of charged particles capable of traversing the  $90^\circ$  bend is:

$$p = \frac{2q}{\pi} \int B \cdot dl \quad (3.1)$$

where the integral of  $B$  is evaluated along the path the particle of charge  $q$  follows. When we can assume a perfect "hard-edge" model for the dipole field, causing the charge to move along a circle, this reduces to:

$$[B\rho] = \frac{p}{q} \quad (3.2)$$

where  $\rho$  is the radius of the circle that the particle will follow. Equations 3.1 and 3.2 are known as the magnetic rigidity of the particle. This latter form of the magnetic rigidity is independent of the particle's angle of deflection.

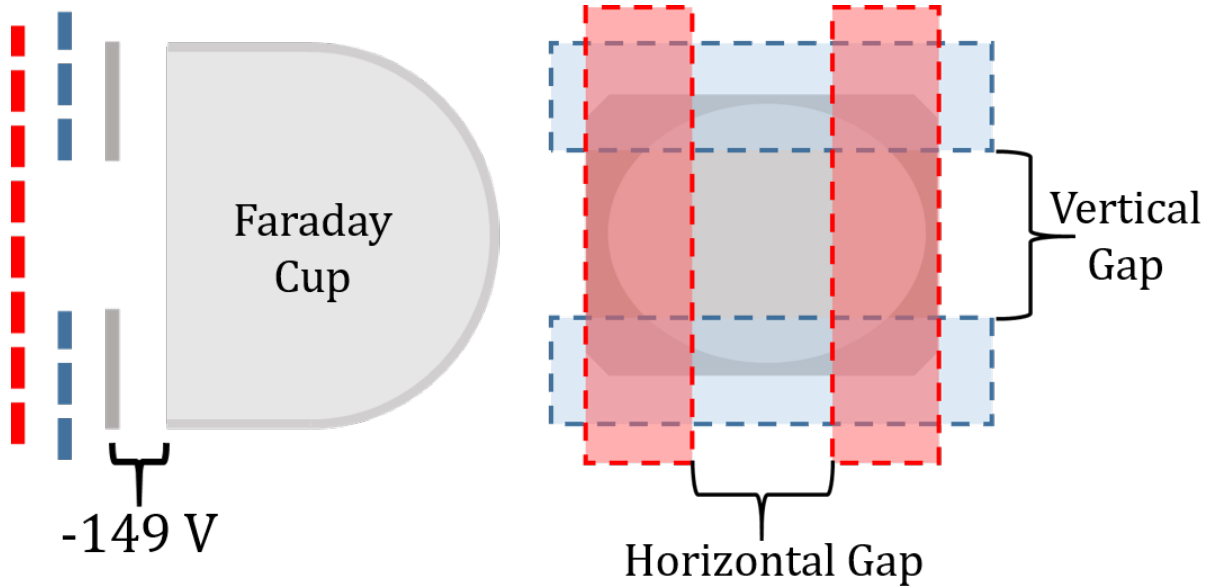


Figure 3.8: The 4-jaw collimator (red and blue) in front of the first Faraday cup (gray) limited the current by closing a gap in the horizontal (dipole bending plane) and vertical directions.

For the case of ions, we can assume all charges coming out of the source are non-relativistic, and equation 3.2 determines the mass-to-charge ratio of an ion by:

$$[B\rho] \approx \frac{m_p v_i}{e} \frac{A}{Q} \quad (3.3)$$

where  $m_p$  is the proton mass,  $v_i$  is the velocity of the ion,  $e$  is the electron charge,  $A$  is the mass number, and  $Q$  is the ion's charge state.

### 3.2.3 4-Jaw Collimator

A set of 4-jaw collimator slits resides within the beamline to control the amount of a single charge state beam going into the solenoid lattice. The collimator consists of two sets of plates that can move to change the width of a gap between them. One set closes down the beamline acceptance in the horizontal plane or the bending plane of the analyzing dipole, and the other in the vertical plane. At largest, each set of plates can open to a maximum and minimum gap width of 35 mm and 5 mm, respectively. Figure 3.8 shows a cartoon of this system.

### 3.2.4 Beam Current

The extracted beam current is the most straight forward diagnostic of the plasma. We are generally safe to assume that  $I_q \sim n_q \sim n_e$  for a given charge state. While it does not provide a detailed description of the plasma electrons, it does give some understanding of the global electron properties. Two Faraday cups reside in the beamline to perform current measurements, one before the focusing solenoid array and one after it. The beam current impinged upon these cups can be measured through a Tektronix MDO3054 oscilloscope or the laboratory beam current monitor (BCM) system. A millisecond or faster range current measurements required an oscilloscope, with the BCM used for slow precision measurements. Both cups come equipped with suppressor rings set to -149 V; to prevent secondary electron emission from the cup. Without the ring, secondary electrons would escape the surface and artificially increase/decrease the amount of current observed or produce a large amount of noise.

The oscilloscope is ideal for taking measurements of the transient profile of extracted particle currents. The Faraday cup-to-oscilloscope transmission line must accommodate 1-100  $\mu\text{s}$  time scale beam current variations, considering the time scale of the emitted microwave and x-ray bursts. Figure 3.9 shows a schematic of the circuit used to connect the Faraday cup to the oscilloscope. It consists of a Twinax cable, a converter box, and the oscilloscope's circuit components. The system converts current to voltage signals at a rate of 40  $\mu\text{A/V}$ . Calculations using the program LTspice predict -3 dB attenuation just before 47 kHz (21  $\mu\text{s}$ ).

The faraday cup/BCM system can measure slowly varying currents on the order of 1 pA. Of course, sampling the current multiple times before recording its value provides the best instrument precision. The system is capable of recording up to 100 samples-per-second (10 ms/sample). The system can also record measurements across several precision ranges. The 300 pA, 3 nA, and 30 nA ranges were the most important for this study. A Keithley 6220 DC Current Source was used to test and calibrate this system across several of those current ranges. Table 3.1 shows selected of the results of that measurement.



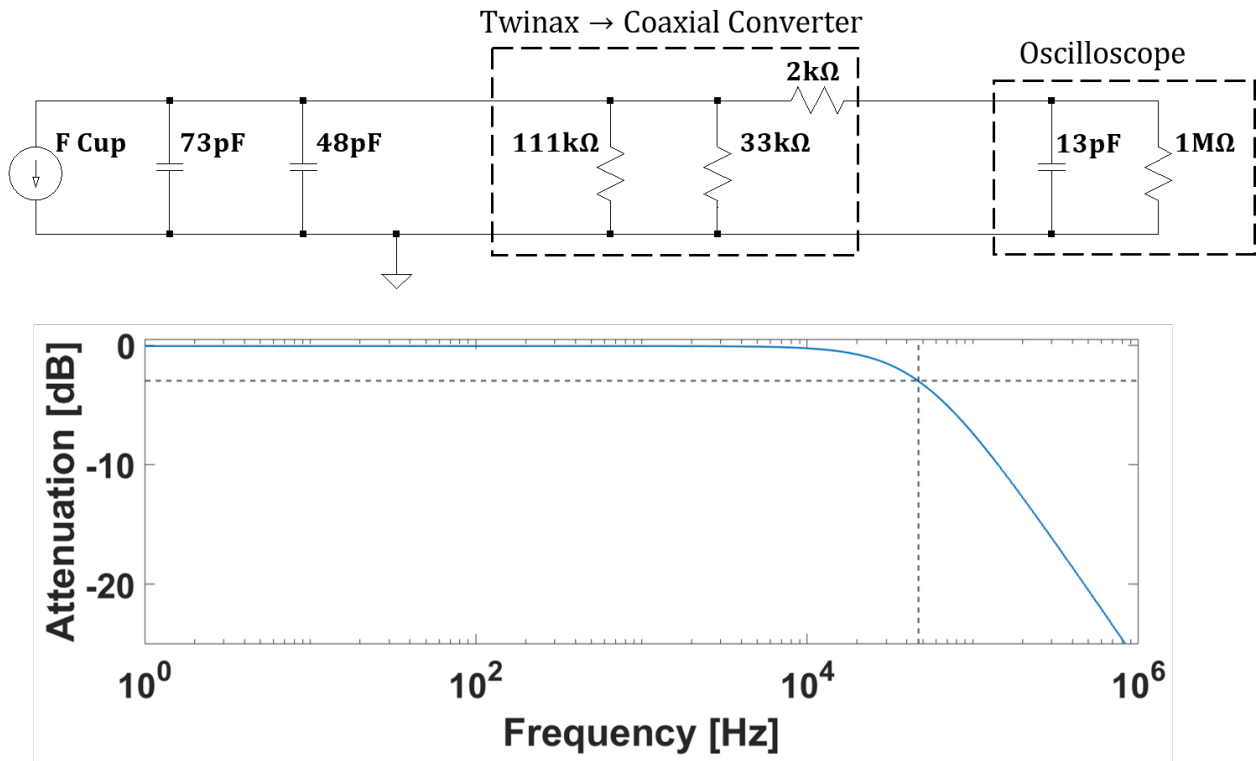


Figure 3.9: The Faraday cup-to-oscilloscope transmission line consists of the cup, a twinax cable, a twinax-to-coax converter box, and the oscilloscope (top). The dashed lines on the attenuation curve show the -3 dB point of the transmission line (bottom). The attenuation plot was generated using LTspice.

Range	Current Set [pA]	BCM read [pA] (100 Samples/s)	Variance [pA]
300 pA	-50	-88.2	0.7
3 nA	-2,000	-2040	2
30 nA	-50,000	-49400	13.5

Table 3.1: The measurable range could be set by the BCM controller. While there is an upper limit of current that each range can measure, the actual value of the range (first column) does not determine the maximum value. That is to say, the first column is more of an order of magnitude reference. Increasing the BCM measurable current range, generally, decreased the relative error of each measurement. The variance increased along side the measurable range, but did not have a significant effect upon each measurement.

### 3.2.5 X-Ray Spectrometer

An Ortec High Purity Germanium (HPGe) detector measured the energy-resolved ion source bremsstrahlung distribution emitted axially from the plasma chamber. Two lead bricks and a tungsten slug, with a 0.81 mm hole drilled through it, provided collimation for the x-ray beam (fig. 3.10). The bricks (green squares in figure 3.1) look into the ion source's longitudinal axis, through a glass window flange, on the analyzing dipole, 218 cm away from the ion source's extraction aperture. A distance of 45.3 cm separates the two collimators. The HPGe detector resides 30-40 cm away from the second brick, housed in a lead bunker. Only the brick closest to the dipole has a tungsten slug in it. The tungsten collimator narrows the diagnostic's acceptance angle down to 5 mrad, projecting a circular acceptance area of  $413 \text{ mm}^2$  (11.46 mm radius) onto the extraction array. The extraction system uses an accel-decel triode, consisting of plasma, puller, and grounded electrodes [95]. The plasma electrode has a radius of 6 mm, the puller a radius of 8 mm, and the ground electrode a radius of 10 mm. The x-ray acceptance area is projected onto all three electrodes, as seen in figure 3.11. In this geometry,  $113 \text{ mm}^2$  of the total acceptance area looks directly into the plasma chamber, with the remaining  $300 \text{ mm}^2$  looking at the extraction array. Interpretations of the bremsstrahlung distribution, which results from using this geometry, must take the mixed origin of photons into account.

Leitner et al. performed simulations of the angular distribution of bremsstrahlung photons moving through a similar collimation system for the VENUS ion source at Lawrence Berkely National Laboratory [41, 62]. The simulation showed that most photons created traveled in the forward direction, and as a result, electrons colliding with the extraction aperture produced the majority of observed photons. As SuSI's extraction system is similar to VENUS's, it stands to reason that, to a good approximation, the same conclusions apply here.

The detector includes a built-in pre-amplifier that then sends pre-amplified, PUR, and busy signals to a rack-mounted amplifier and then into an Ortec Easy-MCA. The multi-channel analyzer (MCA) creates a histogram with 8192 bins. It then fills each bin depending upon the height (voltage) of the pulse signal sent from the amplifier. Initially, the detector will deliver an output similar to

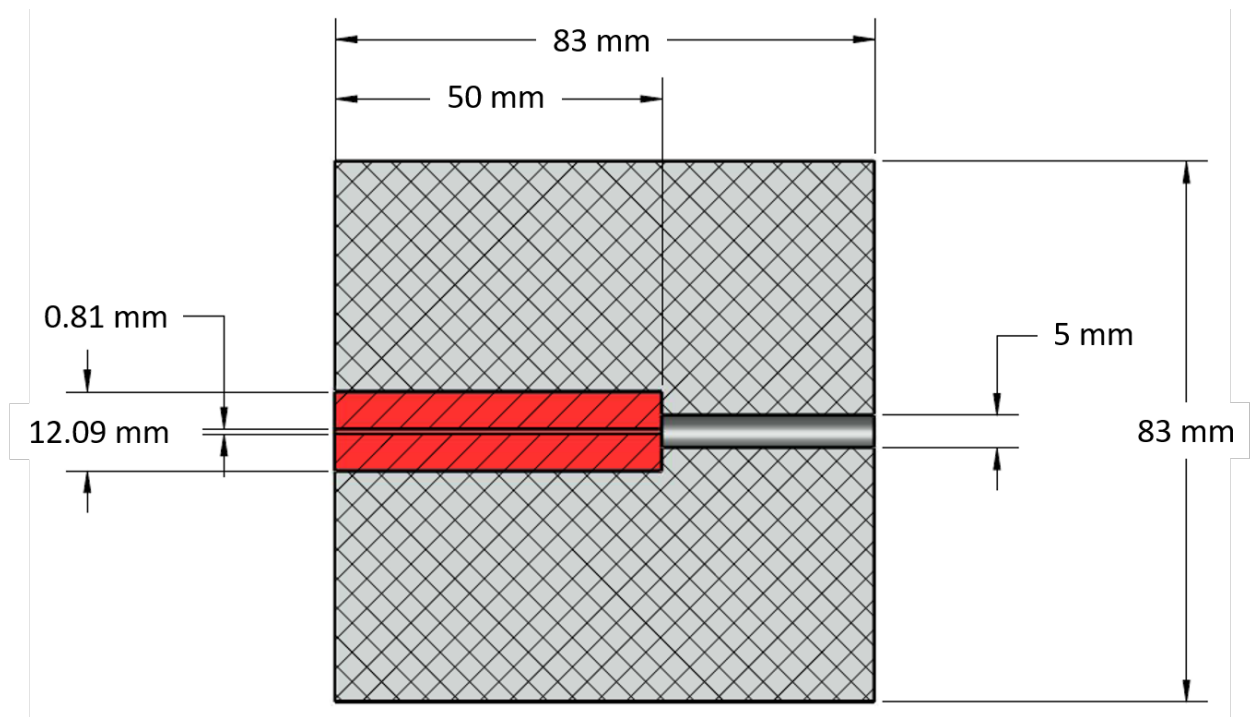


Figure 3.10: Two lead blocks (grey) were used to collimate the x-rays coming from the source. The tungsten slug (red) was only present in the block closest to the dipole (see figure 3.1). Picture has been supplied by the courtesy of Derek Neben.

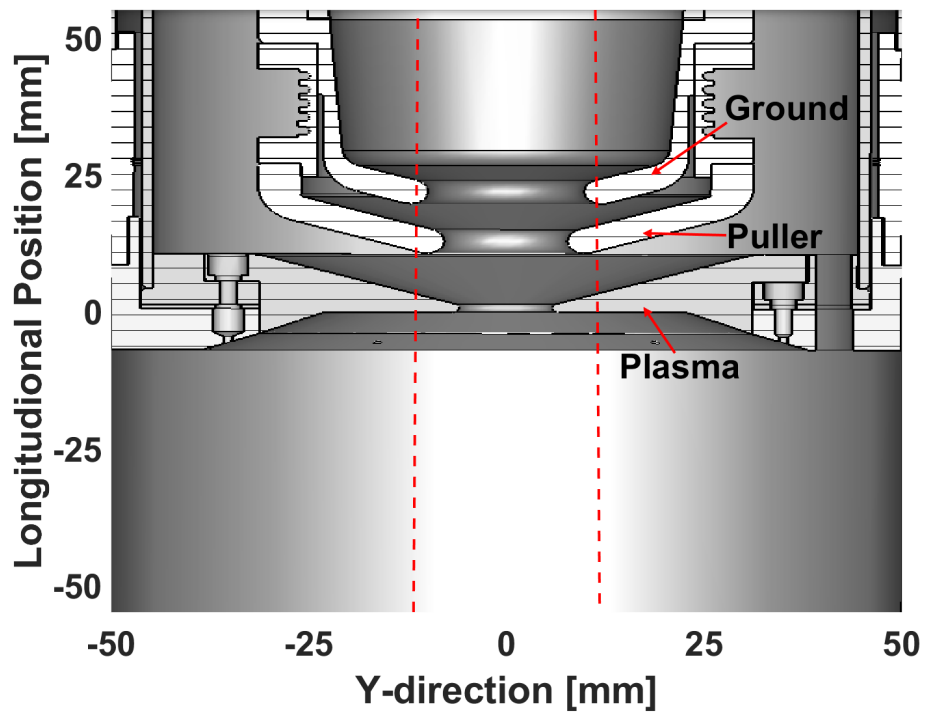


Figure 3.11: The acceptance area of the collimation system (red dashed line) falls on all three electrodes of the extraction system.

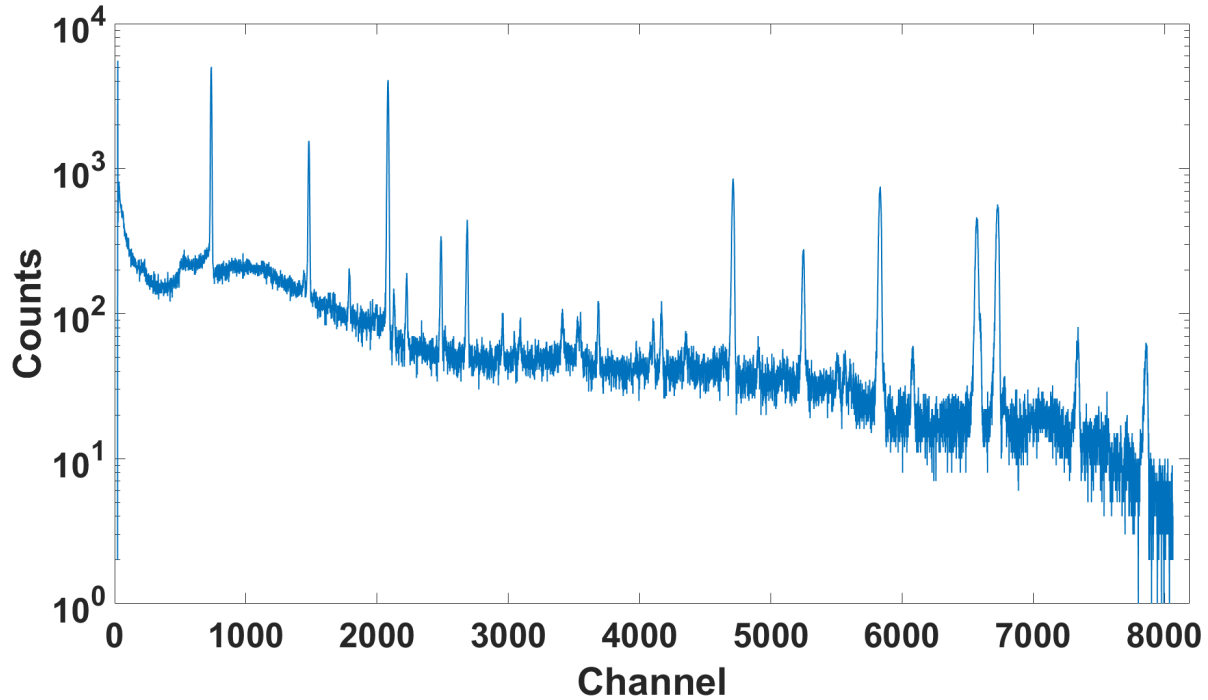


Figure 3.12: An example Eu-152 emission spectrum as measured by the germanium detector used in this study.

figure 3.12. The x-axis is given in channels as the MCA can only record data relative to initial input pulse height. The detector output must undergo channel-to-energy and count rate efficiency calibrations before the results are considered meaningful.

The detector energy calibration relies on the MCA's linearity. Comparing the well known hard x-ray and soft  $\gamma$ -ray emission to the channel numbers associated with the measured emission peaks creates a linear transformation between channel numbers and photon energies. We can compare the relative heights of the emission spectra to that emission line's relative decay probability to determine the energy associated with each peak. Of course, this is easiest for isotopes such as Co-60, which have two emission lines at 1.17 and 1.33 MeV. Using a source like Eu-152, while more difficult, does provide a more accurate calibration over a larger range of energies. As this study focuses on continuous-spectrum bremsstrahlung measurements, it is essential to calibrate the system for a wide range of energies. Data for the source used is given in table 3.2. Figure 3.13 shows an example energy calibration.

Source	$A_0$ [ $\mu\text{Ci}$ ]	$\tau_{1/2}$ (Years)	$A$ [ $\mu\text{Ci}$ ]
$^{152}\text{Eu}$	14.64	13.522	3.26

Table 3.2: Information of the calibration source used.  $A_0$  is the initial source activity, measured on November 1st, 1988.  $A$  is the theoretical activity at the time of the measurement. Calibration data was taken on February 15th, 2018.

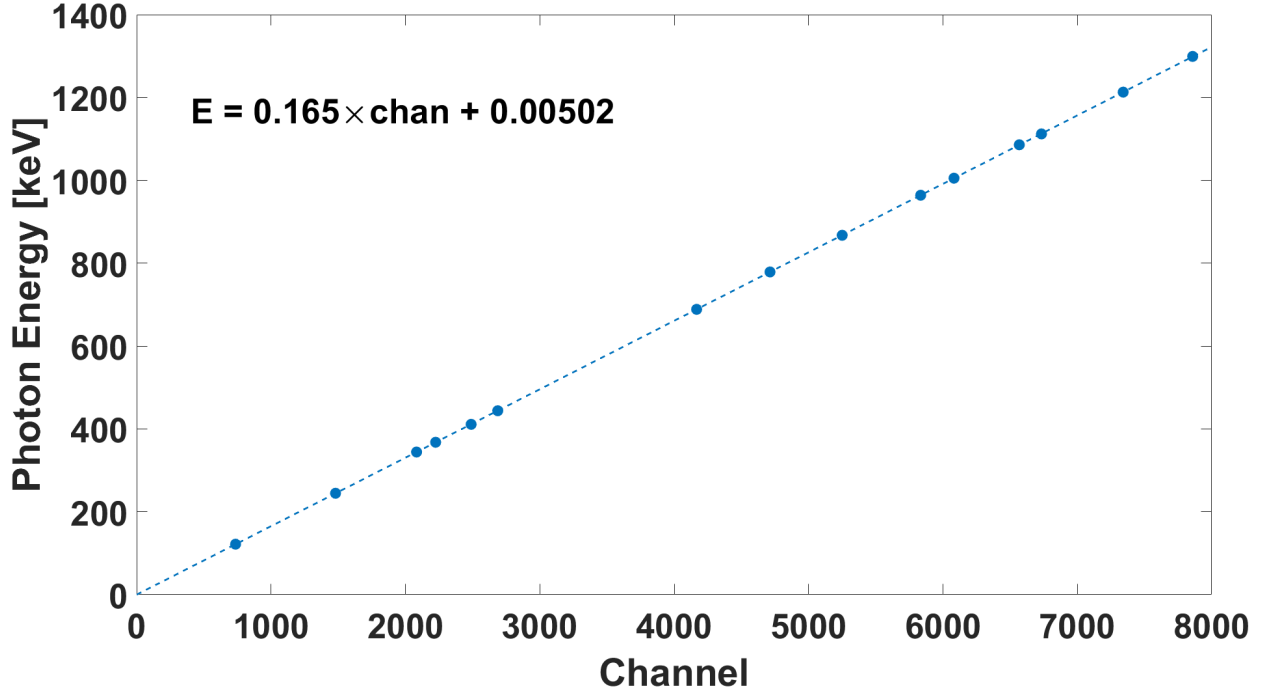


Figure 3.13: Channel-to-energy calibration for the germanium detector used in this study.

To measure the detector’s efficiency curve, the total number of photons observed must be compared to the number of photons emitted from the test source during the calibration measurement. The total number of observed photons is the integral area under each of the measured photon peaks, assuming a Gaussian distribution. An example fit can be seen in figure 3.14. The source’s activity at the time of the measurement,  $A$ , determines the number of photons emitted from the radio-isotope sample [34]:

$$N_{theo} = AP_{\gamma} \frac{\Omega}{4\pi} \Delta t \quad (3.4)$$

where  $P_{\gamma}$  is the decay probability for a given energy level,  $\Delta t$  is the ‘live time’ (active measuring

time) of the detector, and  $\Omega$  is the theoretical solid angle given by [23]:

$$\Omega = \frac{2H \left(1 + \frac{1}{6\rho^2}\right)}{\rho \left[H^2 + (\rho - \pi/4 - (5\rho)^{-1})^2\right]^{1/2}} \quad (3.5)$$

where H is the height of the germanium crystal and  $\rho$  is the distance of the source away from the center of the crystal normalized by the crystal radius. The detector efficiency is then given by:

$$\varepsilon = \frac{N_{meas}}{N_{theo}}$$

The measurement is repeated three times at three different distances in order to confirm the calibration. Moving the source away from the detector makes the solid angle calculation less sensitive to the measurement geometry but decreases the signal to background ratio. If done correctly, all three measurements should agree with one another (see figure 3.15). In some cases, the measurement where the source was closest to the detector did not agree with the two subsequent measurements. In these cases, the final calibration curve included the latter two measurements, and discarding the first. The data sets that agreed with one another were averaged together and fit with a polynomial. Figure 3.16 shows an example of the fit used. An estimate of the measured background counts was subtracted from the measured spectra before applying the efficiency calibration. For this study, the most significant background sources were the other ion source, ARTEMIS, the cyclotrons (during operation), and radiation from activated material within the experimental vault.

We can now take the corrected spectrum, using the measurement's live-time to convert to counts-per-second, and calculate what is known as the 'Spectral Temperature',  $T_s$ . The spectral temperature assumes an approximation of the plasma where  $I_\gamma \propto \exp\left(-\frac{hf_\gamma}{T_s}\right)$ , where  $I_\gamma$  is the bremsstrahlung count rate, h is Planck's constant,  $f_\gamma$  is the photon frequency. This relation comes about by assuming the bremsstrahlung results from a Maxwell-Boltzmann distribution of electrons [2, 30, 41]. The units of  $T_s$  are eV rather than K as the presence of Boltzmann's constant is implicit, as is the convention in much of the literature.

Usually, a linear region of the logarithm of the intensity vs. energy ( $\ln I_\gamma$  vs.  $E_\gamma$ ) can be found. Fitting this region with a line and taking the inverse reciprocal of the slope of that line will return the

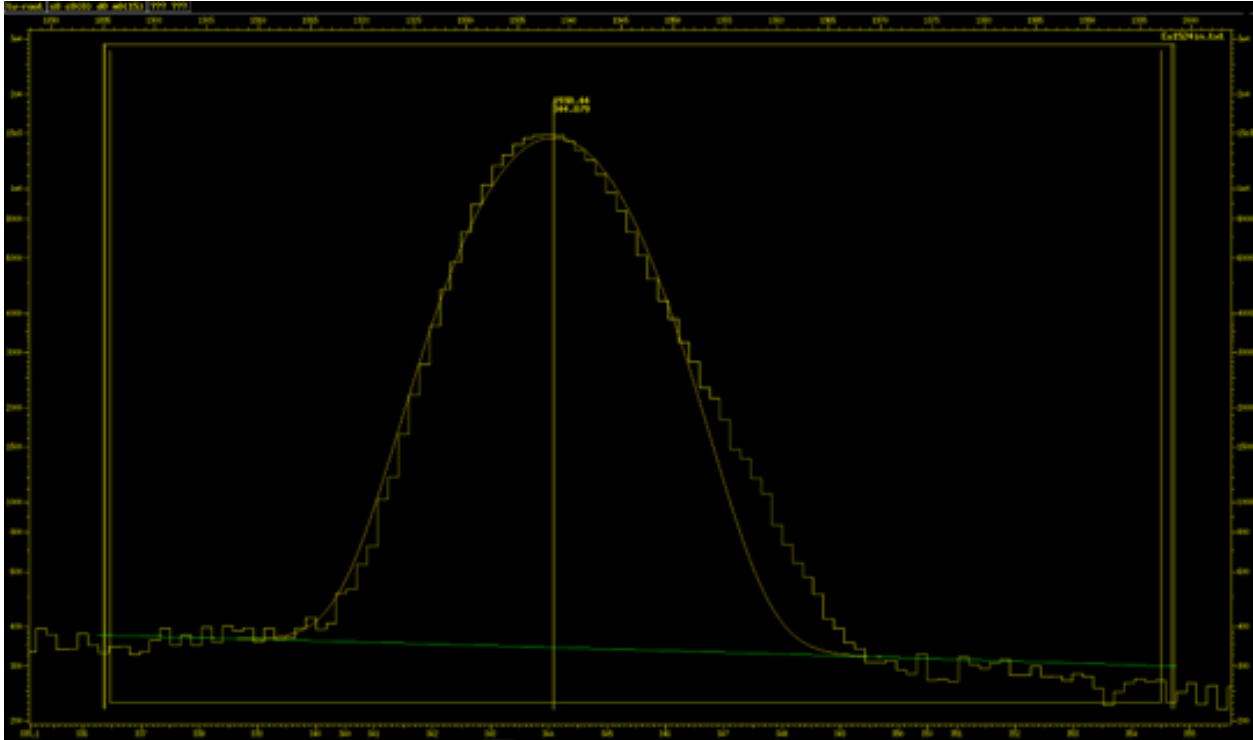


Figure 3.14: The program known as TV, written by Andreas Fitzler from the university of Köln, was used to integrate the observed peaks of the spectra. The program uses the region surrounding the peak to subtract background counts. It then fits a Gaussian distribution to the background subtracted peak and then integrates that Gaussian in order to determine the total number of photons observed.

spectral temperature. Figure 3.17 shows a plot of the log intensity of the measured bremsstrahlung distribution and the fitted region. Alternatively, fitting an exponential,  $y(x) = a \exp(-bx)$ , will return an equivalent value [61]. A weighted least-squares fitting model was used to determine the line given in figure 3.17 [74]. Although reported less often, the x-intercept of the fitted line  $X_{T_s}$  also provides valuable information about the distribution's energy content. Appendix A shows the equations for calculating the linear fit, spectral temperature, and estimates of their respective errors.

While both  $T_s$  and  $X_{T_s}$  are measurements of the energy content of the ion source plasma, any trends found using these measures must be carefully interpreted. For example, an increasing  $X_{T_s}$  may correlate with an increasing maximum electron energy OR an increasing density of high energy electrons. The calculation of the intercept is highly dependent upon the number of observed photons at high energies. If the electron density increases across the entire energy domain, so that

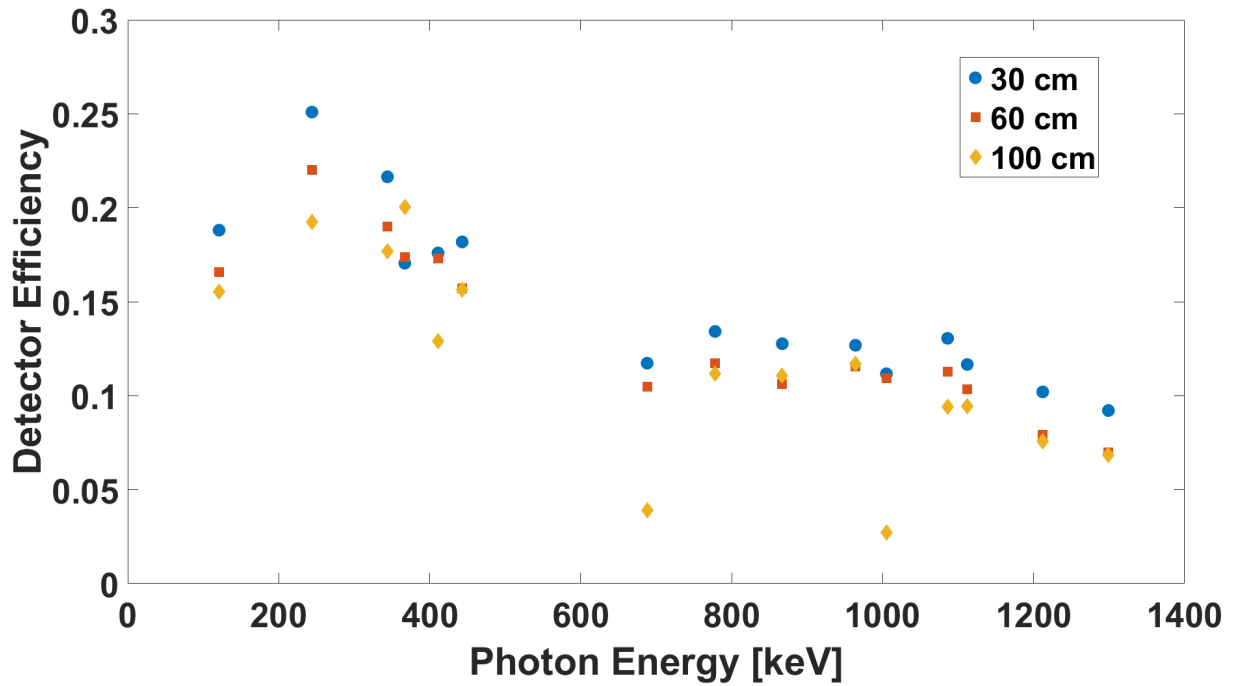


Figure 3.15: Repeating the efficiency calibration three times helps confirm the solid angle calculation. Measurements were taken at 30, 60, and 100 cm distances away from the radial edge of the detector (assuming cylindrical geometry).

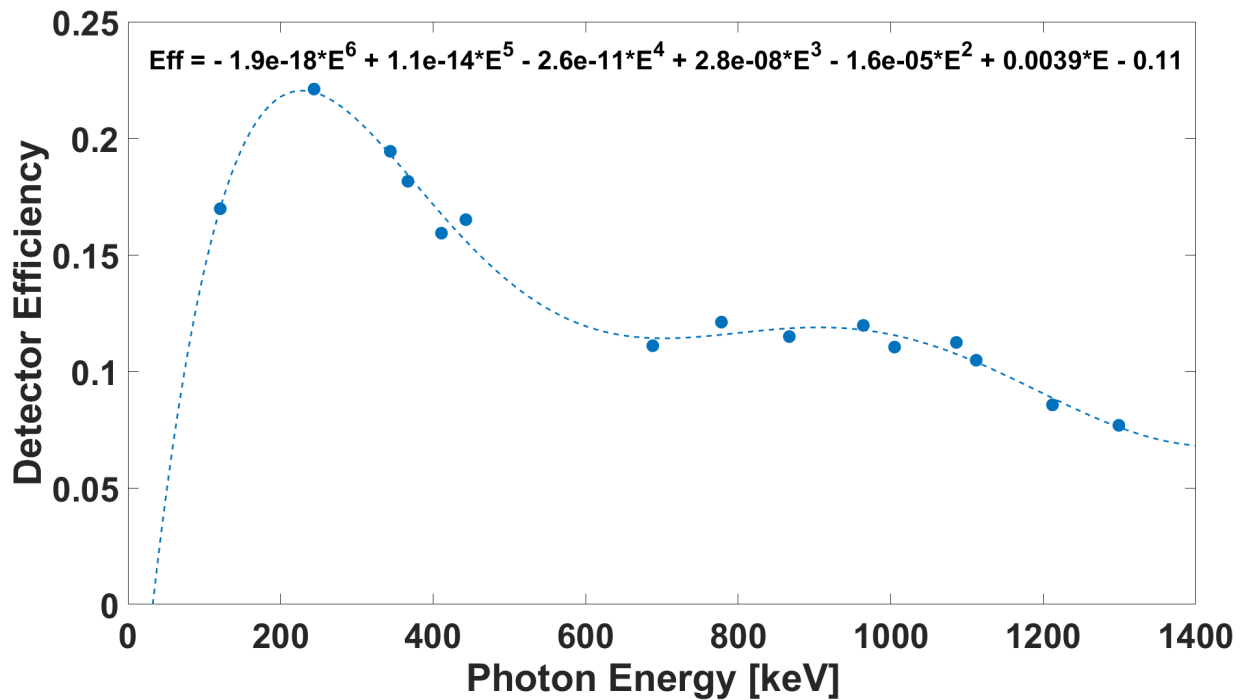


Figure 3.16: The two/three measurements were averaged together and the resulting data set was fit with a 6th order polynomial. The fit was generated by MATLAB's curve fitting tool.



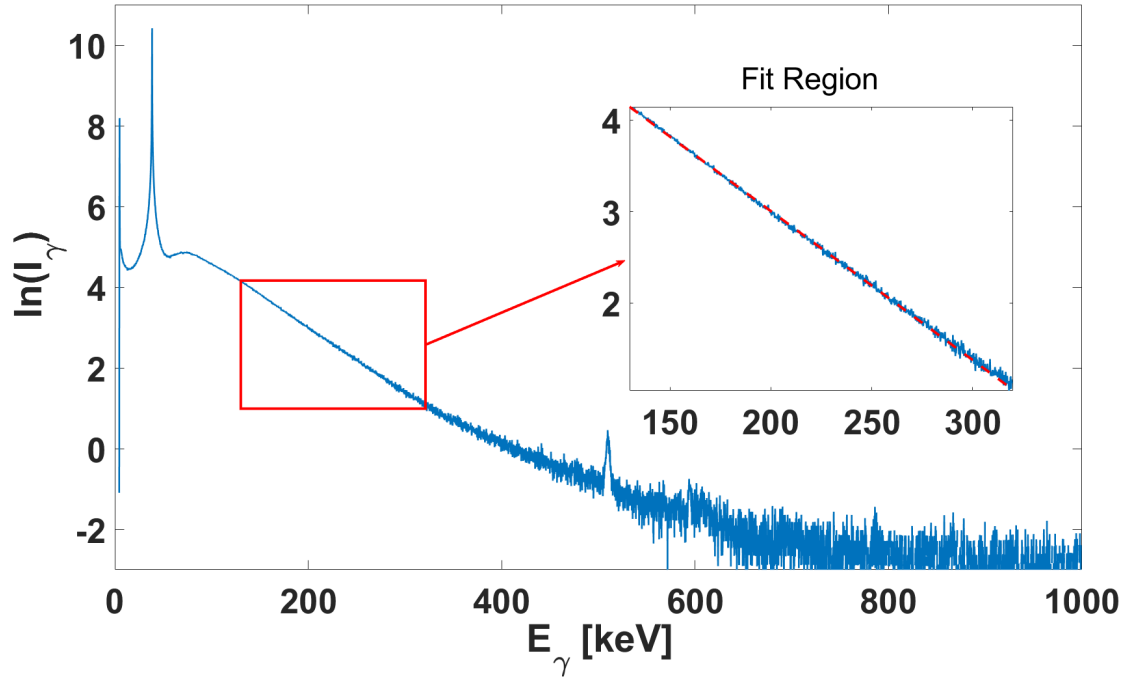


Figure 3.17: Natural log of the bremsstrahlung intensity. The smaller plot show the fit of the linear region of the distribution. The domain was manually chosen to be  $130 \text{ keV} < E_\gamma < 320 \text{ keV}$ . The line is described by  $\ln I_\gamma = -0.01629 \times E_\gamma + 6.261$ , giving a spectral temperature of  $61.39 \text{ keV} \pm 0.599 \text{ keV}$ .

the observation of higher energy electrons becomes more probable, then it will appear as if the plasma's energy content has increased. In reality, the emission rate of those higher energy photons has simply reached above the noise floor of the measurement. Measuring the x-ray distribution for a longer period of time achieves a similar effect, assuming a well-shielded detector or minimal background.

It is essential to know where the log intensity is most linear before fitting the distribution. Unfortunately, many authors will use fixed domains over which to calculate the spectral temperature (see refs. [1, 2, 102].) While there are many practical reasons for doing so, it is best to avoid this practice whenever possible. Other authors have made this same observation, recognizing that the calculation of the spectral temperature changes with the fitting domain [61, 62]. As the purpose of the calculation is to determine a temperature like quantity for the plasma, it is obvious that the energy domain associated with the temperature must change as the energy content of the system

changes. If this were not the case, then it would imply that the model describing the energy distribution itself is changing, making the definition of temperature meaningless.

To fix this, the calculation of spectral temperatures in this study included an algorithm that determined the high and low energy bounds of the fitting domain. Based on work by Kroll et al. [35], this algorithm uses non-linear regression analysis to determine the most linear region of the distribution. An algorithmic approach provides a more objective way of determining a spectrum's linear region while also making the analysis less time-consuming.

The simplest way to determine the upper limit is to truncate the distribution at a fixed count rate. A survey of all measured spectra is necessary to determine the minimum count rate. For this study, an intensity of 0.5 counts/s was sufficient to ensure the fitting domain spanned the spectrum's linear region for all measurements. This procedure is arbitrary and biased towards less energy-dense operating points but is more accurate than fixing the upper limit. The lower energy limit is chosen by progressively truncating the lower energy portion of the distribution until the fit meets a threshold given by the coefficient of determination:

$$R^2 = 1 - \frac{\sum_k (\ln I_{\gamma,k} - y_k)^2}{\sum_k (\ln I_{\gamma,k} - \text{mean}(\ln I_{\gamma,k}))^2} \quad (3.6)$$

where  $y_k$  is the evaluation of the fit given by equations A.1 and A.3. If  $0.99 < R^2 < 1$ , then the fit would be used to calculate the spectral temperature. Otherwise, the code truncated the first 5 points from the data set, and the fitting process began again. Occasionally, the lower limit on  $R^2$  needed to be lowered to 0.985 for the algorithm to work as described. The 0.99 threshold is also arbitrary but is also more accurate than fixing the fitting domain's upper limit. Figure 3.18 shows compares two fits: one with blindly chosen fitting domain and one where the described method chooses the fitting region. Applying the algorithm improves upon the fit without sacrificing too much of the fitting region in the process.

Rigorous analyses of the bremsstrahlung diagnostic and the fitting algorithm are outside the scope of this work. Rather than developing these tools further, section 4.5 discusses the advantages and disadvantages of the presented procedure. While imperfect, this work presents a starting point

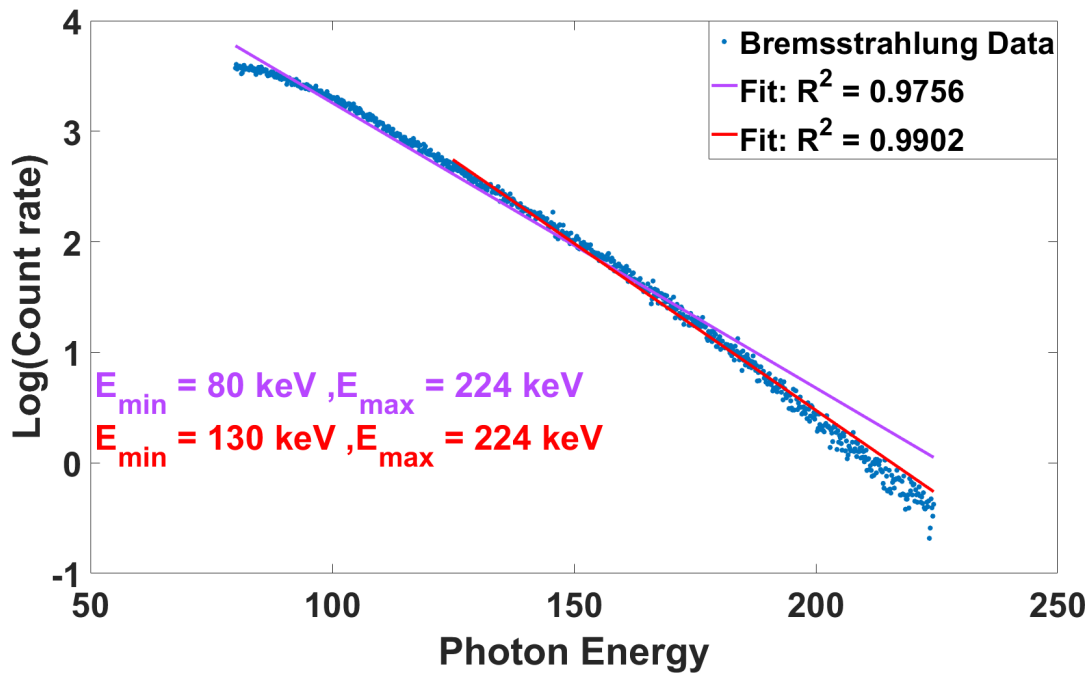


Figure 3.18: Choosing the fitting region algorithmically, rather than blindly fitting over a region which worked for a different operating point, dramatically improves the overall fit. Properly using this method can result in improved analytical results when applied across multiple operating points.

for others to improve upon and refine. The MATLAB code used for determining the spectral temperature can be found in Appendix A.

## CHAPTER 4

### DISTRIBUTION OF ESCAPING ELECTRONS

#### 4.1 Experimental Goals

Understanding the electron velocity distribution function (EVDF) and the electron energy distribution function (EEDF) is imperative for understanding the internal processes of a plasma. Currently, the energy distributions within ECRIS plasmas are poorly understood. As mentioned in section 2.2.3, the distributions are often approximated as a combination of three Maxwell-Boltzmann distributions [28, 52, 57]. However, this is only a phenomenological approximation. Understanding how different ion source parameters affect the plasma requires direct measurements of the plasma.

The number of diagnostics capable of probing the EEDF is limited. Langmuir probes are too invasive and cause an unacceptable perturbation upon the plasma [31, 84]. The traditional non-invasive method for probing the plasma is the characterization of longitudinal and radially emitted bremsstrahlung [2, 50, 61]. However, x-rays are produced as electrons scatter through a material; in this case, the plasma and plasma chamber [34]. It is difficult to de-convolute the effects of electron scattering to varying plasma parameters. At best, we can use these results to make qualitative arguments about how the plasma is changing [2].

A novel measurement method has recently been developed to overcome some of the limitations of the Langmuir probe and bremsstrahlung diagnostics. This new technique looks at the energy distribution of electrons that escape confinement through the extraction aperture [28]. While not perfect, this measurement provides new quantitative insight into the electron distribution and more context to other well-established diagnostics.

## 4.2 Considerations for the Electron Current Measurement

To perform this measurement, most of the optical elements must be de-energized. Starting from the source: The extraction electrode, puller, and einzel lens all need to be grounded. Doing so prevents potential barriers for the escaping electrons. At the NSCL, this can be done by turning on the electrodes' power supplies and setting their voltage to zero.

It was possible that decreasing the extraction voltage could change the characteristics of the plasma. Even relatively small voltages within the source chamber can affect the charge state distribution [31]. We can easily probe this effect by observing the source bremsstrahlung distributions and transient ion currents while decreasing the extraction voltage in progressive steps.<sup>1</sup> The Einzel lens voltage matched the extraction voltage for each measurement. Figures 4.1 and 4.2 show the results of those measurements. A second measurement of the dependence of the bremsstrahlung on the changing extracting voltage can be found appendix C (fig. C.1).

Even though the extracted ion currents decreased dramatically as the extraction voltage decreases, the bremsstrahlung distribution is overwhelmingly unaffected. Figure 4.1 shows no visual distinction across each distribution. While calculations of the spectral temperature suggest a small increase in the system's energy content for higher extraction voltages, each measurement is consistent with every other measurement. The results suggest that the population of electrons with energies above 80 keV were largely unaffected by a changing extraction voltage. This result makes sense as hot-electrons are highly non-collisional and should be minimally affected by changes to the plasma parameters of ions or neutrals that may occur as a result of a changing extraction voltage.<sup>2</sup>

Most of the magnetic optics must also be de-energized during the measurement. Measuring the electrons at the first Faraday cup, immediately after the dipole, removes interference from the solenoids (see Figure 3.2). To precisely measure the electron distribution, the analyzing dipole required a smaller output current supply. Under its standard configuration, the dipole's power

---

<sup>1</sup>While ions do escape confinement at lower voltages (< 2kV), it is difficult to distinguish one charge state from another.

<sup>2</sup>Although not known at the time of this measurement, this trend has been previously observed in other ion sources[78].

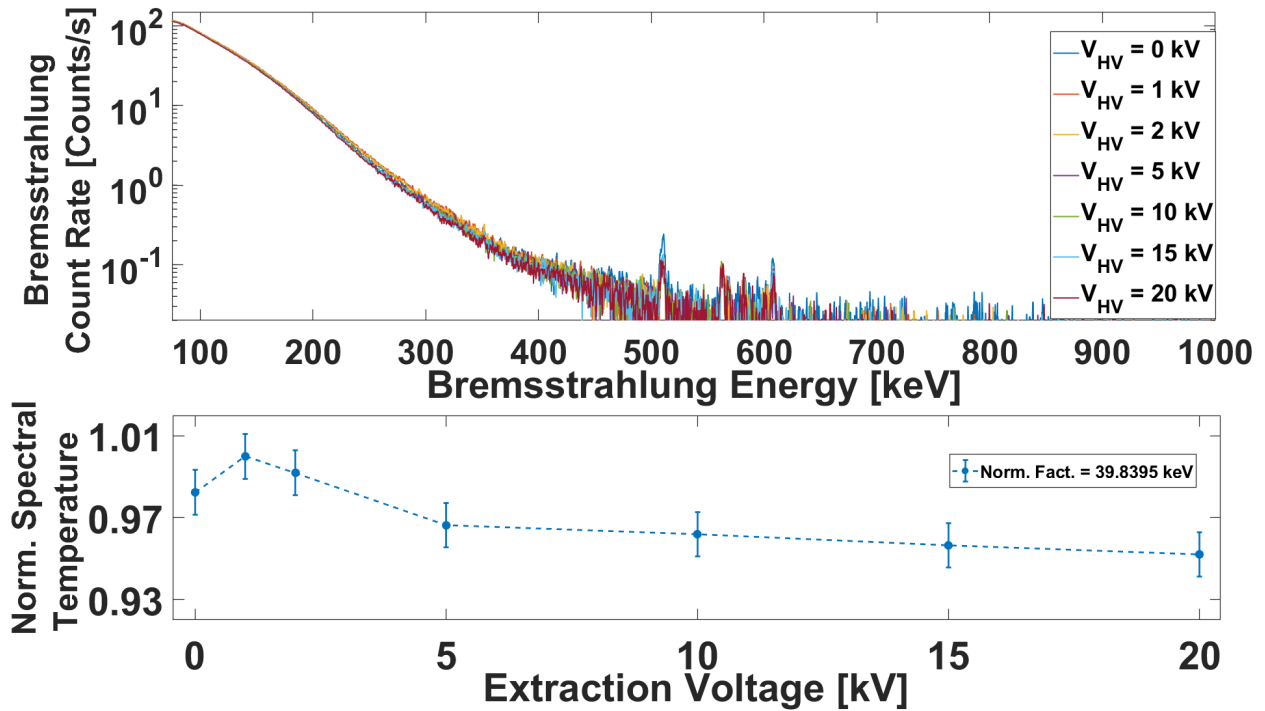


Figure 4.1: A varying extraction voltage has little effect on the hot-electron bremsstrahlung distribution. The spectral temperature seems to fluctuate at low voltages and then decreases higher extraction voltages. This low order deviation is likely an effect of a changing background between measurements due to changing facility operational conditions (compare to figure C.1). Plasma parameters are  $B_{\min} = 0.397$  T,  $P = 350$  W,  $T_{\text{live}} = 600$  s, pressure = 212 nTorr.

supply can output 0 to +500 A, to bend  $\sim 10^7$  s -  $100^7$  s keV ions. For this measurement, we used a bipolar power supply designed to output less current ( $-12$  A  $< I < 12$  A) with more precise regulation ( $\delta I = 10$  mA).

The largest issue, however, is the presence of residual lines of magnetic flux that exist in and around the beamline. Decades of operation have saturated the iron in the surrounding area with a magnetic flux that impedes the electrons' ability to traverse the beamline. The magnitude and direction of the flux were measured using a Lake Shore Model 410 Hall probe. Figure 4.3 shows the results of those measurements. The residual fields act like optical elements which perturb the trajectory of the electrons. The electrons feel a force that pushes them towards the wall of the beam pipe, preventing low energy electrons from entering and passing through the dipole magnet. This effect must be compensated for when looking at the final distribution of electrons. It was

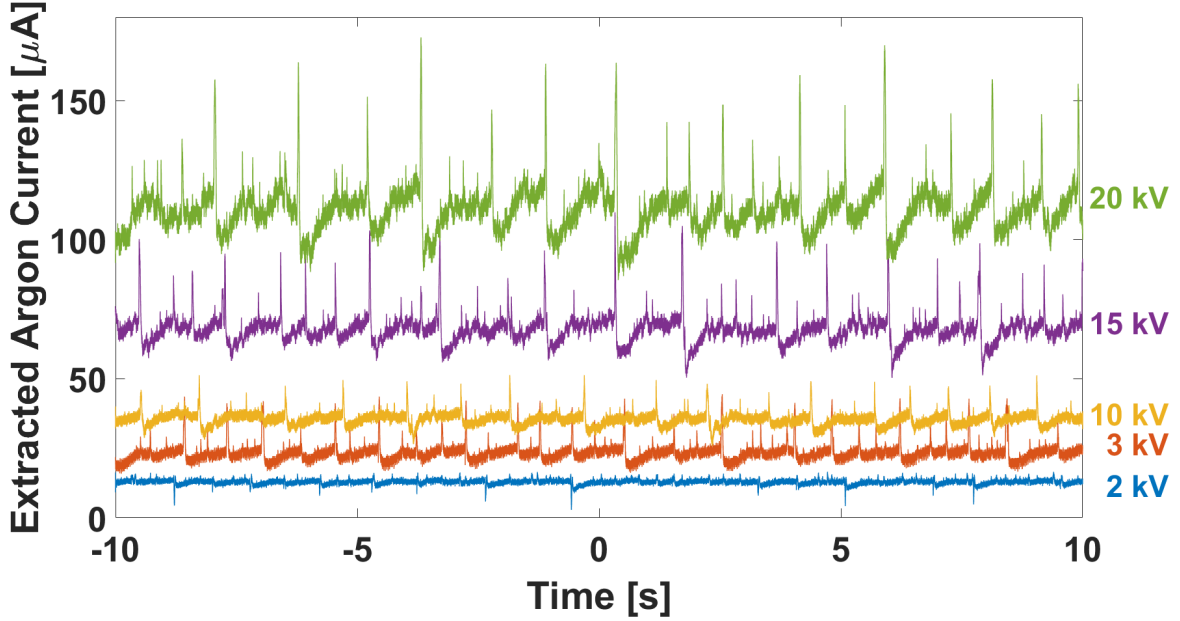


Figure 4.2: The transient profiles of the extracted ion currents were measured for each operating point used in Figure 4.1. While ions do escape confinement at lower voltages ( $< 2\text{ kV}$ ), it is difficult to distinguish one charge state from another.  $B_{\min} = 0.397\text{ T}$ ,  $P = 350\text{ W}$ , pressure =  $212\text{ nTorr}$ .

determined that, at worst, electrons with energies less than  $50\text{ keV}$  were unreliably measured. The model in figure 3.5 it is not sophisticated enough to account for residual fields within all the iron surrounding the beamline. For the remainder of this study, we will consider electrons beneath this limit to be non-meaningful. Izotov et al. published measurements of the transmission-corrected distribution [28].

High energy electrons which escape confinement without being perturbed by the magnetic field will appear as a continuous spectrum. As a result, the dipole no longer acts as a mass-to-charge analyzer but rather a spectrometer. We can determine the energy of electrons selected by the dipole by using Equation 3.1. In this case, we want the integral form of the magnetic rigidity. It is not wise to assume a hard edge model for the dipole, so the effect of magnetic fields must be integrated over their entire trajectory. Assuming relativistic electrons, equation 3.1 becomes:

$$\frac{-2ec}{\pi} \int B \cdot dl = \frac{\sqrt{E_{tot}^2 - m_e^2 c^4}}{c} \quad (4.1)$$

Where  $E_{tot}$  is the total electron energy and  $m_e$  is the electron mass. We can then re-write this to

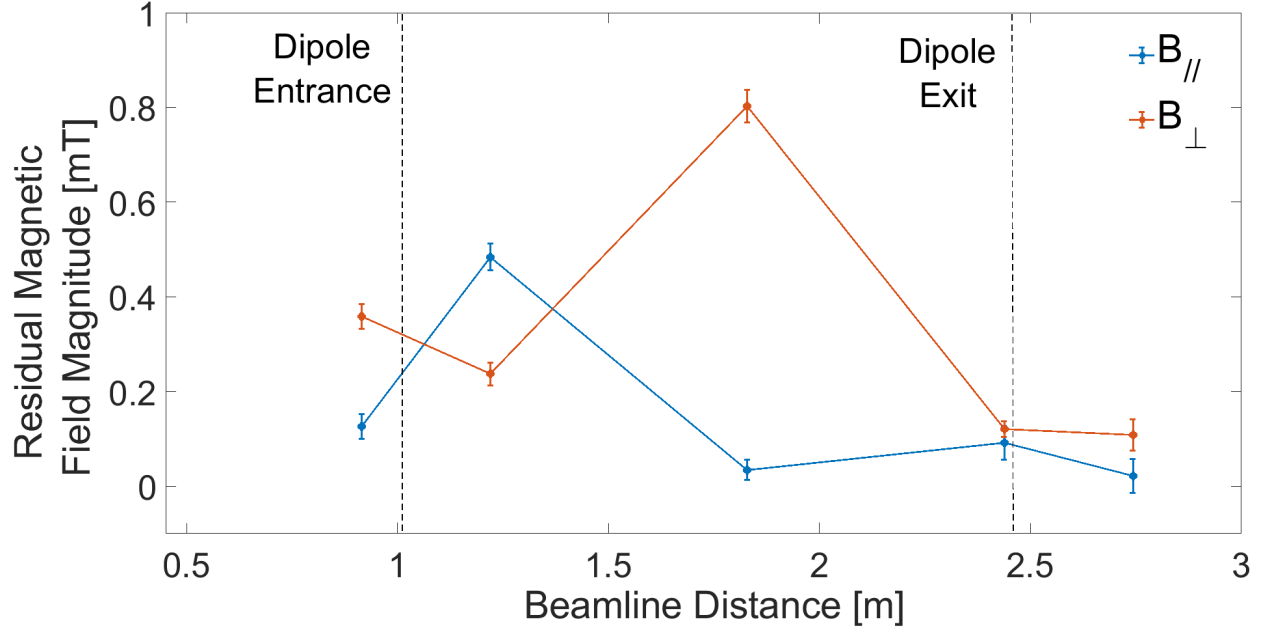


Figure 4.3: The residual magnetic flux parallel and perpendicular to the beamline transverse axis. Measurements were taken while all beamline elements were turned off.

find the kinetic energy of electrons bent at  $90^\circ$ :

$$E_{kin} = \sqrt{\left(\frac{-2ec}{\pi} \int B \cdot dl\right)^2 + m_e^2 c^4} - m_e c^2 \quad (4.2)$$

The integral expression in equation 4.2 can be determined experimentally by combining equations 3.1 and 3.3:

$$\int B(I_{dip}) \cdot dl \approx \frac{\pi m_p v A}{2e Q} \quad (4.3)$$

This calculation breaks down when the magnetic field is large enough to saturate dipole's steel yoke. The permeability of 1010 Steel becomes non-linear for fields larger than 1 T. CST simulations predict coil currents of nearly 500 A are necessary to saturate the yoke, which is well above the maximum current used. This approach also assumes that the electrons follow the same trajectory as the ions.

The program ECRtune sweeps the dipole current and records the charge state distribution of the extracted ions. Equation 4.3 was then applied to the charge state distribution to determine the magnetic rigidity of the system. The measurement was repeated multiple times over different extraction voltages (5 kV, 10 kV, 15 kV, 20 kV) to get the largest span of dipole currents possible. A linear best fit model was then applied to the data using the MATLAB CFit module. Figure 4.4



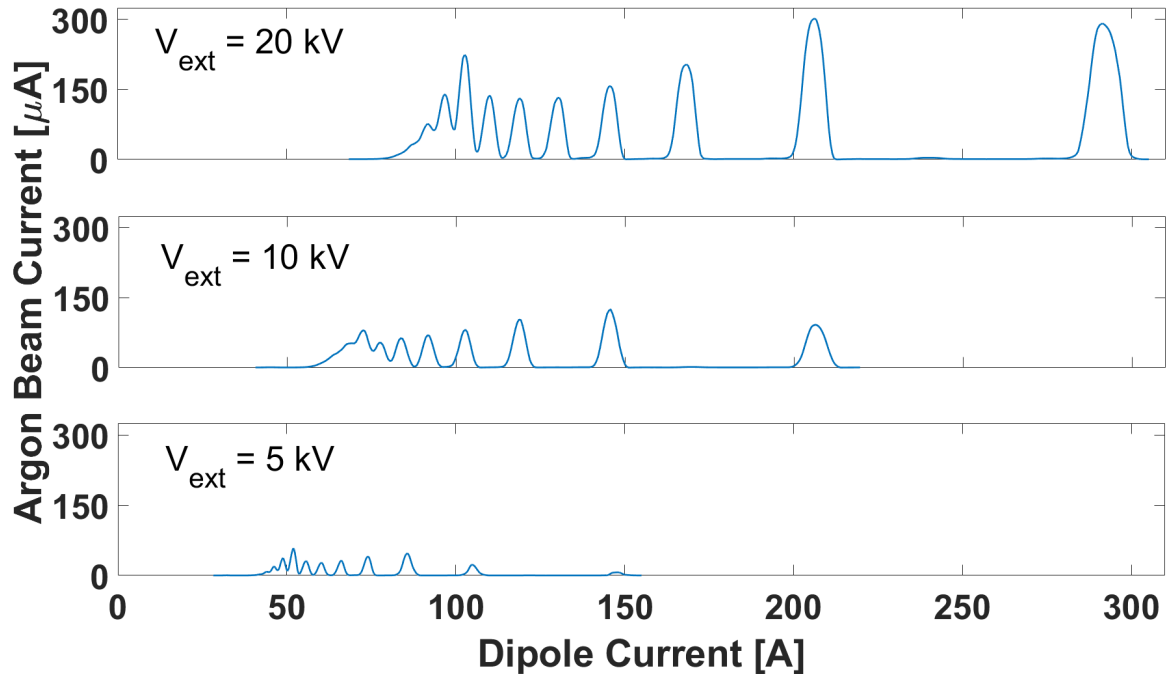


Figure 4.4: Argon charge state distributions from SuSI for 20 kV, 10 kV, and 5 kV extraction voltages measured at the first Faraday cup after the ion source in figure 3.1. Ion charge state increases from right to left, starting at  $Q = 1$ . Once again, we see that the extracted current decreases with decreasing voltage. Compared to figure 4.2, however, the purpose here is simply to increase the domain over which the system’s magnetic rigidity has been measured.

shows examples of the ion distributions, and figure 4.5 shows the resulting peak data and fit from this measurement.

In practice, the ions will be perturbed far less than the electrons by the ambient field. Not to mention, the relation made by combining equations 4.2 and 4.3 may break down for low voltages (as it appears to for extraction voltages lower than 2 kV). For example, figures 4.6 and 4.7 compare the measured energy calibration to an ‘idealized’ simulation of the beamline, using the model described in figure 3.5. The two methods of calibrating the electron energy largely agree; however, the idealized electron system cannot account for ambient field or inter-particle interactions. As a result, the simulation underapproximated the energy of transmitted electrons.

The simulation can also be used to determine the transmission efficiency of electrons moving through the beamline (see figure 4.8). Figure 4.9 shows the results of the transmission calculation

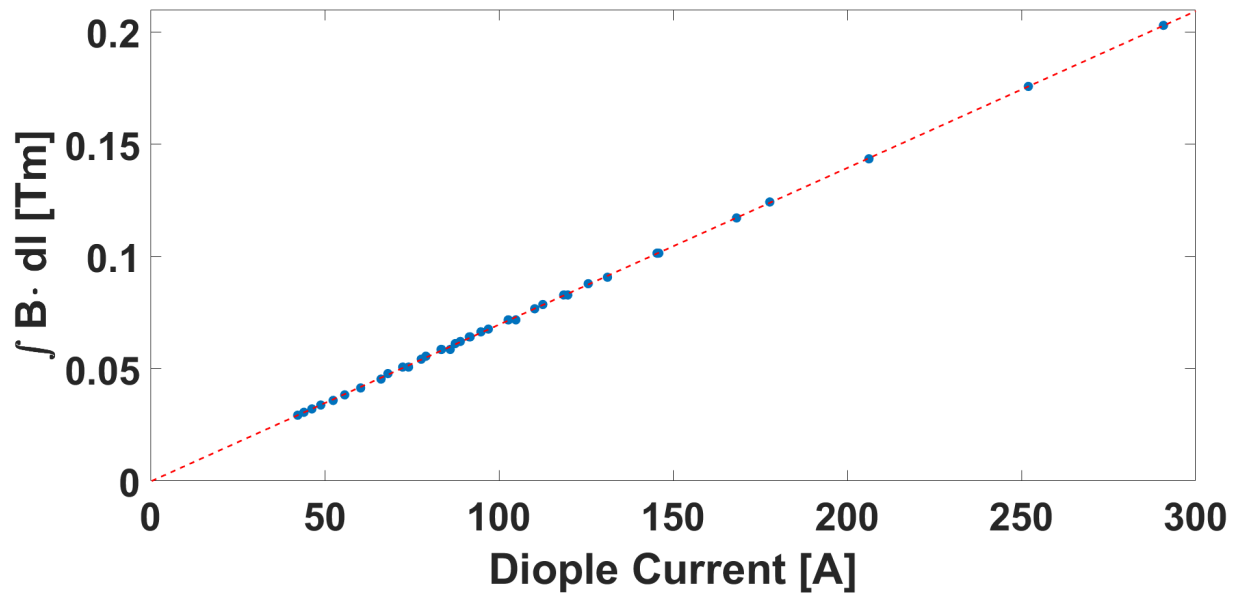


Figure 4.5: Measurements of the integral form of the magnetic rigidity between the ion source and the first Faraday cup. The (red) dashed line shows the linear best fit  $\int B(I_{dip}) \cdot dl = mI_{dip} + b$ , where  $m = 6.98624 \times 10^{-4}$  ( $6.98909 \times 10^{-4}$ ,  $7.01300 \times 10^{-4}$ ) and  $b = 2.47924 \times 10^{-4}$  ( $0.77833 \times 10^{-4}$ ,  $5.73681 \times 10^{-4}$ ).

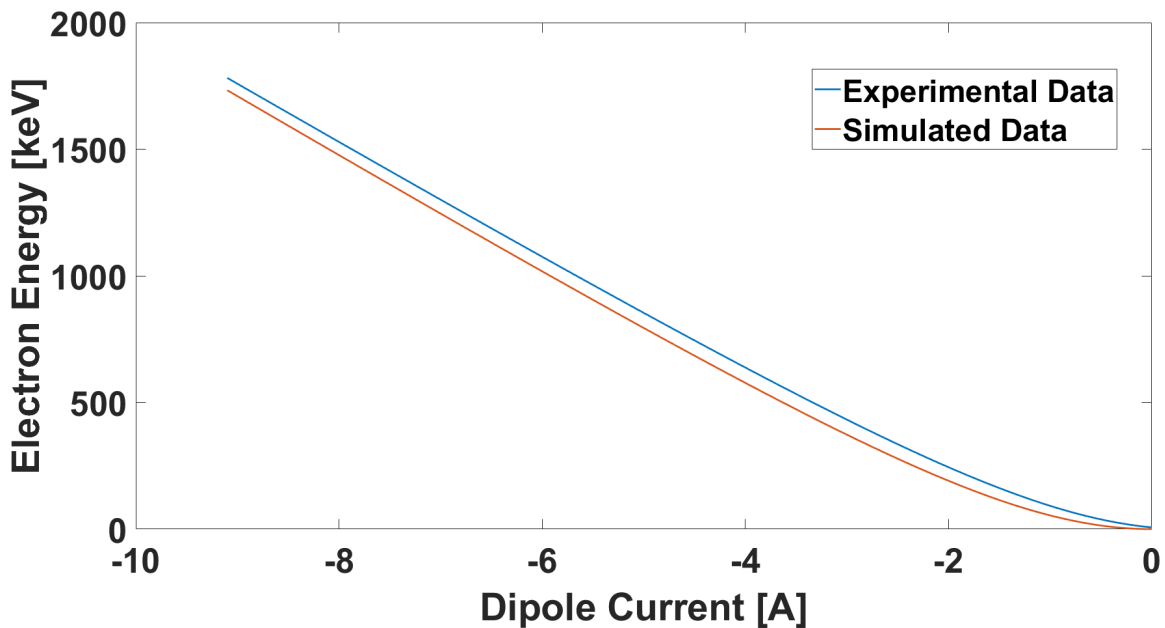


Figure 4.6: The electron simulation under approximates the energy calibration created by measuring the magnetic rigidity of the ions. This is likely due to the presence of ambient and residual magnetic fields, as seen in figure 4.3.

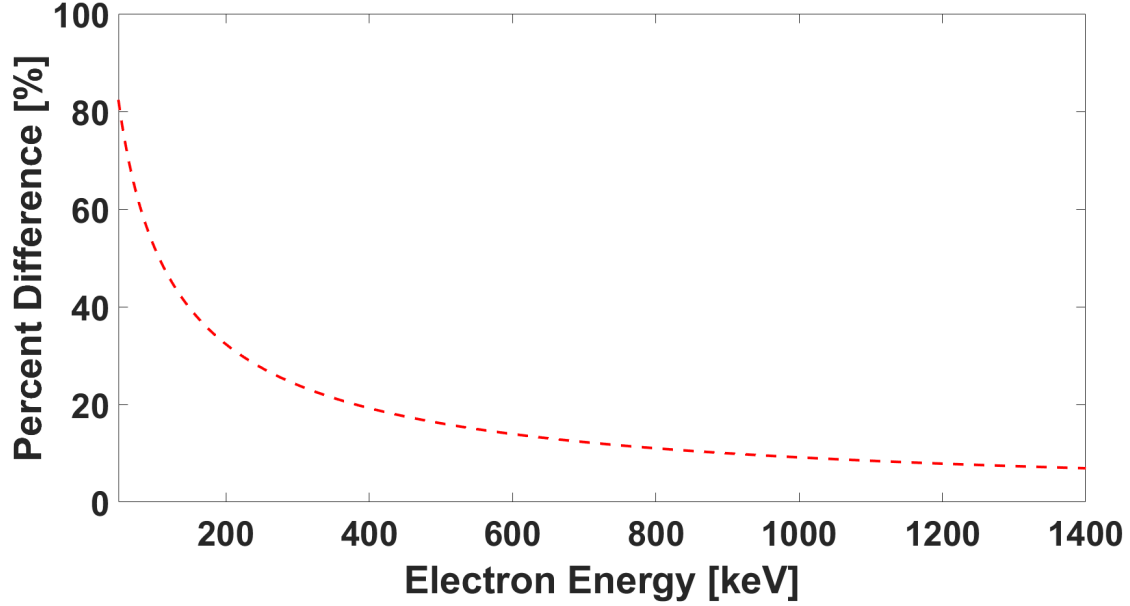


Figure 4.7: The largest differences between the ion rigidity and electron simulation energy calibrations occur at lower energies. This is likely due to the presence of ambient magnetic fields and interparticle interactions, which the simulation did not take into account.

made using the CST model. The simulation model assumed an idealized beamline without residual magnetic field effects, the presence of neutral gas in the beamline, and assumed a uniform and non-divergent beam emittance. As such, the transmission of electrons is affected only by the spatial distribution and energy of electrons as well as the ion source and dipole magnetic fields. For our purposes, the relative efficiency is  $\varepsilon_{Trans} = N_{meas}/N_0$ , where  $N_0$  is the initial number of electrons emitted from an aperture of radius 6 mm,  $N_{meas}$  is the total number of electrons collected in the Faraday cup. The simulation does not include the 4-jaw collimator; thus, the total relative efficiency goes as:

$$\varepsilon_{Tot} = \frac{\varepsilon_{Trans} A_{4-Jaw}}{A_{cup}} \quad (4.4)$$

where  $A_{4-Jaw}$  is the opening area made by the 4-jaw collimator and  $A_{cup}$  is the opening area of the Faraday cup, given by a circle of radius 25 mm.

The coordinate (0,0) was artificially placed into the simulated data set. In reality, the residual field stored within the dipole's iron yoke will cut the electron population off much earlier. The fit from equation 4.3 predicts a lower energy electron cutoff of 6.828 keV, which should also relate

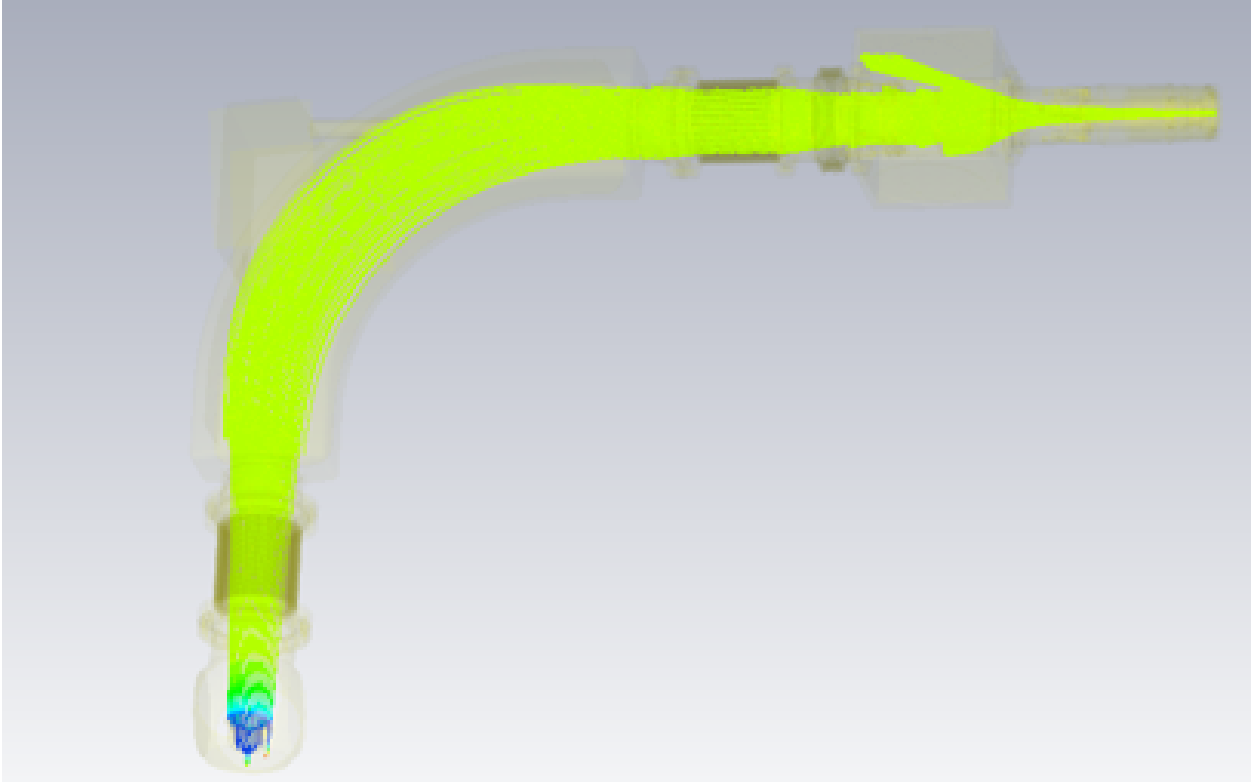


Figure 4.8: The yellow lines represent electron trajectories along the beamline within the model ion source. Trajectories begin at a 5 mm radius extraction aperture and end at the first Faraday cup in figure 3.2. All electrons are emitted in a direction perpendicular to the extraction aperture opening, with no angular divergence. The color of the lines represent their energy. The sudden change to blue at Faraday results from the -149 V potential on the cup's electron suppressor ring.

to a shifting of the entire energy spectrum. The transmission efficiency increases linearly at high energies, but non-linearly at low energies. The data was fit with a rational function to accommodate both high and low energy trends. This way, the fit is not biased by the behavior of lower energy electrons. Figure 4.9 shows the fitted model given by equation 4.5.

$$\varepsilon_{Trans} = \frac{p_1 E_{kin}^2 + p_2 E_{kin} + p_3}{E_{kin} + q_1}$$

$$p_1 = 2.289 \times 10^{-5} (2.227 \times 10^{-5}, 2.35 \times 10^{-5})$$

$$p_2 = 0.002758 (0.002161, 0.003355)$$

$$p_3 = -2.55 \times 10^{-6} (-0.005826, 0.00582)$$

$$q_1 = 8.844 (-1.204, 18.89)$$
(4.5)

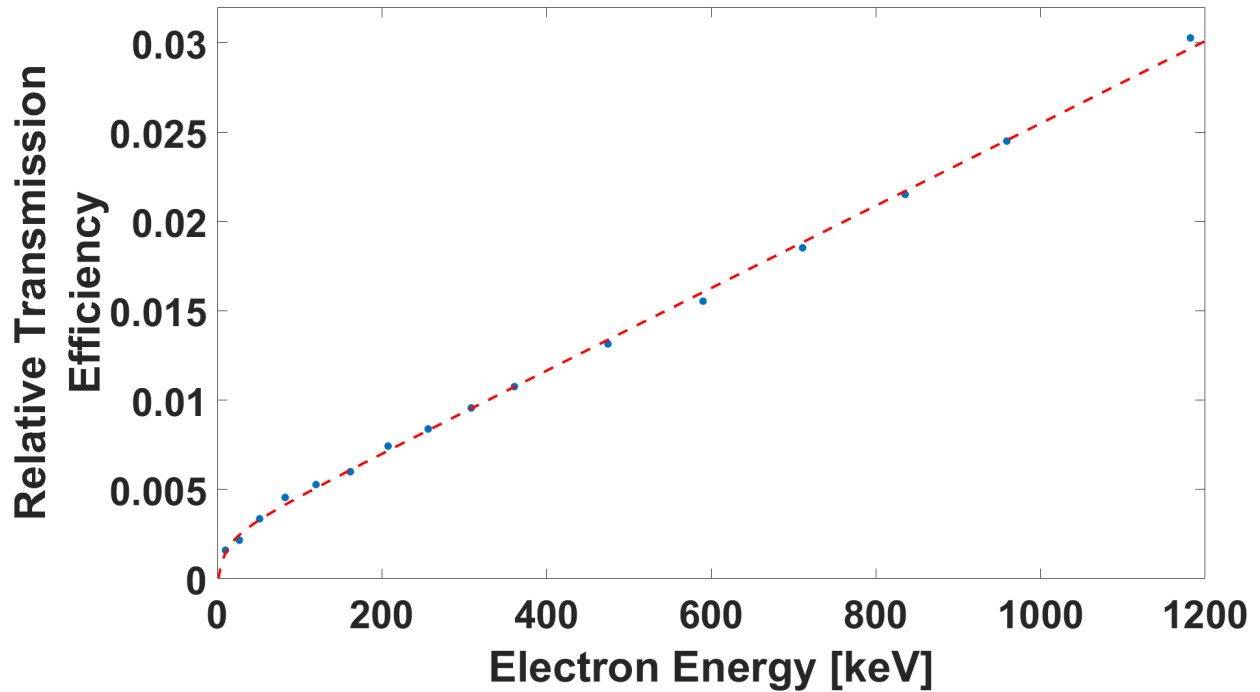


Figure 4.9: The relative efficiency data (blue dots) approach a linear relationship with energy as the energy of electrons increases. Each data point was calculated by dividing the number of electrons emitted from the 6 mm extraction aperture by the number of electrons which reached the Faraday cup. All electrons in a given simulation/calculation were assumed to have escaped parallel to the center axis of the ion source, with no divergence and at a single energy. As such, these results best represent the effect of the ion source's and dipole's magnetic field on the transmission of electrons of a given energy. The fit was performed with MATLAB's CFit module and used a 'Robust' Least Absolute Residual fitting option. The largest contributor to transmissions losses were the fringe fields of the ion source. The charges are deflected away from the beamline center by the locally diverging field lines. This effect can be seen in figure 4.8.

The horizontal gap width of the 4-jaw collimator was set to its minimum of 5 mm for the duration of the measurement. This was to improve the overall energy resolution of the measurement. The vertical gap was allowed to vary, depending on the measurement, with a maximum gap width of 38 mm. Table 4.1 show performance examples of the current collecting system with 38 and 5 mm vertical gaps.

Gap Area	Current Range	Current Var.
5x38 mm <sup>2</sup>	~1 nA	0.2%
5x5 mm <sup>2</sup>	~100 pA	0.7%

Table 4.1: Closing the vertical gap from 38 to 5 mm decreased the observable current by about an order of magnitude. The relative current variance was calculated use values similar to those in table 3.1.

### 4.3 Parameter Space

A primary goal of this study was to determine how different ion source parameters affected the distribution of escaping electrons. To that end, the electron distribution was measured across several different parameter spaces, including confinement configurations, microwave power, and gas pressure. Determining the set of magnetic field parameters to include in the measurement required a good deal of care. One significant constraint when using SuSI is the possibility of quenching the superconducting coils. If the magnetic coil currents change too quickly, the system can lose its superconducting properties, and the field will quickly collapse.

To minimize the risk of quenching, a new "control" operating point was defined and used in every measurement. The operating point was designed to have an extraction side maximum and global minimum that were lower than the standard operating point for facility operations. Having a lower extraction side maximum is the most important consideration as it improves the diffusion of electrons out of the system. If the field were too large, it could prevent the observation of electrons all together. Lowering the magnetic minimum helped prevent quenching that may have occurred from changing the coil current densities for each measurement. This specific operating point produced an unstable ion source plasma. However, it is highly likely to make an unstable ECRIS plasma while varying the magnetic field (see chapter 5 for more details), and attempting to find a set of stable operating points would limit scope of the measurement. Instead, making the BCM take 100 samples before recording the current value helps combat the effect that the instabilities may be having on the observed distribution. A comparison between the control and standard facility operating points are given in Table 4.2.

As described in section 3.1, SuSI's magnetic field is highly flexible with the ability to vary the

	$B_{min}/B_{RF}$	$B_{Inj}/B_{RF}$	$B_{Ext}/B_{RF}$
Standard	0.71	3.96	1.94
Control	0.62	3.68	1.71

Table 4.2: Comparison between the longitudinal field extrema of the NSCL standard operating point for facility operations, and the control field used for this measurement.

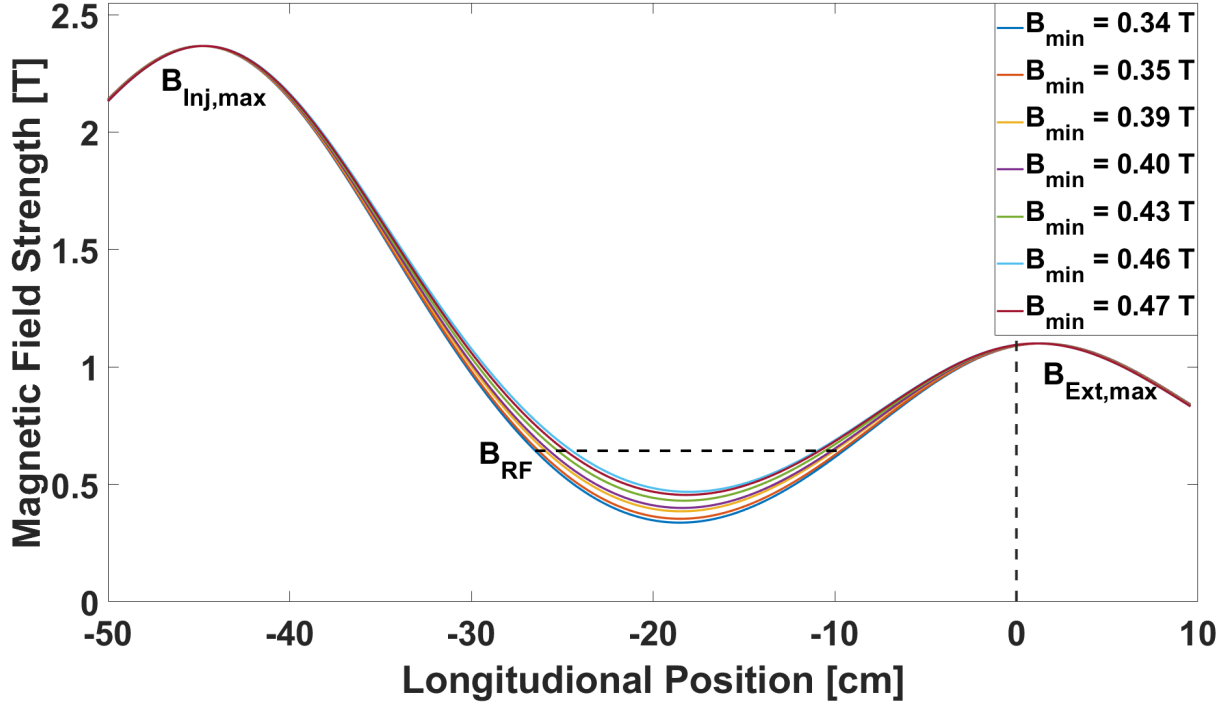


Figure 4.10: The magnetic field maximum at injection and extraction were chosen to be 2.3 T and 1.1 T, respectively. These values roughly follow the scaling laws with  $B_{Inj}/B_{RF} \approx 3.59$  and  $B_{Ext}/B_{RF} \approx 1.72$ . Throughout this measurement the plasma volume and gradient at resonance are allowed to vary. The resonance field is given by the black dashed line. The extraction aperture is represented by the vertical dashed line at  $x = 0$  cm.

magnitude of each of the field extrema independently. This feature allowed the effect of each of the field extrema on the escaping electron distribution to be observed independently on one another. Figure 4.10 shows the longitudinal field profiles used to measure the effect of a varying magnetic minimum. The variation in the loss cone pitch angles for each field profile can be seen in figures 4.11, 4.12, and 4.13. The full set of longitudinal field profiles used can be seen in appendix B.

The effect of varying the hexapole field, microwave power, and neutral gas pressure were performed after observing the effect of varying longitudinal field profiles. Figure 4.14 shows

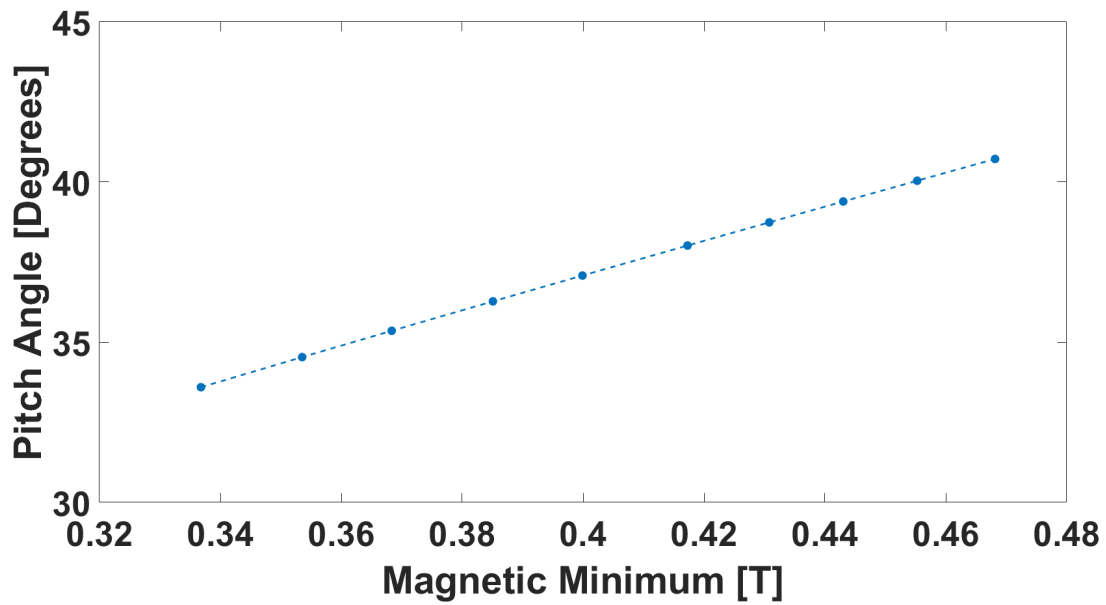


Figure 4.11: Values of the extraction side loss cone pitch angle used while varying the magnetic minimum while holding the extraction maximum constant.

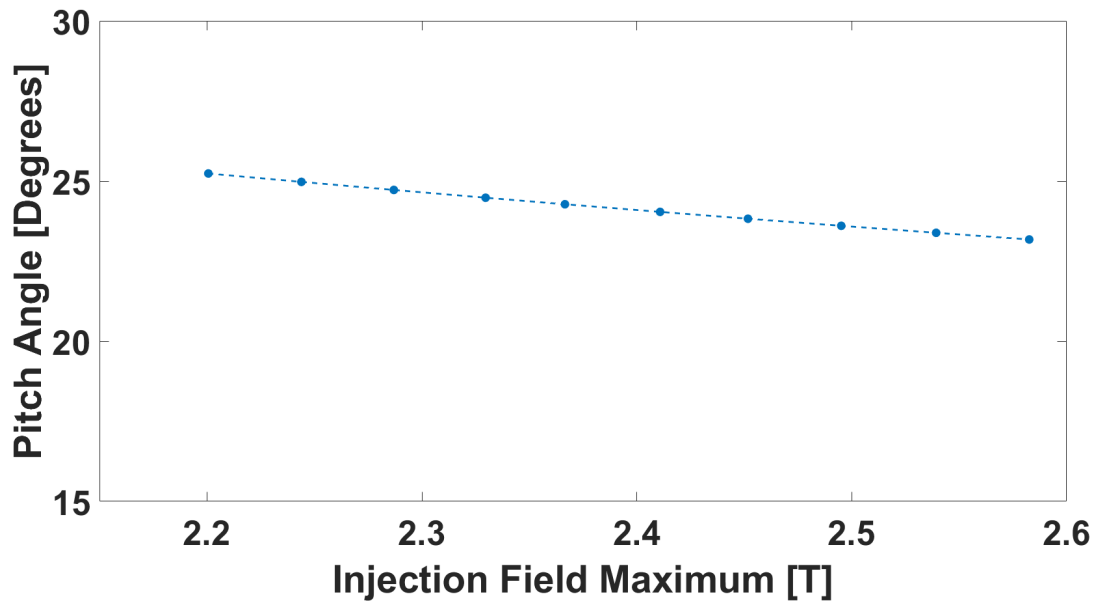


Figure 4.12: Values of the injection side loss cone pitch angle used, here the magnetic minimum is held constant.



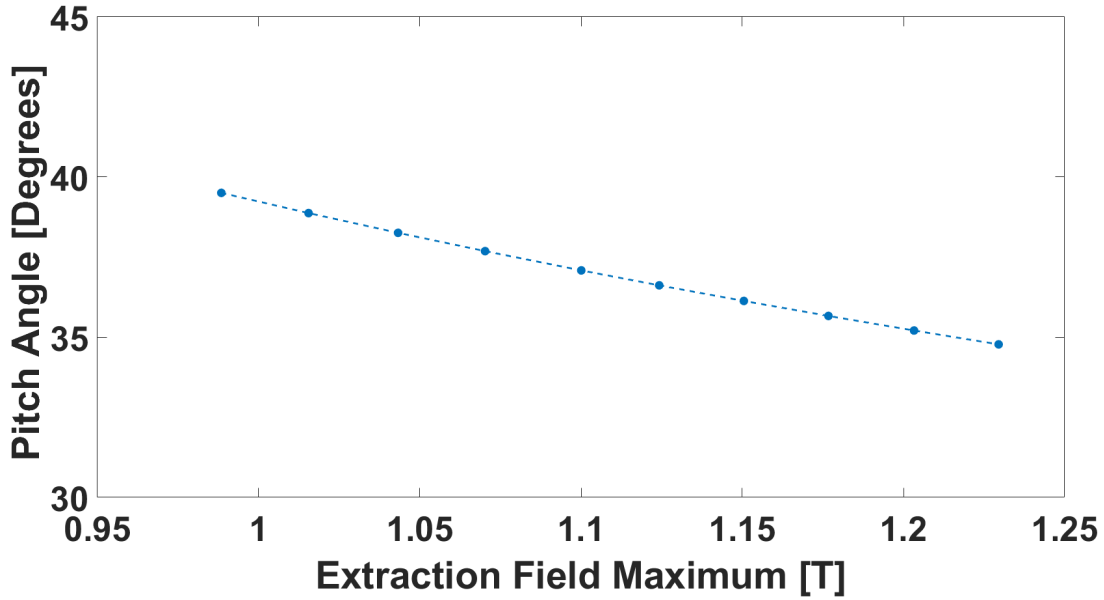


Figure 4.13: Values of the extraction side loss cone pitch angle used while varying the extraction side maximum while holding the magnetic minimum constant.

$B_{min}$ [T]	$B_{Inj,max}$ [T]	$\langle B \rangle$ [T]
0.337	2.367	1.080
0.400	2.200	1.065
0.400	2.583	1.114
0.468	2.367	1.151

Table 4.3: The set of operating points used where chosen to measure the coupling between the magnetic minimum and maximum at injection and other measured parameters.  $\langle B \rangle$  is the average magnetic field between the injection and extraction maxima. The extraction side maxima was held constant at 1.100 T for all operating points.

how the pitch angle varied with the hexapole for each of these measurements. All three of these parameters are known to affect the distribution of ions and electrons. Their effects upon the escaping electrons were measured across multiple operating points with different longitudinal magnetic fields. Table 4.3 summarize the characteristics of theses operating points. For ease of reading, the results from the four auxiliary field measurements can be found in appendix C.

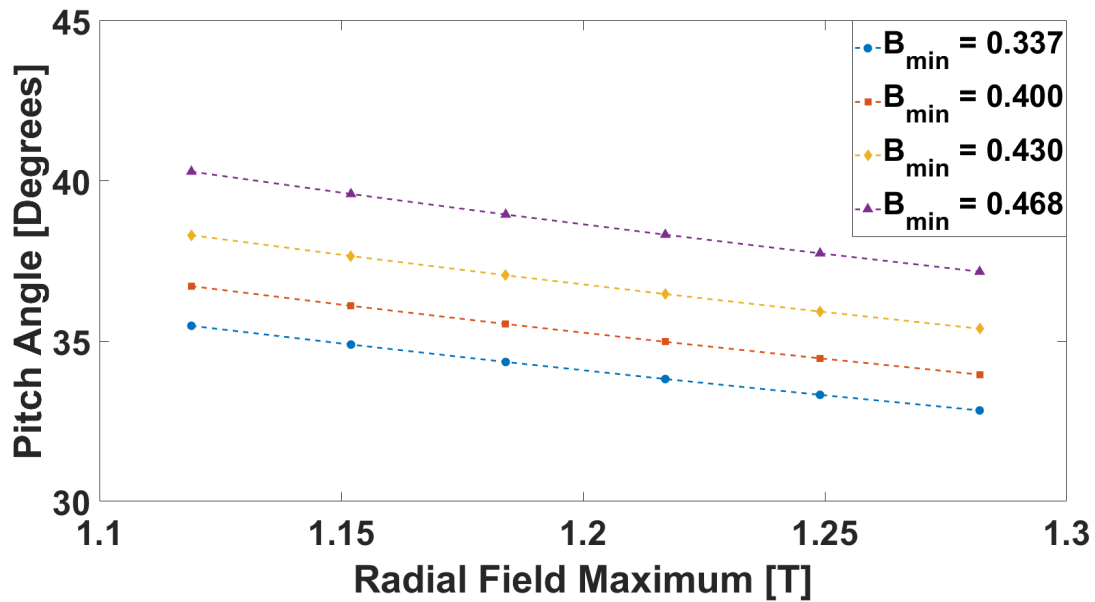


Figure 4.14: Values of the radial loss cone pitch angle used while varying the hexapole with the longitudinal solenoid fields held constant.

#### 4.4 Results

Figure 4.15 shows the measured distribution of escaping electrons while the ion source was in the 'control' operating point. The initial measurement shows a distribution consisting of two peaks, one at high energies (200 - 1000 keV) range and one at more intermediate energies (10 - 70 keV range). The 'low energy peak' falls below the reliability threshold and, as a result, will be ignored for the remainder of this study. However, the high energy peak is well above this threshold and provides a large amount of qualitative and quantitative information on the distribution of escaping electrons. As shown in table 4.1, closing down the acceptance area of the 4-Jaw collimator affected the range of currents measured. Correcting for transmission losses and area between the different gap areas shows a measurable but small difference at low to intermediate energies 4.16. Calculating the total observed electron current measured as a function of the collimator area, such that the acceptance area is a square, varies close to linearly with the acceptance area (see figure 4.17). However, the spatial and momentum distributions of the electrons were not measured. At this time, no such measurement exists in the literature either. The successful measurement of those distributions or

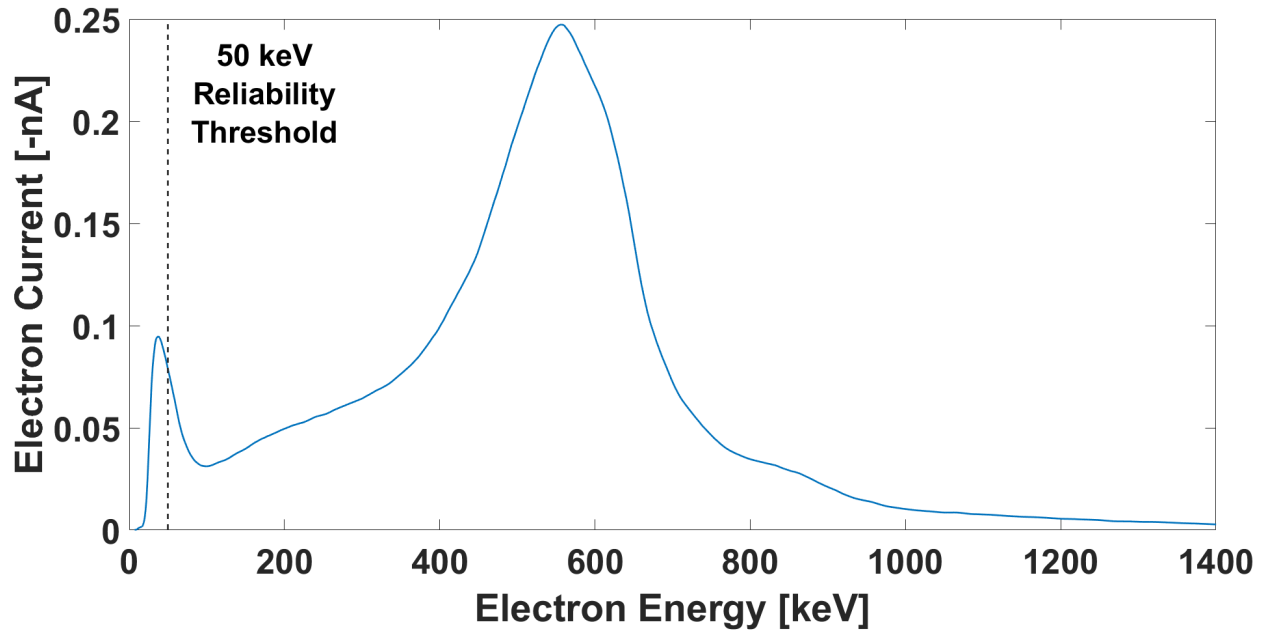


Figure 4.15: Measured electron distribution for the measurements 'control' operating point. The 50 keV reliability threshold is shown by the dashed line.  $B_{\min} = 0.4$  T,  $B_{\text{Inj,max}} = 2.367$  T,  $B_{\text{Ext,max}} = 1.100$  T,  $P_{\mu} = 350$  W, Pressure = 212 nTorr,  $B_{\text{Rad,wall}} = 1.217$  T.

the beam's emittance would help refine this type of measurement, particularly for understanding the high energy peak.

Compared to previous measurements in the literature (see Izotov et al. [28]), the intermediate energy region (50-150 keV) plateaus before reaching the high energy peak (figure 4.15). The population of electrons with energies lower than 50 keV can vary significantly from operating point to operating point. However, the uncertainty in the transmission properties of these electrons makes any arguments based on the number density of electrons difficult to confirm. Thus, the remainder of this section focuses on variations in the high energy peak of the distribution.

#### 4.4.1 Varying Power

The system's energy content was largely insensitive to varying microwave power. This result agrees with previous measurements that have suggested an increasing microwave power has little effect upon electron energies [2, 41, 46]. On the other hand, the increasing microwave power correlates with increased electron currents, likely a result of an increasing plasma density [86]. Figure 4.18

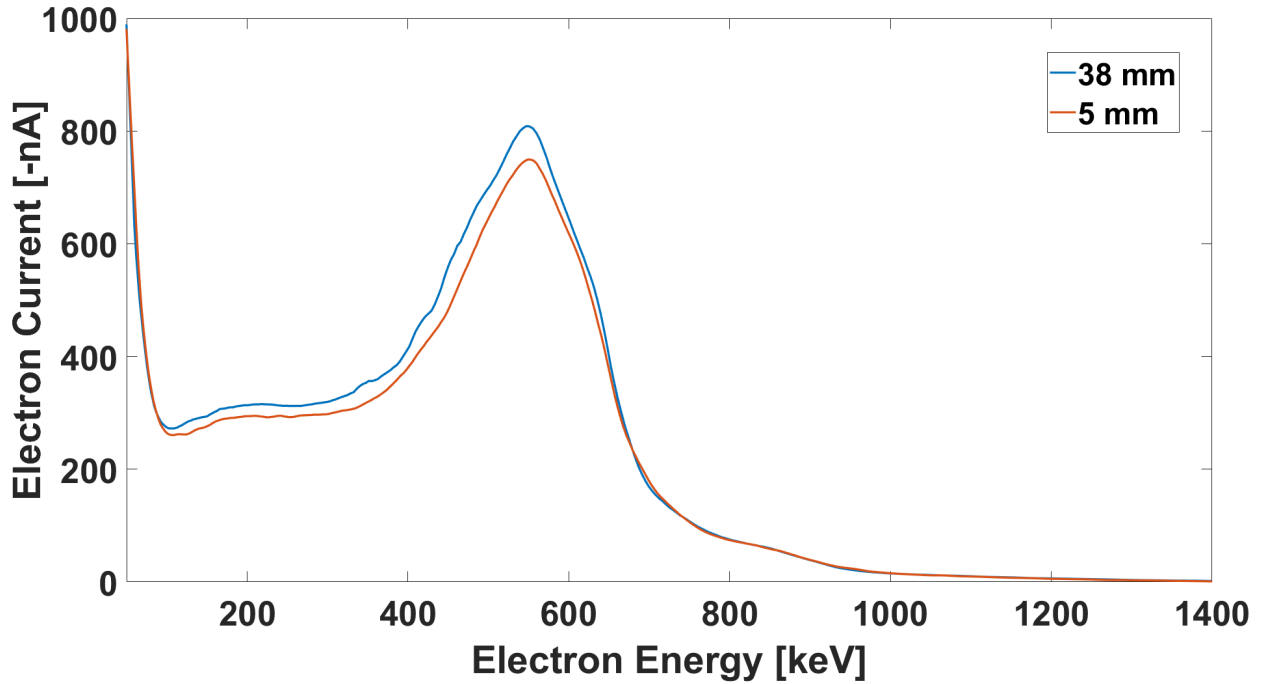


Figure 4.16: By applying the efficiency calibration described in the previous section, the total current observed increases by several orders of magnitude, from  $10^{-1} - 1$  nA to  $10^3$  nA. The changing vertical gap distance had little effect upon the distribution once it was corrected for beamline and gap area transmission.  $B_{\min} = 0.4$  T,  $B_{\text{Inj,max}} = 2.367$  T,  $B_{\text{Ext,max}} = 1.100$  T,  $P_{\mu} = 350$  W, Pressure = 212 nTorr,  $B_{\text{Rad,wall}} = 1.217$  T.

shows how the energy and intensity of the high energy peak vary with microwave power; the latter reflecting the increase in the system's electron density. This growth is well reflected in the bremsstrahlung distribution as the total number of photons observed also increases linearly (see figure 4.19). The top plot in figure 4.20 shows how the high energy peak's central energy and bremsstrahlung distributions spectral temperature and fit x-intercept scale with the power (see sec. 3.2.5 for details on bremsstrahlung analysis). The lower plot shows the effect upon the electron peak's height and the total number of observed photons (without correcting for the detector's efficiency).

The linear fit's x-intercept increases with a downward curvature at higher microwave power settings and likely results from the increased electron density at all energies. The higher population density results in an increased count rate of very high energy photons but produces diminishing

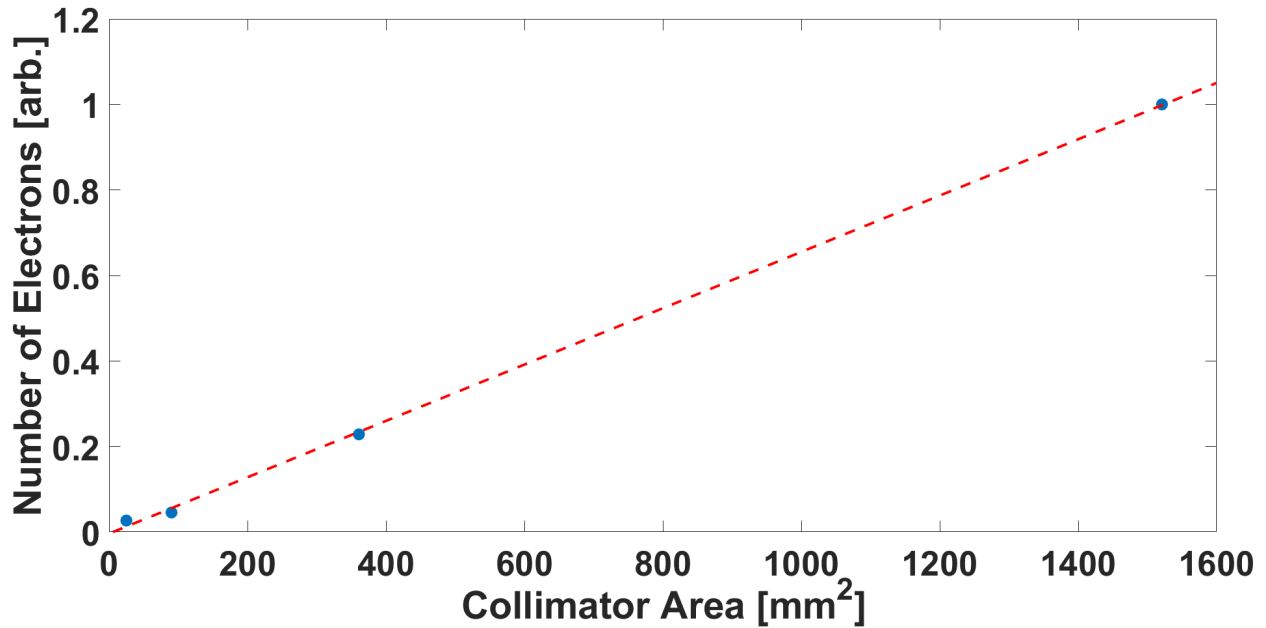


Figure 4.17: The total measured current was found to vary linearly with a varying square acceptance area (equal horizontal and vertical gap widths). The red dashed line demonstrates the linear fit of the data points (blue).

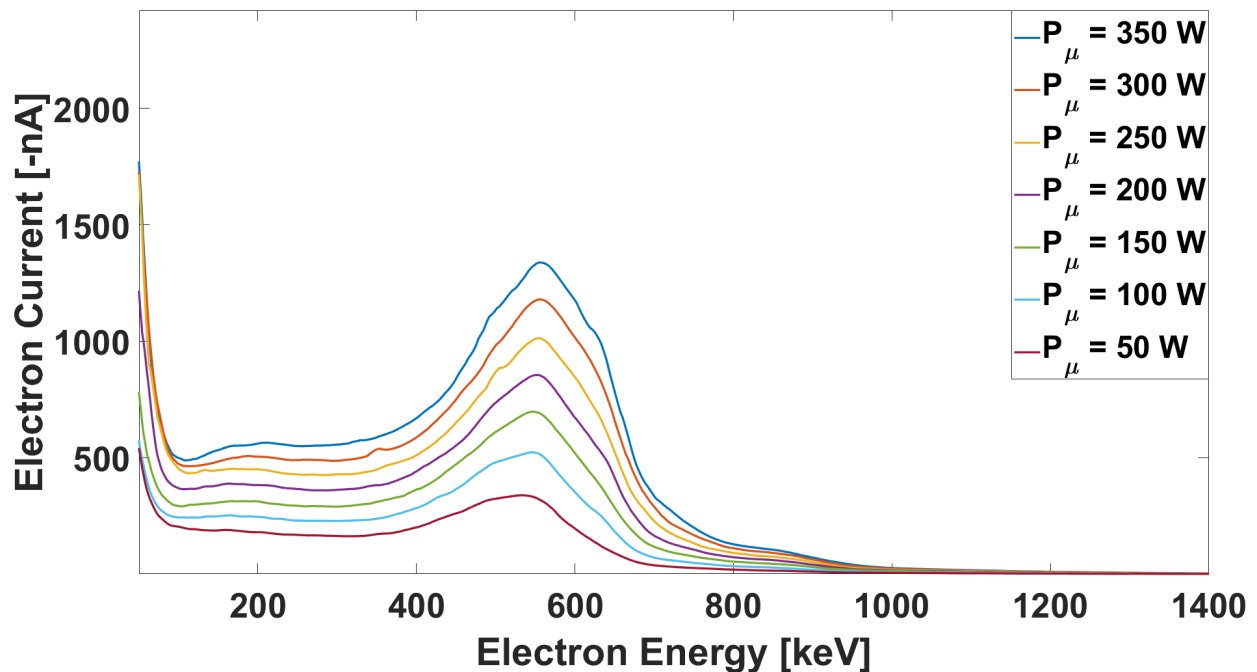


Figure 4.18: Increasing the injected microwave power increased the measured electron current uniformly across the entire energy range. The central energy of the peak was largely unaffected by the changing microwave power.

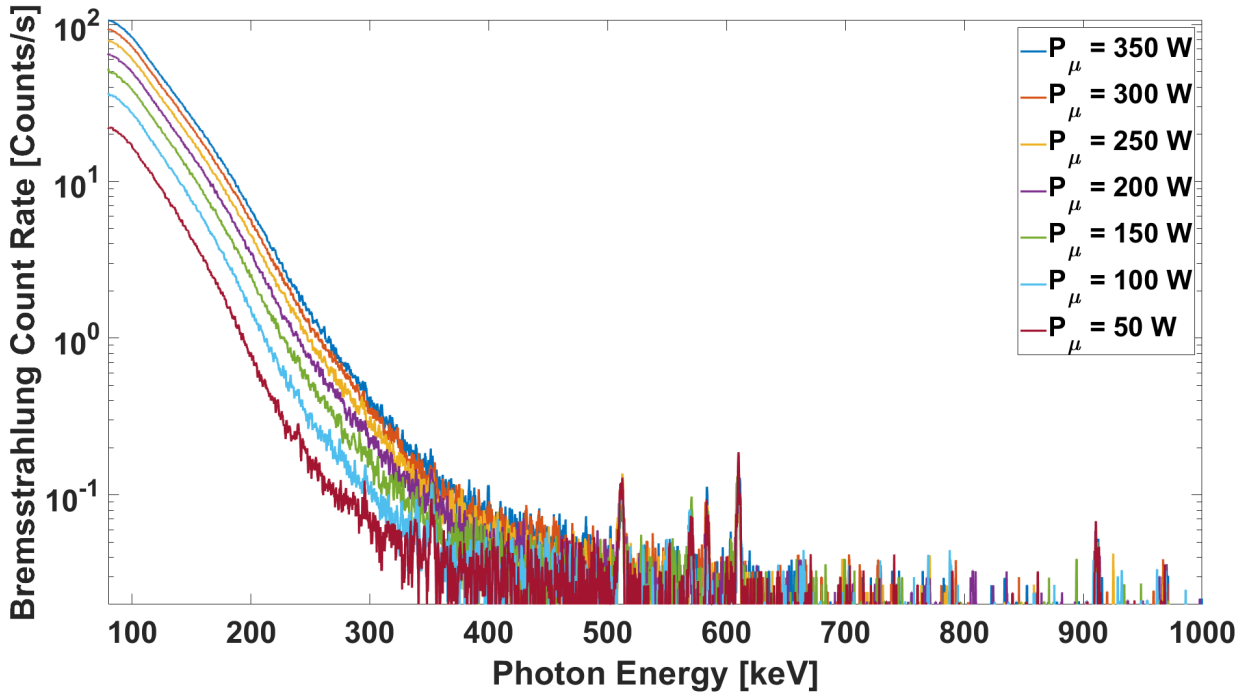


Figure 4.19: The trend in the measured electron distribution is reflected in the bremsstrahlung spectrum as the total number of photons increases while the energy spread remains largely the same.

returns as the power continually increases. On the other hand, the agreement of the spectral temperature's trend with that of the central energy of the electrons peak demonstrates how little effect the power has on the energy content of escaping electrons.

The results of the remaining operating points used for this part of the measurement are shown in figures C.2, C.3, C.4, and C.5. The electron current and photon distributions trends were largely the same regardless of the average magnetic field within the system. While changing the magnetic field configuration does seem to affect the high energy peak amplitude, the trend of each data set shows a near-linear relationship between microwave power and diffusing electron density. Simultaneously, the central energy of the high energy peak is largely insensitive to changing microwave power. The dependence of the spectral temperature on power seems to vary with the magnetic field; however, this may result from the fitting process rather than the effect of changing field strength.

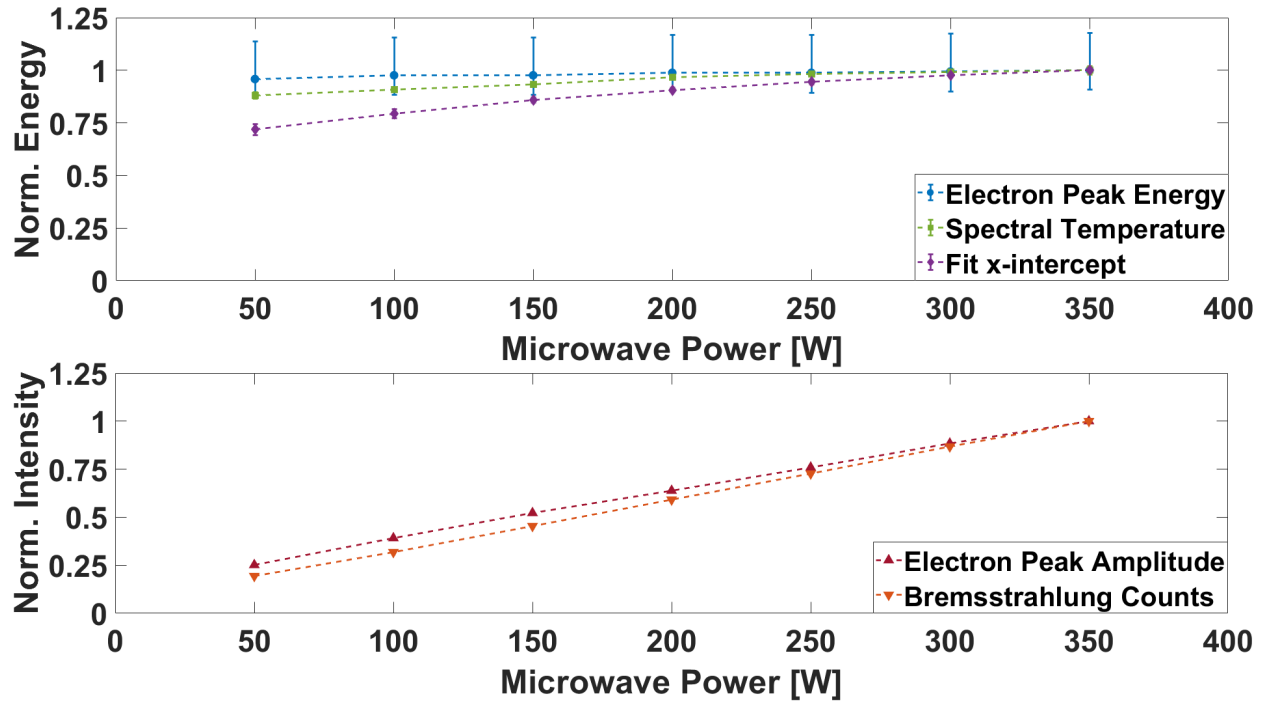


Figure 4.20: The similarities between the measured electron and bremsstrahlung distributions is most easily seen in the comparison between the systems' energy content and measured particle numbers. Overall, the effect of increasing power leads to a more dense electron population, but not a more energetic one. All sets shown have been normalized by the largest values in their sets:  $E_{\text{peak,max}} = 565 \text{ keV}$ ,  $T_{s,\text{max}} = 39.7 \text{ keV}$ ,  $X_{T_s,\text{max}} = 278 \text{ keV}$ ,  $I_{\text{peak,max}} = -1383 \text{ nA}$ , and  $N_\gamma = 5.0 \text{ Mcounts}$ .

#### 4.4.2 Effect of a Variable Pressure

As figures 4.21 and 4.22 show, increasing the neutral gas pressure appears to have a small cooling effect upon the energy content of the diffusing electrons. Figure 4.23 shows that the electron high energy peak's central energy, spectral temperature, and bremsstrahlung fit intercept decrease slightly as a result of increasing gas pressure, suggesting that the increased pressure leads to a cooler plasma. This result matches previous measurements that show the temperature content of the plasma decreases with increasing pressure [1]. The increased density may lead to a more thermal plasma as the collision frequency increases linearly with electron density (eq. 2.8). The effect on the measured distributions should be minimal as the increase in the neutral density is not large enough to substantially affect the collision frequency of hot electrons. Not to mention, we already assume that changes in atomic or ion densities have little effect on the hot electron component

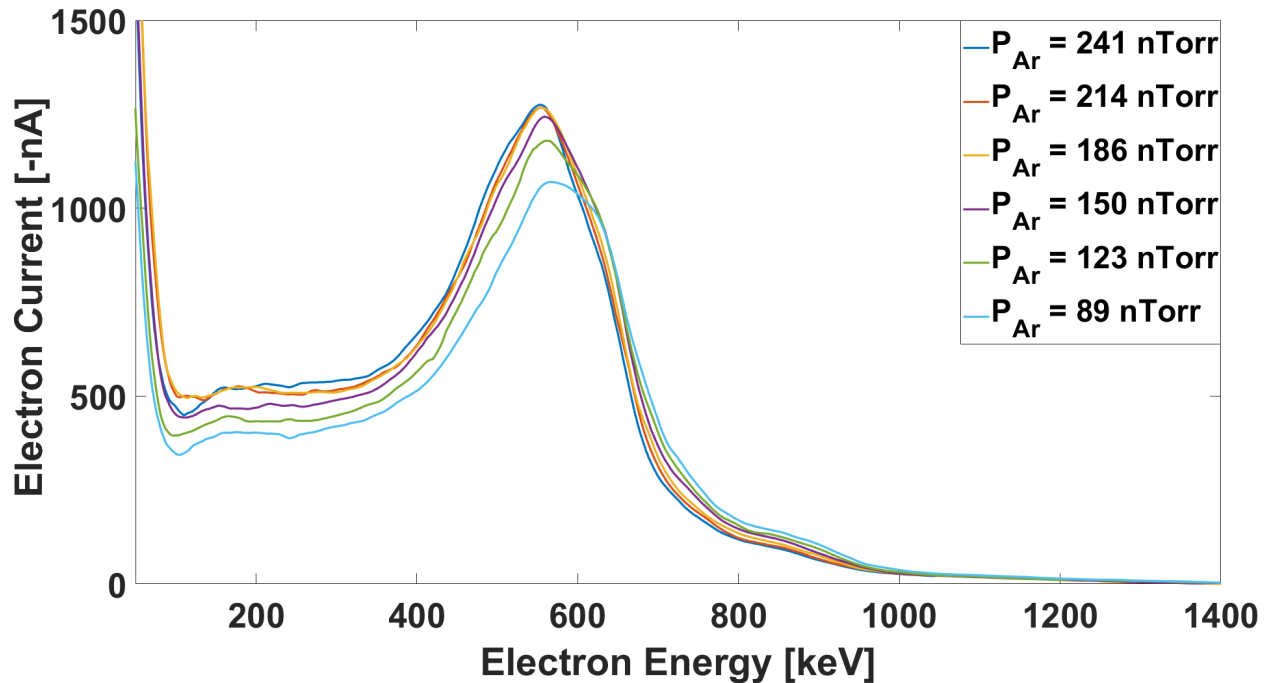


Figure 4.21: The changing electron distribution suggests that increased pressure leads to a cooler, higher density plasma.

of the plasma (fig. 4.1). Oddly, there is also an inverse relationship in the number of measured particles between the electron and bremsstrahlung measurements. This is contradictory to what we would expect for an increased electron density, as the diffusion rate should increase across all diffusion mechanisms. A further progression of this discussion requires a better understanding of how different ion source parameters may affect the system's energy content. For now, it is sufficient to recognize how the pressure affects each of the different distributions.

As in the previous case, varying the magnetic field strength does not appreciably alter how the diffusing electrons respond to changing neutral gas pressure, at least over the range measured. In all cases, an increasing pressure led to significant but small decreases in measured electron energies (Figure C.6). Once again, this is reflected in the bremsstrahlung spectra as the most significant changes across each operating point seem to result from the varying magnetic field (Figure C.7). Figures C.8 and C.9 summarize these results, showing consistent trends in the electron and photon energy distributions for varying magnetic field distributions. Most importantly, each data set shows



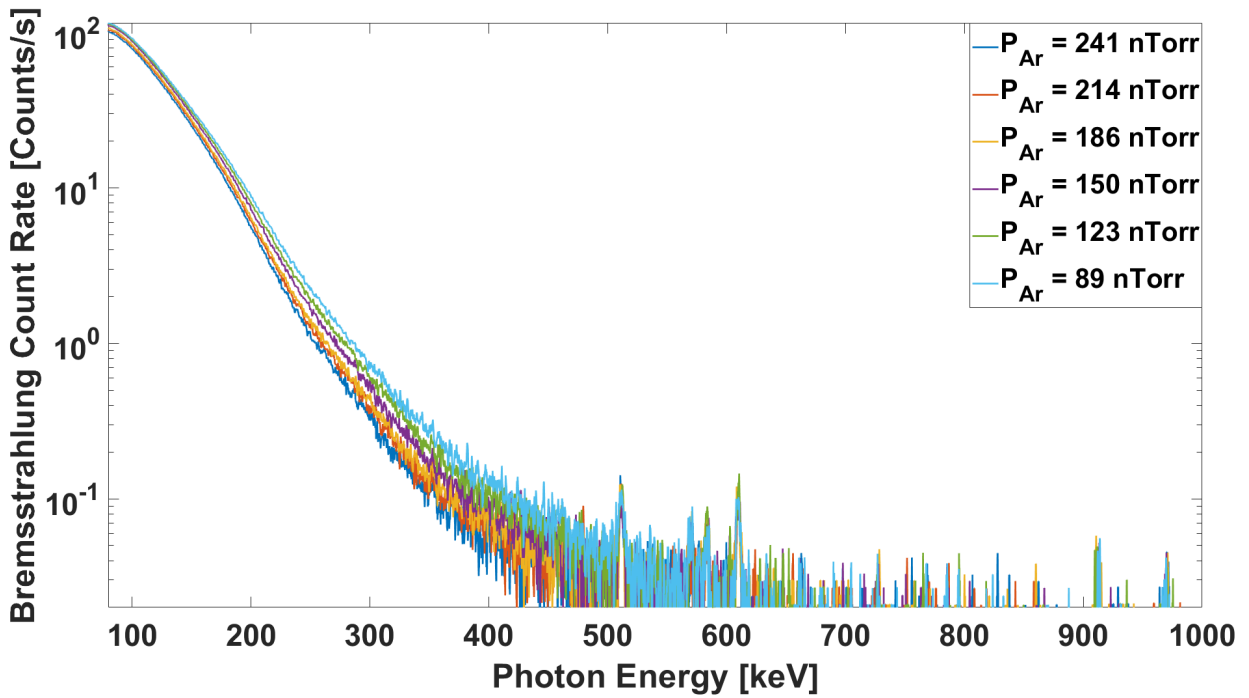


Figure 4.22: As the pressure increases, the measured bremsstrahlung distribution sees a trend towards lower energy photons.

an inverse relationship between the height of the high energy peak and the number of photons observed.

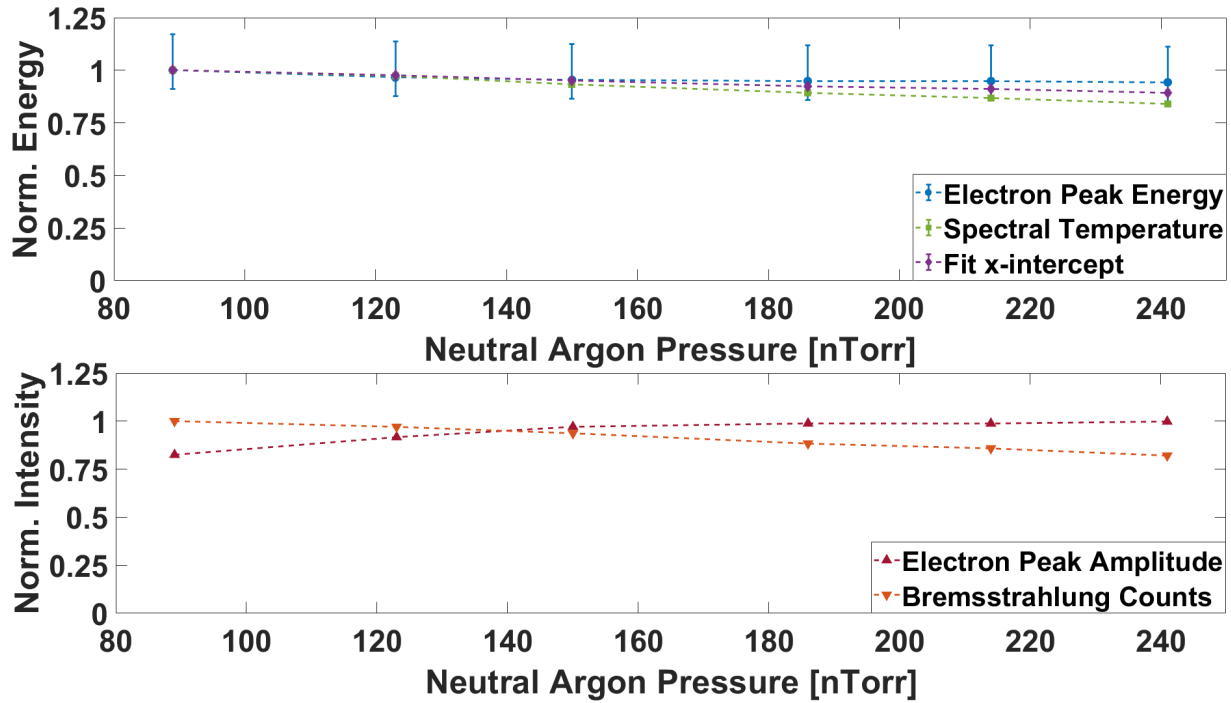


Figure 4.23: While the energy content of both measurements agree to an increased pressure resulting in a cooler plasma, the trend total particles observed are inversely proportional to one another. Both top and bottom plots are normalized by the largest values in their sets:  $E_{\text{peak,max}} = 592$  keV,  $T_{\text{s,max}} = 42.1$  keV,  $X_{T_{\text{s,max}}} = 297$  keV,  $I_{\text{peak,max}} = -1224$  nA, and  $N_{\gamma} = 5.8$  Mcounts.

#### 4.4.3 Effect of a Variable Hexapole

Varying the hexapole field strength also showed significant changes in the number of electrons observed. The height of the high energy peak noticeably increases; however, the bremsstrahlung distribution is mostly unaffected by the varying field. This measurement agreed with previous measurements, which showed an insensitivity of the plasma to a changing hexapole [3], at least over the regime measured. Figures 4.24, 4.25, and 4.26 show the results of these measurements. Unfortunately, a mistake was made during operation and the control operating point was not used for this measurement. Instead, the measurement used an operating point with  $B_{\text{min}} = 0.43$  T. Despite this the other measurements were performed successfully.

A varying longitudinal magnetic field profile does appear to affect how the hexapole affected the plasma. As figure C.10 shows, an increasing average magnetic field causes the hexapole to have a smaller effect upon the diffusion of electrons out of the system. The magnetic minimum has

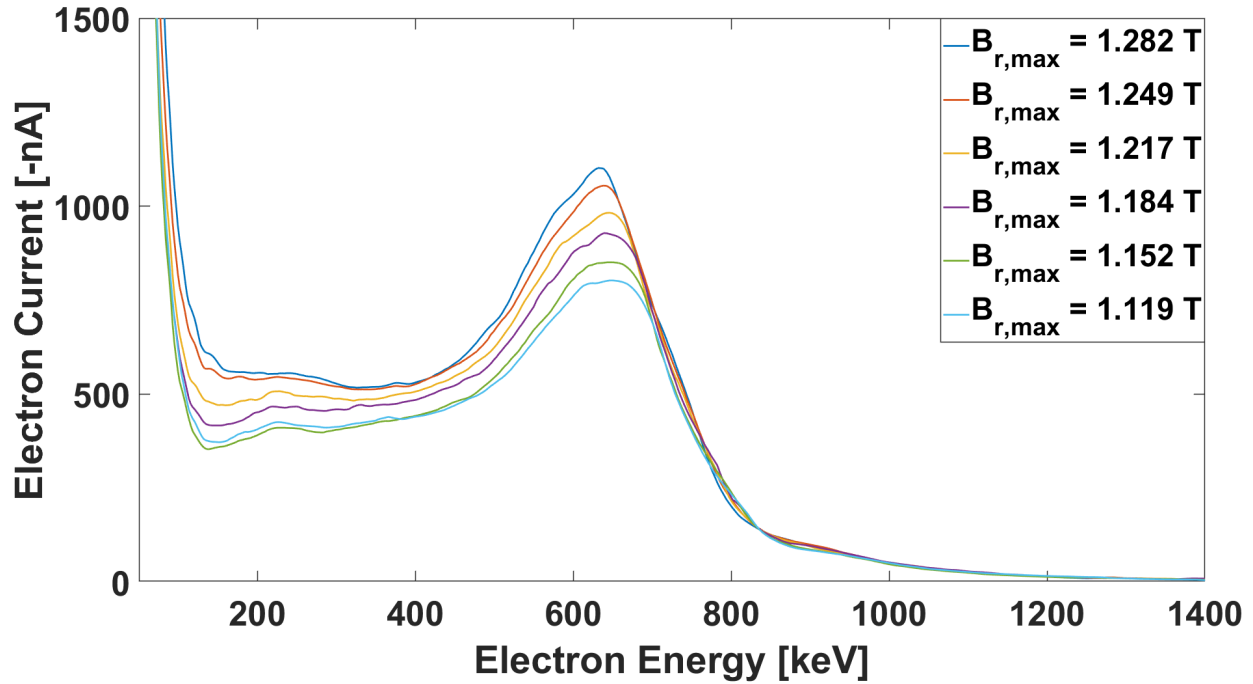


Figure 4.24: The increasing radial field causes the overall current of the distribution to increase, although this effect is minimal compared to varying the microwave power. The central energy of the peak is also, largely, unaffected by the changing radial field.

the largest effect over the scaling response of the electron distribution. Once again, this trend is not reflected in the bremsstrahlung distribution. Figure C.11 shows how little the varying hexapole field affected the measured bremsstrahlung distribution across multiple longitudinal field profiles. Figures C.12 and C.13 numerically summarize the previous results, providing more insight into the issue. All operating points agree to virtually no change to the system's energy content as a result of varying the radial field strength. The electron peak initially sees close to a factor of two increase in its height across the radial fields used. This increase itself decreases to a factor of about 1.5 for the system with the largest magnetic flux. Oddly, this is also the only data set in which varying the longitudinal maximum appears to have a unique effect upon the measured photons. The lower left plot of figure C.13 shows that a varying hexapole field relates to a varying number of photon counts, only when  $B_{\text{Inj,max}} = 2.58 \text{ T}$ .

Together, these results suggest that the hexapole's overall effect, at least longitudinally, is to change the diffusion properties of the plasma. Based upon simulations using the model described

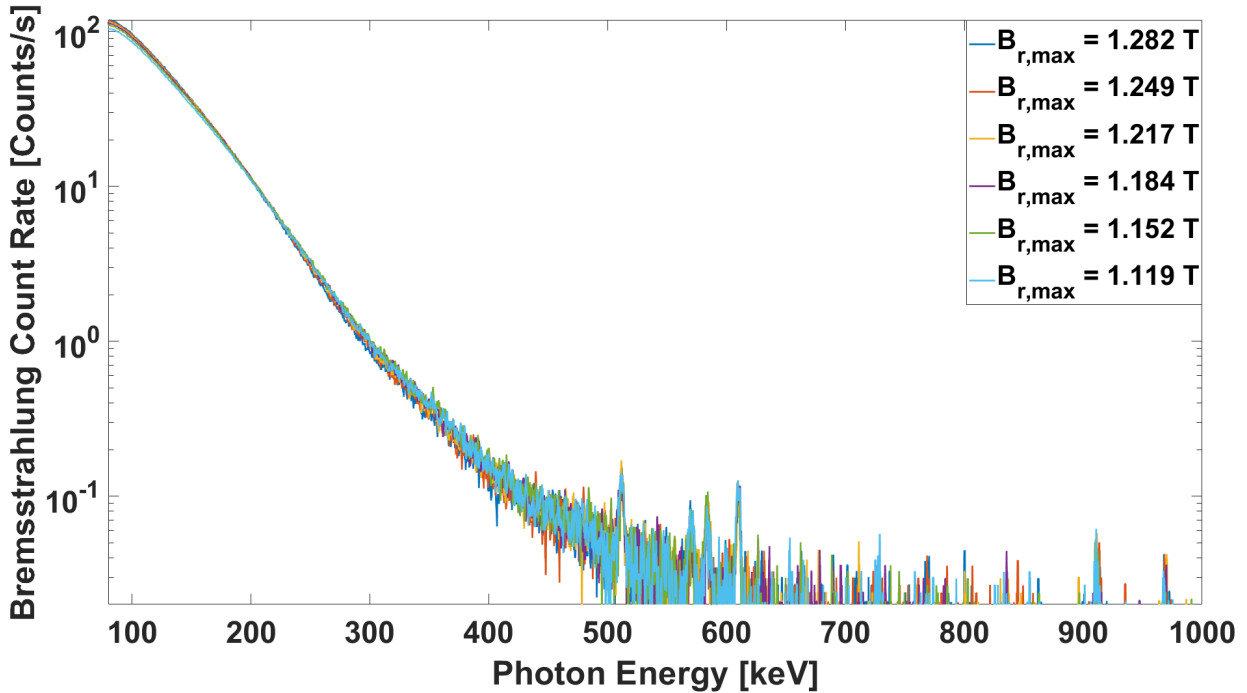


Figure 4.25: The bremsstrahlung distribution was largely unaffected by the changing radial field, however, as the radial field at the wall increases there is a preference for the emission of lower energy photons.

in chapter 3, it is not an optical effect from a lower field at extraction.<sup>3</sup> Most importantly, while there is a significant increase in the number of electrons that diffuse out of the plasma, the number of photons observed changes very little per field setting. Increasing the field strength at injection contradicts this trend. The almost 30% increase in photons can be accounted for by an increased count rate of photons with energies less than 80 keV. Only counting the number of observed photons with energies greater than 80 keV gives the trend in the lower-left plot of figure C.13 a less steep slope, more closely matching the trends in the other three plots. The higher injection side maximum may amplify the effect of the hexapole.

By increasing the radial maximum, we are directly decreasing the pitch angle of their respective loss cones (see figs. 4.12 and 4.14). It becomes easier for electrons to diffuse out of the plasma through the loss cone on the extraction side of the ion source. This could explain why the increase

<sup>3</sup>Varying the hexapole had a negligible effect upon the transmission of electrons through the beamline, even at low energies.

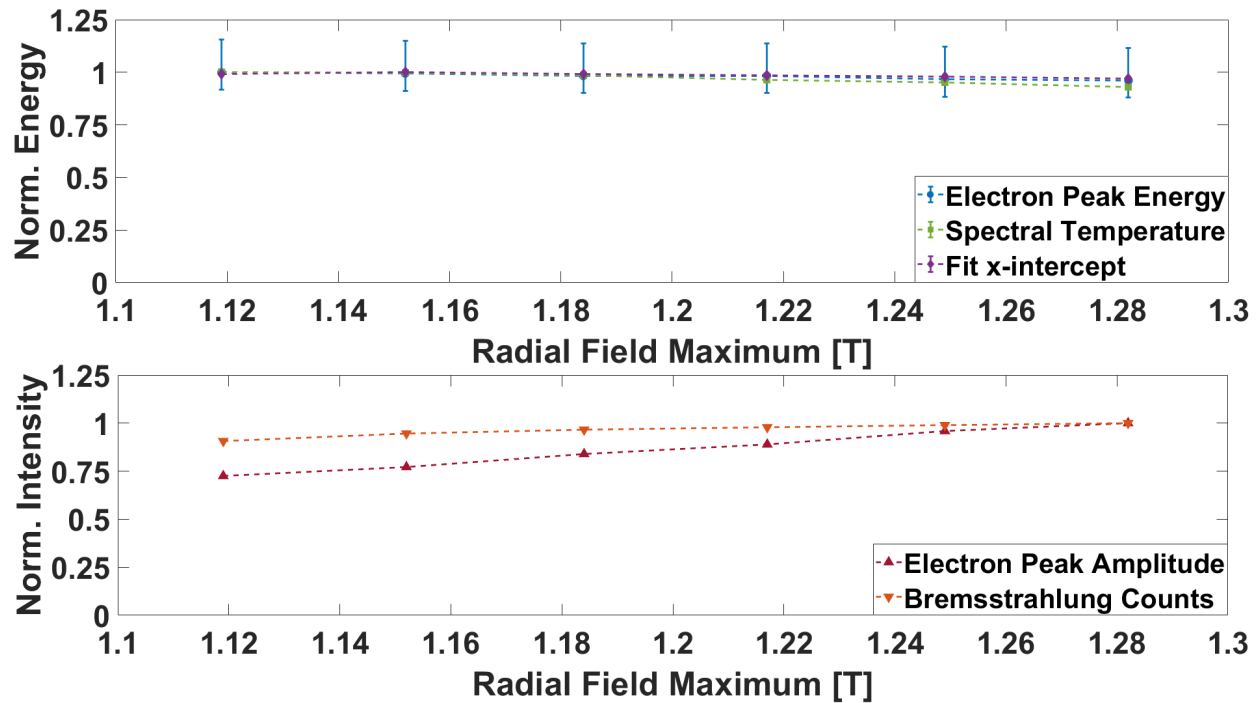


Figure 4.26: The energy content of the distributions were largely unaffected by a changing radial field strength. The increasing radial field causes an increase in the both the height of the electron peak and total number of photons observed.  $E_{\text{peak,max}} = 669 \text{ keV}$ ,  $T_{s,\text{max}} = 46.7 \text{ keV}$ ,  $X_{T_s,\text{max}} = 315 \text{ keV}$ ,  $I_{\text{peak,max}} = -1061 \text{ nA}$ , and  $N_\gamma = 6.3 \text{ Mcounts}$ .

in the current sees diminishing returns as the high energy peak shifts to higher energies. The data also suggests that the plasma density remains relatively constant, as we would expect to see a much larger increase in the number of observed photons across all operating points.

#### 4.4.4 Effect of Varying the Injection Side Magnetic Maximum

Varying the injection side magnetic field also sees only small changes to either the measured electron or bremsstrahlung distributions. Figures 4.27, 4.28, and 4.29 all indicate that the injection side maximum has little to no effect on the distribution of electrons escaping confinement. The increase in the injection side field maximum minimally increases the energy content of the system. The lack of change in the bremsstrahlung spectrum is expected as most of the electrons impacting the plasma chamber's injection side will direct their energy away from the HPGGe detector. Despite this, there is a change in the particle flux to the biasdisk as the injection side field is varied. Figure

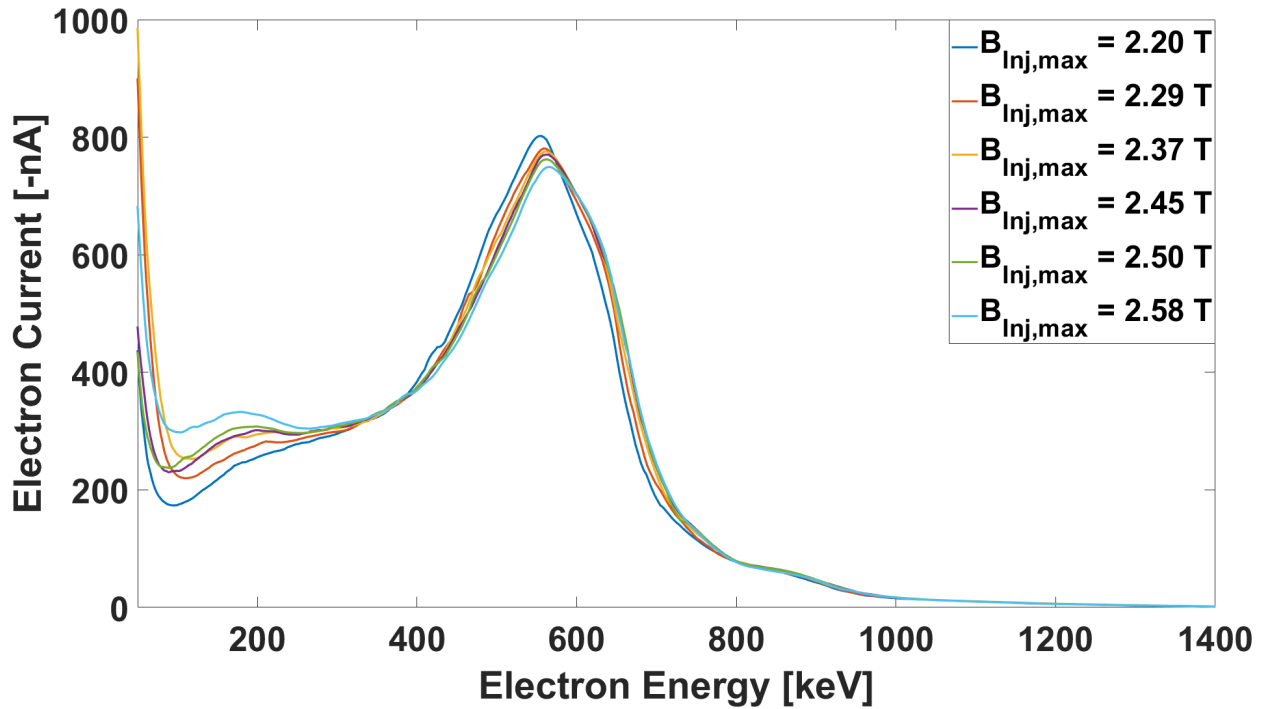


Figure 4.27: The varying injection side magnetic maximum mostly affected the lower energy distribution of electrons, having minimum effect on the high energy peak.

4.30 shows how the trend for the changing positive current deposited on the bias disk as the injection side maximum varies. We once again observed an inverse relationship between the electron peak amplitude and the total number of photon counts observed from the extraction side. This result is unexpected, as the increased injection side magnetic field should partially enhance the diffusion of electrons through the extraction and radial loss cones, and increase both the measured electron and photon intensities. Furthermore, focusing our attention on only x-ray photons with energies greater than 80 keV does *not* change the slope of the trend in the photon count number. This means that changing the electron or ion diffusion characteristics on the plasma chamber's injection side is not entirely responsible for the effect seen in figure C.13.

The near insensitivity of the energy to the injection maximum is also expected. Varying the injection side of the magnetic field profile should principally affect the electron heating rate, not necessarily their maximum energy. This result does not indicate that the injection side field is not important, as performing the same measurement over a much larger magnetic field domain may

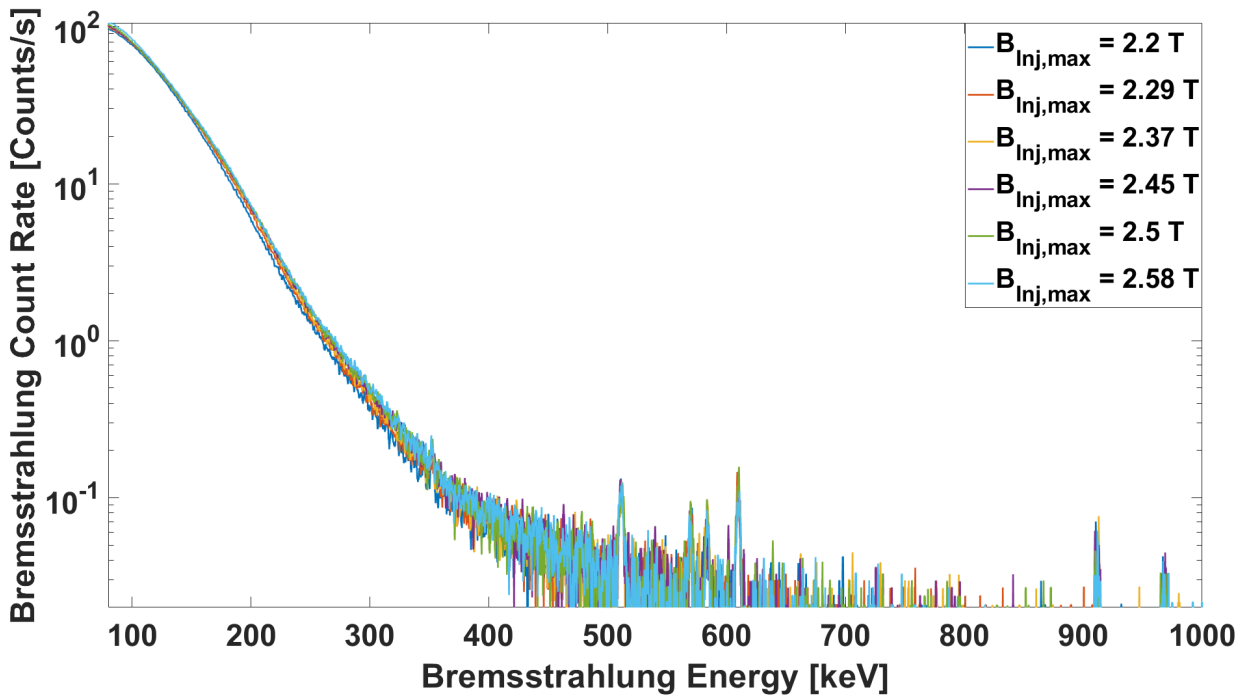


Figure 4.28: The bremsstrahlung distribution was largely unaffected by a varying injection side magnetic maximum.

result in a vastly different response. Particularly as the injection side maximum reaches the same magnitude as the radial or extraction side field maxima.

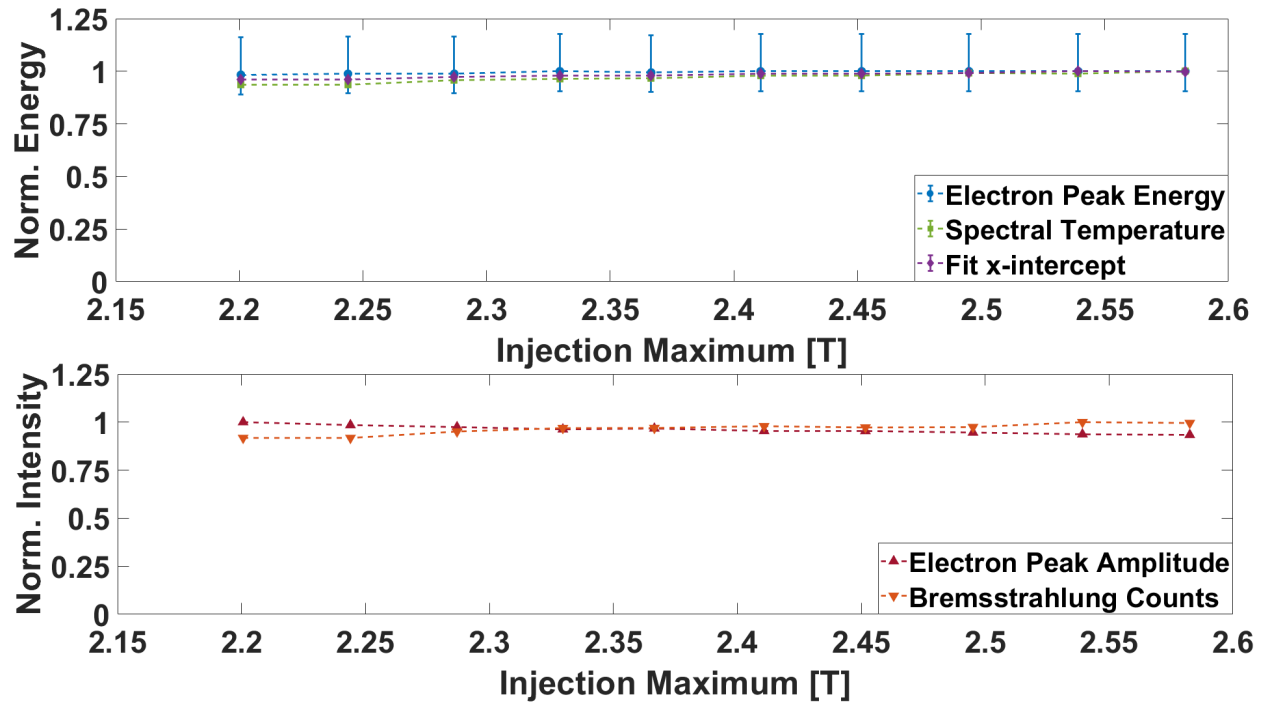


Figure 4.29: All operating points were nearly identical to one another. The inverse relationship between the electron peak amplitude and the total number of observed photons can be seen, however, the largest effect is likely on the lower energy side of the distribution, as the electron measurement suggests.  $E_{\text{peak,max}} = 568 \text{ keV}$ ,  $T_{\text{s,max}} = 38.6 \text{ keV}$ ,  $X_{T_{\text{s,max}}} = 281 \text{ keV}$ ,  $I_{\text{peak,max}} = -1357 \text{ nA}$ , and  $N_{\gamma} = 4.9 \text{ Mcounts}$ .

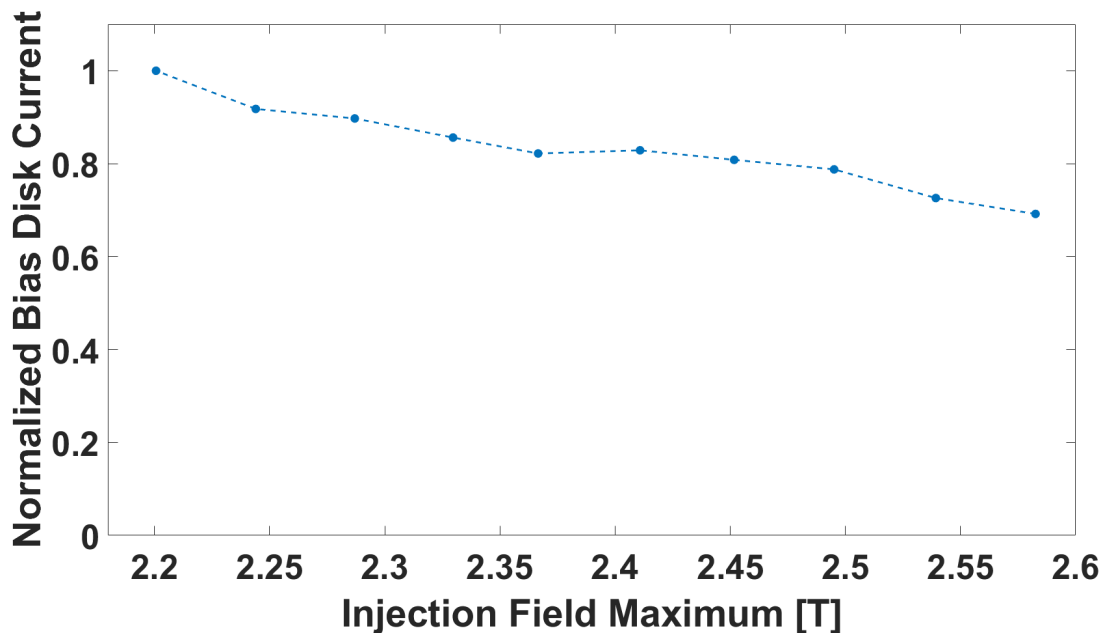


Figure 4.30: The bias disk current decreased as the injection side magnetic field increased,  $|I_{\text{BD,max}}| = 730 \text{ mA}$ .



#### 4.4.5 Effect of Varying the Extraction Side Magnetic Maximum

Varying the extraction side maximum changed the total number of electrons observed at the Faraday cup. This result adds credibility to the hypothesis that the extraction side magnetic field is mostly controlling the diffusion rate of particles out of the system. In figure 4.31, increasing the extraction side maximum above 1.2 T shows a sudden change in the confinement characteristics of the plasma. At this point, the total extracted beam current decreases drastically. These distributions are not corrected for the changes in transmission due to a changing field maximum at extraction. The extraction field affects the transmission coefficient of the system by perturbing the trajectory of electrons. Figure 4.32 shows a similar trend in the total number of bremsstrahlung photons observed, albeit less sensitive to the changing field strength. The large drop in the current at 1.23 T correlates with a sudden decrease in the number of photons observed for the same operating point. The sudden change in both the electron and bremsstrahlung distributions suggests that the jump is not a result of optical changes to the beamline. Figure 4.33 shows that the electron peak amplitude and total number observed of photons see a 62% and 56% decrease in intensity, respectively. The beam current results in figure 4.33 *are* corrected for beamline transmission, resulting in a slower decline in the electron peak amplitude than in figure 4.31.

The decreasing current may result from changing the pitch angle of the loss cone at extraction (see fig. 4.13). As the loss cone pitch angle decreases, a smaller fraction of the electron velocity distribution would exist inside it, decreasing the diffusion rate out of the system. However, without a model for the plasma diffusion processes, or the electron velocity distribution function, it is difficult to compare the varying electron current and photon intensity to the changing loss cone. If the plasma had an isotropic electron velocity distribution, we could say that  $\dot{n} \sim \alpha_0$ ; however, we know that this is not the case. The resonant heating process preferentially increases the transverse energy of electrons, creating a temperature anisotropy. Despite this, the electrons will have non-zero longitudinal momentum at some point during their lifetime in the plasma. Thus, the decreasing loss cone pitch angle will make it more difficult for electrons to escape the system, which decreases the observable current.

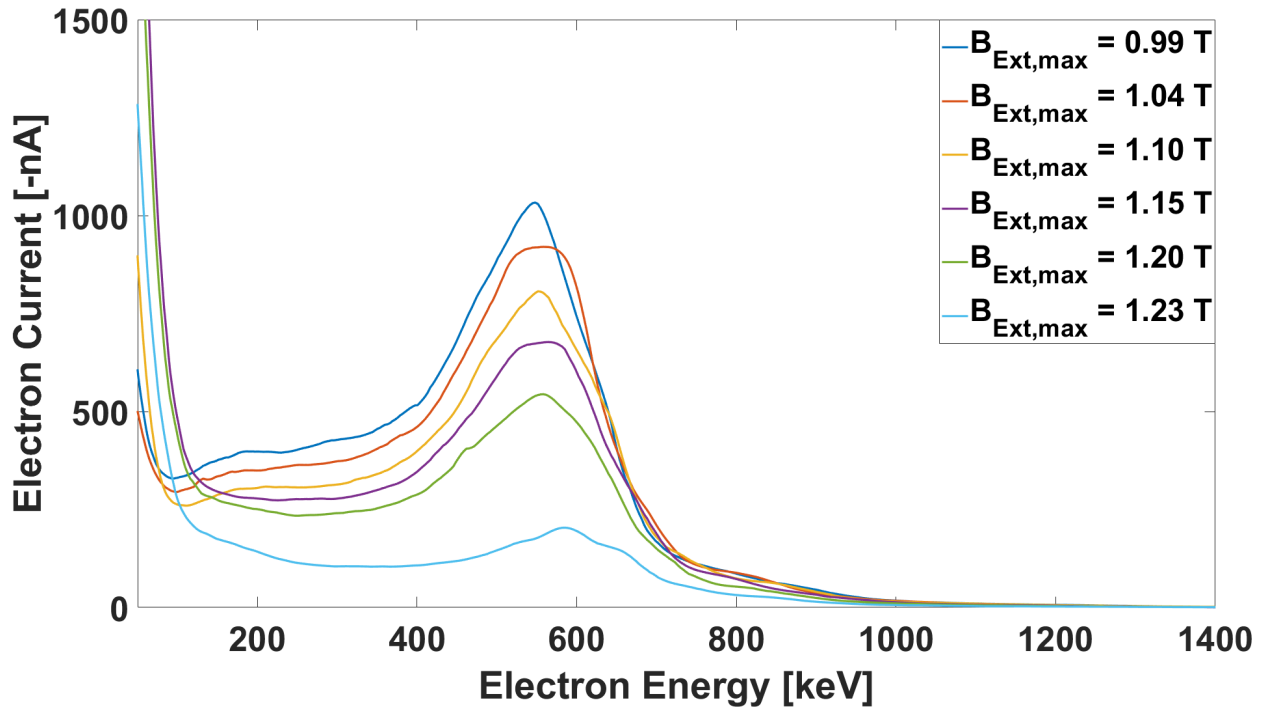


Figure 4.31: Increasing the extraction maximum slowly decreases the amplitude of the high energy peak. Between 1.2 T and 1.23 T the change in peak amplitude increases and results in a dramatic decrease in peaks height. These distributions have not been corrected for changes in the transmission coefficient due to a changing extraction field maximum.

Benitez et al. also reported a change in the behavior of the x-ray distribution while varying the extraction side maximum in the VENUS ion source [3]. They reported that increasing the radial field maximum above that of the extraction field caused the measured spectral temperature to change. This trend may indicate a change in the confinement characteristics of the electron population. While figure 4.31 shows a behavioral change, it is important to note that the results reported here and by Benitez et al. contradict one another. Figure 4.33 shows no change in the spectral temperature, but does see a change in the total number of electrons diffusing out of the plasma chamber. However, a changing confinement scheme for electrons may explain the rapid decrease in the electron diffusion rate between 1.2 T and 1.23 T (the maximum field strength generated solely by the hexapole coils was calculated to be 1.22 T). Setting the extraction side maximum above the radial field maximum could have this effect by encouraging radial diffusion of electrons. However, the total field at the plasma chamber wall, including the effect of the solenoids,

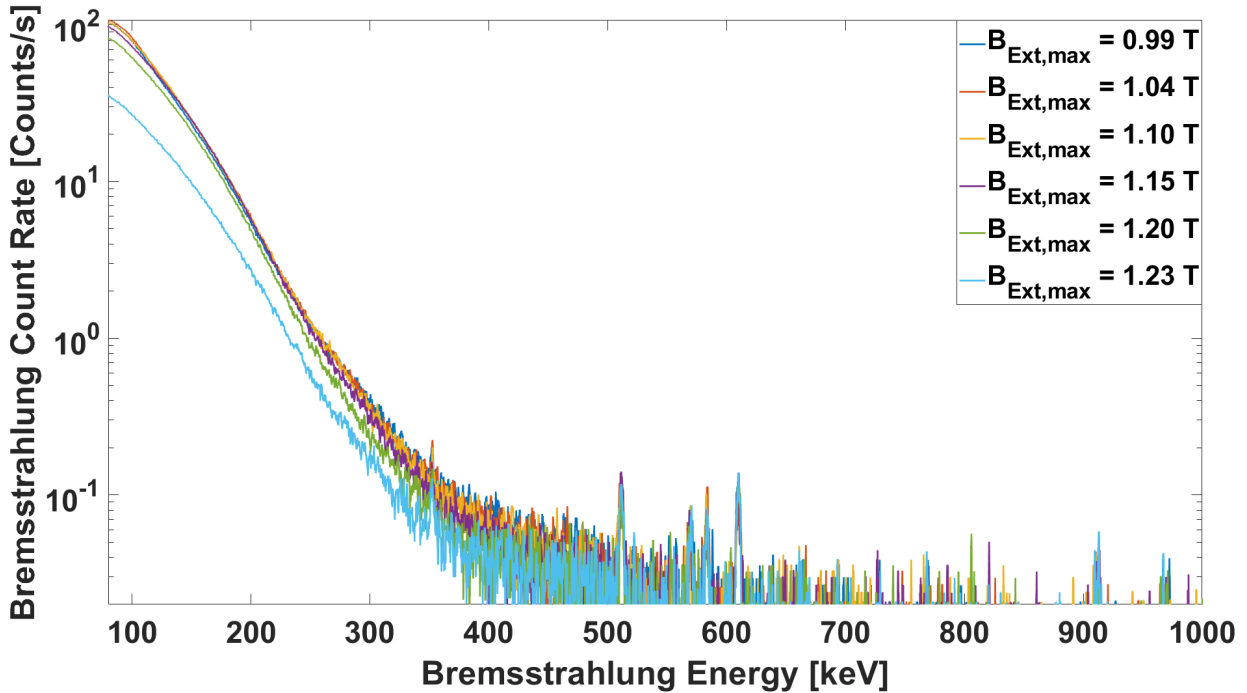


Figure 4.32: The bremsstrahlung distribution remains largely unchanged as a result of a changing extraction field maximum, up to a point. Between 1.2 T and 1.23 T the number of intermediate to low energy photons observed decreases dramatically. These spectra have not been corrected for changes in the beamline transmission coefficient which result from a varying field maximum at extraction.

is complicated and inhomogeneous, making it difficult to confirm this confinement condition. Measuring the bremsstrahlung emitted radially from the ion source as the extraction field is varied would be the best way to determine if such an effect occurred. However, this kind of measurement is difficult to do with the SuSI ion source.

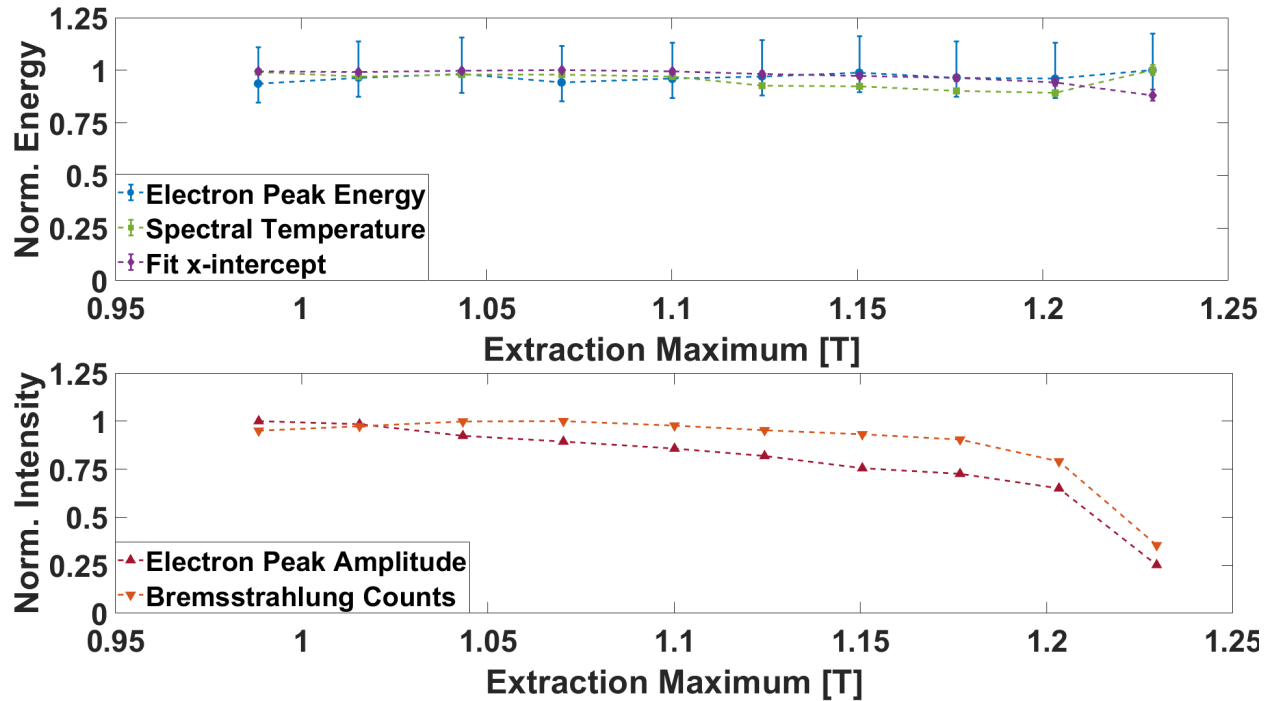


Figure 4.33: While the total number of photons observed decreases only slightly as the extraction maximum is increased, the sudden drop-off in extracted beam current reduces the number of photons observed by more than 50%. No appreciable change in the system’s energy content is observed.  $E_{\text{peak,max}} = 585 \text{ keV}$ ,  $T_{\text{s,max}} = 38.6 \text{ keV}$ ,  $X_{T_{\text{s,max}}} = 270 \text{ keV}$ ,  $I_{\text{peak,max}} = -1756 \text{ nA}$ , and  $N_{\gamma} = 4.9 \text{ Mcounts}$ . Each data set has been normalized by the largest value in their respective sets. The normalized electron peak amplitude has been corrected for changes in the beamline transmission coefficient which result from a varying extraction maximum.

#### 4.4.6 Effect of Varying the Magnetic Minimum

The most striking results came when the magnetic minimum was varied. The energy associated with the high energy peak increased as the minimum magnetic field increased. The magnetic minimum was the only feature of the magnetic field that appreciably varied the peak’s energy. In conjunction with its effect upon the electron distribution, there is a sharp increase in the bremsstrahlung distribution’s spectral temperature with an increasing magnetic minimum. Both distributions seem to agree that there should be a factor of two increase in the system’s high energy content. Figures 4.34, 4.35, and 4.36 show how only changing the magnetic minimum can appreciably affect the energy distribution of electrons and photons escaping the system.

The top plot in figure 4.36 demonstrates how well the energy content of both measured distribu-

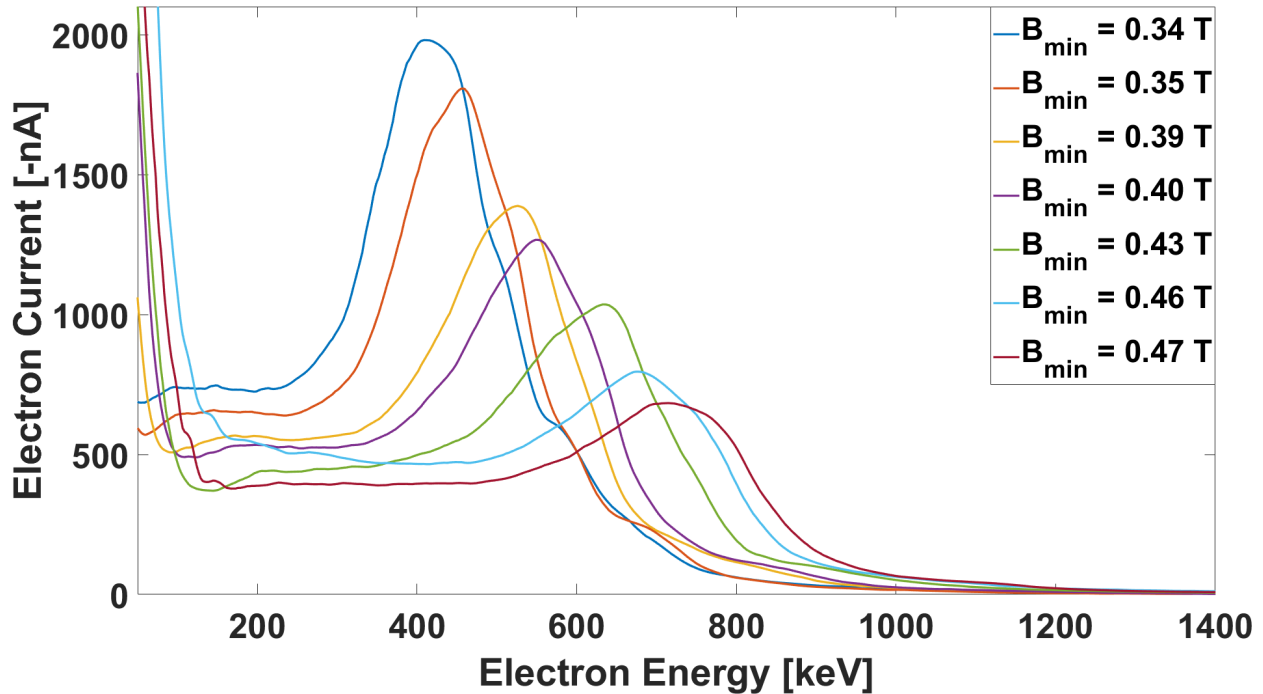


Figure 4.34: There is an obvious change in the energy content of the measured electron distribution resulting from a changing magnetic minimum. While the central energy of the peak increased, the height of the peak decreased.

tions scale with one another. Previous measurements of the ECRIS bremsstrahlung demonstrated the relationship between the energy content of the plasma and the system's magnetic minimum [2, 3, 61]. Noland observed the same effect in the spectral temperature of the radially emitted bremsstrahlung [62]. The high degree of correlation between the linear fit x-intercept and the high energy peak's central energy suggests that there is a relationship between the electron peak and the high energy tail of the bremsstrahlung distribution. In particular, the higher central peak energies correlate with increasing high energy photons in the tail of the bremsstrahlung distribution.

The lag in the spectral temperature may be an artifact of the mixed nature of the total electron distribution. Here we hit upon a limit of the algorithm presented in chapter 3 (sec. 3.2.5). Figure 4.37 makes this failure obvious, as the maximum upper limit on the fitting domain is 372 keV for a field minimum of 0.47 T. This is a bad fit as both the escaping electron and bremsstrahlung distributions have meaningful intensities at energies greater than 500 keV. This error results from the simplicity of the fitting algorithm. Figure 4.35 shows that the linear portion of the photon

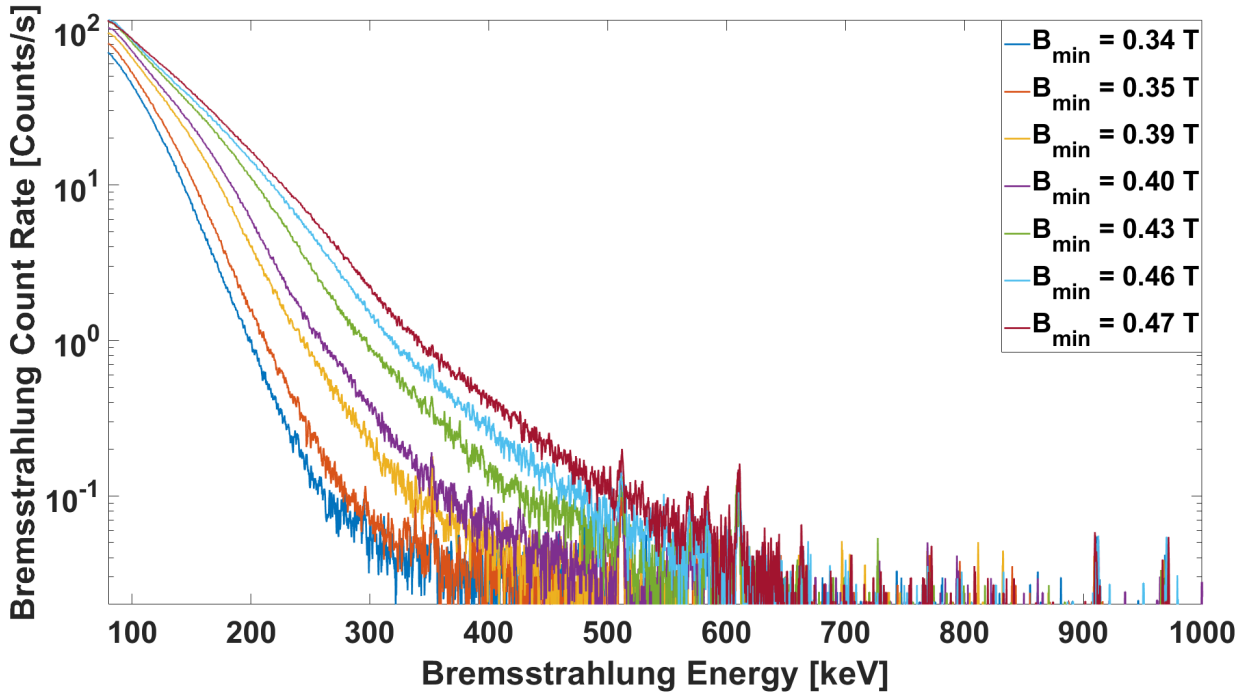


Figure 4.35: Just as in figure 4.34, an increasing magnetic minimum pushes the photon distribution to higher energies. The total number of counts, however, increases where the electron peak's height decreases. This suggests that overall electron density increases, even if the measured electron current decreases.

distribution shifts to higher energies as the magnetic minimum increases, however, the entire log scale distribution itself becomes more linear overall as the minimum increases as well. The careful observer will also notice that, in particular, the log scale high energy tail of the bremsstrahlung distribution also becomes more linear for higher magnetic minimums, especially for regions where the count rate is less than 0.5 counts-per-second. Alongside this, although more linear on average, the lower energy portion, particularly with count rates higher than 0.5 counts-per-second, has a higher degree of curvature to it. This curvature biases the calculation of the spectral temperature toward lower temperature values (large fitted slopes).

The decrease in peak height of the electron distribution is unlikely to result from beamline transport as the beamline transport coefficient increases with increasing energy. Rather, it may present evidence of a quasilinear diffusion process. Recall from chapter 2 that  $D_{ql} \sim \gamma_e^{-2}$ , where  $\gamma_e$  is the Lorentz factor of the quasilinearly diffusing electrons (see eq. 2.39). Increasing the

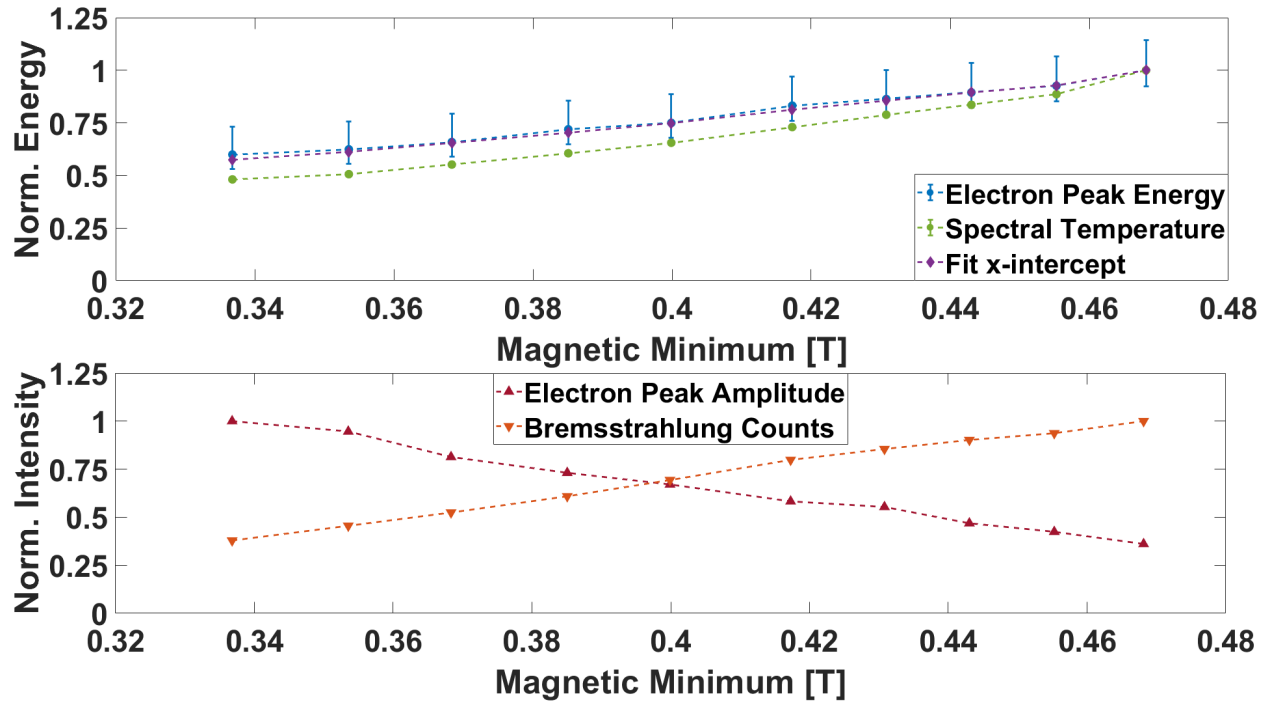


Figure 4.36: Both the electron and bremsstrahlung distributions agree to a near linear increased in the energy content of the plasma. The spectral temperature lags behind due to the influence of lower energy electrons.  $E_{\text{peak,max}} = 742 \text{ keV}$ ,  $T_{s,\text{max}} = 56.47 \text{ keV}$ ,  $X_{T_{s,\text{max}}} = 359 \text{ keV}$ ,  $I_{\text{peak,max}} = -1916 \text{ nA}$ , and  $N_{\gamma} = 6.7 \text{ Mcounts}$ . Each data set has been normalized by the largest value in their respective sets.

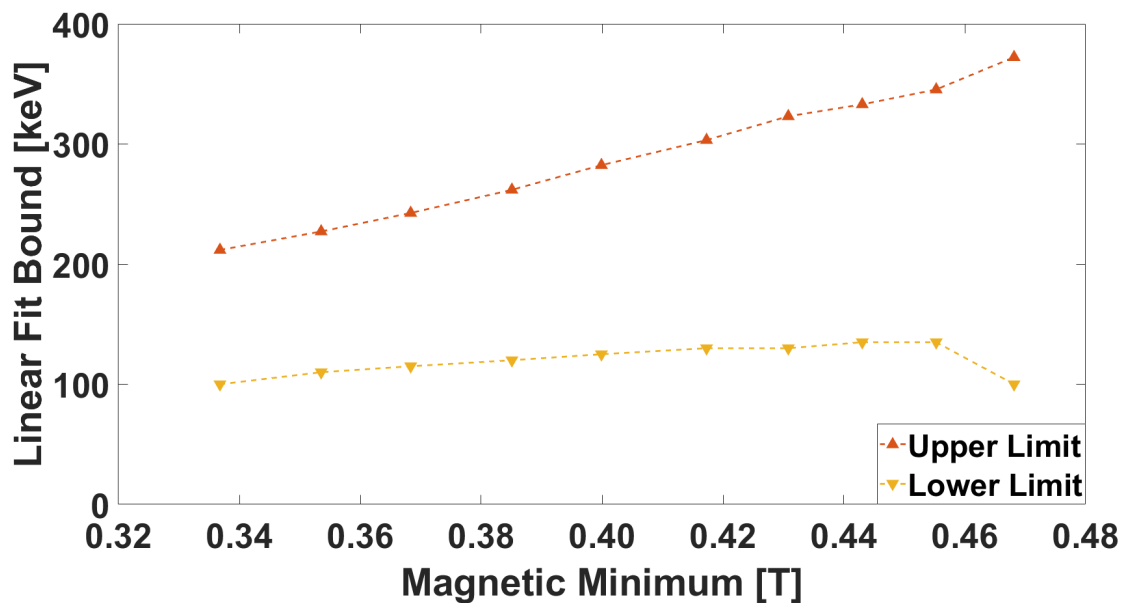


Figure 4.37: Maximum and minimum energy limits for fitting the spectral temperature as the magnetic field is varied.

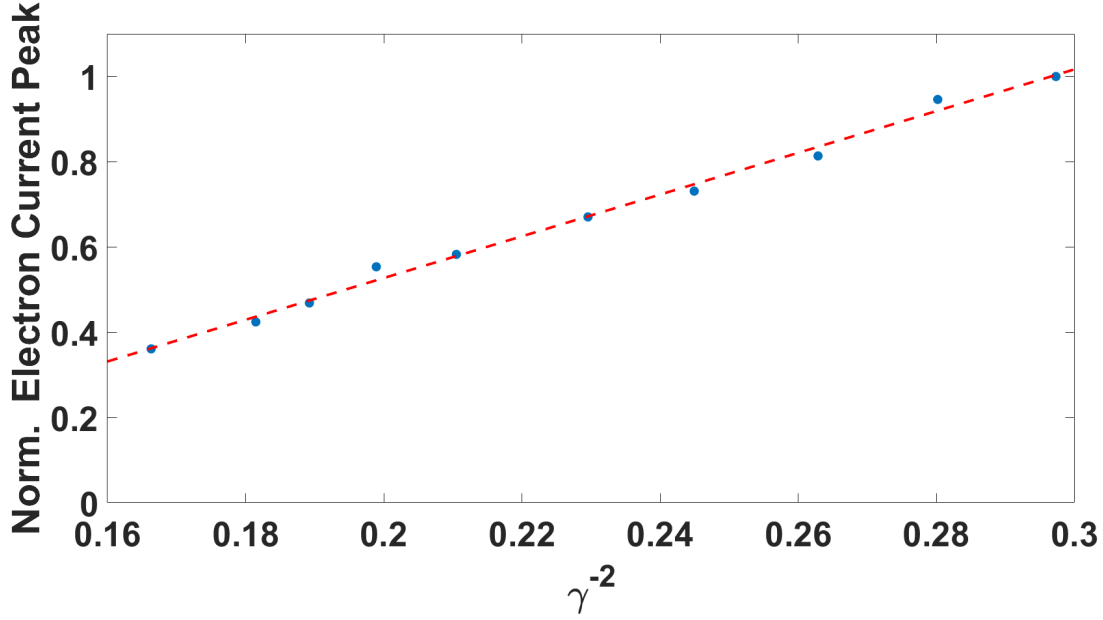


Figure 4.38: There is a linear correlation between the decreasing trend of the height of the high energy peak and the reciprocal square of the central energy of that peak.

$$I_{\gamma}/I_{\gamma,max} = 4.897 \times \gamma^{-2} - 0.4523, R^2 = 0.9938.$$

resonant energy of electrons will result in a decreasing diffusion coefficient [73]. We should then expect that:

$$I_e = \frac{dQ}{dt} \sim -e \frac{dn_e}{dt} \sim D_{ql} n_e \sim \frac{n_e}{\gamma_e^2},$$

where  $I_e$  is the electron current diffused by quasilinear diffusion (high energy peak). Figure 4.38 shows that the peak amplitude increases linearly as the central energy of electrons in the high energy peak decreases, by fitting the current against  $\gamma_e^{-2}$ . This does assume that the density of electrons interacting with the electromagnetic waves is relatively constant.

An alternative explanation for this might be that the electron current decreases as the diffusive interactions focus on higher energy electrons. The trend is then more of a demonstration of the decreasing density in the high energy tail of the electron energy distribution. However, it is not obvious what kind of mechanism would be responsible for the diffusion of electrons. As figure 4.39 shows, the direction of the field lines at the source's extraction aperture are essentially parallel to the longitudinal axis of the plasma chamber. As a result, we can discount both fully ionized and Bohm diffusion models (eqs. 2.14 and 2.15) as they require diffusion across magnetic field lines. Classical



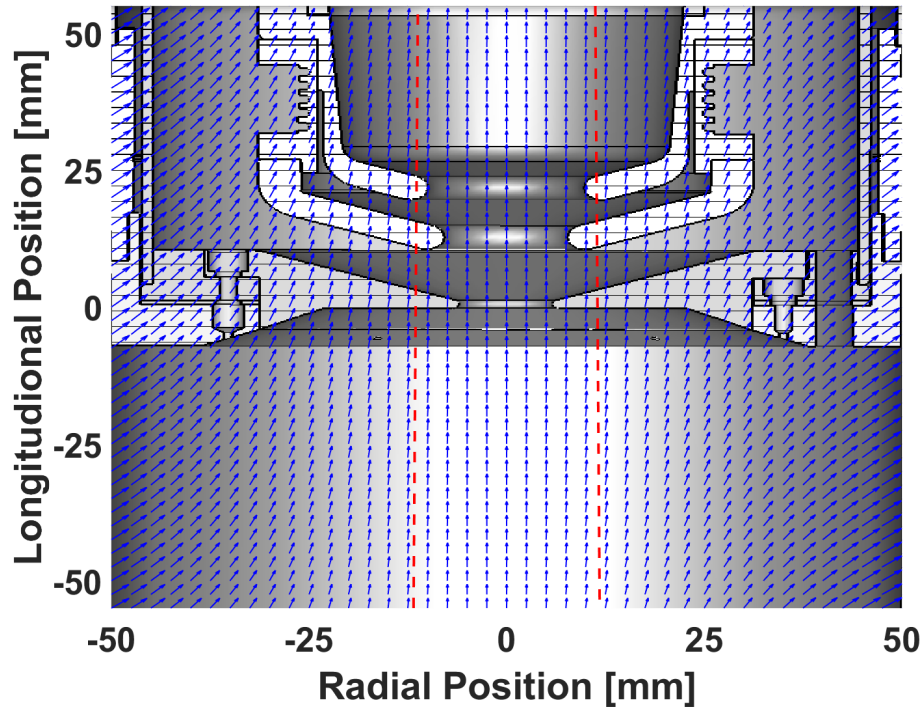


Figure 4.39: The magnetic field lines (blue arrows), within the acceptance area of the extraction aperture (red dashed lines), are primarily parallel to the longitudinal axis of the plasma chamber.

'free' diffusion and ambipolar diffusion can act along magnetic field lines, but are independent of the magnetic field and have diffusion coefficients which scale with electron temperature (eqs. 2.11 and 2.13). Lastly, this may be the result of pitch angle scattering, but this hypothesis would require numerical simulations to replicate the observed energy and amplitude trends.

The increased photon count rate does provide evidence for a classical electron diffusion model, as the increasing loss cone would encourage electron diffusion (see fig. 4.11). The wider angle would encourage more electrons to escape from confinement through all diffusion mechanisms and across all energies. However, the height of the high energy peak and the total number of photons observed by the HPGe detector appear inversely correlated. Figure 4.40 shows the relationship between the total number of detected photons and the height of the high energy peak. Alongside this, figure 4.34 brings into question whether a simple increase in the diffusion of electrons across all energies and momenta makes sense. If that were the case, we might expect the observed electron currents to increase across all energies, except those in the peak. This trend is not observed, as the

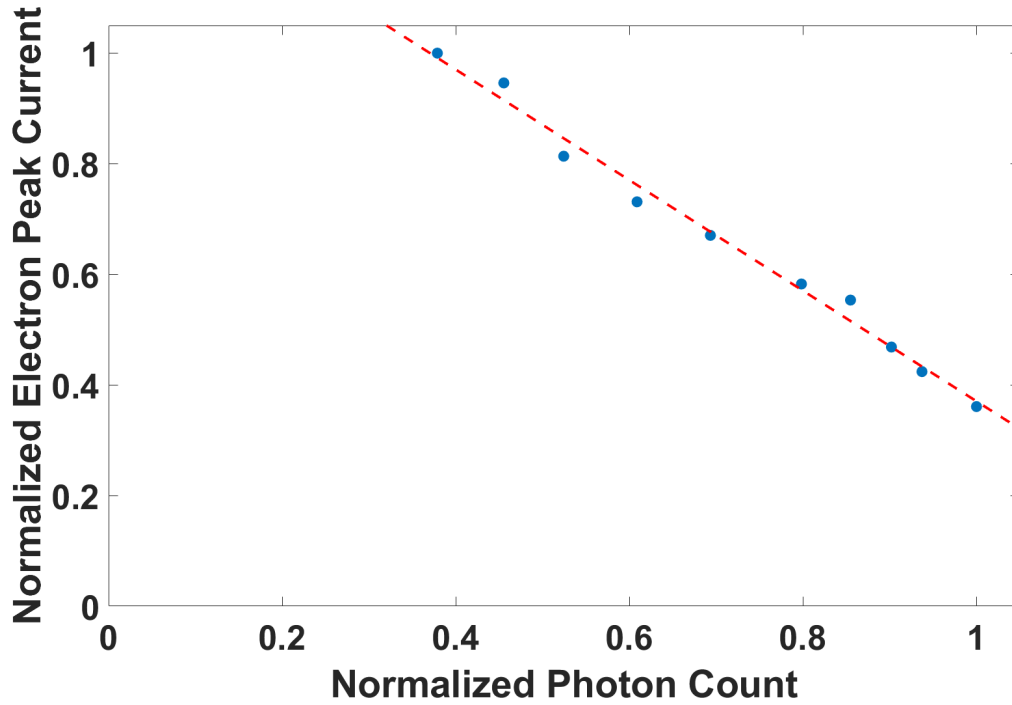


Figure 4.40: There is a near-perfect inverse correlation between the trends of the decreasing height of the high energy peak and the increasing number of photons observed  
 $I_e/I_{e,max} = -0.9998 \times N_\gamma/N_{\gamma,max} - 1.37, R^2 = 0.9888$

measured distributions trends towards lower total electrons at the high energy side of the distribution. This result implies that the number of electrons escaping from confinement increases in regions outside of the extraction aperture's opening as the magnetic minimum increases. This effect could result from a *spatially* wider distribution of diffusing electrons, with a smaller concentration of electrons escaping through the extraction aperture. Determining such a change will require rather precise measurements of the emittance of escaping electrons and bremsstrahlung photons.

## 4.5 Concluding Thoughts

The results here agree with results seen in other measurements regarding the energy distribution of the plasma with varying plasma parameters, both in regards to the bremsstrahlung [2, 3, 62] and measured electron distributions [28, 73]. The magnetic minimum has the most control over the energy content of the system. While injected microwave power, neutral pressure, and the radial field's maximum can affect the system's energy content, their effects are minimal compared to the

effect of the magnetic minimum. The magnetic maxima had a minimal, if not negligible, effect on the diffused electrons' energy content.

The intensities of both electron and photon distributions were found to be highly correlated, particularly in through the electron high energy peak. The total rate of diffusion of electrons out of system increased linearly with increasing microwave power, with little effect upon the energy content of the system (figs. 4.20, C.4, and C.5). The radial field maximum was correlated with the total observed electron current, although it had a minimal effect upon bremsstrahlung distribution (figs. 4.26, C.12, and C.13). While changing the magnetic maximum at injection was found to appreciably change the rate of current deposition on the bias disk (fig. 4.30), the varying field maximum had little effect upon the diffusing electrons (fig. 4.29). The extraction maxima had a much larger effect upon the distribution, particularly after the field maximum surpassed the radial field maximum. In agreement with Benitez et al., increasing the extraction maximum's magnitude above that of the radial maximum caused a change in the plasma's diffusion characteristics (fig. 4.33) [3]. This suggests that changing the magnetic maximum relative to the radial maximum at the wall, or vice versa, greatly affects the plasma's diffusion characteristics. However, without corresponding radial measurements, it cannot be said whether this is a global or only a local effect. Finally, changing the magnetic minimum affected both the energy content and intensity of electrons diffusing out of the plasma.

The measurements revealed several correlations between the energy content of the ion source bremsstrahlung and diffusing electrons. However, the decreasing electron current appears inversely correlated with the intensity of x-rays emitted from the ion source. Moreover, the energy content in both the bremsstrahlung and electron distributions increases as the minimum of the ion source's magnetic field increases. In section 4.4.6, it was suggested that this could be the result of a changing spatial distribution of diffusing electrons. Although significantly smaller, the same effect was observed in sections 4.4.2 and 4.4.4. This could indicate that the pressure and injection field maximum can measurably affect the energy distribution of diffusing electrons (see figs. 4.23, C.8, and 4.29). Although, if true, these parameters minimally affect the energy of the diffusing electrons.

It also implies that, unlike in the case of power, the predominant effect of varying the neutral gas pressure is not to increase the density of hot electrons.

The high energy peak, or the 'hump' described in Izotov et al. [28], may result from the quasilinear diffusion of electrons out of the magnetic trap, as described in section 2.4.3. This may imply that that measured electron distribution is the combination of two distributions: one where diffusion is caused by scattering<sup>4</sup> and one which is quasilinearly diffused. However, proving this hypothesis would be difficult and would require more evidence than was provided by these measurements.

The correlation between the high energy peak's amplitude and its central energy does provide some evidence for this hypothesis. The  $\gamma_e^{-2}$  trend is predicted by the quasilinear diffusion theory (see eq. 2.39) [73]. On the other hand, the central energy of the high energy peak does not match the predictions made by Shalashov et al., at least for single frequency diffusion. Let us use figure 4.15 as an example. Assuming  $B_{Ext,max}/B_{RF} \approx 1.72$ , equation 2.43 determines that the central energy of the high energy peak should occur at 727 keV, which is substantially greater than the measured peak (550 keV). Furthermore, sections 4.4.5 and 4.4.6 demonstrated that the central energy is dependent on the magnetic minimum, rather than the field maximum in the direction of diffusion. The introduction of at least one other microwave frequency could allow electrons to quasilinearly diffuse out at lower energies [73]. However, no observations of excited electromagnetic modes during the stable operation of the source have ever been reported. SuSI's diagnostic array is also not designed to make such a measurement. However, more traditional diffusion mechanisms also do not explain the observed trends, as described in section 4.4.6. Pitch angle scattering may be able to produce the observed peaks, but a simulation such as NAM-ECRIS would be necessary to provide further evidence of the scattering process.

Comparing the electron and bremsstrahlung distributions further suggests that the measured electron distributions are a combination of two different distributions. This was most evident when comparing the central energy of the high energy peak, spectral temperature, and the resulting fit's

---

<sup>4</sup>These can include either particle-on-particle Coulomb scattering or pitch angle scattering. Recall that collisional scattering is very improbable at these energies [20].

x-intercept. The x-intercept near-perfectly followed the high energy diffusion peak as the peak shifted towards higher energies. On the other hand, the spectral temperature varied slower due to the convolution of the scattered electrons and those in the high energy peak. Moreover, as  $B_{\min}$  increases, both the electron and photon distributions' high energy sides decrease more smoothly. The distribution of diffused electrons in the high energy peak becomes more distinct as its central energy increases, correlating with an increasingly linear bremsstrahlung high energy tail. Together, these suggest that the linear portion of the log-scale bremsstrahlung intensity is a measure of the high energy electron peak. The non-linear region *may* result from some combination of pitch angle, electron-electron, and electron-ion collisions. Further investigations, including computational simulations, are necessary in order to further develop this hypothesis.

The importance of using a variable region for determining the spectral temperature cannot be understated. Figure 4.41 shows the difference in calculated spectral temperatures as a function of power across two different operating points. The correction applied to the low field measurement is significantly greater than the one with higher field strength. Looking back at C.3, we see that the increasing magnetic field results in a qualitative change to the distribution. This result implies several things: first, that the initial guess for the calculation domain for spectral temperature was more appropriate for higher energy systems. Secondly, a significant enough change to the distribution of photons in the system requires a re-evaluation of the spectral temperatures fitting region. This is a result of the correlation between the high energy peak and the linear region of the log-scale bremsstrahlung distribution. The greatest improvement to the algorithm described in section 3.2.5 would be the addition of a non-*a priori* method of determining the maximum energy of the electron fit. In its current form, the algorithm requires the user to provide knowledge about the minimum meaningful photon intensity within the distribution, i.e., where the distribution begins to flatten. Figure 4.35 shows an example of the linear region extending into beyond the 0.5 counts/s limit. A more objective way to determine the upper limit of the fitting domain would improve the algorithm.

Lastly, it can be seen that the low energy portion of the electron distribution, the 'low energy

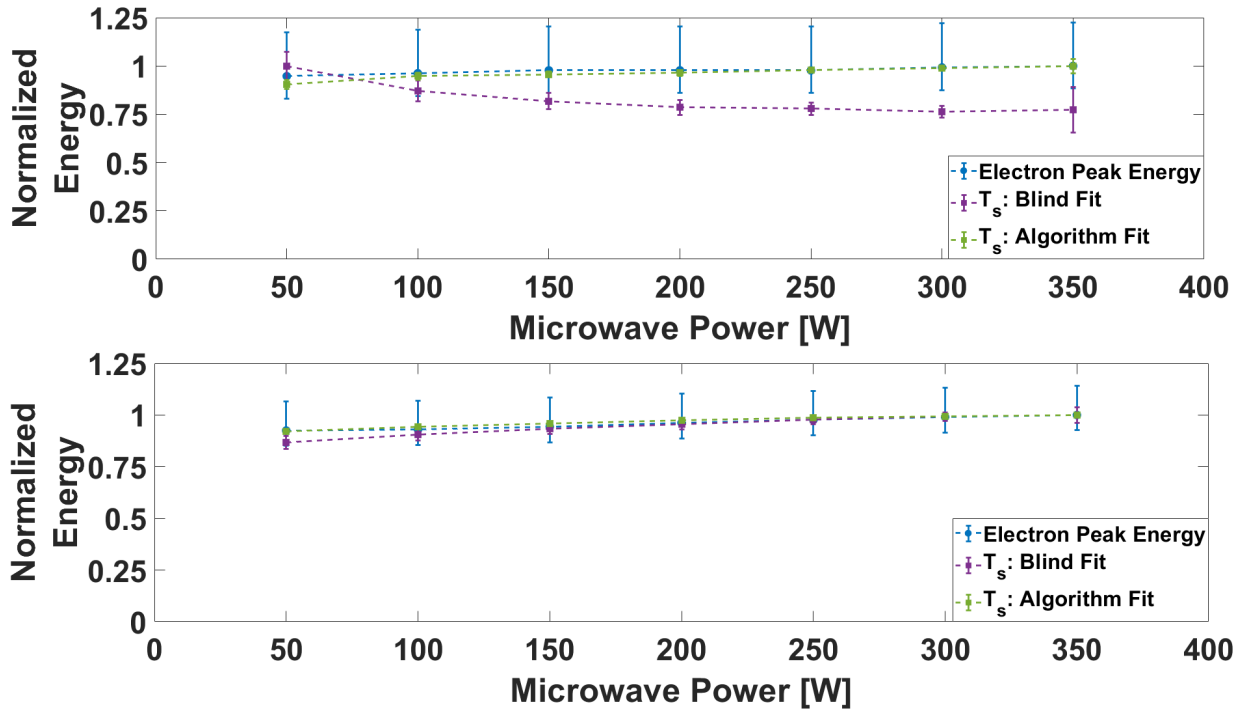


Figure 4.41: Bremsstrahlung distributions analyzed using the algorithm described in section 3.2.5 show much better agreement with the electron distribution data than those where an arbitrary energy domain was blindly applied to all operating points. In this case, the disagreement is larger for operating points with lower magnetic fields. Top plot:  $B_{\min} = 0.337$  T. Bottom plot:  $B_{\min} = 0.468$  T.

peak', does vary with varying ion source parameters. In particular, its height and width seem to vary, most notably, with the injected microwave power, average longitudinal magnetic field, and neutral gas pressure (see figs. 4.18, C.2, 4.21, C.6, 4.27, 4.31, and 4.34). As discussed earlier, the residual and ambient magnetic fields present around and throughout the beamline make analyzing this peak difficult, and any trends or conclusions non-meaningful. Better understanding of the escaping electrons in this energy range will require further refinement of both the electron and bremsstrahlung measurements. First, an electron spectrometer with a 10's eV precision would be necessary to measure it properly. SuSI's beamline is presently incapable of this kind of precision. Secondly, an x-ray detector that can accurately measure 100 eV - 100 keV photons would be necessary to measure the bremsstrahlung distribution, which results from this peak.<sup>5</sup> Most importantly, like with the high energy peak, some simultaneous observation of an excited mode,

<sup>5</sup>This should be done concurrently with measurements in the 100 keV - 1 MeV range.

responsible for the diffusion of electrons, would be necessary to confirm the hypothesis.

Altogether, the results presented here indicate that previous measurements of the bremsstrahlung distribution may need to be re-interpreted. Previous measurements, such as those presented by Noland [62], assume that a electrons obeyed a Maxwell-Boltzmann energy distribution. We have seen that this is not the case. Future measurements will need to consider the apparent relationship between the electron high energy peak and the bremsstrahlung distribution. Preferably, future studies of the ECRIS axial bremsstrahlung will be performed concurrently with measurements of the axially diffusing electrons and radially emitted bremsstrahlung.<sup>6</sup> Further experimental studies of the quasilinear diffusion mechanism will be necessary to determine the validity of the hypothesis, as well as its effect on ECR ion sources' overall performance.

---

<sup>6</sup>The detector should be placed to look into the hexapole pole tip, as this will be the direction which electrons diffuse outward from the center axis.

## CHAPTER 5

### PARAMETER SWEEP

#### 5.1 Goals

It is well understood that the kinetic instabilities turn on and off depending upon the value of the magnetic field and injected microwave power [83, 81]. The goal of this measurement was to search for similar thresholds while taking advantage of the flexibility of SuSI's magnetic field. However, the transient behavior of the extracted beam current is complex and almost immediately revealed previously unknown qualitative characteristics. In exchange, the new complexity provided a new perspective for understanding the kinetic cyclotron maser and its effect upon the plasma. This necessitated multiple 'stability maps' of SuSI's parameter space and highlighted the non-linear relationship between the plasma, Min-B field structure, and externally injected microwave power. Despite this, many interesting and reproducible trends were discovered, pointing toward stabilizing the plasma and maximizing extracted high charge state currents.

#### 5.2 Parameter Space

A group for four sets of fields was calculated to probe SuSI's parameter space, with the intent of probing the magnetic scaling laws [46]. Contrary to the parameter spaces described in chapter 4, none of the extrema were fixed for the duration of this measurement. This was done to observe the largest possible range of magnetic minima while preventing the superconducting coils from quenching. Rather, the field maxima were set to either follow or deviate from the scaling laws throughout each of the chosen parameter spaces. Each of the parameter spaces spanned 8 different magnetic field operating points such that  $B_{\min}/B_{RF} \in [0.55, 0.6, \dots, 0.9]$ . Table 5.1 shows the average of the ratios between the magnetic maxima and cold resonance field used in each set of measurements. Appendix D shows a full list of operating points used. The exception to this



	Standard	Range 1	Range 2	Range 3	Range 4
$B_{inj}/B_{RF}$	3.96	4.09	3.71	3.43	4.11
$B_{ext}/B_{RF}$	1.94	2.02	1.78	1.95	1.61

Table 5.1: The field maxima used were scaled to either be on average larger or smaller than the scaling laws prescribe. The values above are there to demonstrate the relative range of values used as the magnetic minimum was varied. As calculated, the fields in each of the four ranges corresponds to  $B_{min}/B_{RF} = 0.725$ . The standard facility operating point uses  $B_{min}/B_{RF} = 0.711$ .

procedure was range 4, where operating the source at  $B_{min}/B_{RF} = 0.9$  was unsafe for operation.<sup>1</sup> In this case, the upper limit was set at  $B_{min}/B_{RF} = 0.85$ ; however, since the intention was to go higher, table 5.1 shows the of the average field ratios including  $B_{min}/B_{RF} = 0.9$ .

Each of the longitudinal field ranges were measured three times using each of the following hexapole field maxima,  $B_{Hex,wall} = 1.1$  T, 1.2 T, and 1.322 T ( $B_{Hex,wall}/B_{RF} = 1.71, 1.86, 2.05$ ). For reference, SuSI’s standard operational field setting uses  $B_{Hex,wall} = 1.22$  T. During the measurement the microwave power was swept from 50 W to 550 W in 100 W steps for each magnetic field setting. The extracted beam current and reflected microwave power were observed and recorded to determine if and when the plasma became unstable. A map of the source’s stability characteristics was created by recording the transient characteristics of the extracted beam current *and* microwave power at each operating point used.

### 5.3 Results

As most of this section will focus on unstable beam currents, it is essential to define what is meant by ‘unstable.’ This is not an easy task, however, as multiple authors have shown. Shalashov et al. mathematically determined the unstable plasma to be a result of resonant interactions of electrons with unstable electromagnetic modes along the quasilinear diffusion lines [72]. While precise, this definition is impractical to use when the unstable modes cannot be measured. Similarly, Naselli et al. created a parameter,  $I_s$ , which can determine when the plasma is unstable [60]. In essence, this parameter calculates the integral power of all microwave frequencies emitted from

---

<sup>1</sup>The plasma became too unstable with large variation in the neutral gas pressure and very large bursts in x-ray energy.

the plasma, which are not reflections of the externally injected heating frequency. Once again, this method requires us to have a way to discriminate the frequencies of the microwave power coming from the source chamber.

In the absence of microwave spectrometry, we have to look at particle distributions emitted from the source. Perhaps the best way is to have a scintillator and photomultiplier tube detector nearby the source to detect bursts of bremsstrahlung radiation coming from the plasma chamber [81]. The plasma is then unstable when quasi-periodic bursts of x-ray radiation are detected. This creates other issues as the plasma does not produce battery-like steady states of charge diffusion, there will always be some fluctuation. Not to mention, the so-called 'CW mode' of the instability appears to be stable with minimal energy and current fluctuations, but by the theory of Shalashov et al., is still unstable [28, 73, 69]. So how do we know when the plasma is unstable? Is it when the beam currents begin fluctuation wildly, or steering is lost through the accelerator's injection line? Perhaps it is better to start with what we *expect* of a stable operating point. Figure 5.1 shows an example beam current and microwave power signal traces from a stable operating point, as measured on an oscilloscope. An 'unstable' operating point will then be defined by the effect of the instability upon the observed microwave power signal and extracted beam current.

The complexity of the electron and ion dynamics makes the application of plasma physics models to the extracted beam current exceptionally difficult. As such, the results shown here provide a general understanding of how the extracted beam current is affected by the instabilities to learn more about the concurrent state of the plasma. Beginning in section 5.3.1, a model for describing the transient beam current extracted from an unstable plasma is defined. Applying this model to observed beam currents 'defines' the stability of the different operating points used in the parameter sweeping measurements described in the previous section. Comparing the proposed model to the measured beam current from each of the operating points makes it easier to determine trends in the ion source plasma's changing stability characteristics. These results create 'stability maps' of the different measured parameter spaces. The maps and trends which result from them will be discussed in section 5.3.2. Sections 5.3.3, 5.3.5, and 5.3.6 then look at the effect that

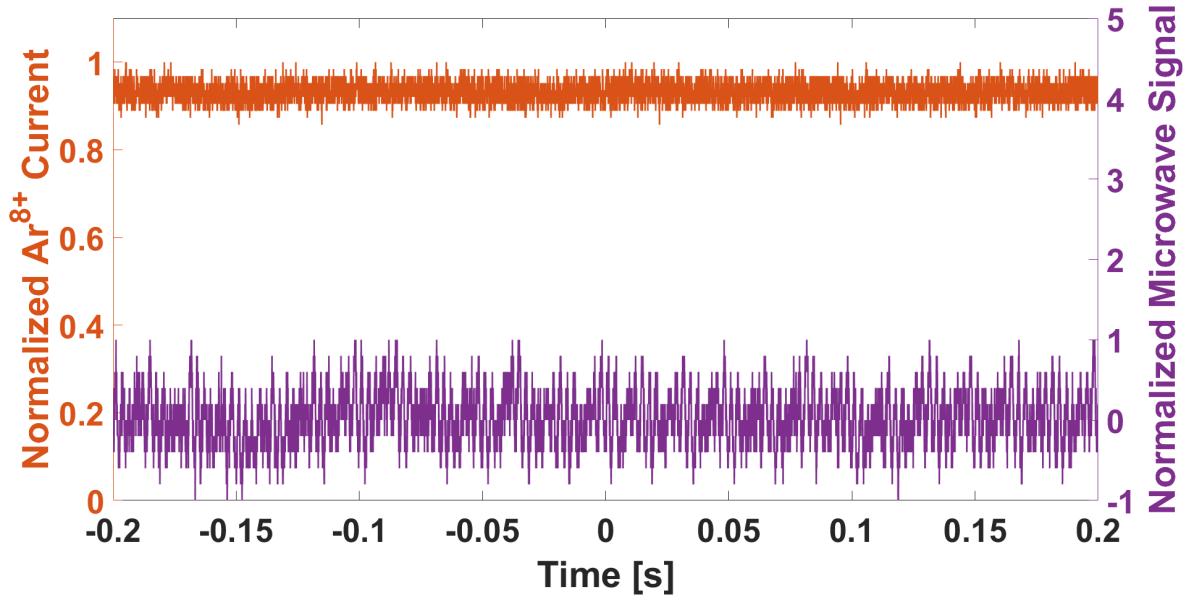


Figure 5.1: Example  $\text{Ar}_{8+}$  current (orange) and microwave power (purple) diagnostics while operating a stable ECR ion source plasma. The signals have been normalized to their maximum value over a 400 ms period. The extracted  $\text{Ar}_{8+}$  beam varies up to several percent even under stable conditions, in this case  $\delta I_{\text{Ar}_{8+}} \sim 7\%$ . The 60 Hz noise, and its harmonics, in the microwave signal results from the facility power source and is persistent throughout the lab.

specifically varying the extraction and radial field maxima and then the magnetic minimum has upon the extracted current. In this case, the same operating points described in chapter 4 provide a way to investigate the effect of the varying field extrema. This way, the trends found during the electron measurement can be more easily applied to trends discovered while observing the extracted ions. Finally, these results will be brought together in section 5.3.7 which will discuss what the results in sections 5.3.2, 5.3.3, 5.3.5, and 5.3.6 imply about the model introduced in section 5.3.1 and produce hypotheses as to the nature of the underlying physics behind it.

### 5.3.1 Beam Current Transient Profiles

Let us begin our discussion by looking at how the extracted beam current is affected in time by the instability. At the beginning of the instability, a burst of microwave energy, lasting for 100's - 1000's ns, is observed [81]. Almost immediately afterward, there is a rapid loss of electrons from confinement, most often seen as a burst of bremsstrahlung that can last for 100's us. It is

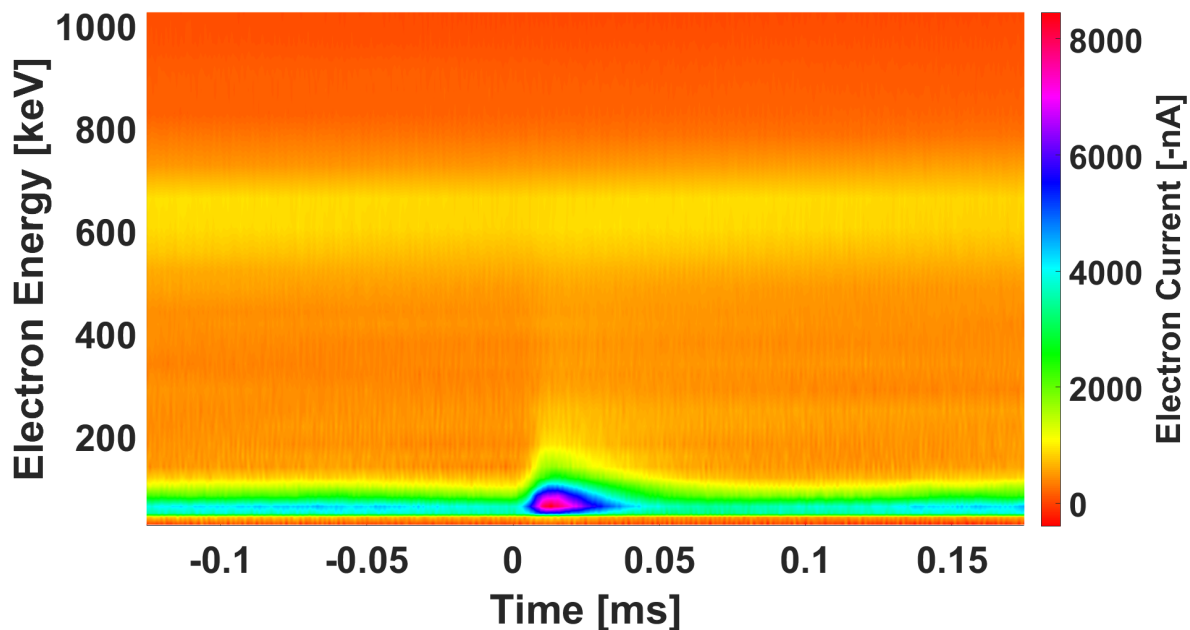


Figure 5.2: Multiple measurements of the transient current of escaping electrons, at different energies, were taken using an oscilloscope. The energy of electrons was selected by varying the energy in the dipole. The traces were then averaged 128 using the oscilloscopes averaging function. Those traces were put together, side-by-side, to plot the transient electron energy distribution. The peak current is 8460 nA at an electron energy of 62.88 keV, almost twice the central energy of the 'low energy peaks' seen in chapter 4. Higher energy electrons are minimally affected by the instability and the high energy peak is unaffected by the instability.

possible to observe this burst of electrons from confinement using the procedure for measuring the escaping electron distribution described in chapters 3 and 4. Figure 5.2 shows an example of such a measurement on SuSI's beamline. Following this loss of electrons from confinement, the extracted ion beam current will experience beam current variations on the order of 1 - 100's ms. The literature often focuses on operating points where a majority of the extracted high charge state beam current is lost [75, 83, 81]. However, the beam current can be affected by the instabilities in multiple different ways. Depending upon the ion source settings, high charge state currents can either increase or decrease on average. Furthermore, the time scale over which the average current changes depends upon the injected microwave power and magnetic field settings. Figure 5.3 shows a general transient profile model of the extracted beam current while operating with an unstable plasma.

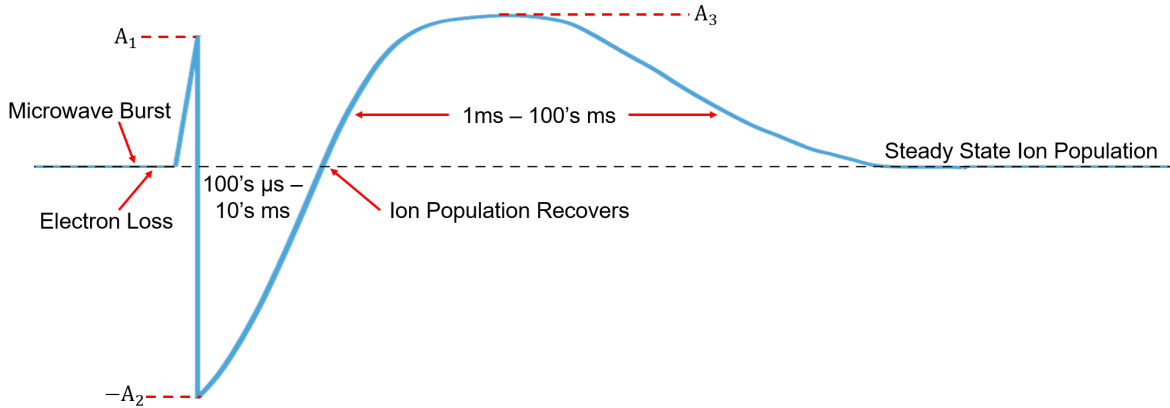


Figure 5.3: The general semi-quantitative model of the transient ion current during the unstable operation of an ECR ion source.  $A_1$ ,  $A_2$ , and  $A_3$  represent the amplitudes of the three predominant period of beam current variations that result from an instability event. The time scales are meant to represent general ranges over which the variation occurs. Not every instability event will result in all three and, under most circumstances, there is one predominant feature which best describes the beam. However, under rare circumstances, all three can occur simultaneously.

A burst of ions, described by  $(t_1, A_1)$ , follows the loss of electrons from confinement. The enhanced extraction of ions typically lasts for 100's  $\mu\text{s}$  to milliseconds and ends with a rapid decrease in current over 10's - 100's  $\mu\text{s}$ . This leads to  $(t_2, A_2)$  where the electron and ion populations have reached a minimum [85]. Over the next 1-10's ms, the hot electron and ion populations recover.  $A_2$  tends to be the largest for intermediate repetition frequencies (10 - 100 Hz). Under some circumstances, the extraction of high charge state currents increases above the steady-state level and reaching a maximum at  $(t_3, A_3)$ . After 1-100's ms, the current will exponentially decay back to the steady-state level until the next instability event.  $A_3$  tends to be the largest for lower frequencies (0.1 - 10 Hz). The decreasing frequency range described above is no coincidence, as high instability repetition frequencies prevent the accumulation of high charge state ions. Thus, operating points with lower instability repetition rates tend to have higher extracted currents, for both average and instantaneous currents.

The 'ion burst' effect is likely an instability driven afterglow event. Measurements have demonstrated that up to 10% of the electrons escape from the confinement following an instability event [85]. Other measurements estimate that enough electrons are lost to increase the plasma

potential to over 1 kV [83]. The 'ion loss' effect results from a loss in the ion population due to this burst, as well as a suppressed ionization rate. The physics of the 'over-extraction' effect is poorly understood and is one of the major focuses of this study.

In practice, the extracted beam current will usually, but not always, have a single dominant feature to it, either  $A_1$ ,  $A_2$ , or  $A_3$ . In many cases, one of the values is  $\sim 0$ . The different 'transient modes' can also be distinguished by the transient pattern of the microwaves emitted from the source chamber. Operating points where  $A_1$  is dominant tend to have a tall, broad burst of microwave power at the beginning of the instability. This burst decays roughly on the time scale of the recovering beam current. If  $A_2$  is the dominant amplitude, then it is most typical for there to be a massive burst of microwave power, which decays on an order of magnitude faster time scales than the beam current recovers. A 'hump' in the measured microwave power follows this burst and recovers with the beam current. Lastly, when  $A_3$  is dominant, the microwave seldom demonstrates a burst of microwave power. Rather, there is usually a 'hump' which decays with the recovering beam current. The 'hump' seen in the latter two cases likely results from a changing reflection coefficient in the plasma chamber, rather than plasma emission. The fact that it decays alongside the varying beam current, and therefore plasma density, supports this idea. Without a way of measuring the frequency of the emitted microwaves, it is impossible to be certain. Figures 5.4, 5.5, and 5.6 demonstrate all three 'transient modes', respectively.

If the time between instability events is shorter than the production time of high charge state ions, then the system's ability to produce those high charge state ions is effectively suppressed [83]. The plasma never reaches a steady-state that balances the production of ions between different atomic interactions and so there is a greater emphasis on the production of lower charge state ions. Ion burst and ion loss dominated transient modes are most often responsible for the observed decrease in ECRIS performance. Although, the repetition frequency is, by far, the most detrimental quantity to high charge state *production*, as it prevents the accumulation of ionizing electrons altogether.

Lastly, each of the modes acts differently across each of the extracted charge states. The ion burst and ion loss dominated modes respond with an increased average beam at low charge states

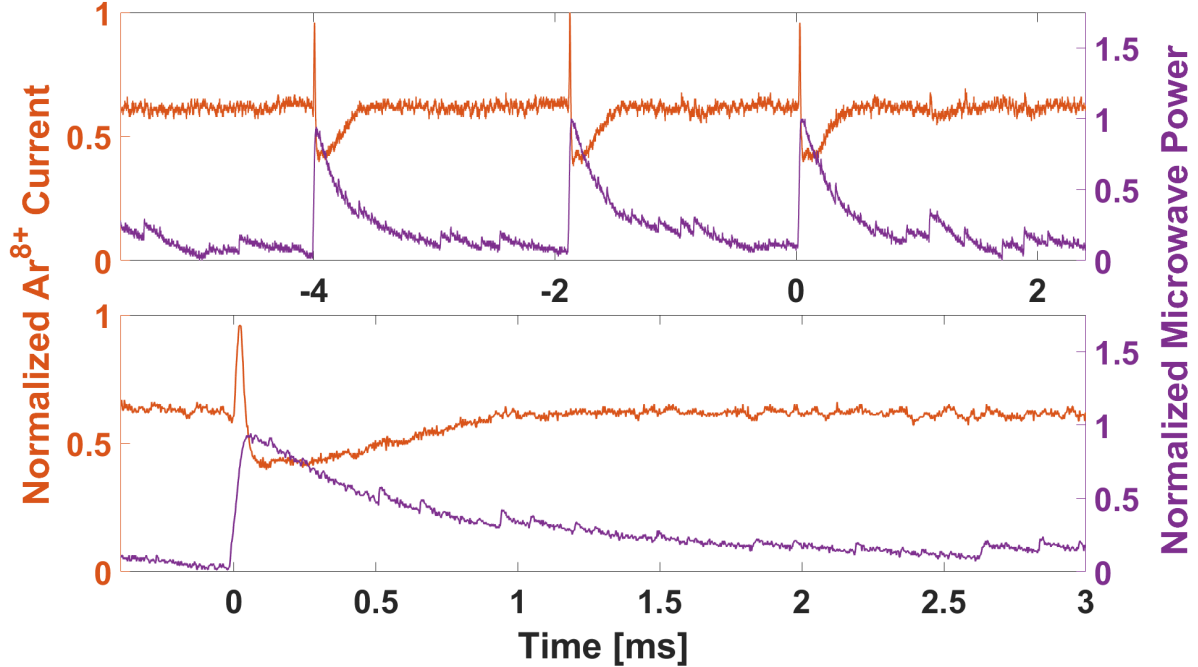


Figure 5.4: An example of the observed time resolved beam current (orange) and microwave power (purple) diagnostics seen during a transient profile dominated by the 'ion burst' effect. Notice how there is a large but short-lived burst in ions immediately after the burst of microwave energy. While present, the 'ion loss' profile is not dominant. The majority of the microwave power is emitted over a several milliseconds.  $\text{Ar}^{8+}$ ,  $B_{\text{min}} = 0.39 \text{ T}$ ,  $B_{\text{Hex,wall}} = 1.2 \text{ T}$ ,  $P_{\mu} = 150 \text{ W}$ ,  $p_{\text{Ar}} = 131 \text{ nTorr}$ .

and decreased beam at high charge states, as was reported in the literature [81]. The time scale of the low charge state enhancement matches that of the 'ion loss' at higher charge states. Interestingly the over-extraction mode demonstrates the opposite effect, decreasing the extracted beam current for low charge states and increasing it for high charge states. Once again, this occurs on the order of tens of milliseconds to seconds, being far longer than the observed losses of electrons from confinement. Figures 5.7, 5.8, and 5.9 show a comparison between the transient modes for  $\text{Ar}^{2+}$  and  $\text{Ar}^{8+}$ .

At first glance, the 'over-extraction' effect would appear to appreciably change the average extracted current from the ion source plasma, although in many cases this is not true. Figure 5.10 shows the extracted beam currents of argon ions from the 1+ to 12+ charge states. Notice how, despite the large increases in amplitude, the time over which that increase exists is relatively short.

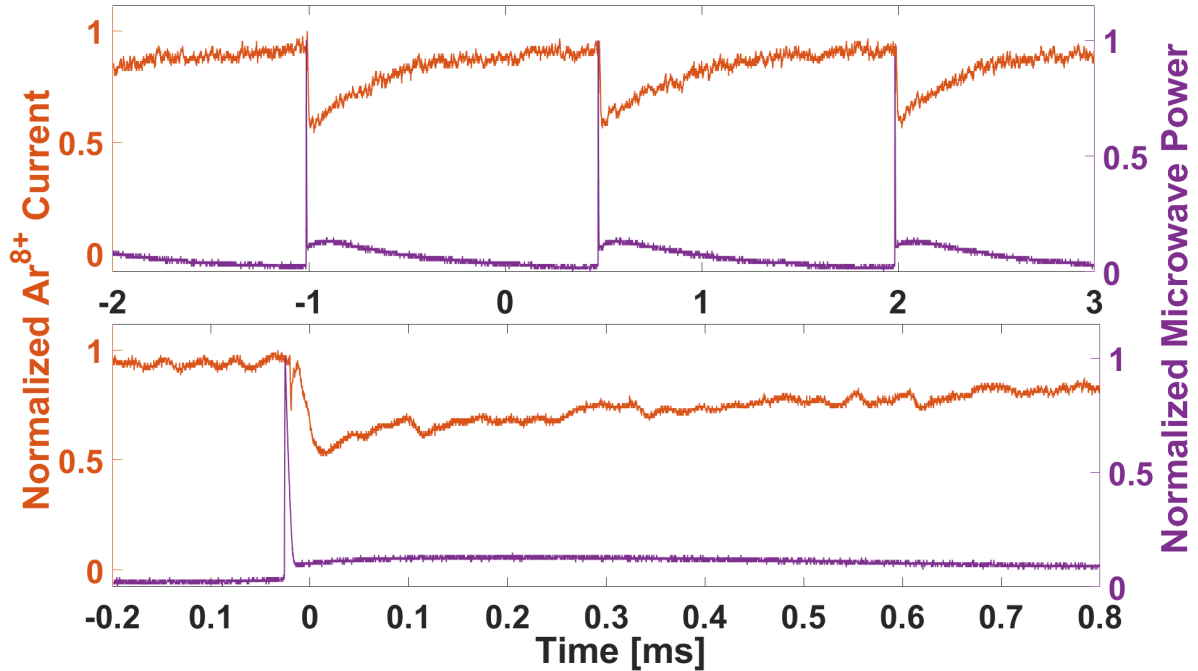


Figure 5.5: An example of the observed time resolved beam current (orange) and microwave power (purple) diagnostics seen during a transient profile dominated by the 'ion loss' effect. Notice that almost 50% of the steady state current is lost following the microwave burst. While present, the 'ion burst' profile is not dominant, and can only be seen by focusing on the 100's  $\mu\text{s}$  time scale (bottom plot). The majority of the microwave power is emitted over 10's  $\mu\text{s}$  and very rapidly decays. The 'hump' in the emitted power is believed to result from a changing reflection coefficient within the plasma chamber.  $\text{Ar}^{8+}$ ,  $B_{\text{min}} = 0.48 \text{ T}$ ,  $B_{\text{Hex,wall}} = 1.2 \text{ T}$ ,  $P_{\mu} = 250 \text{ W}$ ,  $p_{\text{Ar}} = 131 \text{ nTorr}$ .

Figure 5.11 emphasizes this by comparing the peak, average, and steady-state beam currents to one another for the same operating point. While the average extracted current is similar to the steady-state current, the peak current is substantially larger. The overall effect also scales with increasing charge state. The percentage increase in the extracted beam current can be increased by setting the bias disk voltage to positive values.

As a final remark, under certain conditions, it is possible to convert one transient mode into another, usually by varying the neutral gas pressure. Although common, the effect depends on the magnetic field and injected power sustaining the plasma. Figure 5.12 shows an example of this phenomenon by increasing the neutral gas pressure in the plasma chamber.



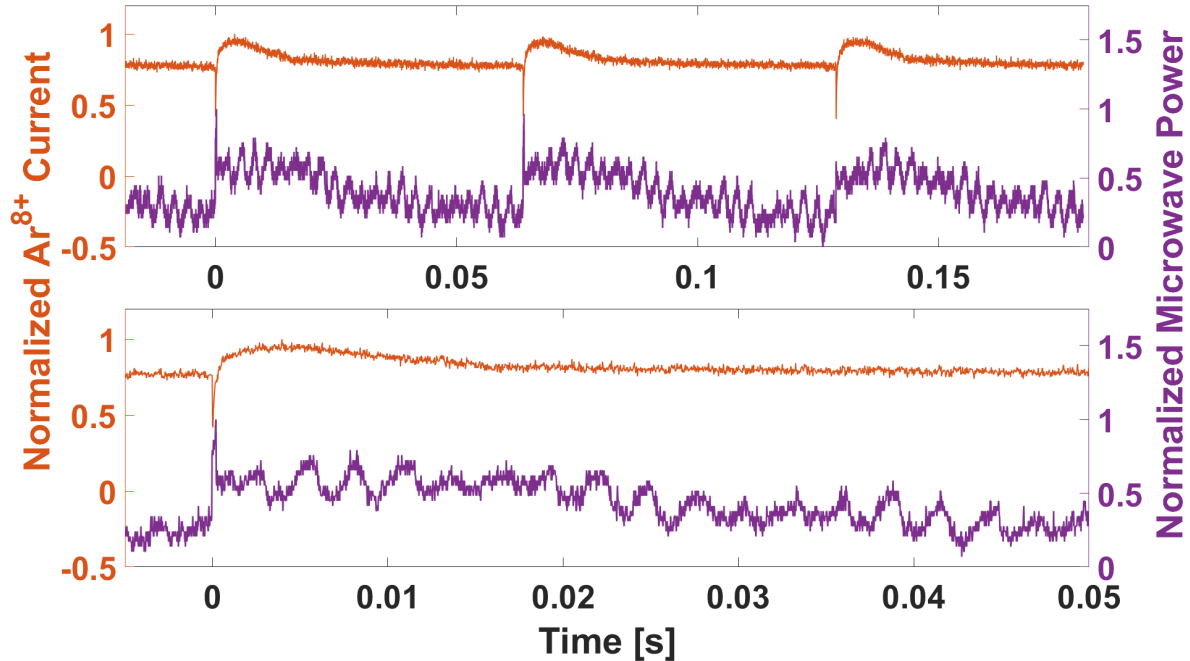


Figure 5.6: An example of the observed time resolved beam current (orange) and microwave power (purple) diagnostics seen during a transient profile dominated by the 'over-extraction' effect. Extracted Notice the almost 30% increase in extracted beam current following the exceptionally small burst of microwave power from the system. While present, the 'ion loss' profile is not dominant. Most importantly, this repetition frequency of this transient profile is on the order of 10's Hz, compared to figures 5.4 and 5.5 which are on the order of 100's Hz (top plot). The emitted microwave power is exceptionally small compared to the previous two cases (bottom plot). The 'hump' in the emitted power is believed to result from a changing reflection coefficient within the plasma chamber.  $\text{Ar}^{8+}$ ,  $B_{\min} = 0.48 \text{ T}$ ,  $B_{\text{Hex,wall}} = 1.32 \text{ T}$ ,  $P_{\mu} = 350 \text{ W}$ ,  $p_{\text{Ar}} = 131 \text{ nTorr}$ .

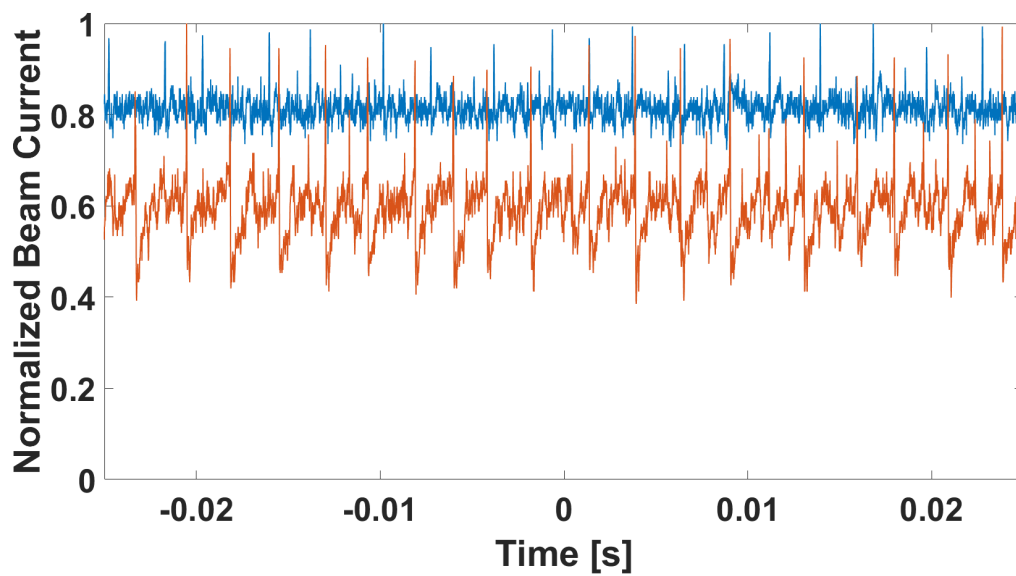


Figure 5.7: 'Ion burst' dominated transient profiles are characterized by an increase in the average extracted current at low charge states ( $\text{Ar}^{2+}$ , blue, top trace) and a decreased in the average extracted current for high charge states ( $\text{Ar}^{8+}$ , orange, bottom trace). Both current traces have been normalized to the largest value in their respective scope traces.  $B_{\text{min}} = 0.45 \text{ T}$ ,  $B_{\text{Hex,wall}} = 1.2 \text{ T}$ ,  $P_{\text{mu}} = 50 \text{ W}$ ,  $p_{\text{Ar}} = 141 \text{ nTorr}$ ,  $V_{\text{BD}} = -17 \text{ V}$ .

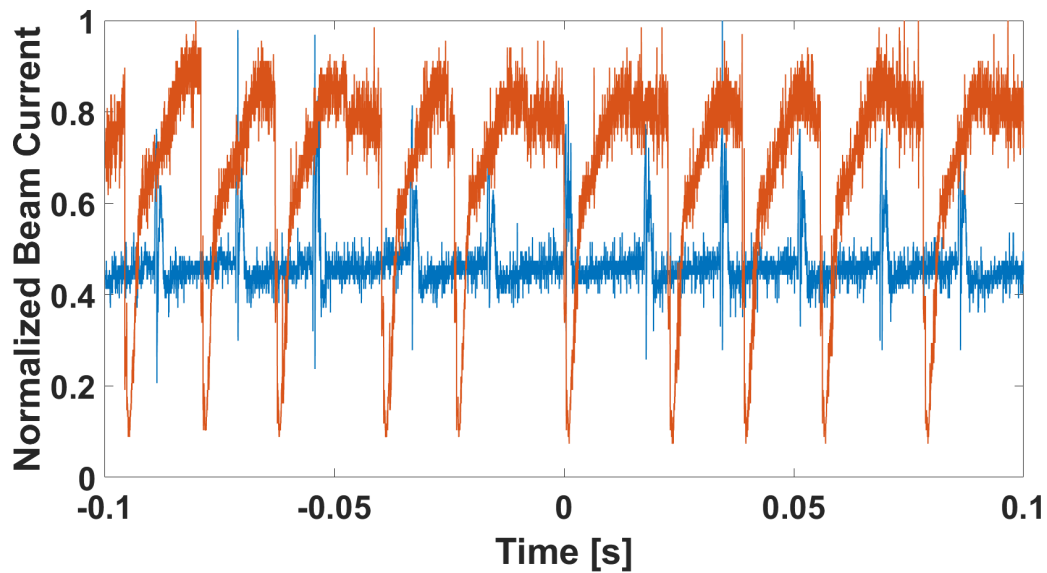


Figure 5.8: 'Ion loss' dominated transient profiles are characterized by an increase in the average extracted current at low charge states ( $\text{Ar}^{2+}$ , Blue, bottom trace) and a decreased in the average extracted current for high charge states ( $\text{Ar}^{8+}$ , orange, top trace). The plasma is also perturbed to a greater degree, compared to the 'ion burst' case. High charge state ion losses can be upwards of 80 - 100% of steady state beam currents, with much larger bursts in current for low charge states. Both current traces have been normalized to the largest value in their respective scope traces.  $B_{\min} = 0.52$  T,  $B_{\text{Hex,wall}} = 1.2$  T,  $P_{mu} = 350$  W,  $p_{\text{Ar}} = 123$  nTorr,  $V_{\text{BD}} = -17$  V.

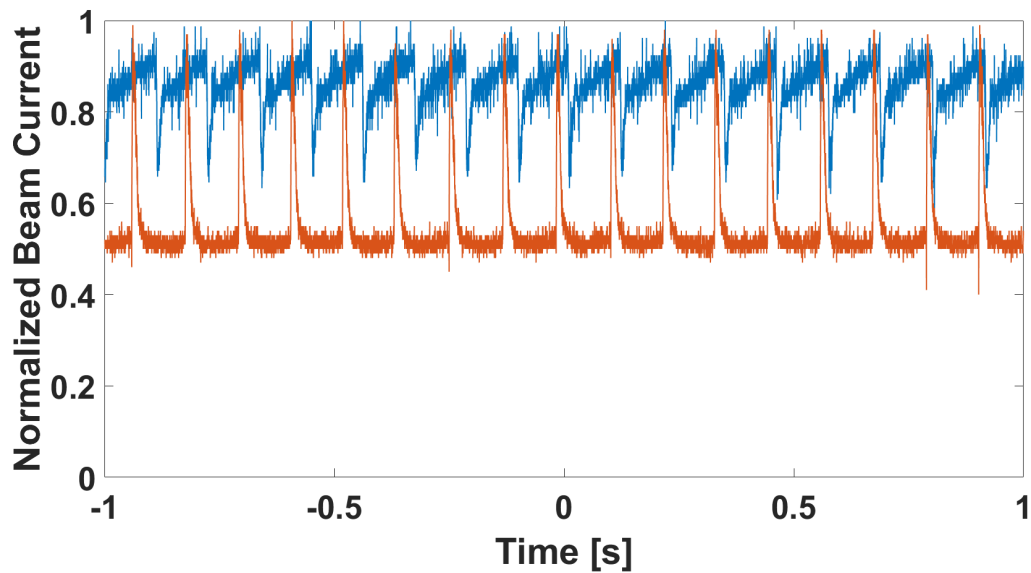


Figure 5.9: Unlike the other two cases, 'over-extraction' dominated transient profiles are characterized by a decrease in the average extracted current at low charge states ( $\text{Ar}^{2+}$ , blue, top trace) and an increase in the average extracted current for high charge states ( $\text{Ar}^{8+}$ , orange, top trace). Both current traces have been normalized to the largest value in their respective scope traces.  $B_{\min} = 0.42$  T,  $B_{\text{Hex,wall}} = 1.2$  T,  $P_{\mu} = 250$  W,  $p_{\text{Ar}} = 131$  nTorr,  $V_{\text{BD}} = 20$  V.

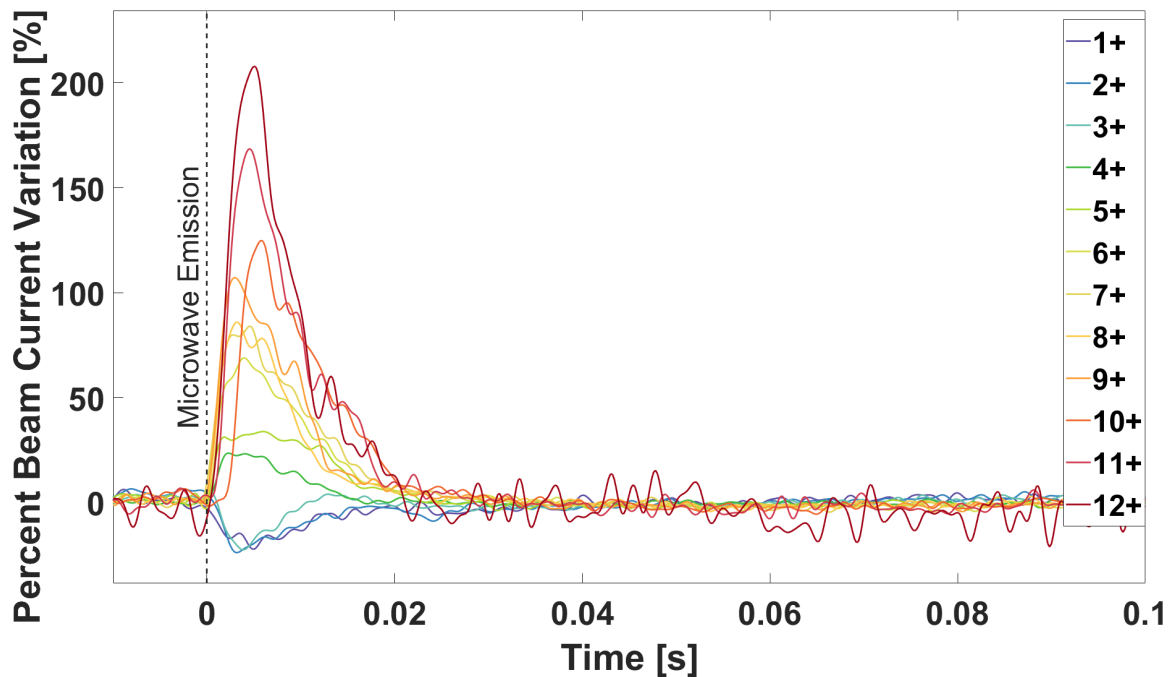


Figure 5.10:  $B_{\min} = 0.42$  T,  $B_{\text{Hex,wall}} = 1.2$  T,  $P_{\mu} = 350$  W,  $p_{\text{Ar}} = 131$  nTorr,  $V_{\text{BD}} = +20$  V.

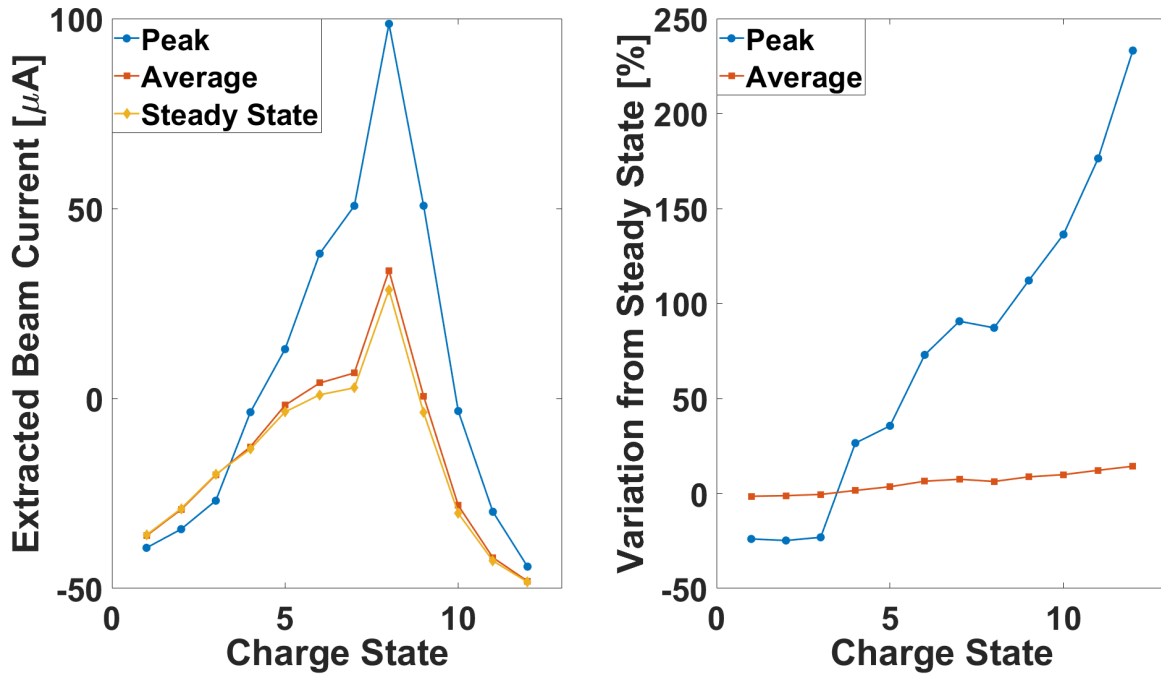


Figure 5.11:  $B_{\min} = 0.42$  T,  $B_{\text{Hex,wall}} = 1.2$  T,  $P_{\mu} = 350$  W,  $p_{\text{Ar}} = 131$  nTorr.  $V_{\text{BD}} = +20$  V

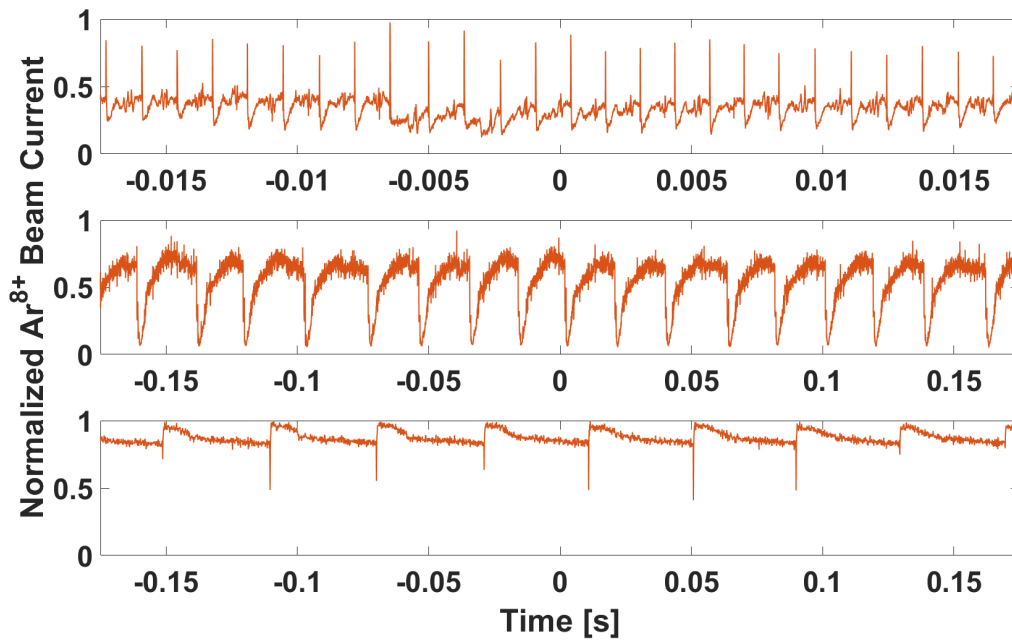


Figure 5.12: Increasing the neutral gas pressure often changes the dominant transient mode of the extracted beam current during unstable operating.  $B_{\min} = 0.515$  T,  $B_{\text{Hex,wall}} = 1.2$  T,  $P_{\mu} = 350$  W. (Top)  $p_{\text{Ar}} = 96$  nTorr, (Middle)  $p_{\text{Ar}} = 123$  nTorr, (Bottom)  $p_{\text{Ar}} = 159$  nTorr.

### 5.3.2 Stability Maps

It was initially believed that a 'stability threshold' existed in the magnetic field vs. power parameter space of the ion source [81]. A non-linear curve separated stable and unstable regions in this parameter space, and even small variations in either quantity could change the stability of the plasma. The neutral gas pressure, neutral species, and the source's extraction potential controlled the position of the threshold [83, 81]. Our first measurement attempted to find this threshold in SuSI, albeit over a broader set of magnetic field parameters. While the stability condition is still sensitive to small parameter changes, the system lacks a singular division between stable and unstable operating points.<sup>2</sup> Instead, large and distinct unstable regions surround a smaller number of stable operations points. A 2D color map replaced the stability threshold with the different colors representing different predominant transient modes (see 5.3.2). Figures 5.13, 5.14, 5.15, and 5.16 show the colormaps generated by sweeping the parameter space in the SuSI ECR ion source. Each figure shows the results from one set of pre-calculated magnetic field parameters, as described in section 5.2 and table 5.1, measured across three hexapolar field maxima.




Designation	Description	Color Reference
Stable	No Oscillation or Microwave Burst	
Ion Burst	100's-1000's Hz	
Ion Loss	10's-100's Hz	
Over-Extraction	0.1's - 10's Hz	

Table 5.2: Each of the different transient profiles has been assigned a different color. Generally speaking each of the different profiles exists over a different repetition frequency range, with ion burst dominated events occurring over the smallest time scale and over-extraction events occurring over the longest.

Immediately, we can see several trends that appear through the stability maps. The 'ion burst' transient profiles (light blue) prefer lower energy density operating points, with low magnetic fields or injected microwave powers. 'Ion loss' (yellow) and 'over-extraction' (red) transient profiles appear most often in operating points with large energy densities, high microwave powers and

<sup>2</sup>Even small changes to the plasma parameters can make the plasma unstable. In one case, increasing the current by 1 A, or about 2%, through a single solenoid coil induced a periodic instability.

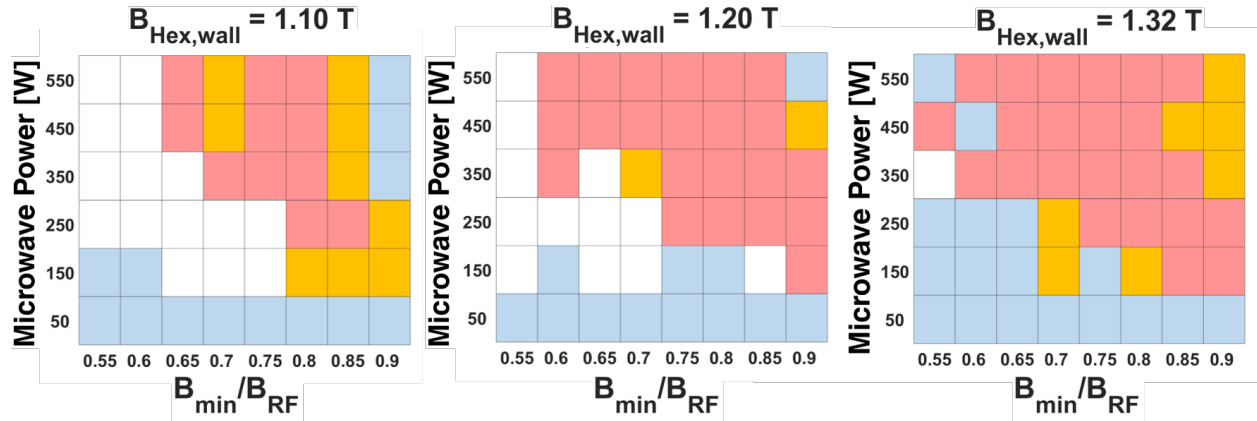


Figure 5.13: Field maps for operating points where the average injection and extraction maxima were above the limits described by the scaling laws:  $\overline{B}_{Inj,max}/B_{RF} \approx 4.09$ ,  $\overline{B}_{Ext,max}/B_{RF} \approx 2.02$ .

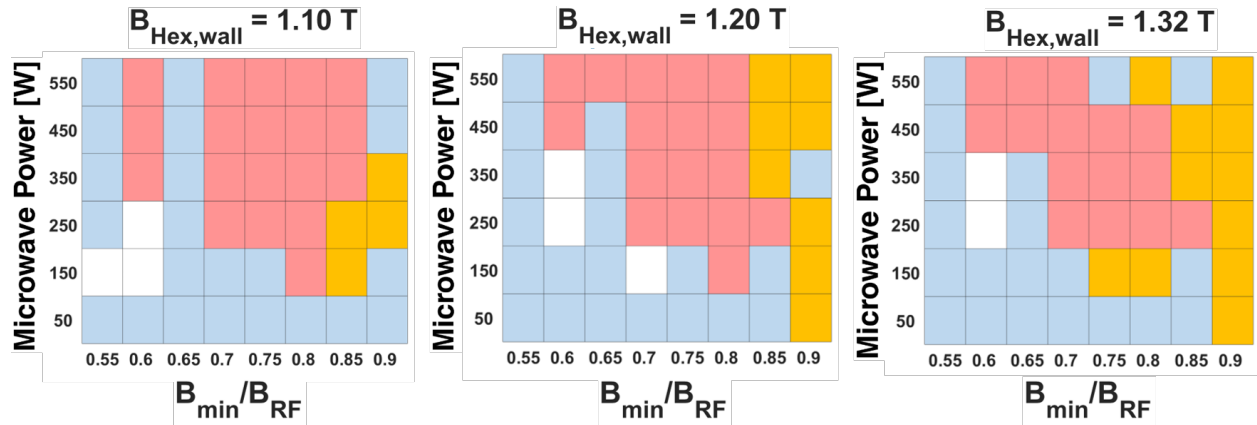


Figure 5.14: Field maps for operating points where the average injection and extraction maxima were above the limits described by the scaling laws:  $\overline{B}_{Inj,max}/B_{RF} \approx 3.71$ ,  $\overline{B}_{Ext,max}/B_{RF} \approx 1.78$ .

magnetic fields. The presence and size of a stable region depend upon the topology of the magnetic field. The measurement with the most stable regions appeared in range 1 (fig. 5.13), where the systems used the largest magnetic fields. In general, larger fields at extraction correlate with a higher number of stable operating points. Lower extraction fields appear to make the ion burst profile occur more regularly, even at higher energy densities. The injection side field appears not to affect the ion source plasma's stability characteristics, at least over the measured range.

Stronger magnetic fields at the wall correlate with an increased probability of the plasma

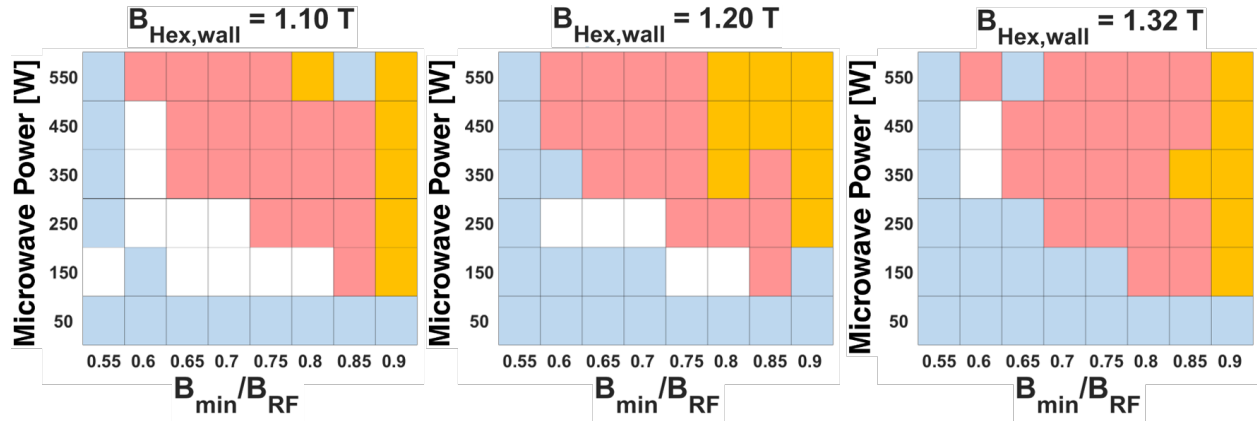


Figure 5.15: Field maps for operating points where the average injection and extraction maxima were above the limits described by the scaling laws:  $\overline{B}_{Inj,max}/B_{RF} \approx 3.43$ ,  $\overline{B}_{Ext,max}/B_{RF} \approx 1.95$ .

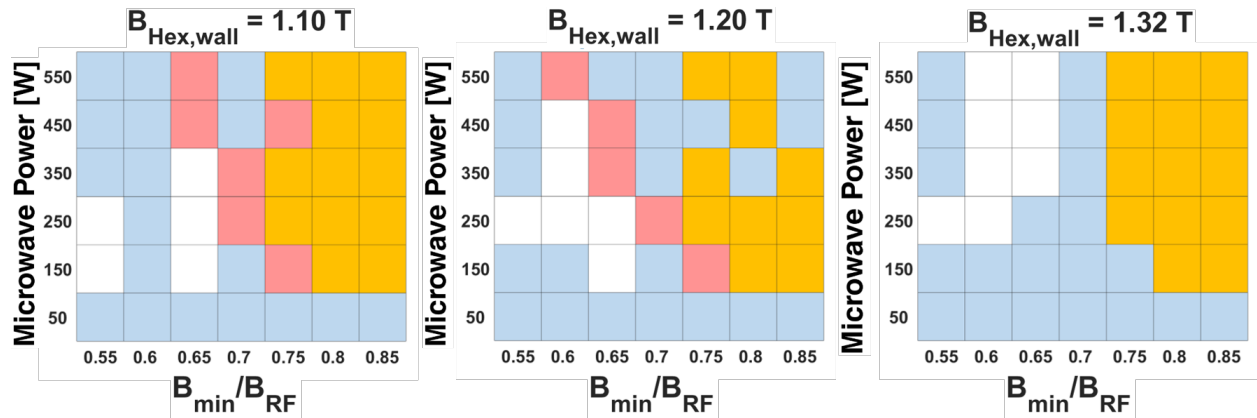


Figure 5.16: Field maps for operating points where the average injection maximum was larger than and extraction maxima small than the limits described by the scaling laws:  $\overline{B}_{Inj,max}/B_{RF} \approx 4.11$ ,  $\overline{B}_{Ext,max}/B_{RF} \approx 1.61$ .

becoming unstable, as can be seen in figures 5.13, 5.14, and 5.15. The larger hexapole field also causes the two unstable regions to converge upon the stable region. In some cases, almost all the stable operating points disappear at the highest hexapole field strength used. The final experimental range reversed that trend, as the increasing radial field correlated to an increase in the number of stable operating points. The third map in figure 5.16 lacks the presence of over-extraction operating points altogether. This case also happens to have the lowest field extraction field strength of all the operating points.



We can look at the difference in overall performance between the different experimental ranges as well. Figures 5.17, 5.18, and 5.19 show the percentage of operating points measured with average extracted  $\text{Ar}^{8+}$  currents larger than 60, 80, and 100  $\mu\text{A}$ , respectively. These plots were made by counting up the number of operating points with average currents and dividing them by the total number of operating points in each range ( $N = 48$ ). Recall that in range 4 all operating points with  $B_{\min}/B_{\text{RF}} = 0.9$  were excluded so that  $N_{\text{R4}} = 42$ . Through this metric, we see that the operating points with lower extraction maxima have, overall, larger extracted currents. The injection side magnetic field had little effect on the ion source's performance (ranges 1 and 4 have large injection side maximums). Increasing the radial field maximum had little, or at most an inconsistent effect, on these statistics, with no visible pattern seen between the different ranges. The number of stable operating points does not seem to play a role in determining trends in the average extracted current. Both operating ranges 1 and 3, which had the largest number of stable operating points, are consistently outperformed by ranges 2 and 4. The trend in range 4 is the most interesting by comparison as the lack of a large number of 'over-extraction' operating points does not affect the average extracted  $\text{Ar}^{8+}$  current. By comparison, ranges 1 and 3 have an abundance of 'over-extraction' operating points, but with very few operating points capable of boasting average extracted currents up to 100  $\mu\text{A}$ .

Conversely, figures 5.20, 5.21, and 5.22 show the percentage of operating points measured with maximum losses of  $\text{Ar}^{8+}$  currents larger than 30%, 60%, and 80%, respectively. The losses measure the decrease in current from the steady-state ion population in figure 5.3, making this a measure of  $A_2$ . Ranges 2 and 4, on average, lost the most current per instability event. Range 1, with the largest injection and extraction field maxima, performed best by this metric in large part due to the number of stable operating points within its parameter space. Overall, the number of operating points which lose more than 80% of their steady-state current is quite low, with a maximum of  $\sim 20\%$  in range 4. Ranges 2,3, and 4 all perform similarly by this metric.

Lastly, we can look for similar trends in the peak current across each of the experimental ranges. This is an indirect measure of either  $A_1$  or  $A_3$ , as the peak is determined without reference to the

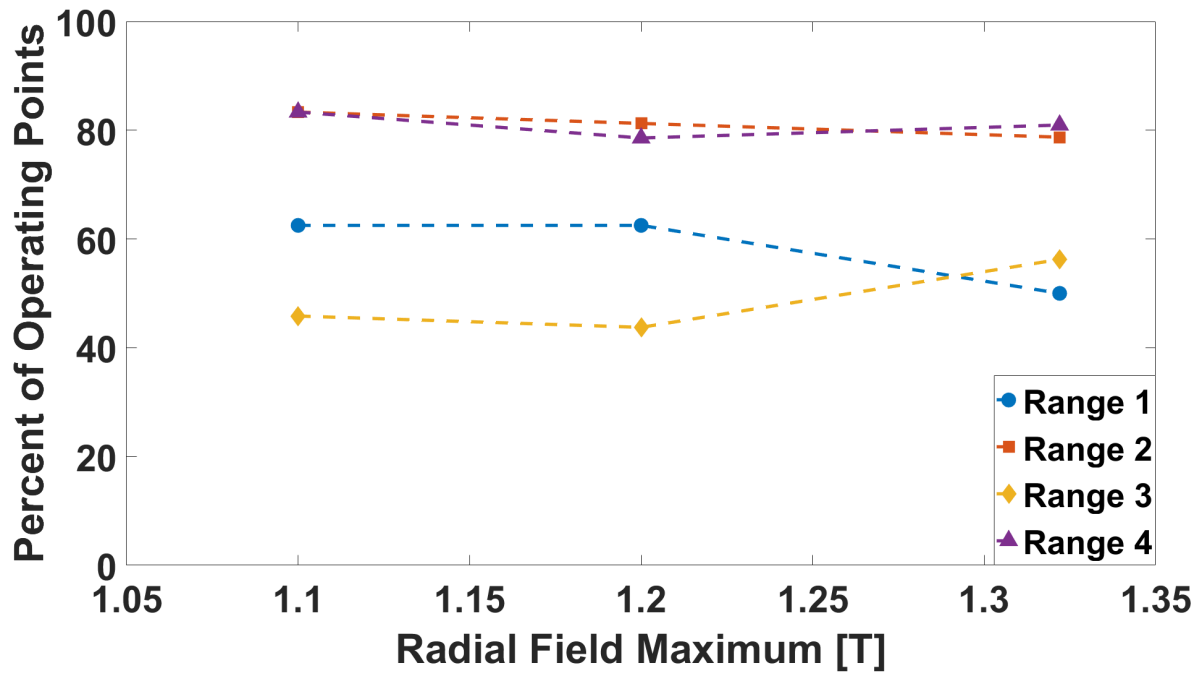


Figure 5.17: Percentage of measured operating points with average currents greater than  $60\mu A$ .

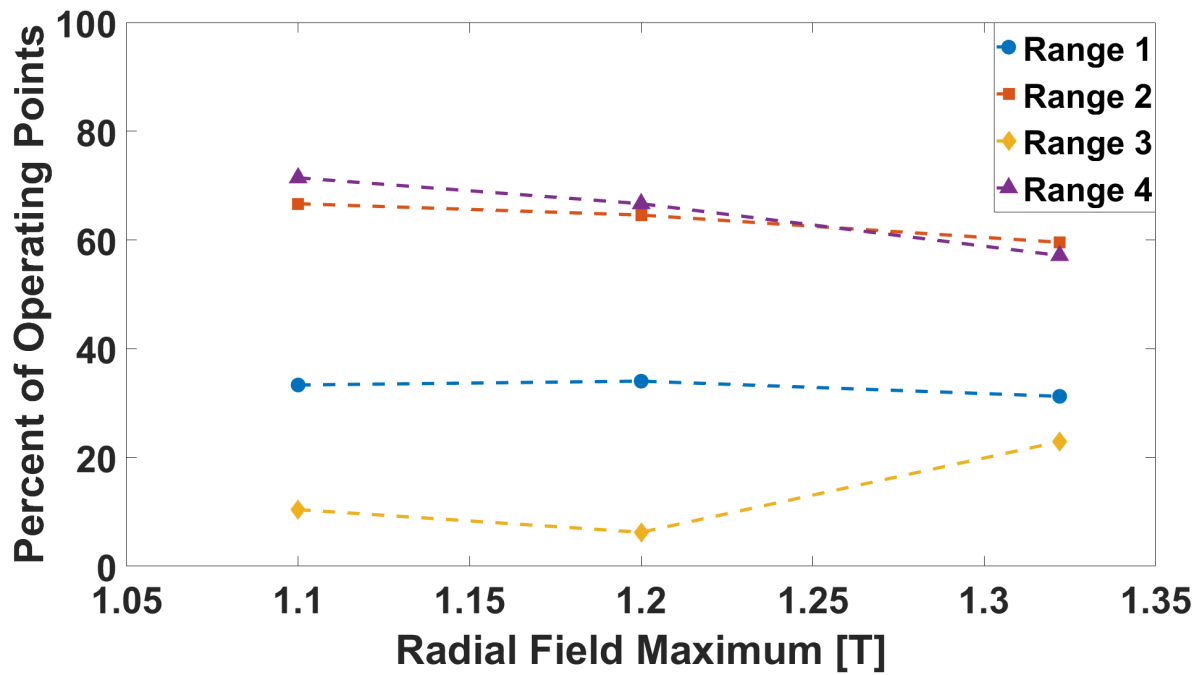


Figure 5.18: Percentage of measured operating points with average currents greater than  $80\mu A$ .

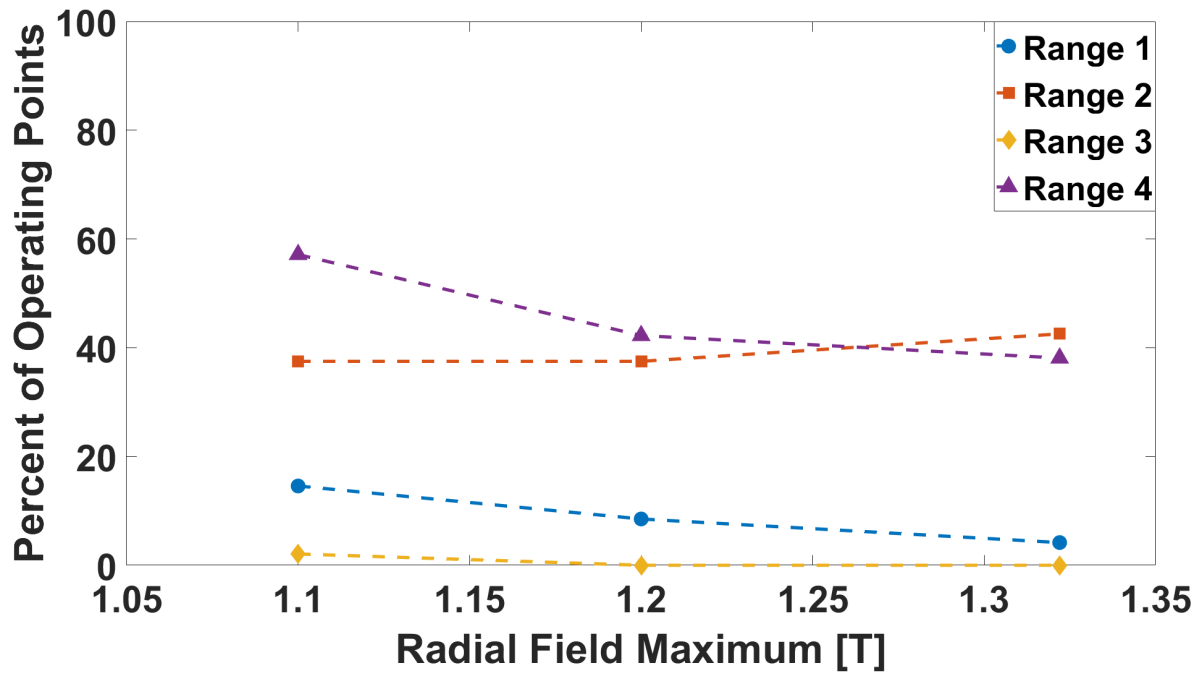


Figure 5.19: Percentage of measured operating points with average currents greater than  $100\mu A$ .

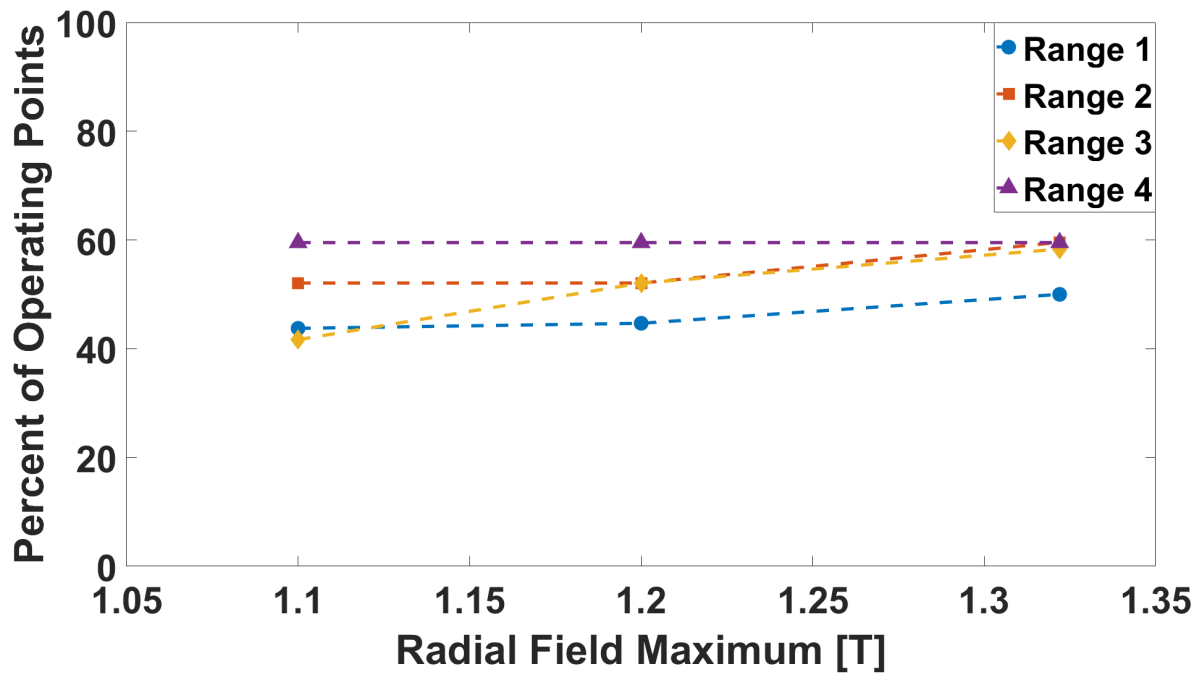


Figure 5.20: Percentage of measured operating points where beam loss was greater than 30%.

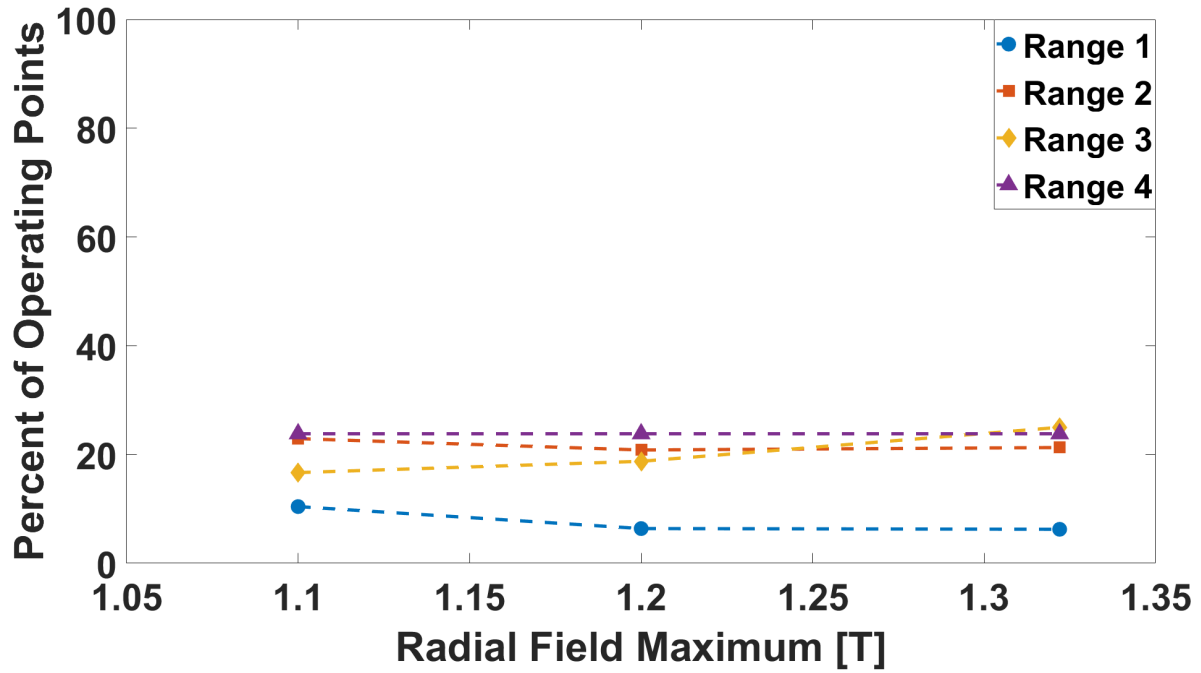


Figure 5.21: Percentage of measured operating points where beam loss was greater than 60%.

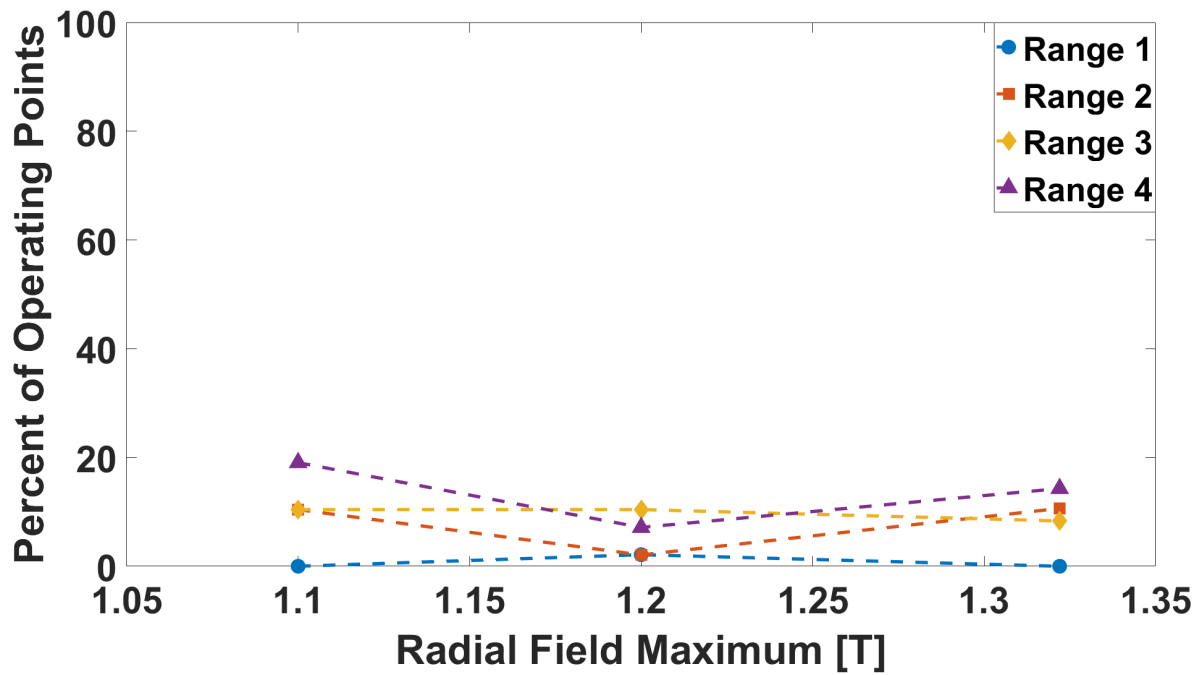


Figure 5.22: Percentage of measured operating points where beam loss was greater than 80%.

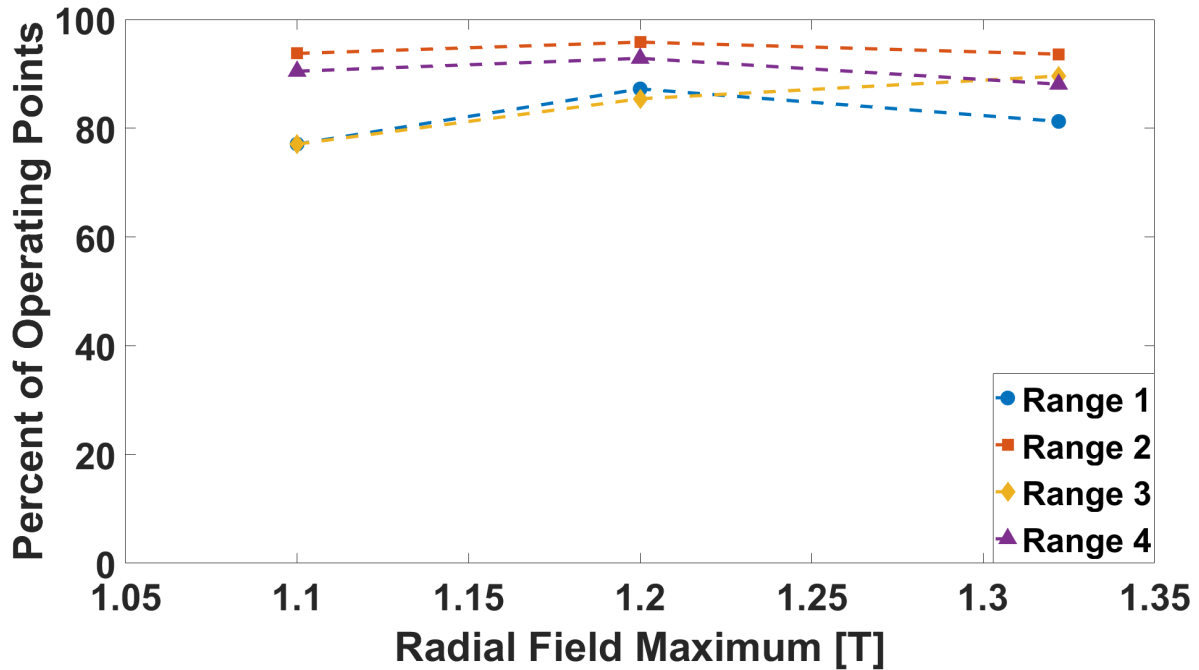


Figure 5.23: Percentage of measured operating points with peak currents greater than  $60\mu\text{A}$ .

steady-state current or the microwave burst (the distinction between 'ion burst' and 'over-extraction' is ignored). Figures 5.23, 5.24, and 5.25 show the percentage of operating points with peak extracted  $\text{Ar}_{8+}$  currents larger than 60, 80, and  $100\mu\text{A}$ , respectively. Once again, ranges 2 and 4 perform the best by this metric, with most of their peak currents being greater than  $100\mu\text{A}$ .

Together, these metrics seem to indicate that having a lower magnetic maximum at extraction has a large effect upon the stability of the plasma. While increasing the hexapole field made the plasma more unstable overall, its effect upon the average ion source performance appears negligible, at least across the measured parameter ranges. As mentioned previously, ranges 2 and 4 were designed with extraction fields close to or less than what is prescribed by the scaling laws (sec. 2.3.4). There is no doubt that the extraction side field affected both the performance and overall stability characteristics of the plasma. The magnetic minimum also plays a very large role in determining how the plasma will become unstable, with there being a clear correlation between the energy density of the plasma and how the instability affects the extracted beam current. The next section focuses on direct measurements of the changes that varying plasma parameters cause

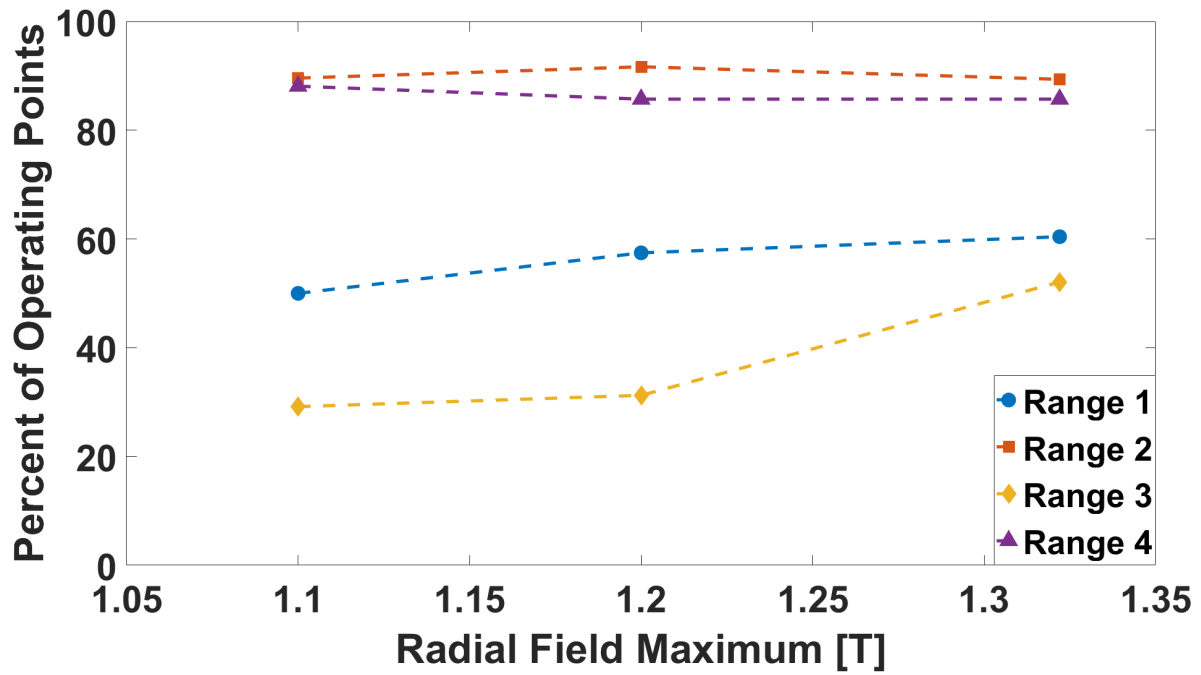


Figure 5.24: Percentage of measured operating points with peak currents greater than  $80\mu A$ .

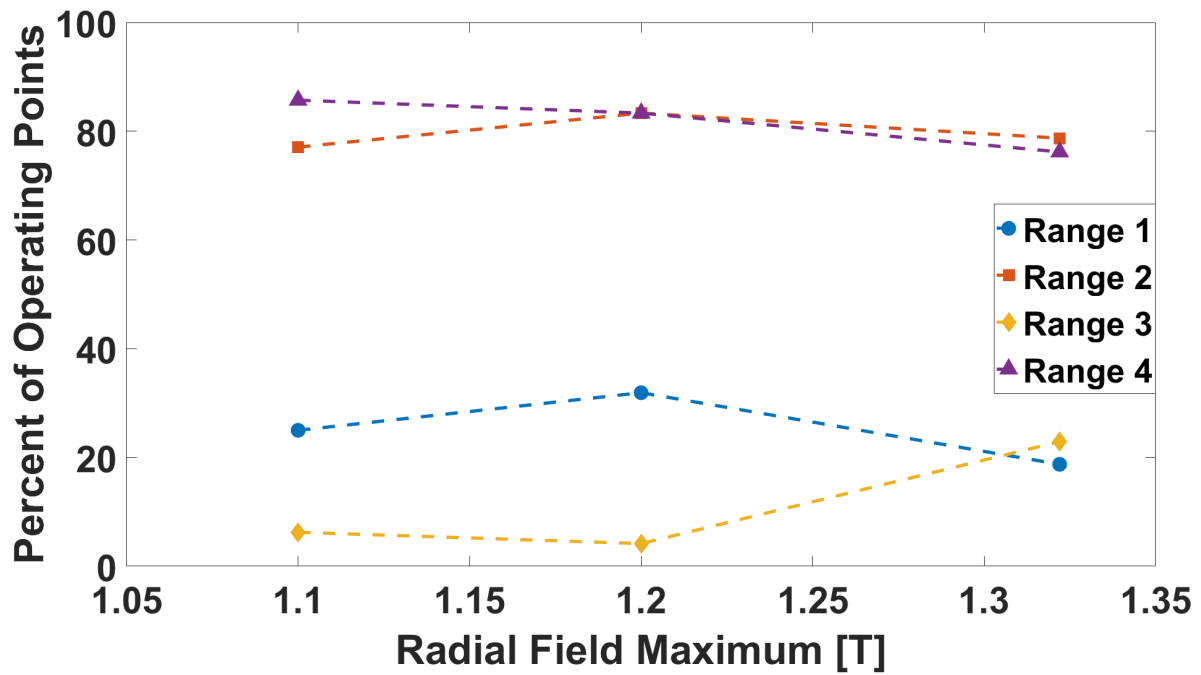


Figure 5.25: Percentage of measured operating points with peak currents greater than  $100\mu A$ .

by directly measuring the transient beam current profile on an oscilloscope.

### 5.3.3 Varying the Hexapolar Field Maximum

We begin our discussion by looking at the radial field's effect upon the measured ion transient profile. The same operating points used in chapter 4 were used here with two notable exceptions. First, the extraction voltage and einzel lens voltages were fixed at 20 kV; however, the puller remained grounded. Secondly, the correct 'control' operating point was used ( $B_{\min} = 0.4$  T,  $B_{\text{Inj,max}} = 2.367$  T,  $B_{\text{Ext,max}} = 1.100$  T,  $P_{\mu} = 350$  W, Pressure = 213 nTorr,  $B_{\text{Hex,wall}} = 1.217$  T).<sup>3</sup>

Figure 5.26 shows the beam current for different hexapole field strengths. The 'ion burst' effect dominates the beam current's transient profile, with  $A_1 > A_2 > A_3 = 0$ . Overall, changing the hexapole had a negligible qualitative effect over the measured range. Quantitatively, the increasing hexapole field saw the beam current decrease on average. Figure 5.27 demonstrates this more clearly through the maximum, average, and minimum currents measured over a 200 ms period. Across most of the domain, the maximum and minimum currents also begin to converge towards an increasingly smaller average current.

The microwave signal also shows similar trends, with the repetition frequency and amplitude of large microwave bursts (large area beneath peak in microwave power) increasing with the hexapolar field. This gives way to a gradual decline in the maximum burst amplitude, as seen in figure 5.28. The microwave diagnostic shows an increase in the repetition frequency of the instabilities, with relatively little change compared to the plasma's response to a changing extraction maximum. The Fourier transform of the microwave power signal, in figure 5.29, shows the shift in the frequency content of the emitted microwave signals more clearly. Initially, the power across all frequencies increases but then the signal appears to settle, but then begins to settle at higher field strengths. Figure 5.30 further clarifies this, showing that average microwave power is insensitive to the hexapole field.

---

<sup>3</sup>The wrong operating point was used for the 'control' operating point during the electron measurement.

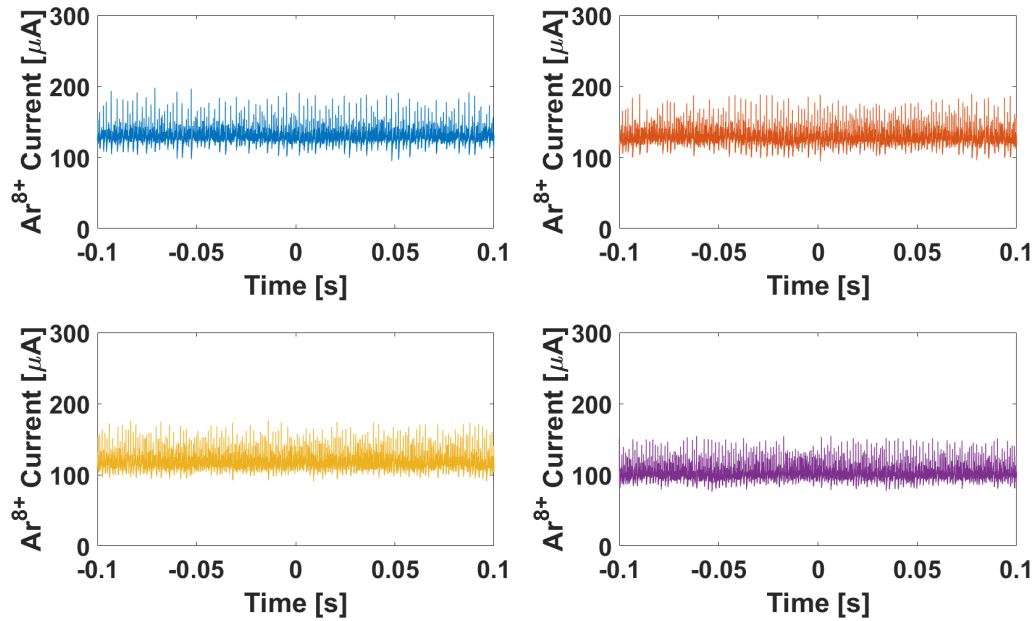


Figure 5.26:  $\text{Ar}^{8+}$  beam current for a varying hexapole field maxima: (Top left)  $B_{\text{Hex,wall}} = 1.12$  T, (Top right)  $B_{\text{Hex,wall}} = 1.18$  T, (Bottom left)  $B_{\text{Hex,wall}} = 1.22$  T, (Bottom right)  $B_{\text{Hex,wall}} = 1.28$  T.  $B_{\text{min}} = 0.4$  T,  $P_{\mu} = 350$  W,  $p_{\text{Ar}} = 213$  nTorr. Signals have been treated with a digital low pass filter using the Matlab signal processing toolkit, with a cutoff frequency of 333 kHz.

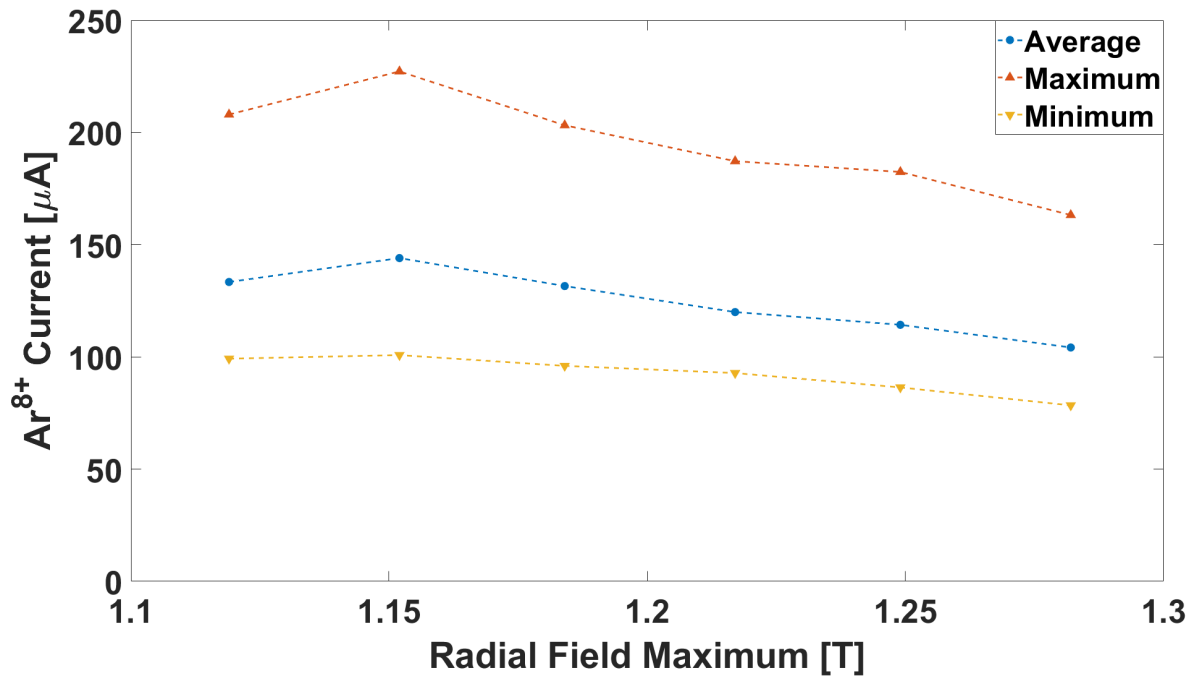


Figure 5.27: Average, maximum, and minimum beam current measurements of extracted  $\text{Ar}^{8+}$  beam current for varying hexapole field maxima:  $B_{\text{min}} = 0.4$  T,  $P_{\mu} = 350$  W,  $p_{\text{Ar}} = 213$  nTorr.



In chapter 4, the electron measurement demonstrated that the increasing hexapole field had little effect on the system's energy content, but did seem to increase the diffusion of hot electrons out of the system. Interestingly, the increased electron current coming from the plasma (see figure 4.24) is not reflected with an increase in extracted ions, as we would expect if the ions were diffusing ambipolarly. There is also little change to the plasma except for a slow decrease in the extracted current at higher field strengths. Instability events do appear to occur more often, which may indicate an increase in the density of electrons outside of the loss cone. This could explain the increased current seen in chapter 4, as the increased current could result from more wave-particle interactions between well-confined electrons and excited waves. The better-confined electrons could also output more microwave power into the background plasma. Alternatively, an increased axial diffusion rate, resulting from changing confinement parameters, could globally affect the non-linear interactions of the electrons with the excited waves. Further study of this effect may require more sophisticated diagnostics to fully understand the effect the hexapole field plays on the system.

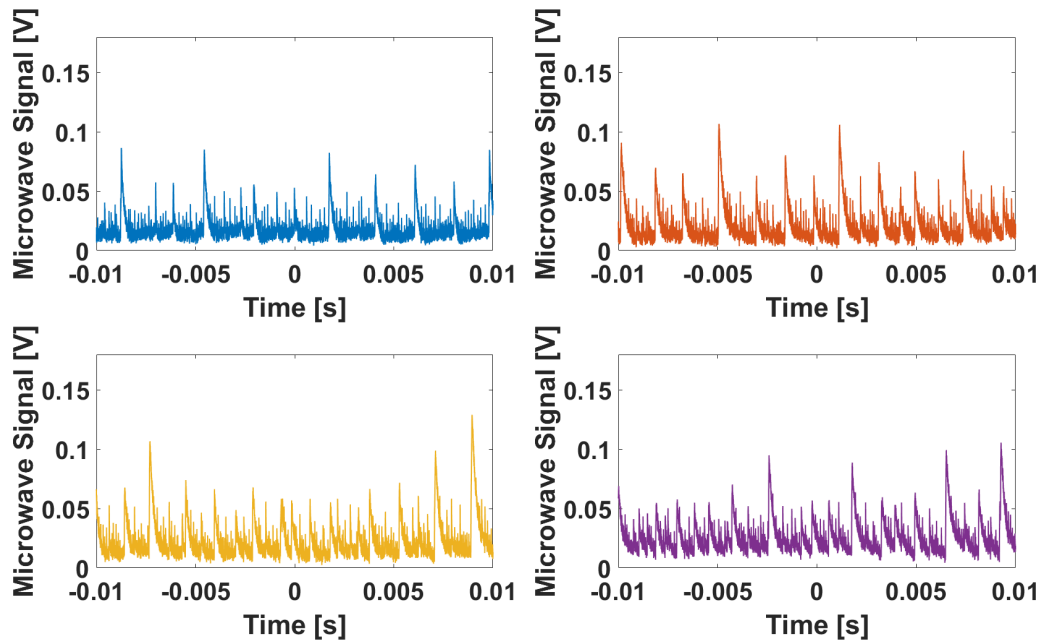


Figure 5.28: Microwave power signals for a varying hexapole field: (Top left)  $B_{\text{Hex,wall}} = 1.12$  T, (Top right)  $B_{\text{Hex,wall}} = 1.18$  T, (Bottom left)  $B_{\text{Hex,wall}} = 1.22$  T, (Bottom right)  $B_{\text{Hex,wall}} = 1.28$  T.  $B_{\text{min}} = 0.4$  T,  $B_{\text{Ext,max}} = 1.1$  T,  $P_{\mu} = 350$  W,  $p_{\text{Ar}} = 213$  nTorr. Microwave power has been offset by its minimum value, over the entire 100 ms measurement period, to account for the AC coupling of the oscilloscope. Signals have been treated with a digital low pass filter using the Matlab signal processing toolkit, with a cutoff frequency of 333 kHz.

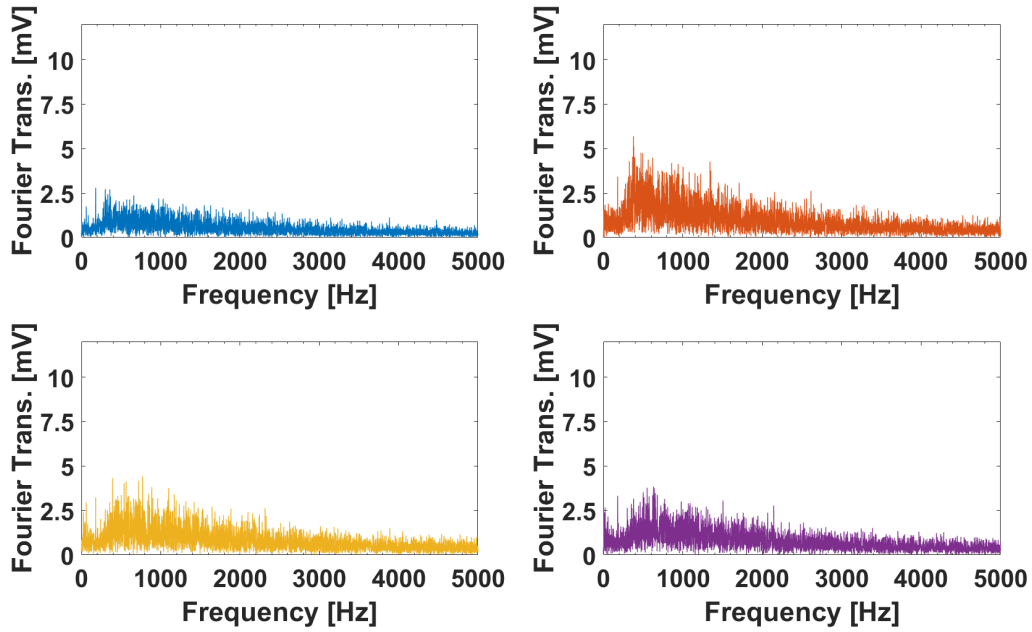


Figure 5.29: Fourier transform of the microwave power signals emitted from the ion source for a varying hexapolar field: (Top left)  $B_{\text{Hex,wall}} = 1.12$  T, (Top right)  $B_{\text{Hex,wall}} = 1.18$  T, (Bottom left)  $B_{\text{hex,max}} = 1.22$  T, (Bottom right)  $B_{\text{hex,max}} = 1.28$  T.  $B_{\text{min}} = 0.4$  T,  $B_{\text{Ext,max}} = 1.1$  T,  $P_{\mu} = 350$  W,  $p_{\text{Ar}} = 213$  nTorr.

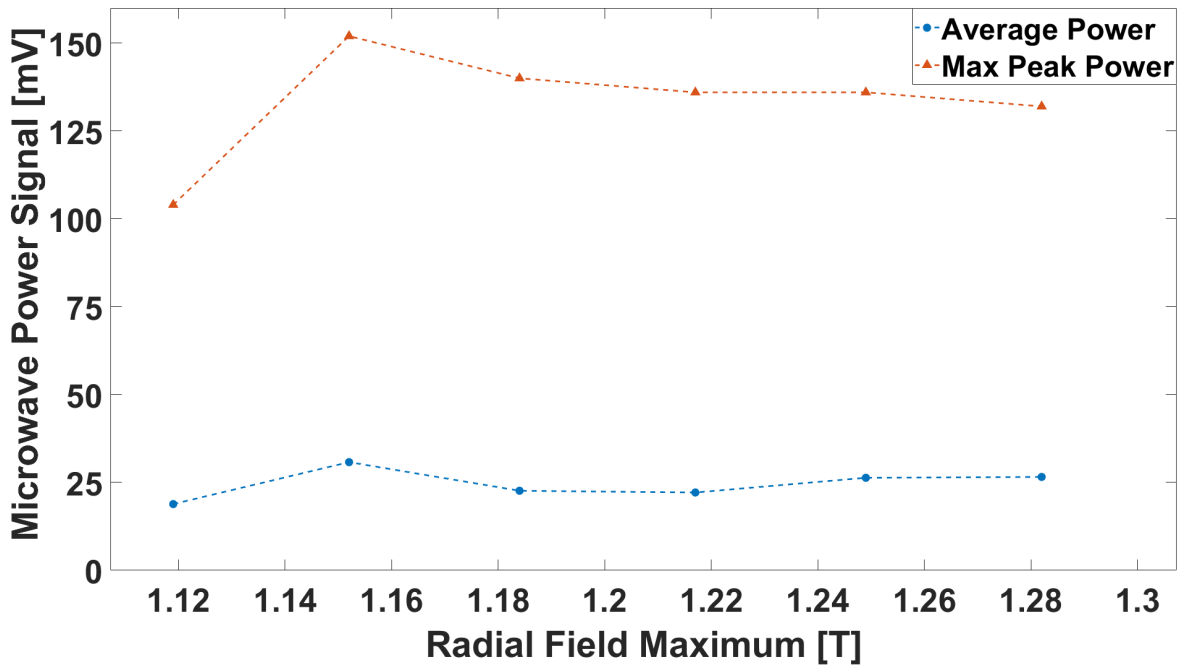


Figure 5.30: Average and maximum peak microwave power for a varying hexapole field maxima:  $B_{\text{min}} = 0.4$  T,  $B_{\text{Ext,max}} = 1.1$  T,  $P_{\mu} = 350$  W,  $p_{\text{Ar}} = 213$  nTorr.

### 5.3.4 Effect of the Injection Side Magnetic Field upon Plasma Stability

In chapter 4, it was shown how little of an effect the injection side magnetic field had upon the diffusion of electrons out of the system. The stability maps reinforced this conclusion, demonstrating that the injection side magnetic field maximum appears largely uncorrelated to the plasma's stability or performance, at least over the measured domains. By looking specifically at the ion beam current, we do see a degree of meaningful change for the first time. Increasing  $B_{\text{Inj,max}}$  over the domain described in chapter 4, causes the extracted beam current to increase very slowly. Initially, the 'ion burst' effect dominates current transience. As the field increases, both  $A_1$  and  $A_2$  begin to increase, though the 'ion burst' effect remains the predominant feature of the transient profile. Figures 5.31 and 5.32 show how the current varies across the magnetic field domain. The increase in burst amplitude correlates with a decrease in the repetition frequency of the instabilities. As the injection side field increases, the maximum and minimum measured currents begin diverging from the average extracted current.

Once again, the effect on the repetition frequency is easiest to see in figures 5.33 and 5.34, which shows the microwave power signals and their respective Fourier transforms for selected operating points. While the microwave power peak amplitude and signal frequency content generally decrease over the measured domain, the average emitted power does appear constant. Figure 5.35 shows how both the maximum and average microwave power are largely unaffected by an increasing injection side maximum. This trend is a result of the width of individual microwave bursts increasing, despite the decrease in their amplitude.

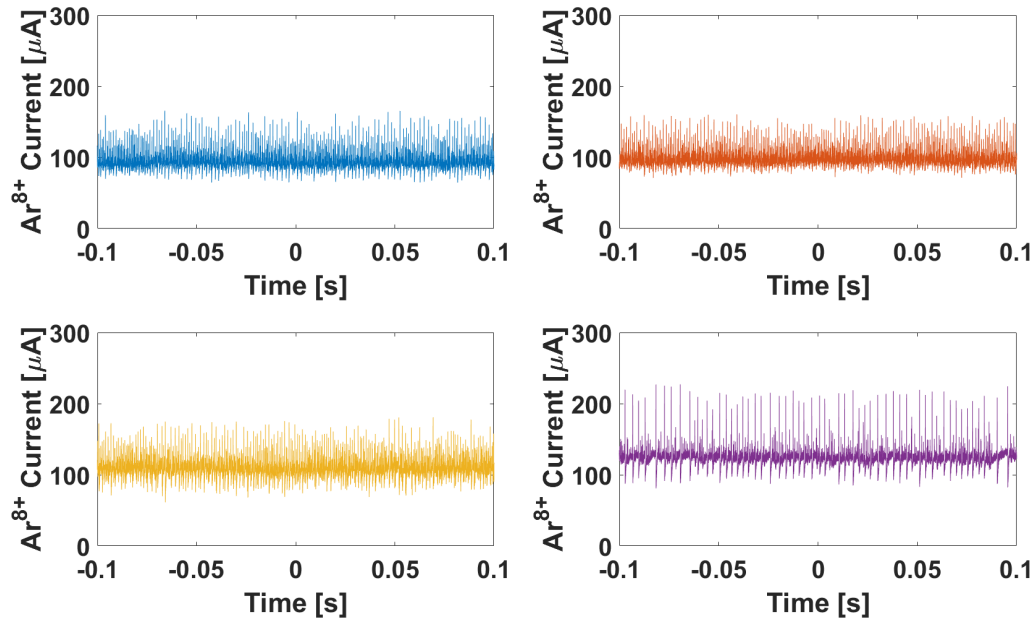


Figure 5.31:  $\text{Ar}^{8+}$  beam current for a varying injection field maxima: (Top Left)  $B_{\text{Inj,max}} = 2.20$  T, (Top Right)  $B_{\text{Inj,max}} = 2.33$  T, (Bottom Left)  $B_{\text{Inj,max}} = 2.45$  T, (Bottom Right)  $B_{\text{Inj,max}} = 2.58$  T.  $B_{\text{min}} = 0.4$  T,  $P_{\mu} = 350$  W,  $p_{\text{Ar}} = 213$  nTorr. Signals have been treated with a digital low pass filter using the Matlab signal processing toolkit, with a cutoff frequency of 333 kHz.

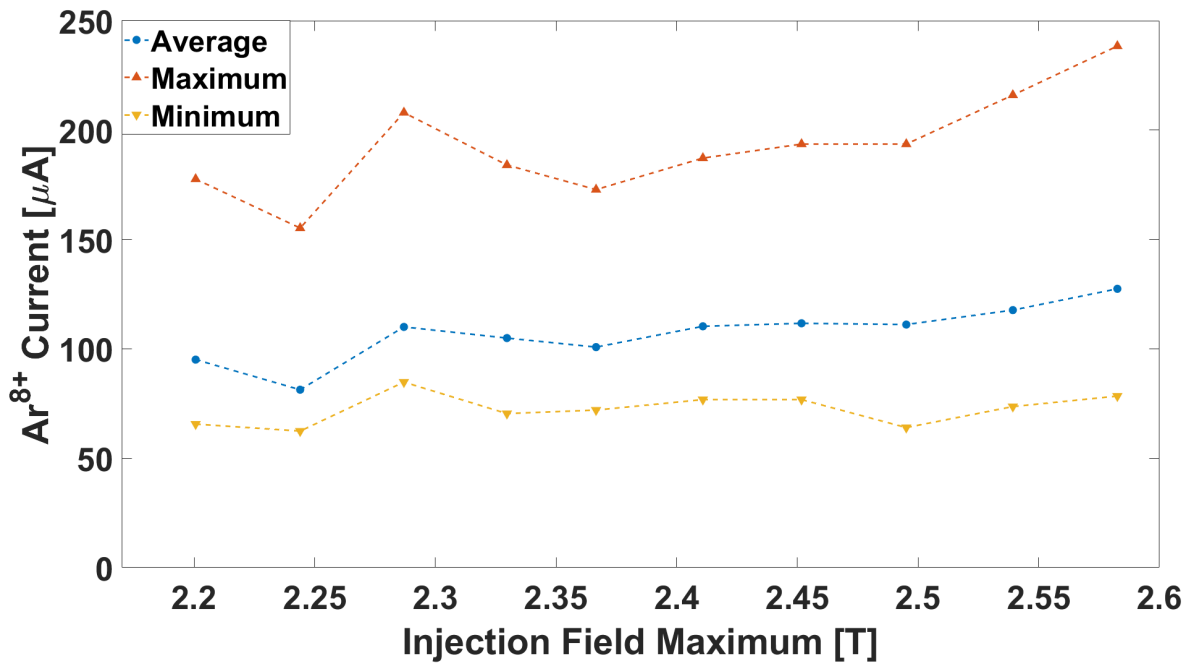


Figure 5.32: Average, maximum, and minimum  $\text{Ar}^{8+}$  beam currents, measured over a 100 ms period, for a varying injection field maxima:  $B_{\text{min}} = 0.4$  T,  $P_{\mu} = 350$  W,  $p_{\text{Ar}} = 213$  nTorr.

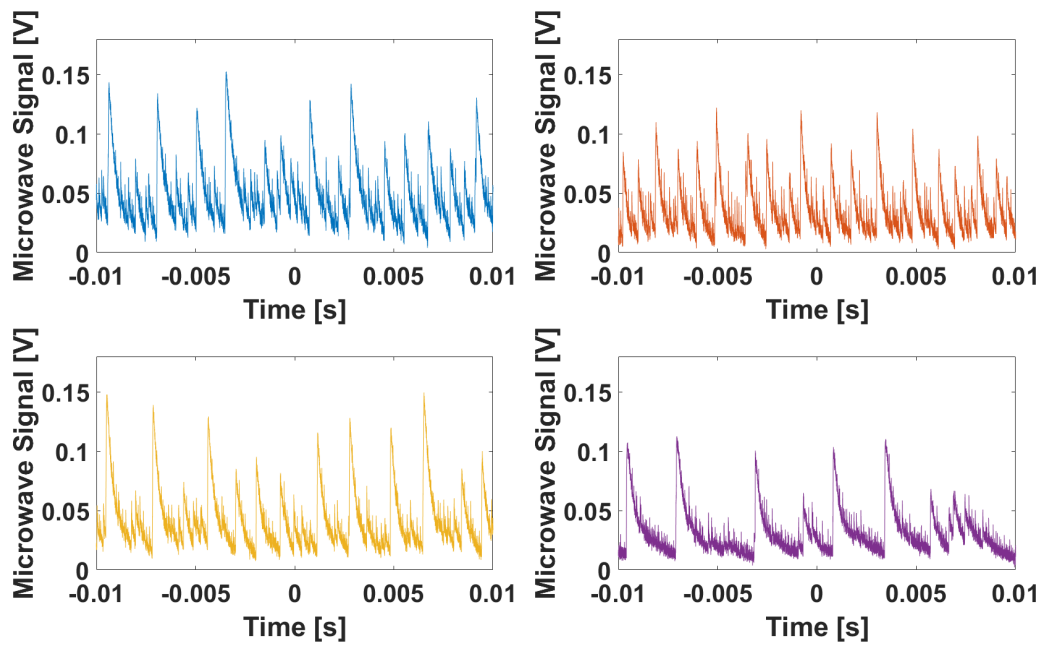


Figure 5.33: Microwave power signals for a varying injection field maxima: (Top Left)  $B_{\text{Inj,max}} = 2.20$  T, (Top Right)  $B_{\text{Inj,max}} = 2.33$  T, (Bottom Left)  $B_{\text{Inj,max}} = 2.45$  T, (Bottom Right)  $B_{\text{Inj,max}} = 2.58$  T.  $B_{\text{min}} = 0.4$  T,  $P_{\mu} = 350$  W,  $p_{\text{Ar}} = 213$  nTorr. Microwave power has been offset by its minimum value, over the entire 100 ms measurement period, to account for the AC coupling of the oscilloscope. Signals have been treated with a digital low pass filter using the Matlab signal processing toolkit, with a cutoff frequency of 333 kHz.

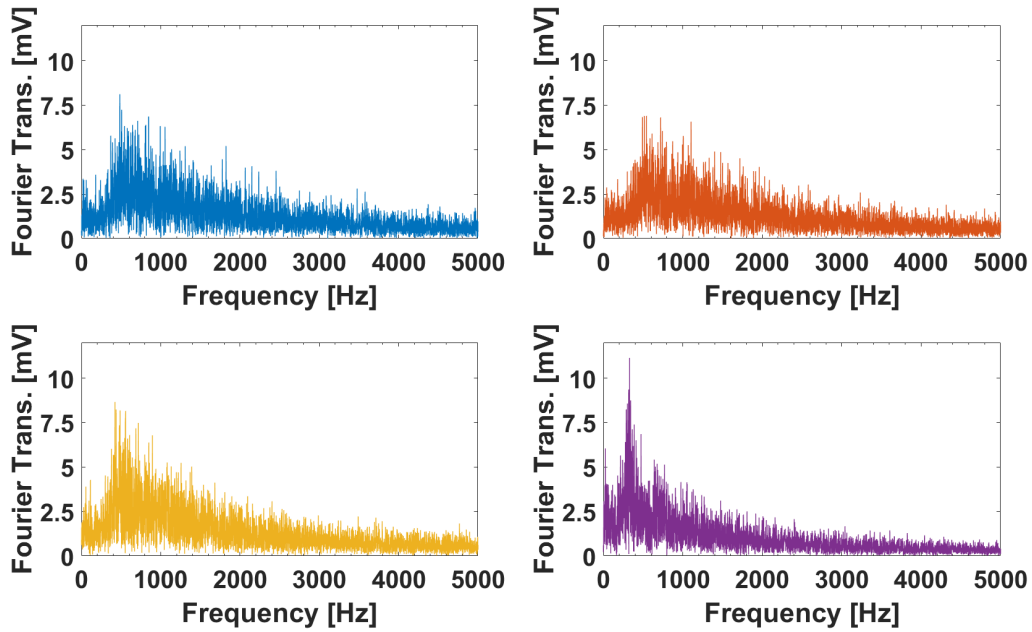


Figure 5.34: Fourier transform of the microwave power signals emitted from the ion source for a varying injection field maximum: (Top Left)  $B_{\text{Inj,max}} = 2.20$  T, (Top Right)  $B_{\text{Inj,max}} = 2.33$  T, (Bottom Left)  $B_{\text{Inj,max}} = 2.45$  T, (Bottom Right)  $B_{\text{Inj,max}} = 2.58$  T.  $B_{\text{min}} = 0.4$  T,  $P_{\mu} = 350$  W,  $p_{\text{Ar}} = 213$  nTorr.

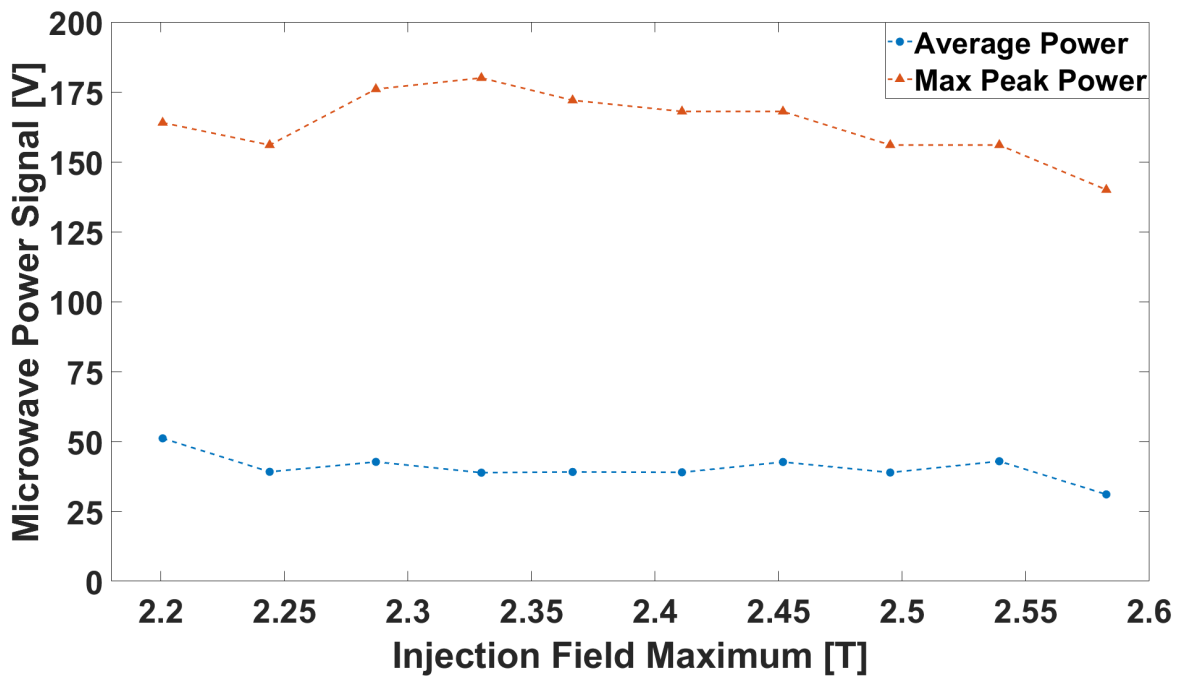


Figure 5.35: Average and maximum output microwave power, measured over a 100 ms period, for a varying injection side field maximum:  $B_{\text{min}} = 0.4$  T,  $P_{\mu} = 350$  W,  $p_{\text{Ar}} = 213$  nTorr.

### 5.3.5 Varying the Extraction Field Maximum

Two rather interesting things happen as the maximum magnetic field strength at extraction increases while the plasma is unstable. First, the instability repetition rate increases while both  $A_1$  and  $A_2$  decrease. At the same time, the average current increases to a maximum at  $B_{\text{Ext,max}} = 1.15$  T,  $B_{\text{Ext,max}}/B_{\text{RF}} = 1.8$ , and then decreases as the field continues to increase. The standard deviation of the current decreases on average until the average current reaches a maximum; the standard deviation then reaches a local maximum at or around 1.2 T. Figures 5.36, 5.37, and 5.38 show these trends through direct measurements and calculated values of scope traces of extracted  $\text{Ar}^{8+}$  current. As seen in the previous section, there appears to be an inverse correlation between the size of the instability induced perturbation and its repetition frequency.

The microwave power emitted from the source varies quite dramatically over the measured domain. As the field strength increases, the amplitude of emitted microwaves first increases then decreases as the repetition rate of microwave bursts increases. Figure 5.39 shows examples of the emitted microwave power, as seen on an oscilloscope, with their corresponding Fourier transforms in figure 5.40. Initially, the repetition frequency and emitted peak power increase. While the frequency continues to increase, the power emitted per instability decreases. At the highest field setting, the emitted microwave power is almost indistinguishable from electronic noise, particularly in figure 5.40. Figure 5.41 compares the average and maximum microwave power across all operating points measured. The peak microwave power reaches a maximum at a field strength of 1.07 T and continues to decrease for higher magnetic fields. However, this increase in the peak amplitude correlates with a decrease in the pulse duration, which maximizes the average power at 1.02 T.

Notably, there is no dramatic change in the behavior of either the emitted ions or microwave power at 1.2 T. The electron and bremsstrahlung distributions in chapter 4 saw a dramatic decrease in their respective intensities after 1.2 T (see 4.4.5). However, concurrent measurements of the bremsstrahlung distribution taken while measuring the ions show that the effect still occurs. Figure 5.42 compares the trends in the total number of observed photons during both the ion and electron



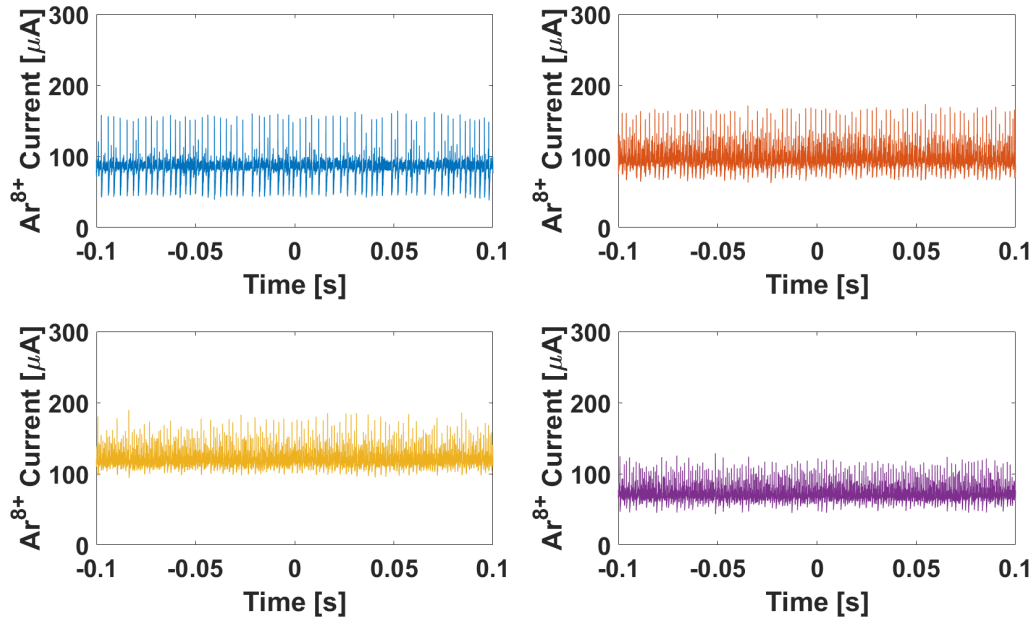


Figure 5.36:  $\text{Ar}^{8+}$  beam current for a varying extraction field maxima: (Top Left)  $B_{\text{Ext,max}} = 0.99$  T, (Top Right)  $B_{\text{Ext,max}} = 1.07$  T, (Bottom Left)  $B_{\text{Ext,max}} = 1.15$  T, (Bottom Right)  $B_{\text{Inj,max}} = 1.23$  T.  $B_{\text{min}} = 0.4$  T,  $P_{\mu} = 350$  W,  $p_{\text{Ar}} = 213$  nTorr. Signals have been treated with a digital low pass filter using the Matlab signal processing toolkit, with a cutoff frequency of 333 kHz.

measurements. In both cases, the total number of observed photons decreases dramatically. There is a 48% decrease while the extraction voltage is fixed at 20 kV and 55% while the electrode is grounded. While the extracted beam current and emitted microwave power sharply decrease beyond 1.6 T, we only observe the beginnings of the trend towards decreased electron diffusion (see figures 5.37 and 5.41). More measurements are necessary to determine how the ion distribution is affected by the sudden change in diffusing electrons' behavior.

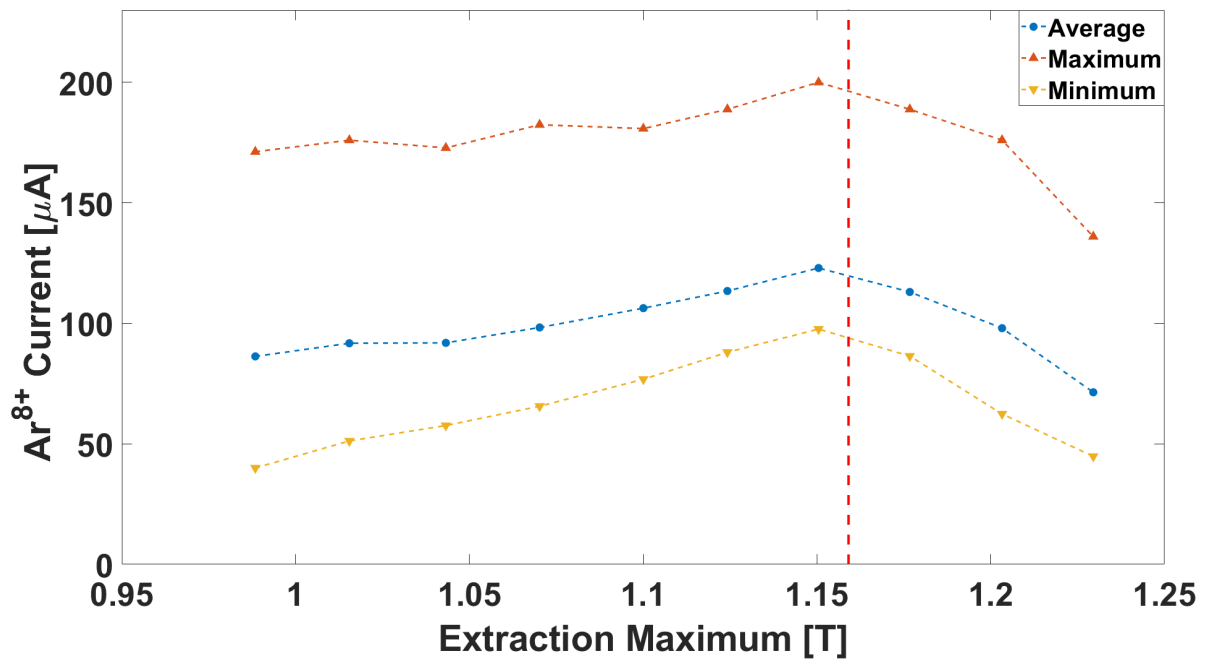


Figure 5.37: Average, maximum, and minimum Ar<sup>8+</sup> beam currents, measured over a 100 ms period, for a varying extraction field maxima:  $B_{\min} = 0.4$  T,  $P_{\mu} = 350$  W,  $p_{\text{Ar}} = 213$  nTorr. The dashed vertical line show where  $B_{\text{Ext,max}}/B_{\text{RF}} = 1.8$ .

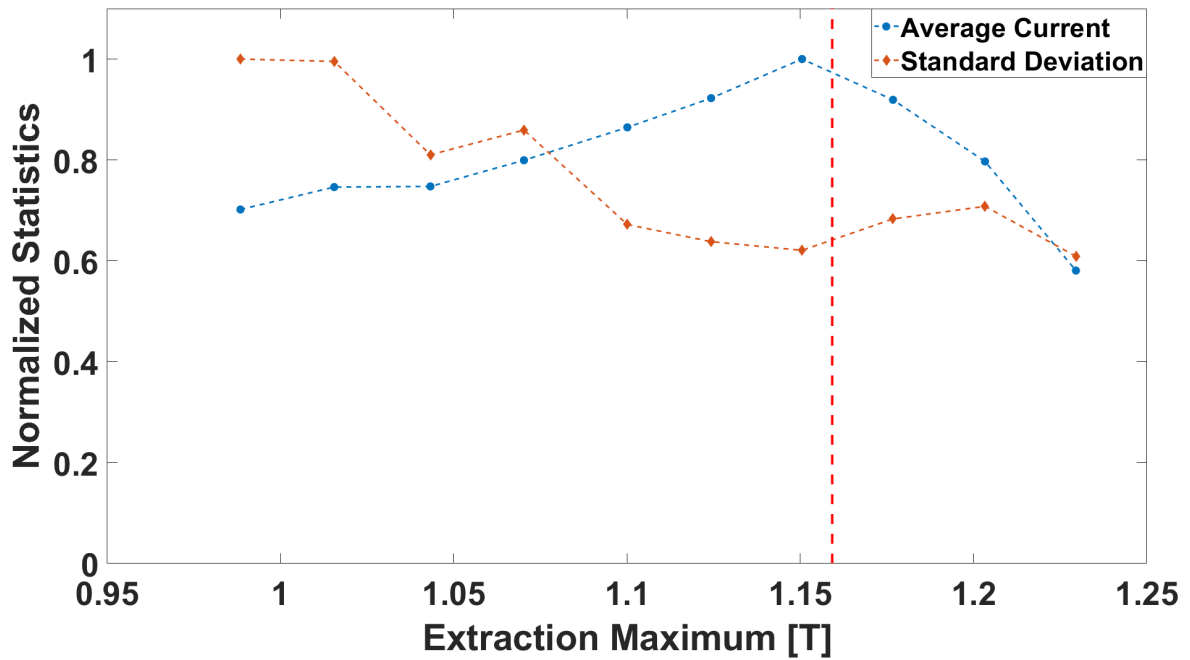


Figure 5.38: Trends of the average and standard deviations of the average extracted  $\text{Ar}^{8+}$  beam current as the extraction field maximum is varied, normalized to the largest values in their respective sets:  $B_{\min} = 0.4$  T,  $P_{\mu} = 350$  W,  $p_{\text{Ar}} = 213$  nTorr. The vertical dashed line shows where  $B_{\text{Ext,max}}/B_{\text{RF}} = 1.8$ .

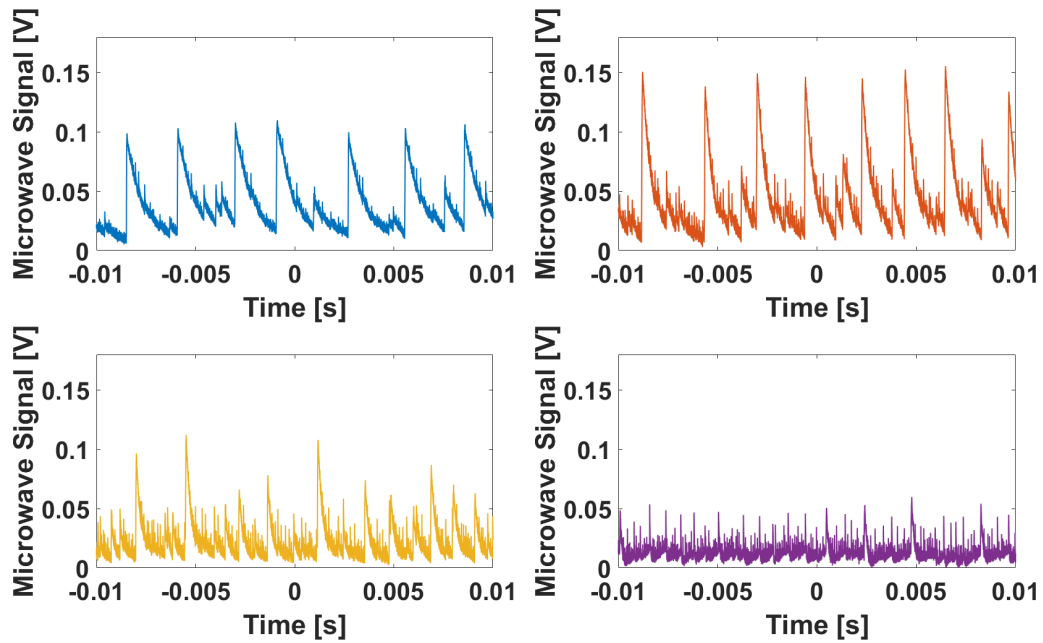


Figure 5.39: Microwave power signals for a varying extraction field maxima: (Top Left)  $B_{\text{Ext,max}} = 0.99$  T, (Top Right)  $B_{\text{Ext,max}} = 1.07$  T, (Bottom Left)  $B_{\text{Ext,max}} = 1.15$  T, (Bottom Right)  $B_{\text{Inj,max}} = 1.23$  T.  $B_{\text{min}} = 0.4$  T,  $P_{\mu} = 350$  W,  $p_{\text{Ar}} = 213$  nTorr. Microwave power has been offset by its minimum value, over the entire 100 ms measurement period, to account for the AC coupling of the oscilloscope. Signals have been treated with a digital low pass filter using the Matlab signal processing toolkit, with a cutoff frequency of 333 kHz.

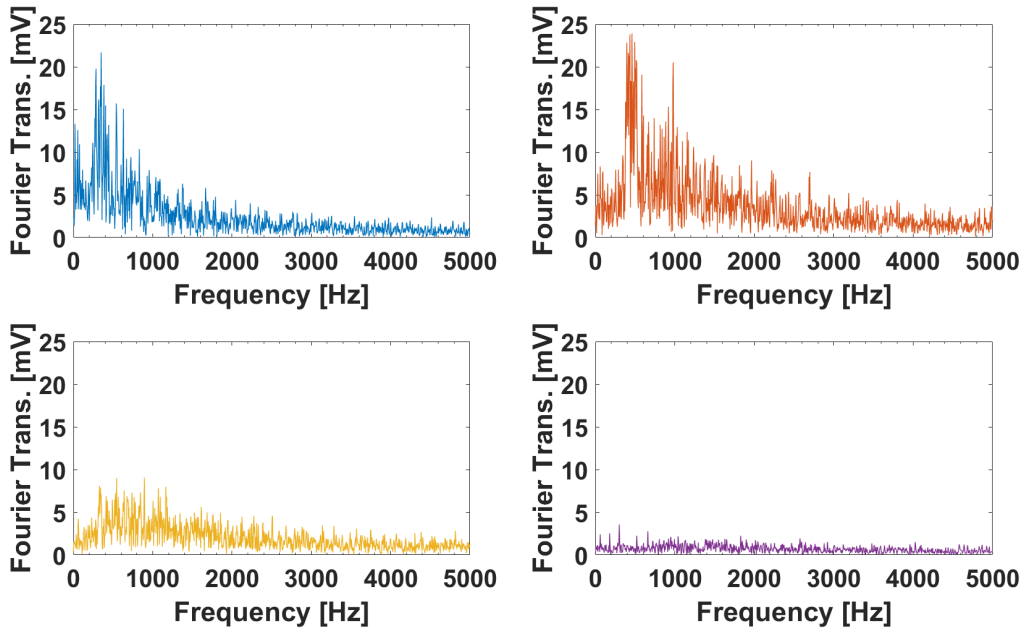


Figure 5.40: Fourier transform of the microwave power signals emitted from the ion source for a varying extraction field maxima: (Top Left)  $B_{Ext,max} = 0.99$  T, (Top Right)  $B_{Ext,max} = 1.07$  T, (Bottom Left)  $B_{Ext,max} = 1.15$  T, (Bottom Right)  $B_{Inj,max} = 1.23$  T.  $B_{min} = 0.4$  T,  $P_{\mu} = 350$  W,  $p_{Ar} = 213$  nTorr.

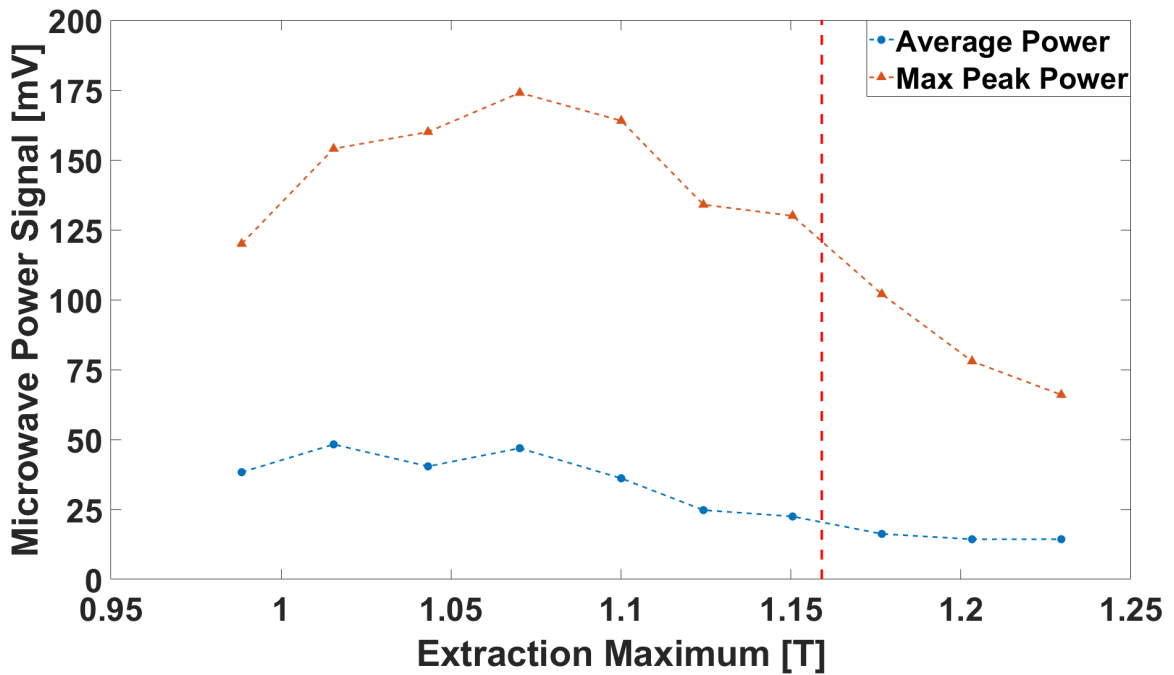


Figure 5.41: Maximum output microwave power for a varying extraction field maxima:  $B_{min} = 0.4$  T,  $P_{\mu} = 350$  W,  $p_{Ar} = 213$  nTorr. The dashed vertical line shows where  $B_{Ext}/B_{RF} = 1.8$ .

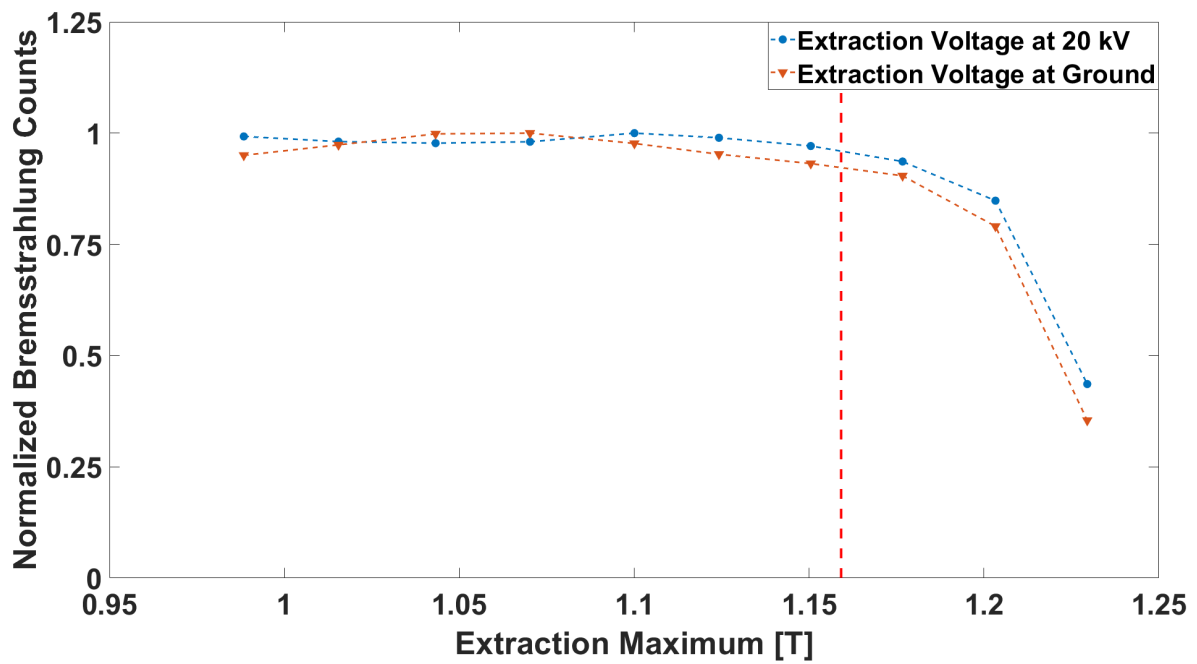


Figure 5.42: Average and maximum output microwave power, measured over a 100 ms period, for a varying extraction field maxima:  $B_{\min} = 0.4$  T,  $P_{\mu} = 350$  W,  $p_{\text{Ar}} = 213$  nTorr. The dashed vertical line shows where  $B_{E_{xt}}/B_{RF} = 1.8$ .

### 5.3.6 Source stability for a varying magnetic minimum

In chapter 4, it was seen that the magnetic minimum controls the central energy of the high energy peak. However, that trend tells us little about the plasma's stability or how it is affected by a varying magnetic minimum. To that end, figures 5.43 and 5.44 show eight examples of the changing extracted beam current as the magnetic minimum is varied, as seen by an oscilloscope. Initially, the system extracts approximately  $100 \mu\text{ A}$  of  $\text{Ar}^{8+}$  and displays a combined ion burst and ion loss transient profile. Increasing the minimum magnetic field strength causes both the average extracted current and the ion bursts amplitude to increase. At the same time,  $A_2$  decreases as the 'ion loss' effect becomes less prominent. At  $B_{\text{min}} = 0.43$ , the repetition frequency begins to decrease noticeably, and the beam current begins showing signs of 'over-extraction'. At this point,  $A_1$  increases with the field strength,  $A_2$  becomes visible once again, and the scope trace shows at least one instance where  $A_3$  is non-zero. At a value of  $0.47\text{ T}$ ,  $B_{\text{min}}/B_{\text{RF}} = 0.73$ , the beam current reaches its maximum while minimizing its upward and downward deviations. Figure 5.45 looks at the average, maximum, and minimum currents observed over a  $200\text{ ms}$  period of observing each operating point. The maximum current diverges away from the average current between  $0.4 < B_{\text{min}} < 0.44$  and converges at higher magnetic fields. In this case, the increasing magnetic field appears to bring a degree of stability to the plasma, at least over the measured domain. The average, maximum, and minimum currents show this by converging together as the average beam current increase.

It is also important to look at the microwaves emitted from the system during this measurement. The increasing magnetic field leads to an increase in the burst repetition frequency and while decreasing their amplitude. Figures 5.46 and 5.47 show scope traces of the measured microwave power for various operating points, with the corresponding Fourier transforms in figures 5.48 and 5.49. The frequency content of emitted microwaves changes appreciably as the minimum field increases. Initially, the height, duration, and repetition frequency of the emitted microwaves approximately uniform. At higher fields, the emitted power spreads out over a wider region of the frequency domain. The higher field strengths restore some of the uniformity of the signal, but this

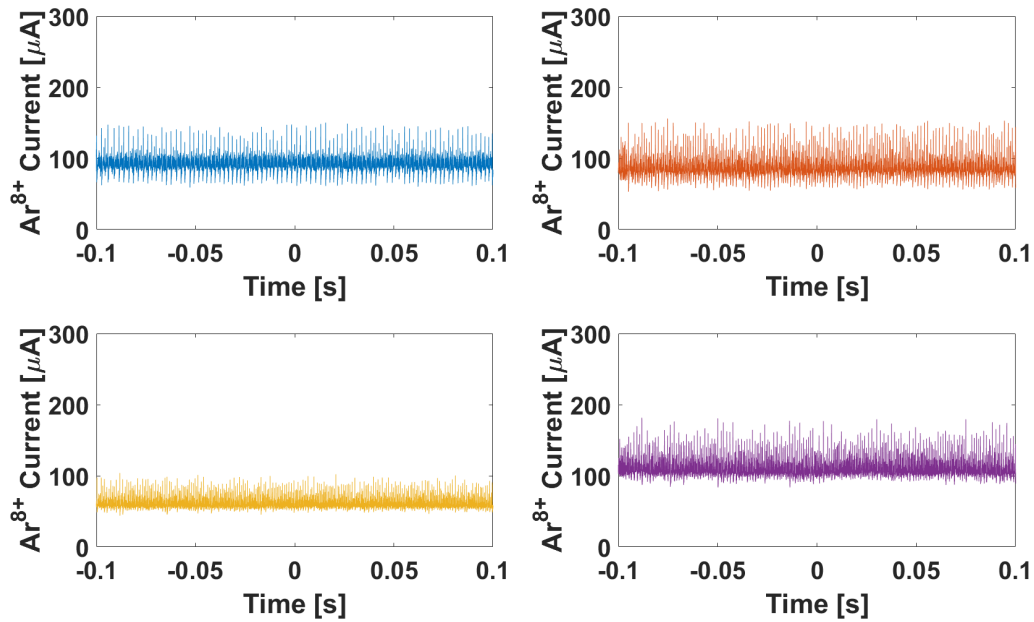


Figure 5.43:  $\text{Ar}^{8+}$  beam current for varying magnetic minimums (Top left)  $B_{\min} = 0.34$  T, (Top right)  $B_{\min} = 0.35$  T, (Bottom left)  $B_{\min} = 0.37$  T, (Bottom Right)  $B_{\min} = 0.4$  T.  $P_{\mu} = 350$  W,  $p_{\text{Ar}} = 213$  nTorr. Signals have been treated with a digital low pass filter using the Matlab signal processing toolkit, with a cutoff frequency of 333 kHz.

comes with a dramatic decrease in the repetition frequency of the emitted microwaves. Eventually, the quasi-periodically emitted bursts of microwave power decrease beneath the system's noise floor.

Figure 5.50 compares average emitted microwave power to the maximum measured power from the plasma chamber. There is a local maximum in the maximum emitted microwave power at  $B_{\min} \sim 0.4$ , which then decreases at either higher or lower field strengths. At larger field strengths, the maximum emitted power decreases rapidly while the average power remains constant. This can be seen in figure 5.47 where the microwave power signal becomes noisy, but otherwise appears stable. This is also where the extracted current reaches a maximum (see figure 5.45). Once again, there is a strong correlation between the lack of magnitude and frequency variations in the emitted microwave power and large extracted currents. However, a vital measurement of the ion source is absent from this discussion: the predominant frequencies emitted during the unstable event. While both beam current and microwave signals reach a degree of stability, it is difficult to make a strong claim about the stability of the plasma in the absence of knowledge of the microwaves' frequency



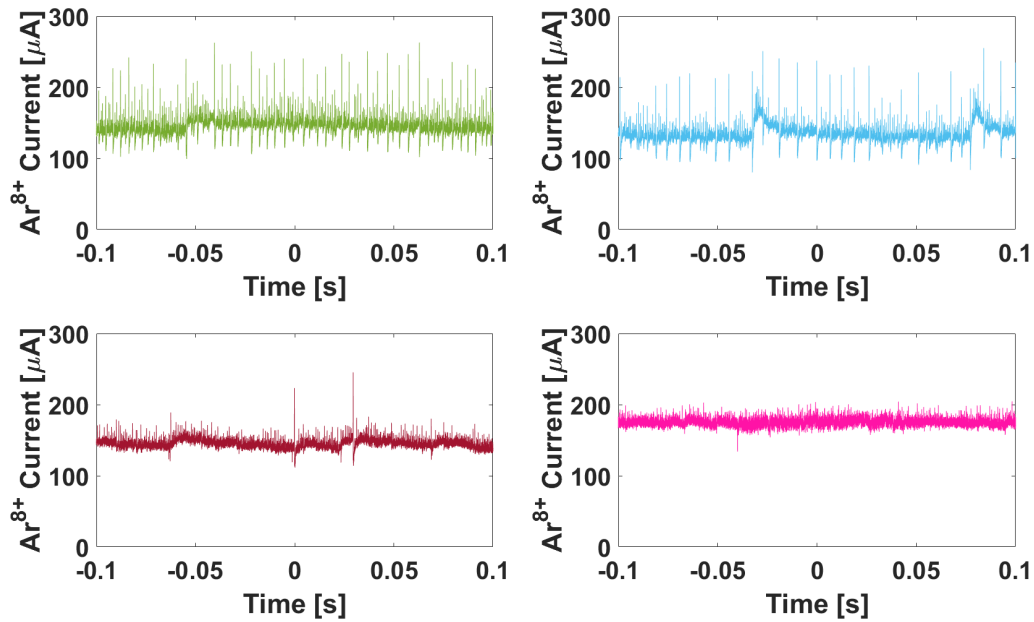


Figure 5.44:  $\text{Ar}^{8+}$  beam current for varying magnetic minimums (Top left)  $B_{\text{min}} = 0.43$  T, (Top right)  $B_{\text{min}} = 0.44$  T, (Bottom left)  $B_{\text{min}} = 0.46$  T, (Bottom Right)  $B_{\text{min}} = 0.47$  T.  $P_{\mu} = 350$  W,  $p_{\text{Ar}} = 213$  nTorr. Signals have been treated with a digital low pass filter using the Matlab signal processing toolkit, with a cutoff frequency of 333 kHz.

composition.

The data acquired here reflects several of the trends seen in sections 5.3.3 and 5.3.5. Initially, increasing the magnetic minimum increases the amplitude of ion burst instability events while decreasing the overall instability repetition frequency. Once again, the extracted current correlates less with the total emitted power per instability event and more about the number of instability events that occur over time. To that end, a wider loss cone pitch angle correlates to less frequent large bursts of microwave power and electron losses from the system. The qualitative change in the behavior seen in figures 5.43 and 5.44 is unique to varying the magnetic minimum. As seen in section 4.4.6, varying the magnetic minimum was also the *only* way to produce substantial changes in the energy distribution of either the measured electrons or bremsstrahlung. As a result, the qualitative change may result from a change in excited photons' frequency or the energy of lost electrons. Even if that were the case, this does not explain why the plasma seemingly becomes stable as the magnetic minimum increases.

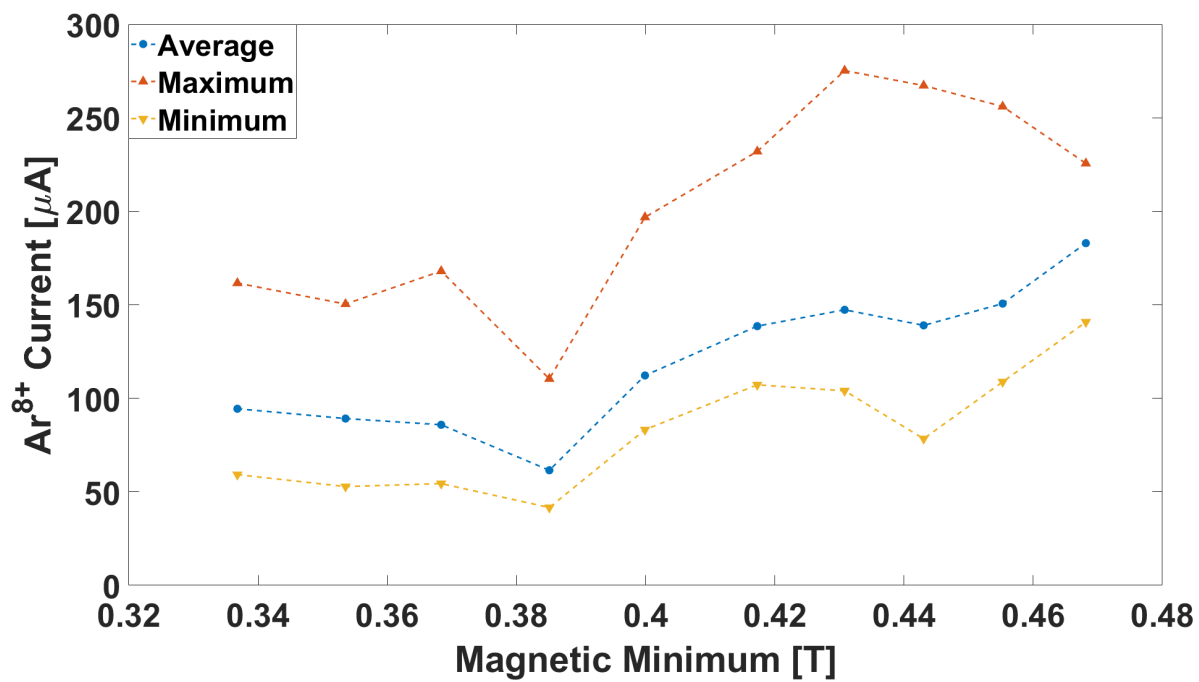


Figure 5.45: Average, maximum, and minimum Ar<sup>8+</sup> beam currents, measured over a 100 ms period, for a varying magnetic minimum.

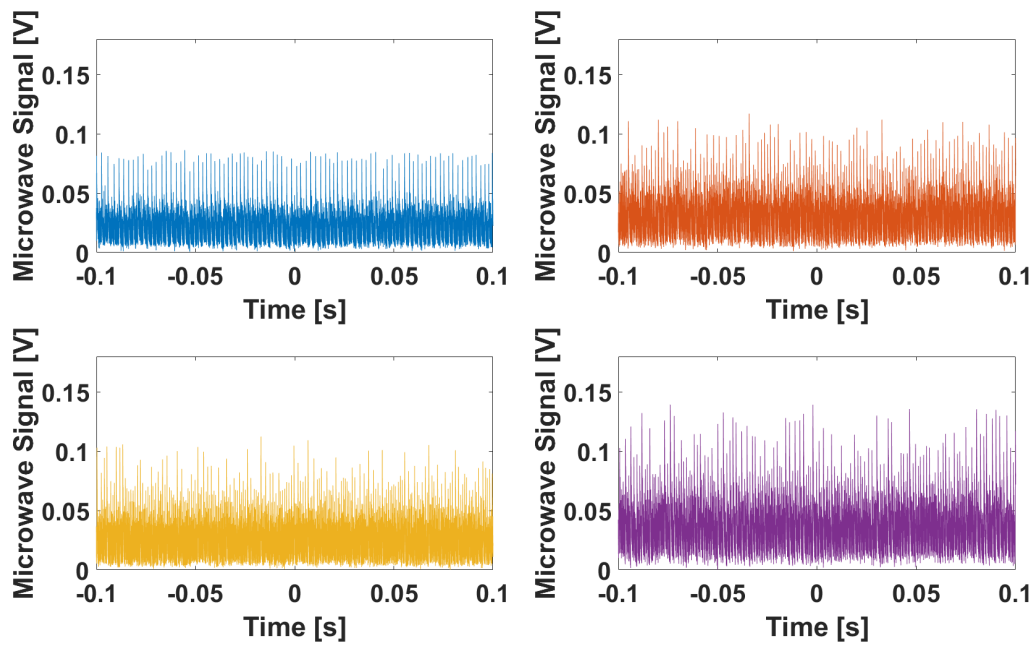


Figure 5.46:  $\text{Ar}^{8+}$  beam current for varying magnetic minimums (Top left)  $B_{\min} = 0.34$  T, (Top right)  $B_{\min} = 0.35$  T, (Bottom left)  $B_{\min} = 0.37$  T, (Bottom Right)  $B_{\min} = 0.4$  T.  $P_{\mu} = 350$  W,  $p_{\text{Ar}} = 213$  nTorr. Microwave power has been offset by its minimum value, over the entire 100 ms measurement period, to account for the AC coupling of the oscilloscope. Signals have been treated with a digital low pass filter using the Matlab signal processing toolkit, with a cutoff frequency of 333 kHz.

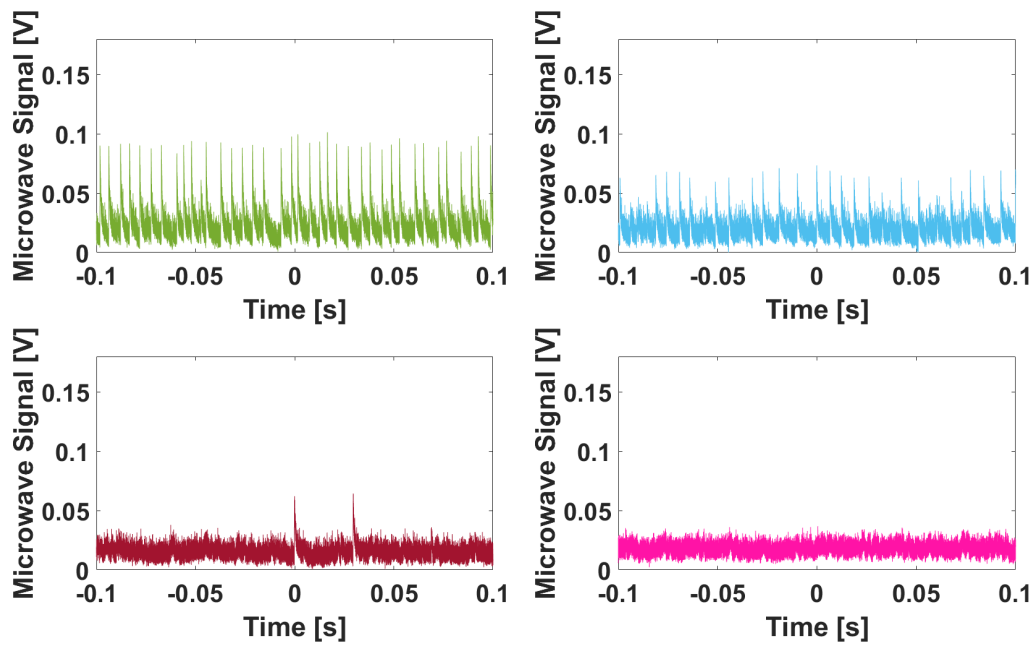


Figure 5.47:  $\text{Ar}^{8+}$  beam current for varying magnetic minimums (Top left)  $B_{\text{min}} = 0.43$  T, (Top right)  $B_{\text{min}} = 0.44$  T, (Bottom left)  $B_{\text{min}} = 0.46$  T, (Bottom Right)  $B_{\text{min}} = 0.47$  T.  $P_{\mu} = 350$  W,  $p_{\text{Ar}} = 213$  nTorr. Microwave power has been offset by its minimum value, over the entire 100 ms measurement period, to account for the AC coupling of the oscilloscope. Signals have been treated with a digital low pass filter using the Matlab signal processing toolkit, with a cutoff frequency of 333 kHz.

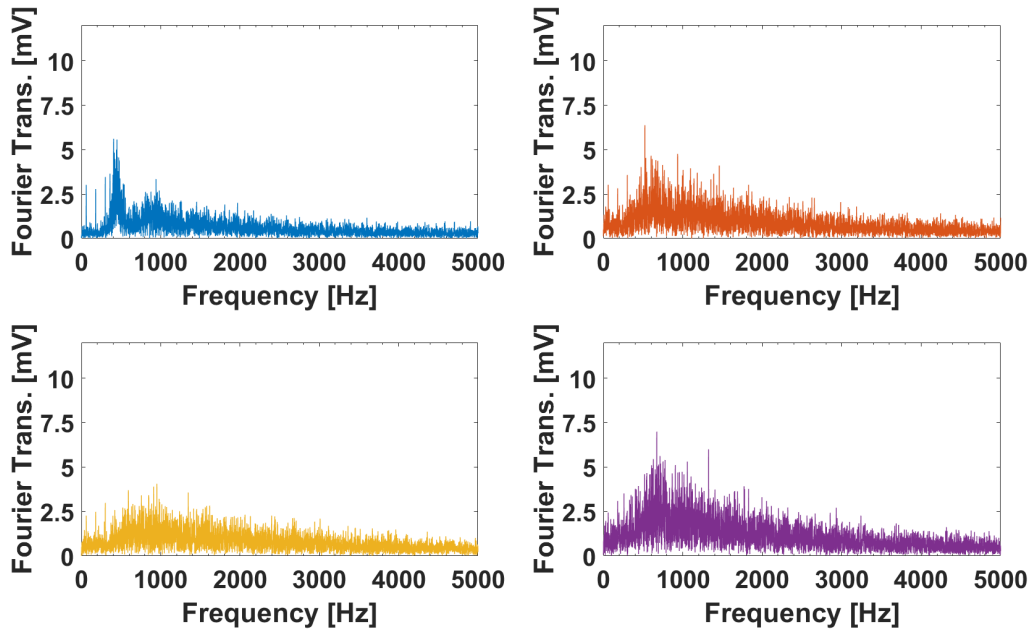


Figure 5.48: Fourier transform of the microwave power signals emitted from the ion source for a varying magnetic minimums (Top left)  $B_{\min} = 0.34$  T, (Top right)  $B_{\min} = 0.35$  T, (Bottom left)  $B_{\min} = 0.37$  T, (Bottom Right)  $B_{\min} = 0.4$  T.  $P_{\mu} = 350$  W,  $p_{\text{Ar}} = 213$  nTorr.

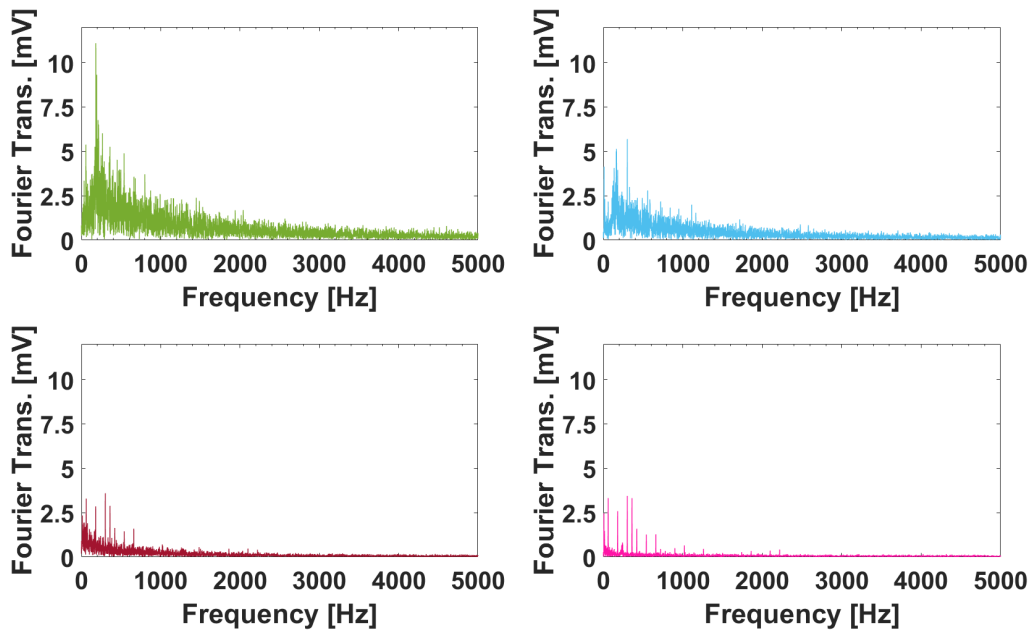


Figure 5.49: Fourier transform of the microwave power signals emitted from the ion source for a varying magnetic minimums (Top left)  $B_{\min} = 0.43$  T, (Top right)  $B_{\min} = 0.44$  T, (Bottom left)  $B_{\min} = 0.46$  T, (Bottom Right)  $B_{\min} = 0.47$  T.  $P_{\mu} = 350$  W,  $p_{\text{Ar}} = 213$  nTorr

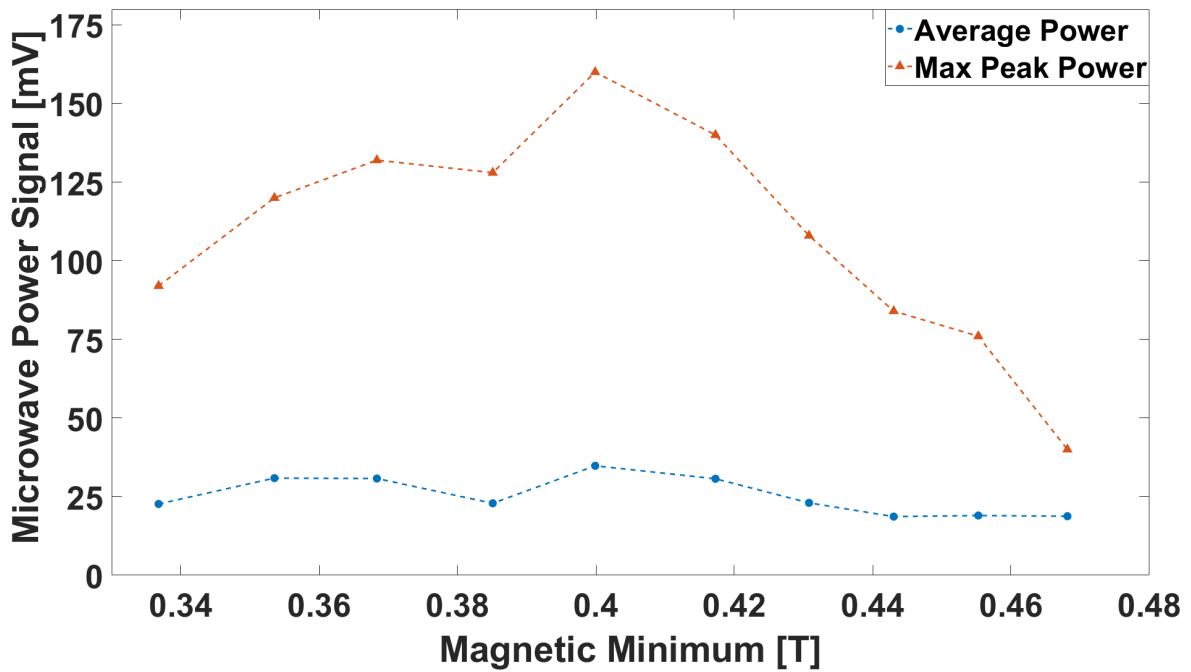


Figure 5.50: Average and maximum output microwave power, measured over a 100 ms period, for a varying magnetic minimum.

### 5.3.7 Understanding the 'over-extraction' transient profiles

As discussed earlier, the 'ion burst' effect is most likely an afterglow event resulting from losses of electrons due to an instability event. The afterglow phenomenon can also explain the 'over-extraction' mode. Using the evidence presented throughout this chapter, we can see that the 'over-extraction' effect occurs in high energy density systems, particularly those with large magnetic fields. Increasing the magnetic field may cause wave-electron interactions to occur at higher energies or causes excitation of lower frequency unstable electromagnetic plasma modes [25, 26]. For sufficiently strong magnetic fields, the affected population would be the electrons responsible for the potential dip, very high energy hot electrons. If this population were to escape confinement suddenly, then the potential dip would decrease, as  $\Delta\Phi \sim (n_i - n_e)$ . The sudden increase in the potential would degrade the confinement of highly charged ions within the system. This type of afterglow is most similar to the so-called 'second afterglow' described by Geller [18].

This latter hypothesis is rather difficult to prove as it is nearly impossible to probe that deeply into the plasma. However, it does make sense in the grand scheme of ECR operations and explains many of the phenomena seen in the 'over-extraction' mode. First, the low repetition frequency and recovery time are some of the strongest evidence for an afterglow effect on the high energy electrons. Time-resolved bremsstrahlung measurements have shown that it can take 10's-100's ms to produce steady-state hot-electron populations within ECRIS plasmas [33, 65, 66]. In fact, as figures 5.10 and 5.51 show, the decay of the enhanced current goes as  $I_q \sim Z^{-2}$ , as we would expect for collisionally diffused ions. Although there is not enough data to show it, the decay time does appear to be inversely dependent upon the magnetic field, as we would expect for either Bohm or cross-field diffusion [86].

This effect may also explain the decrease in the extracted current of low charge state ions. As the ion-ion collision frequency goes as  $\nu_{ii} \sim \bar{q}$ , a temporary decrease in high charge state populations may result in *better* confinement of low charge states. As discussed in section 2.3.2, low charge states may be magnetically confined and their diffusion will not be appreciably affected by losses of hot electrons. Using equations 2.5 and 2.9 while assuming an ion temperature 5 eV, electron

density of  $10^{11} \text{ cm}^{-3}$ , and average magnetic field of 1 T shows that the ion-ion collision frequency overtakes the ion cyclotron frequency between 2+ and 4+, with  $\langle \nu_{ii} \rangle / f_{ci} \sim 1$  for argon 3+. This estimate agrees well with the trends seen in figure 5.10, which shows the percent change of extracted ion currents for argon ions up to charge state 12+.

Lastly, the appearance of the 'over-extraction mode in high field operating points suggests increased interactions with higher energy electrons (see sec. 5.3.2). Izotov et al. demonstrated that microwave power is predominantly emitted at lower microwave frequencies as the ion source magnetic field increases [26]. This could result from resonant interactions with increasingly higher energy electrons, as  $f_{ce} \sim B/\gamma_e$ .<sup>4</sup> This relation presents two logical extremes that allow for a decreasing resonance frequency. If the magnetic field where the resonant interaction occurs remains constant, then the interaction must be occurring for a larger number of higher energy electrons. Under the potential dip hypothesis, these electrons exist more towards the center of the trap. If the energy of the interacting electrons remains constant, then the interaction must occur deeper inside the plasma, due to the min-B field structure (see sec. 2.3.1). Either way, the lower value of the dominant emitted frequency suggests that electrons in the center of the trap are more likely to diffuse during unstable operation with higher magnetic fields.

This hypothesis may also explain one of the stranger effects observed with 'over-extraction' operating. The absence of large (or sometimes any) microwave bursts immediately before any beam current variations (see Figure 5.6). This effect is notable, especially with the observations of sizeable microwave power bursts during instability events that perturb the plasma to a lesser degree. Electron losses focused at the center of the plasma may explain this observation. High energy electrons would predominately resonate with microwaves at substantially lower frequencies than in the other modes. If the majority of the plasma's density appears around its extremities, as simulations suggest, then the increasing density away from the center of the plasma would make it difficult for microwave radiation to penetrate out of the plasma [58, 80]. As a low order approximation we can suppose a cold plasma that is divided into three spatially distinct regions: I)

---

<sup>4</sup>As an example of this trend, 100 keV electrons at the cold RF resonance position,  $f_{RF} = 18 \text{ GHz}$ , will resonate at 15.1 GHz and 1 MeV electrons will resonate at 6.1 GHz, excluding Doppler effects.



$\omega > \omega_p(x)$  on  $-\text{inf} < x < 0$  II)  $\omega_p(x) > \omega$  on  $0 < x < L$  III)  $\omega > \omega_p(x)$  on  $L < x < \text{inf}$ . Here,  $\omega$  is the frequency of the excited and propagating wave, and  $\omega_p(x)$  is the spatially varying plasma frequency. The transmission coefficient is given by [80]:

$$T = \left( e^\eta + \frac{1}{4} e^{-\eta} \right)^{-2} \quad (5.1)$$

where

$$\eta = \frac{1}{c} \int_0^L \sqrt{\omega_p^2(x) - \omega^2} dx. \quad (5.2)$$

If we assume that electron losses occur at the plasma boundary, for 'ion burst' and 'ion loss' profiles, then  $\eta \sim \omega_p^2 \sim n_e(x)$ , and therefore T, would decrease along the plasma boundary. However, as the debye length is of the order of mm's (in a system with a characteristic length of 50 - 100 cm), even significant losses at the plasma's center could have little to no effect upon the electromagnetic boundaries within the system. Thus, it would be equally difficult for the excited microwaves to penetrate through the plasma boundary during an 'over-extraction' type instability event. The waves which can escape must then pass through a WR-62 waveguide, which has a lower cutoff frequency of 9.5 GHz, making the observation of the excited electromagnetic modes unlikely. To this author's knowledge, no one has observed the excitation of microwaves with frequencies lower than about 5 GHz. However, measurements show that the emitted spectral density of microwaves prefers lower frequencies when the source is operated at higher magnetic minimums [27, 26].

The hypothesis assumes the existence of the potential dip or, at a minimum, a collection of hot electrons in the center of the magnetic trap. Such a population of electrons itself is also a hypothesis (see section 2.3.2), as measuring it without perturbing the plasma is nearly impossible. However, in the absence of a better understanding of the source's volumetric energy distribution, its presence provides the best explanation for this measurement and many others [36, 49].

## 5.4 Concluding Thoughts

In this chapter, measurements of the stability of the SuSI ion source across a wide range of ion source parameters were shown. The transient model for beam currents during unstable operation provided a means to view and characterize trends across numerous operating points. These trends,

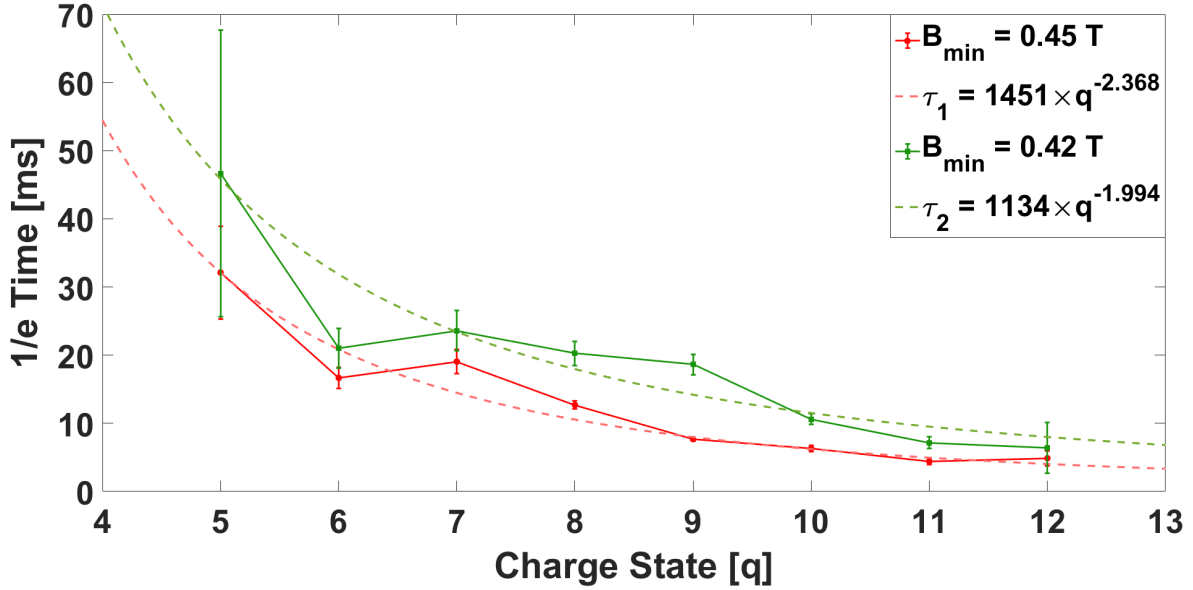


Figure 5.51: The exponential decay time of the 'over-extracted' current scales roughly as  $q^{-2}$ . The deviation can result from non-linear effects in the plasma, such as continuous heating, charge exchange, and ionizing collisions.  $B_{\text{Hex,wall}} = 1.2$  T,  $p_{\text{Ar}} = 131$  nTorr, For the red curve:  $P_{\mu} = 350$  W. For the green curve:  $P_{\mu} = 250$  W.

seen through 2D color maps, demonstrated relationships between the system's magnetic field topology and the plasma's stability. Using the same operating points described in chapter 4, brought further insight into the maps' trends by individually varying important field parameters. Ultimately, as suggested by the maps, the magnetic minimum appears responsible for the transient behavior of the extracted beam current.

The transient model provides a semi-quantitative method of characterizing the beam extracted from an unstable plasma. Moreover, it revealed several patterns and trends across different operating parameter ranges (sec. 5.3). Those statistical trends across the stability maps clearly showed that the best performing operating points were those with lower magnetic fields at extraction (sec. 5.3.2). Systematically varying the different extrema of the magnetic field topology demonstrate correlations between high instability repetition frequencies and the suppression of extracted high charge state currents. In general, longer-lasting microwave emission which causes large plasma perturbations were correlated with higher extracted currents (secs. 5.3.4 and 5.3.5). The maximum extracted current occurred when the size of the instability induced perturbations balanced against

their repetition frequency. However, it is the magnetic minimum that has the largest effect on both the transience and overall stability of the plasma (sec. 5.3.6).

The dependence of the beam current transience upon the magnetic field indicates the presence of an energy or frequency selection process occurring before or during an instability event. An afterglow hypothesis best explains the 'over-extraction' transient mode seen in energy-dense plasmas. As both the 'ion burst' and 'over-extraction' effects rely on the same underlying phenomenon, we can attempt to generalize the effect using the knowledge that the magnetic minimum controls the plasma's energy content (sec. 4.4.6). As described in sections 2.4.1 and 5.3.7, varying the magnetic minimum shifts the emitted microwave power to lower frequency microwaves [25, 26]. As such, the microwaves will resonate with increasingly higher energy electrons during an instability event [47]. At low field strengths, the emitted microwave power shifts towards higher frequencies, which would resonate with electrons near the extremity of the plasma. This causes the 'ion burst' effect, an afterglow event similar to the externally driven afterglow phenomena [89]. At high enough field strengths, the electron losses predominantly focus on electrons with lower gyration frequencies in the center of the plasma. In this case, the 'over-extraction' afterglow is caused by a collapse of the potential dip, leading to a loss of confinement for high charge state ions. The ion loss predominant profiles likely exist in some energy region in between these two extremes. This may also explain the phenomena where increasing the neutral gas pressure changes the observed transient mode (fig. 5.12). Izotov et al. observed that changes to the neutral gas species or pressure can affect the spectral power density of emitted microwave radiation [26]. Although Izotov et al. changed both the pressure and neutral species at the same time, and it is currently unknown if changing only one of these variables will lead to the same effect.

Under this hypothesis, the energy distribution of electrons driven out of the plasma could vary significantly across the different transient modes. Unfortunately, time-resolved measurements of the electron distribution are difficult to perform. Figure 5.2 demonstrated losses of electrons predominantly centered over a narrow band of energies in the 65-80 keV range (fig. 5.2). This operating point corresponded to an 'ion burst' dominated transient profile. Izotov et al. success-

fully performed multiple time-resolved electron measurements across various operating points and heating schemes (CW and pulse mode) [28]. The measurements showed that the instability affected the entire warm and hot electron populations [28]. However, the authors do not establish whether the warm electron population is always affected. They did not report details of the corresponding ion beams. Also, neither study included measurements of the frequency composition of emitted microwaves. As a result, it cannot be concluded whether the resonance frequency or energies of lost electrons determine the predominant ion transient profile. Further understanding of the beam current transient and its relation to the properties of the unstable plasma would require simultaneous measurements of the frequency composition of unstable microwaves and time-resolved measurements of the escaping electron energy distribution.

Lastly, the results of these ion measurements revealed trends towards optimizing the ion source's overall performance by maximizing high charge state currents. The magnetic field controls many aspects of the plasma's stability and performance. As demonstrated in sections 5.3.4, 5.3.5, and 5.3.6, even the individual field extrema affect the transient state of the extracted ion beam.

Overall, a lower extraction side magnetic field correlates to higher extracted  $\text{Ar}^{8+}$  currents, regardless of the injection side or hexapole field maxima (sec. 5.3.2). Across all experimental ranges, an extraction side maximum less than 1.16 T,  $B_{\text{Ext,max}} \approx 1.8 B_{\text{RF}}$ , produced the highest extracted currents. The results even seem to disagree with previous work which suggested the extraction field for optimal performance scales as  $B_{\text{Ext,max}} \approx 1.8 - 2 B_{\text{RF}}$  [24, 46]. However, a higher extraction side magnetic field can produce a more stable plasma overall, suggesting that there may be a balance between the stability and intensity of extracted currents for a given operating point. The higher field also correlates with less perturbative, but more frequent, instability events. Bremsstrahlung measurements also demonstrated a change in the diffusion characteristics of the plasma, which begins at field strengths between 1.16 and 1.2 T (see fig. 5.42). Further studies are necessary to understand this effect; however, it may provide insight into the physical mechanisms which limit the extracted current at higher field strengths. At this time, the effect is not a good diagnostic for optimizing performance. Observing the extracted beam current is more efficient and

effective, by a large margin (compare the slopes in figs. 5.37 and 5.42).

The role of the injection and radial field maxima upon the stability of the plasma is unclear. Varying injection side field changes the repetition rate and amplitude of microwave bursts, with an increasing amplitude at larger field strengths (sec. 5.3.4). This contradicts the trend seen by varying the extraction side field, where larger amplitude instability events occurred at lower field strengths. It is possible that the trends shown in section 5.3.5 are a result of a changing electron diffusion rate (see sec. 4.4.5). However, if that were the case, we would expect that varying the injection side would produce similar trends. More measurements will be necessary to understand these effects.

Section 5.3.2 also demonstrated an odd relationship between the radial magnetic field, by varying the hexapole coils, and the stability of the plasma. While varying the hexapole affected the ion current extracted from the ion source, it did little to change the plasma's transient characteristics (sec. 5.3.3). However, it can significantly affect the global stability of the ion source's magnetic field and power parameter space when coupled with a varying longitudinal magnetic field topology (sec 5.3.2). The larger radial fields make the plasma more unstable, overall, except when using experimental range 4, where the increased field improved the stability characteristics of the plasma. The extraction side magnetic field was lowest across this range (see fig. B.2), and the change in the characteristics of the plasma may result from the improved diffusion of electrons out of the system. Sections 4.4.3 and 4.4.5 showed how an increasing hexapolar field and a decreasing radial field both lead to improved diffusion of electrons out of the plasma. Combining these effects could effectively suppress some instability events by increasing the diffusion of hot electrons out of the plasma. Measurements that focus entirely upon the relationship between the hexapole and extraction fields should be performed. Unfortunately, there are few ion sources capable of performing such a measurement.

In total, these measurements revealed that the best-performing ion sources require as much control over the confining magnetic field as possible. At minimum, the longitudinal configuration of future ECR ion sources should include three solenoids. This will provide a greater degree of

control over all three field extrema, at least more so than the two coil configurations. In particular, separating the value of the magnetic minimum from that of the extraction side maximum will provide a much greater degree of control of both the stability and performance of the ion source.

## CHAPTER 6

### CONCLUSION

Electron cyclotron resonance ion sources are a powerful tool for producing high intensity, high charge state ion beams. However, the dynamics of the resonantly heated plasma are poorly understood. High energy electrons within the system can excite electromagnetic modes, inciting kinetic instabilities that can enhance or suppress extracted high charge state currents. This study attempted to better understand the dynamics of the plasma by measuring distributions of diffusing electrons and ions extracted from the source during unstable operation. This work can provide insight into improvements for the design of future ECR ion sources and directions for optimizing the ion source's performance during operation.

The quasilinear diffusion mechanism may provide a pathway for hot electrons to enter the Min-B field structure's loss cone. However, a vital piece of the hypothesis, the excited plasma modes, has never been observed during the stable ion source operations. Such a measurement would be necessary to prove the hypothesis and, as such, further investigations of electron diffusion mechanics are necessary.

Several different parameters affect the energy and density of the diffusing electrons. The system's magnetic minimum overwhelmingly controls the central energy of diffused electrons. Most importantly, the distribution of diffusing electrons and the emission of hard x-rays are highly correlated. This result has significant implications for interpreting the bremsstrahlung diagnostic going forward, particularly in regards to the spectral temperature. If the underlying diffusion mechanism includes an energy selection process that depends upon the magnetic minimum, it may falsely imply an increase in the temperature of plasma electrons. At a minimum, it will make it more challenging to determine the difference between an increase in the energy of trapped electrons and escaping electrons. Narrowing the x-ray collimator's acceptance angle, such that it does not look onto the extraction aperture, may make the bremsstrahlung diagnostic a better reflection of the energy distribution of plasma electrons.

The development of a semi-quantitative model of the beam current transience allowed for a more detailed understanding of the plasma's parameter space stability characteristics. Replacing the idea of a stability threshold with a stability map enables us to characterize the plasma over a wider domain of parameters. While the stability threshold may be valuable as a way to fine-tune ion source parameters along the border between stable and unstable regions, it lacks a global insight into the relationship between the plasma's stability and the Min-B field structure.

The stability maps exposed correlations between the size of stable regions, the solenoid magnetic field profile's topology, and the hexapole field strength. In general, systems with larger magnetic fields are less stable. However, increasing the extraction side magnetic field increases the stability of the magnetic field-power parameter space. Conversely, lower field strengths at extraction maximize the extracted current at the cost of a more unstable operating parameter space. These results also provided insight into the semi-quantitative beam transience model.

The results from chapters 4 and 5 suggest that the three extrema of the transient profile result from an energy or microwave frequency selection process. Low energy, high-frequency events cause afterglow events similar to the more traditional externally driven afterglow process, causing the 'ion burst' effect. The data also suggests that high energy, low-frequency events result from unstable interactions with hot electrons and result in an afterglow event most similar to the 'second afterglow'. These 'over-extraction' events may result from hot-electron losses, which perturb the plasma's potential dip. However, evidence of such a population is necessary to confirm this hypothesis. Understanding these different effects will help further the understanding of ion source operation and performance during unstable operation. These results will provide insight into wave-plasma interaction within the ion source and direct research and operators towards more reliable and optimal operating points.

The work presented here, while revealing much about the ion source plasma, demonstrates that both the escaping electron and bremsstrahlung diagnostics require further development. Expanding the breadth and resolution of energy domain measurements to include 0.1 - 10 keV electrons and photons is necessary to understand the ionization process within the source plasma. Focusing



solely on hot electrons and hard x-rays, while important, is complicated by the multitude of diffusion mechanisms within the plasma. Furthermore, time-resolved versions of these measurements may provide better insight into the plasma dynamics. These results also indicate the need for flexible magnetic field configurations. Future ECR ion sources should include a minimum of three longitudinal solenoid coils, to have greater independent control over the field's extrema. Further studies of new heating mechanisms, including two frequency heating, are necessary to increase these ion sources' performance.

## **APPENDICES**

## APPENDIX A

### MATLAB CODES

This appendix will cover the necessary steps for calculating the fit of the log scale bremsstrahlung distribution used to calculate the spectral temperature (see. 3.2.5). The slope of the log distribution is given by:

$$slope = \frac{\left(\sum_i \frac{E_i}{e_i^2}\right) \left(\sum_i \frac{\ln I_{\gamma,i}}{e_i^2}\right) - \left(\sum_i \frac{E_i \ln I_{\gamma,i}}{e_i^2}\right) \left(\sum_i \frac{1}{e_i^2}\right)}{\left(\sum_i \frac{E_i}{e_i^2}\right)^2 - \left(\sum_i \frac{E_i^2}{e_i^2}\right) \left(\sum_i \frac{1}{e_i^2}\right)} \quad (A.1)$$

with the standard deviation of the slope given by

$$\delta(slope) = \sqrt{\frac{\left(\sum_i \frac{1}{e_i^2}\right)}{\left(\sum_i \frac{E_i^2}{e_i^2}\right) \left(\sum_i \frac{1}{e_i^2}\right) - \left(\sum_i \frac{E_i}{e_i^2}\right)^2}} \quad (A.2)$$

where i indexes each energy bin with a central value of  $E_i$  filled with  $I_{\gamma,i}$  photon counts per second.

The y-intercept of this line is the given by:

$$Y_0 = \frac{\left(\sum_i \frac{E_i}{e_i^2}\right) \left(\sum_i \frac{E_i \ln I_{\gamma,i}}{e_i^2}\right) - \left(\sum_i \frac{E_i^2}{e_i^2}\right) \left(\sum_i \frac{\ln I_{\gamma,i}}{e_i^2}\right)}{\left(\sum_i \frac{E_i}{e_i^2}\right)^2 - \left(\sum_i \frac{E_i^2}{e_i^2}\right) \left(\sum_i \frac{1}{e_i^2}\right)} \quad (A.3)$$

with a standard deviation of:

$$\delta Y_0 = \sqrt{\frac{\left(\sum_i \frac{E_i^2}{e_i^2}\right)}{\left(\sum_i \frac{E_i^2}{e_i^2}\right) \left(\sum_i \frac{1}{e_i^2}\right) - \left(\sum_i \frac{E_i}{e_i^2}\right)^2}} \quad (A.4)$$

The per-bin error is given by:

$$e_i = \frac{\partial \ln I_{\gamma,i}}{\partial I_{\gamma,i}} \delta I_{\gamma,i} = \frac{1}{I_{\gamma,i}} \sqrt{I_{\gamma,i}} = \frac{1}{\sqrt{I_{\gamma,i}}}$$

The spectral temperature is then calculated as:

$$T_s = -\frac{1}{slope} \quad (A.5)$$

with a standard deviation of:

$$\delta T_s = \frac{\delta(slope)}{slope^2}. \quad (A.6)$$

and the x-intercept is given by:

$$X_{T_s} = -\frac{Y_0}{slope} = -Y_0 T_s \quad (A.7)$$

with a standard deviation of:

$$\delta X_{T_s} = \sqrt{(T_s \delta Y_0)^2 + (Y_0 \delta T_s)^2}.$$

```
function output = linReg(Ene,xraycounts)
R2 = 0;
l1 = 0;
Emin = 80;
Emax = 800;
while R2 < 0.99 %Define lower limit on regression
T1a = [];
T2a = [];
T3a = [];
T4a = [];
lc = [];
logerr = [];
[a,b] = min(abs(Ene - Emin)); %Find bin position of Minimum Energy
[c,d] = min(abs(Ene - Emax)); %Find bin position of Maximum Energy
en = Ene(b:d); %Use only the energy values between the Min and Max
m = 0;
n = 0;
Errsq = [];
G = [];
```

```

%Reshape the array which stores count rate data to be the same
%length as energy array.
k = 0;
for k = 1:(d-b+1)
    if xraycounts(k+b) > 0.5 %Lower limit on photon intensity
        counts = xraycounts(k+b);
        lc = [lc ;log(counts)]; %create log(intensity) array
        logerr = [logerr 1/sqrt(counts)]; %calculate error
        m = m +1;
    elseif ((xraycounts(k+b) == 0.5) || (xraycounts(k+b)<0.5))
        Emax = en(k-1); %Set max energy based upon min intensity
        en = en(1:k-1); %Set energy array to match intensity array
        break;
    end
end
end
%http://www.che.udel.edu/wp-content/uploads/2019/03/FittingData.pdf
%(citation)

%calculation of linear fit/fit error
for j = 1:length(lc)
    errsqr = 1/(logerr(j)*logerr(j));
    Errsq = [Errsq ; errsqr];
    T1a = [T1a ; en(j)*errsqr];
    T2a = [T2a ; lc(j)*errsqr];
    T3a = [T3a ; en(j)*lc(j)*errsqr];
    T4a = [T4a ; en(j)*en(j)*errsqr];
end
T1 = sum(T1a);
T2 = sum(T2a);
T3 = sum(T3a);
T4 = sum(T4a);
E = sum(Errsq);

```

```

slope = (T1*T2-T3*E)/(T1*T1-T4*E);
serror = sqrt(E/(T4*E-T1*T1));
intercept = (T1*T3-T2*T4)/(T1*T1-T4*E);
interror = sqrt(T4/(T4*E-T1*T1));

%test the fit against minimum regression limit
testY = slope*en+intercept;
numerator = (lc-testY).^2;
denominator = (lc-mean(lc)).^2;
R2 = 1-sum(numerator)/sum(denominator);
Emin = Emin+5;
l1 = l1+1;
end
%output final results.
output = [slope serror intercept interror Emin Emax];

end

```

## APPENDIX B

### LONGITUDINAL FIELD PROFILES FOR THE MEASUREMENT OF THE DISTRIBUTION OF ESCAPING ELECTRONS

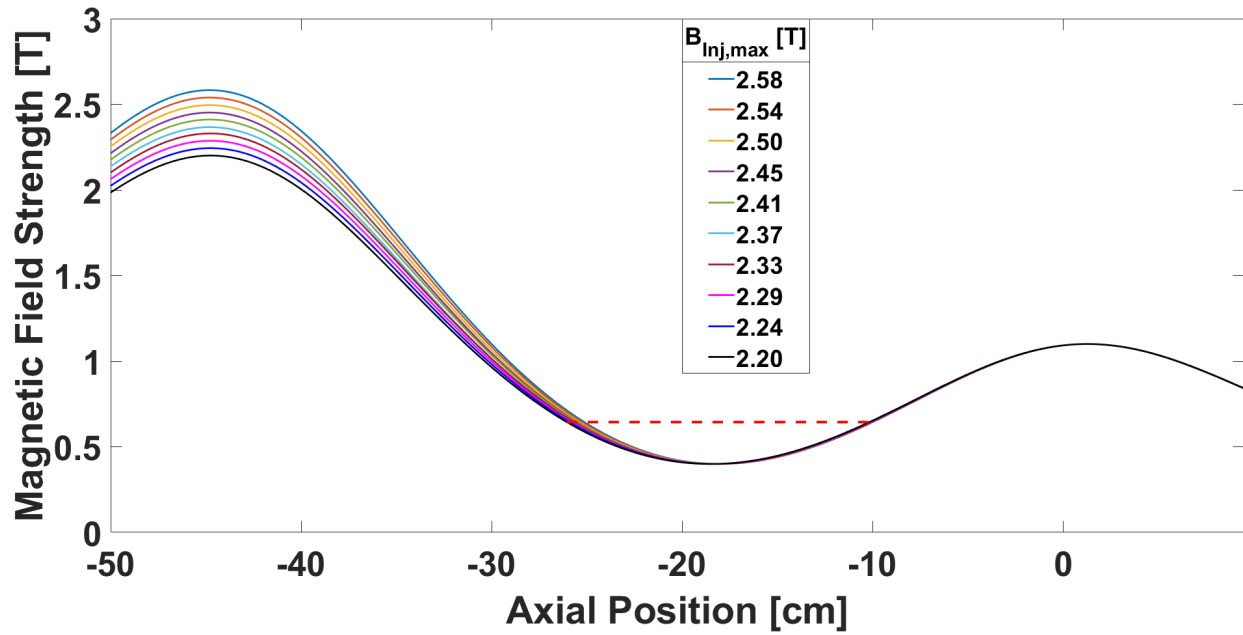


Figure B.1: Measured electron distribution for the measurements 'control' operating point. The 50 keV reliability threshold is shown by the dashed line.  $B_{min} = 0.4$  T,  $B_{Inj,max} = 2.367$  T,  $B_{Ext,max} = 1.100$  T.

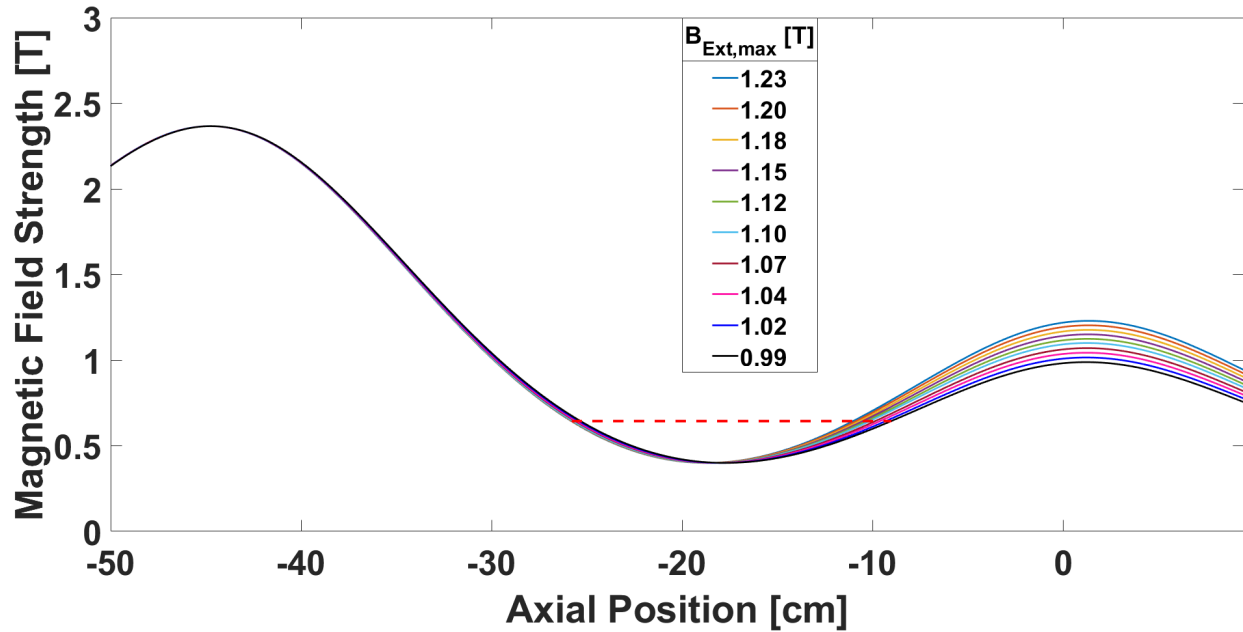


Figure B.2: Measured electron distribution for the measurements 'control' operating point. The 50 keV reliability threshold is shown by the dashed line.  $B_{min} = 0.4$  T,  $B_{Inj,max} = 2.367$  T,  $B_{Ext,max} = 1.100$  T.

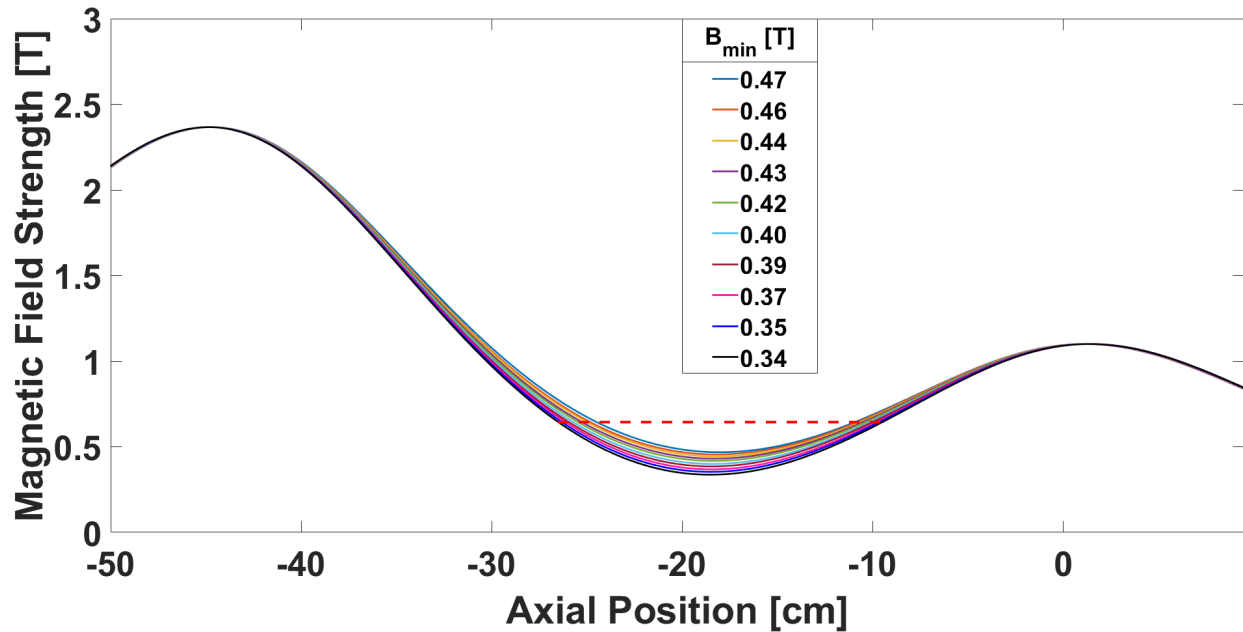


Figure B.3: Measured electron distribution for the measurements 'control' operating point. The 50 keV reliability threshold is shown by the dashed line.  $B_{min} = 0.4$  T,  $B_{Inj,max} = 2.367$  T,  $B_{Ext,max} = 1.100$  T.



## APPENDIX C

### EXTRA DATA FROM THE MEASUREMENT OF THE DISTRIBUTION OF ESCAPING ELECTRONS

#### C.1 Effect of a varying extraction voltage on the energy-resolved ion source bremsstrahlung distribution

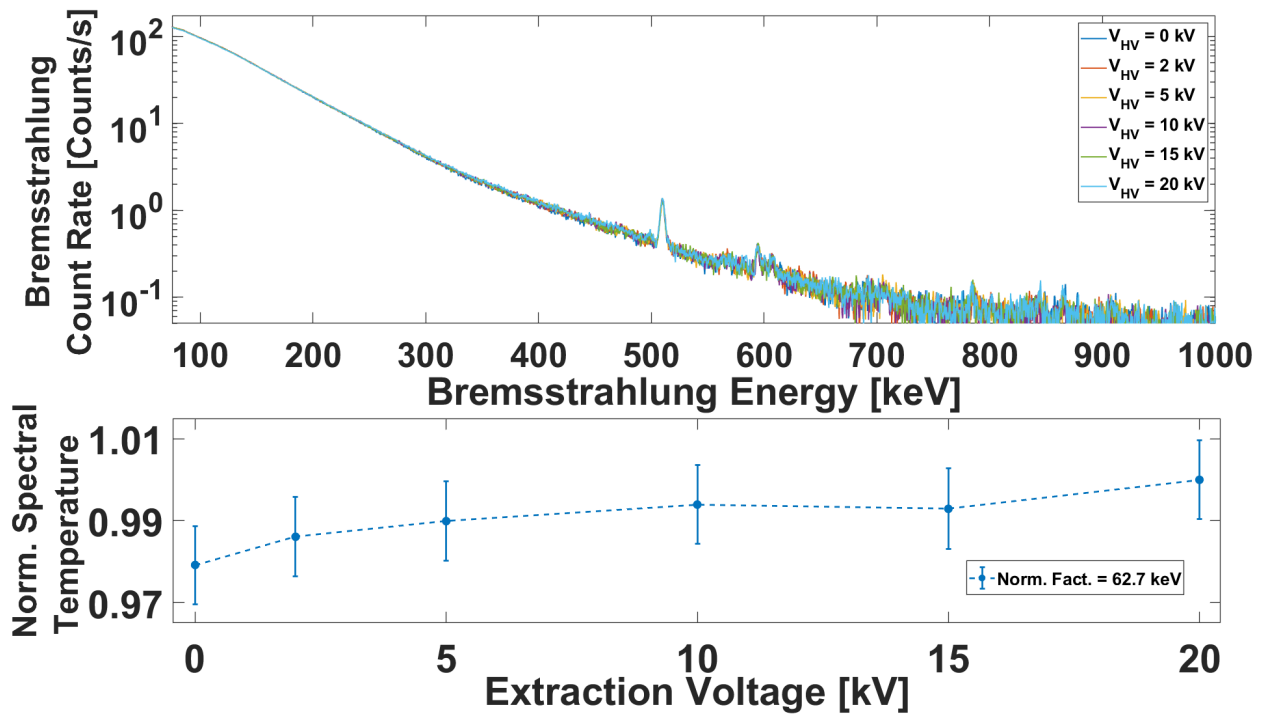


Figure C.1: A varying extraction voltage has little effect on the hot-electron bremsstrahlung distribution. The count rate and bremsstrahlung are much more stable than in figure 4.1 due to the much more consistent background during the measurement. The stability of the nuclear peak at 510 keV demonstrates this most clearly. Plasma parameters are  $B_{\min} = 0.397$  T,  $P = 350$  W,  $T_{\text{live}} = 600$  s, pressure = 212 nTorr.

#### C.2 Effect of a Variable Power

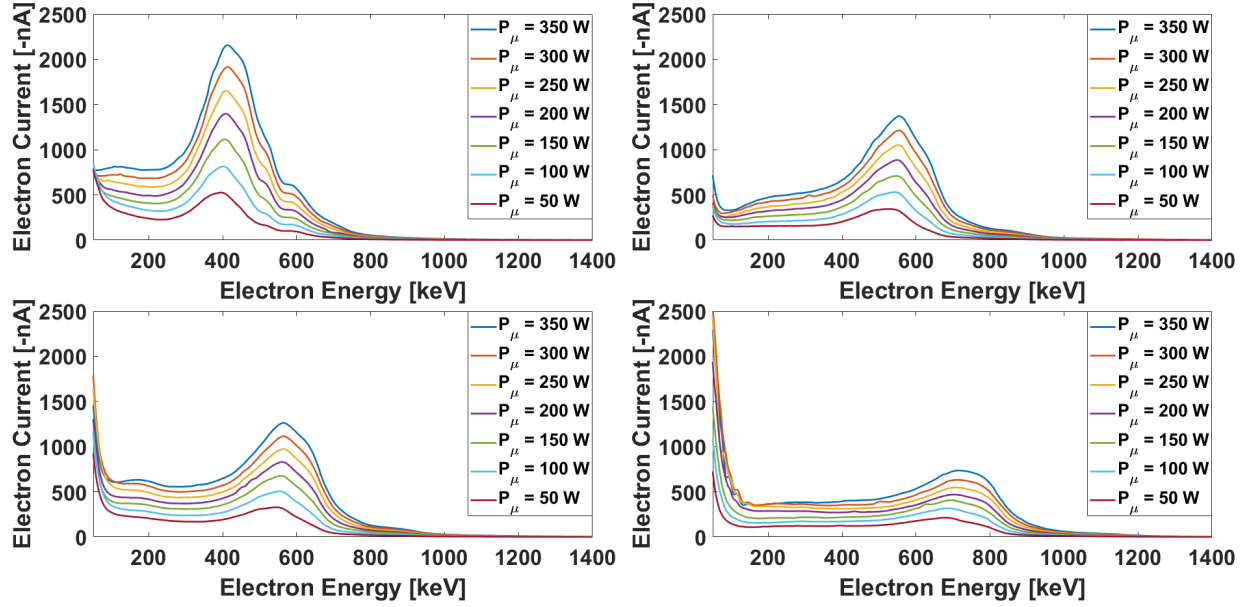


Figure C.2: A varying magnetic field does not appreciably change how the injected microwave power affects the measured electron distributions.

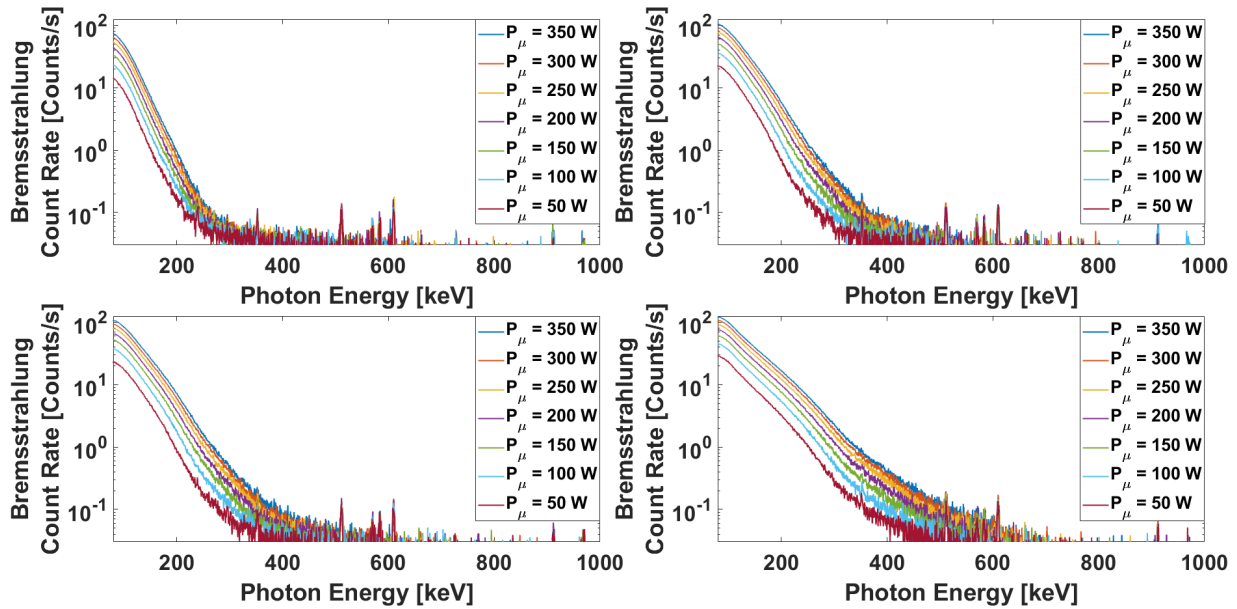


Figure C.3: Similar to figure C.2, a varying magnetic field does not appreciably change how the injected microwave power affects the measured bremsstrahlung distributions.

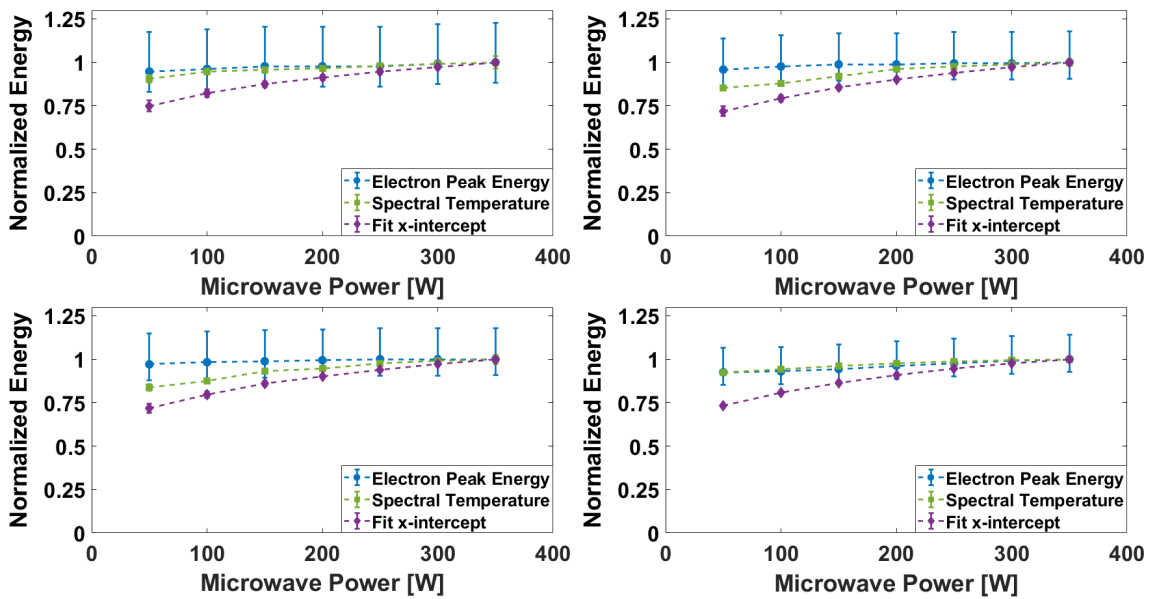


Figure C.4: All field distributions agree to a linear increase in the number of measured particles with respect to the microwave power. Although a small change in the spectral temperature is seen as the injection side magnetic field is varied, the overall trend indicates an insensitivity of electron energy to microwave power.

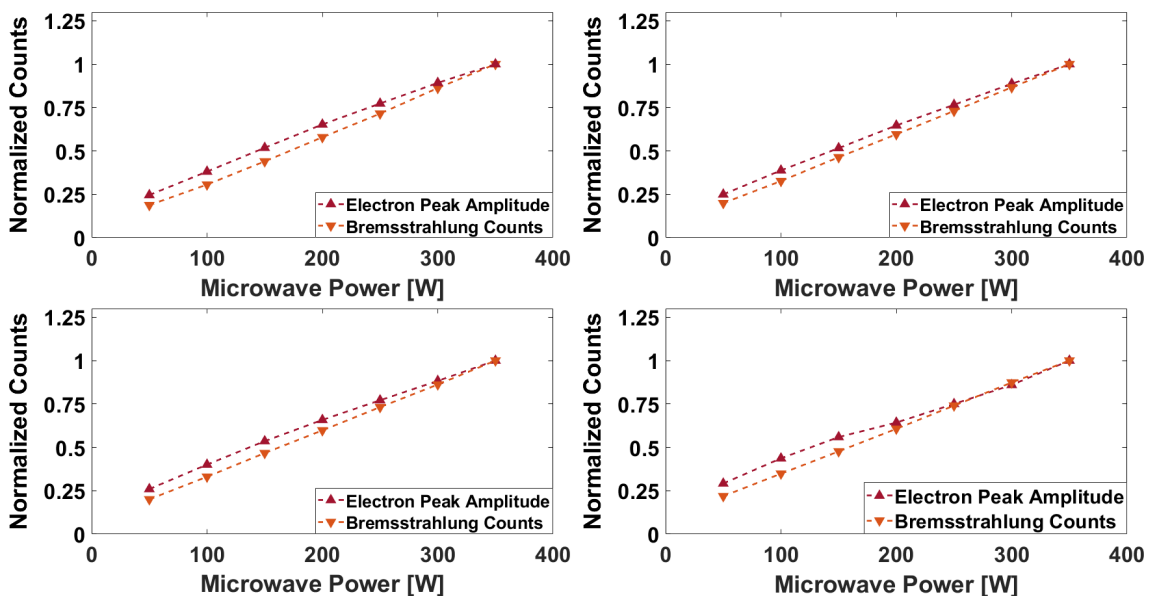


Figure C.5: All field distributions agree to a close to linear increase in the number of measured particles with respect to the microwave power. Although a small change in the spectral temperature is seen as the injection side magnetic field is varied, the overall trend indicates an insensitivity of electron energy to microwave power.

### C.3 Effect of a Variable Pressure

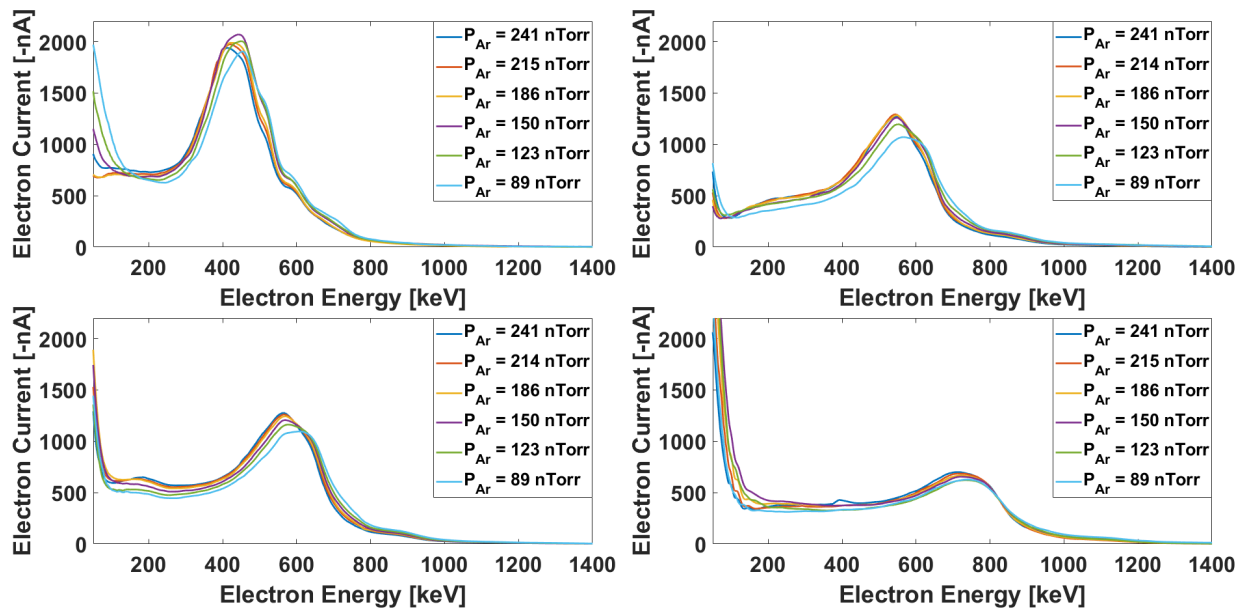


Figure C.6: The dependence of the high energy electron distribution on pressure was not appreciably affected by a varying longitudinal field profile. Although out of the scope of this study, it should be recognized that low energy portion of the distribution ( $E_{kin} < 70keV$ ) is affected by the both the pressure and the average magnetic field within the source chamber.

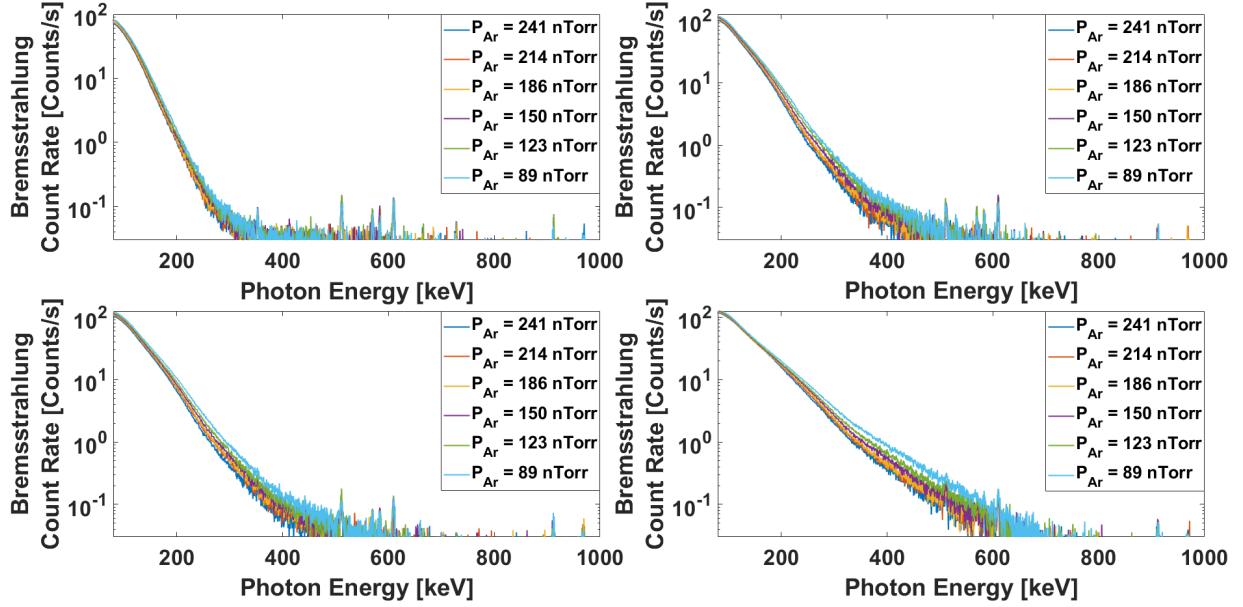


Figure C.7: The dependence of the bremsstrahlung distribution on pressure was not appreciably affected by a varying longitudinal field profile.

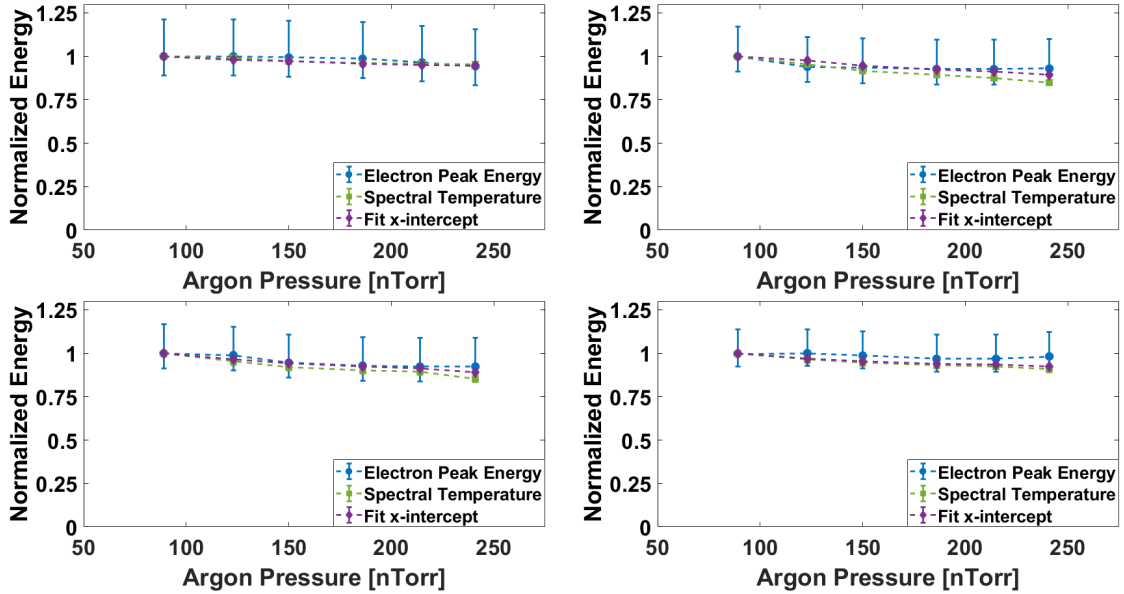


Figure C.8: All measurements agreed to the same overall trend, regardless of longitudinal field profile.

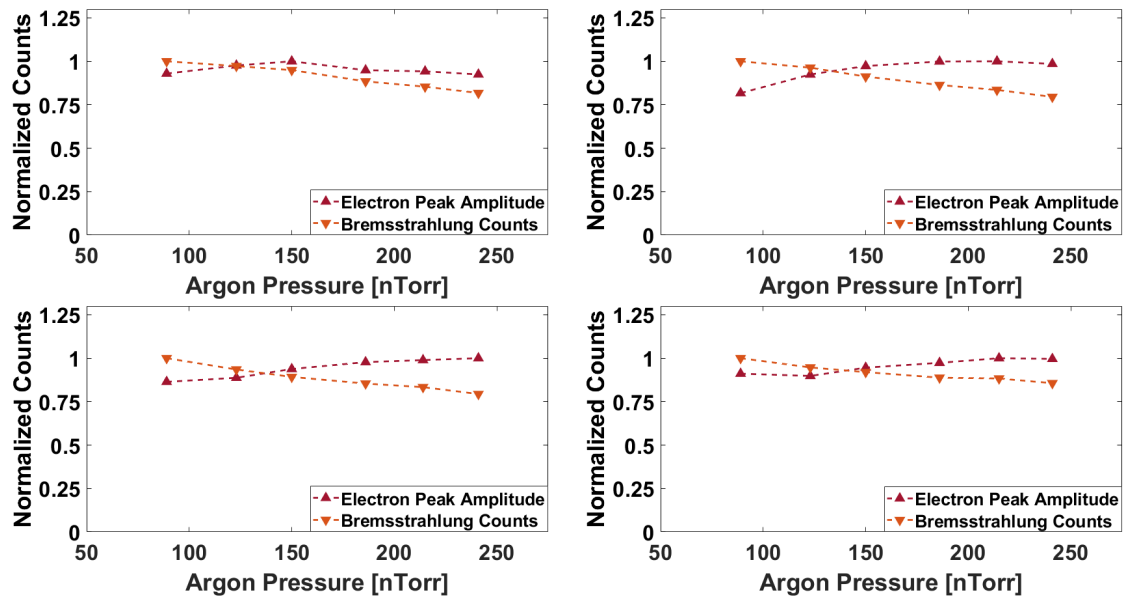


Figure C.9: All measurements agreed to the same overall trend, regardless of longitudinal field profile.

### C.4 Effect of a Variable Hexapole

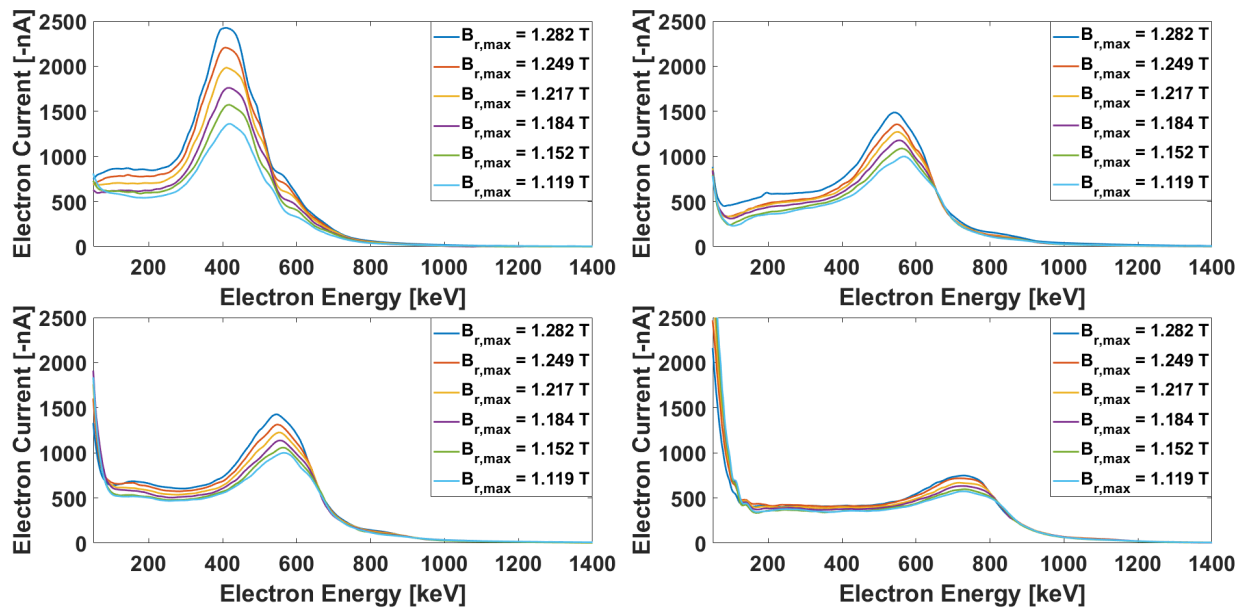


Figure C.10: There was a greater effect upon the measured electron distribution's height as a function of the radial magnetic field maximum as the magnetic minimum increased.

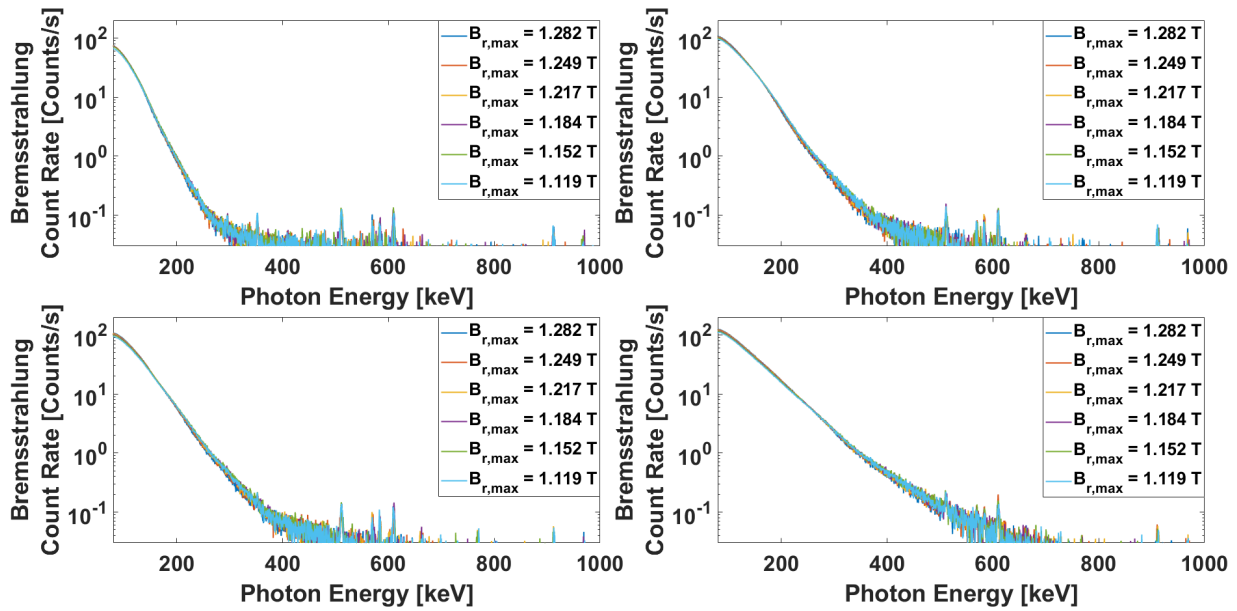


Figure C.11: The longitudinal magnetic field had no effect on the measured bremsstrahlung distribution for high energy photons.

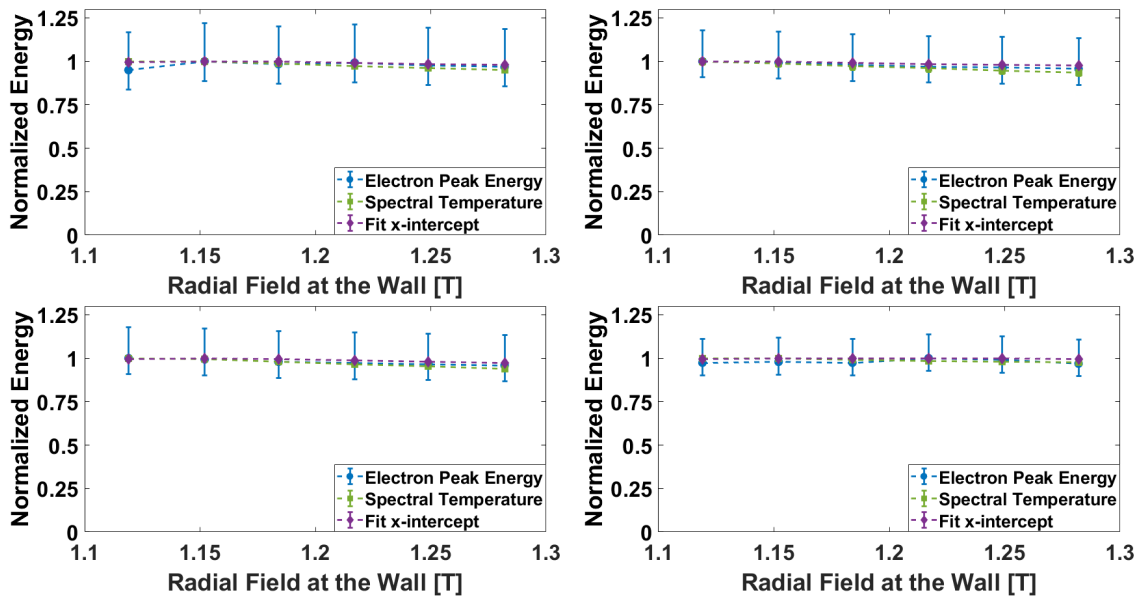


Figure C.12: Comparison between the electron peak energy/intensity and bremsstrahlung spectral temperature/total photon counts for across multiple ion source longitudinal magnetic field profiles with varying radial field maximum.

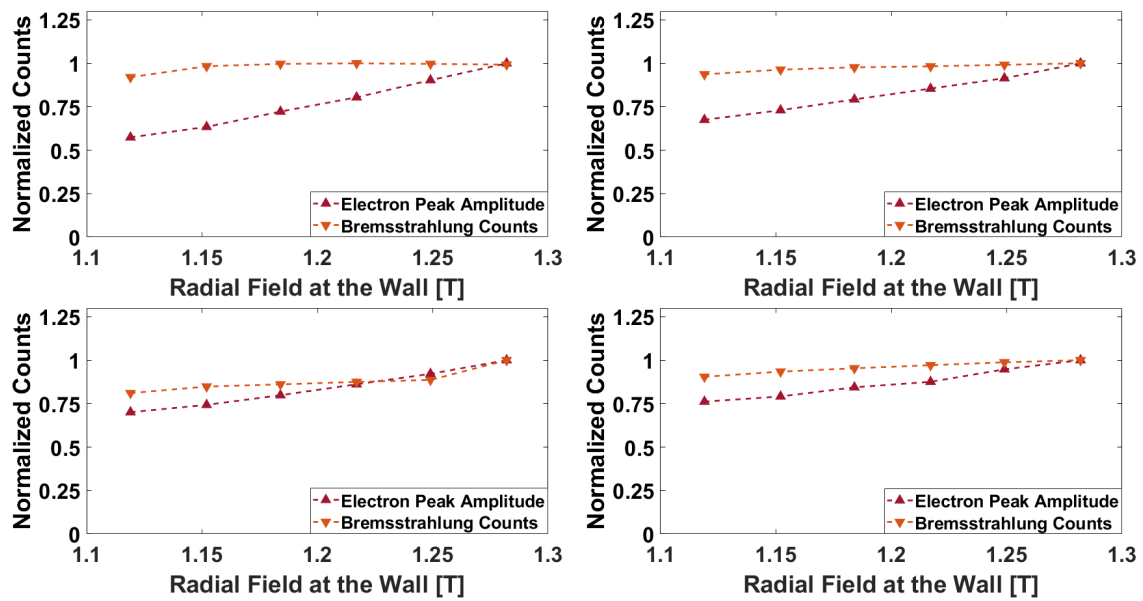


Figure C.13: Comparison between the electron peak energy/intensity and bremsstrahlung spectral temperature/total photon counts for across multiple ion source longitudinal magnetic field profiles with varying radial field maximum.



## APPENDIX D

### LONGITUDINAL FIELD PROFILES FOR THE PARAMETER SWEEP MEASUREMENT OF ION STABILITY

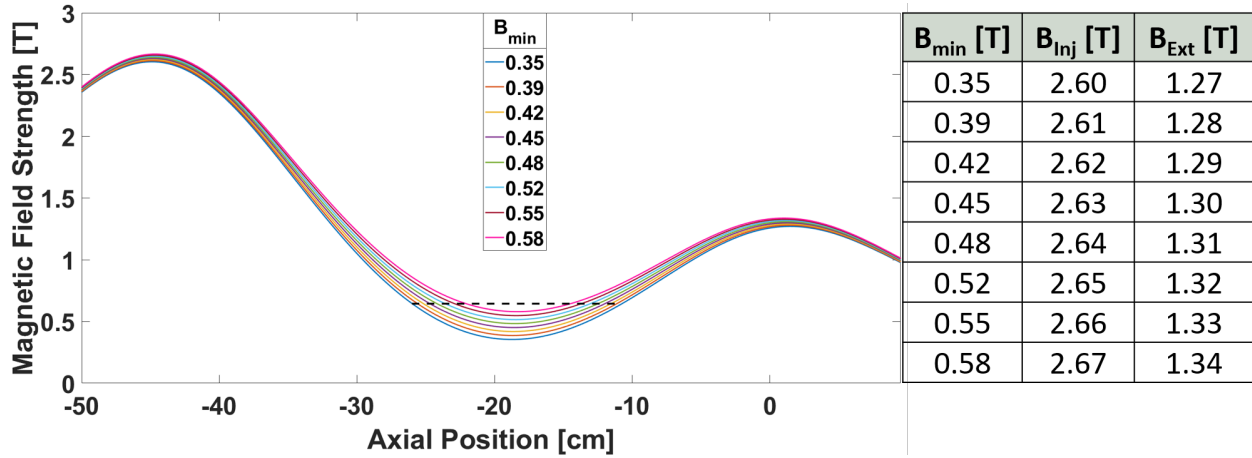


Figure D.1: Measured electron distribution for the measurements 'control' operating point. The 50 keV reliability threshold is shown by the dashed line.  $B_{\min} = 0.4$  T,  $B_{\text{Inj,max}} = 2.367$  T,  $B_{\text{Ext,max}} = 1.100$  T.

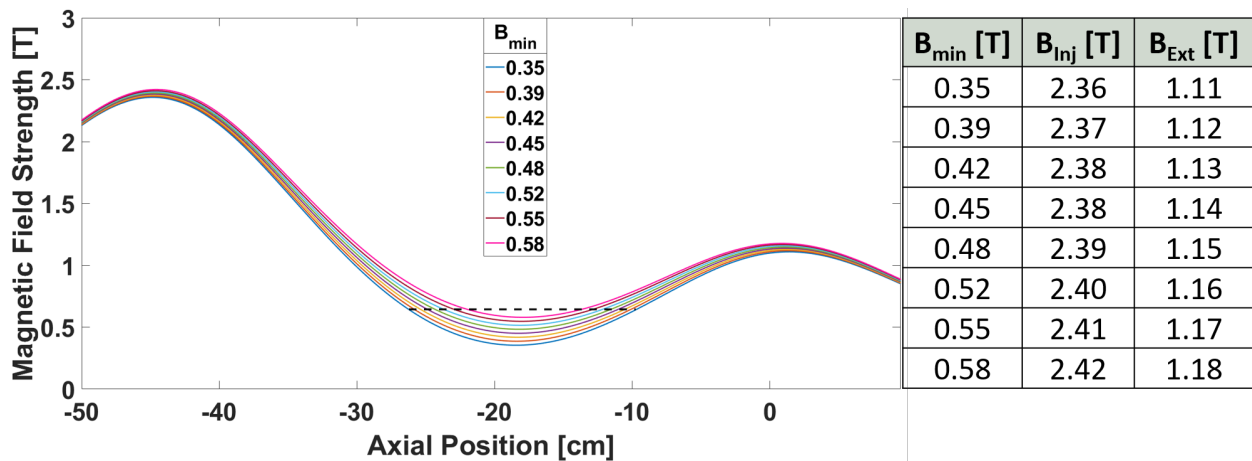


Figure D.2: Measured electron distribution for the measurements 'control' operating point. The 50 keV reliability threshold is shown by the dashed line.  $B_{\min} = 0.4$  T,  $B_{\text{Inj,max}} = 2.367$  T,  $B_{\text{Ext,max}} = 1.100$  T.

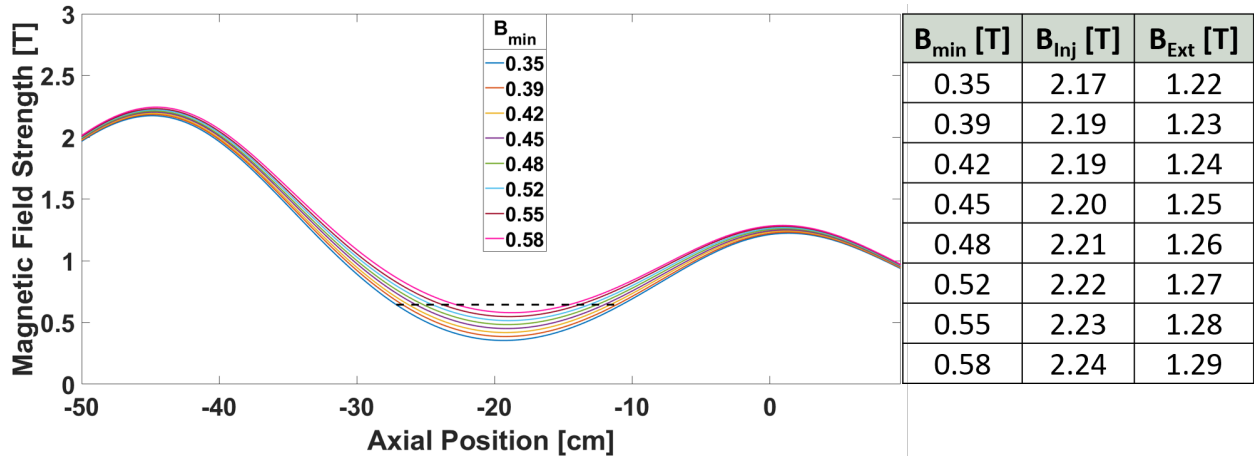


Figure D.3: Measured electron distribution for the measurements 'control' operating point. The 50 keV reliability threshold is shown by the dashed line.  $B_{\min} = 0.4$  T,  $B_{\text{Inj,max}} = 2.367$  T,  $B_{\text{Ext,max}} = 1.100$  T.

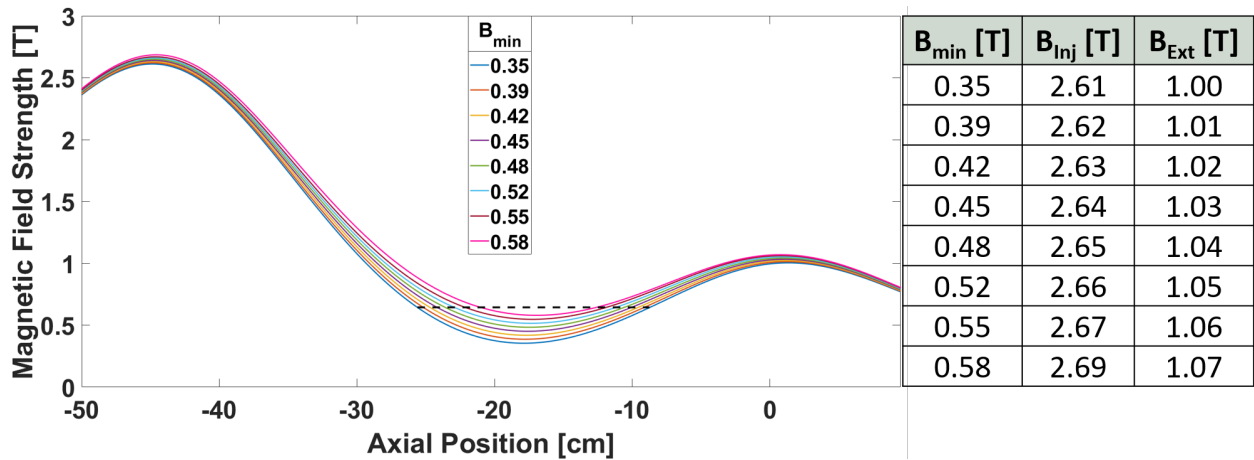


Figure D.4: Measured electron distribution for the measurements 'control' operating point. The 50 keV reliability threshold is shown by the dashed line.  $B_{\min} = 0.4$  T,  $B_{\text{Inj,max}} = 2.367$  T,  $B_{\text{Ext,max}} = 1.100$  T.

## **BIBLIOGRAPHY**

## BIBLIOGRAPHY

- [1] C. Barué, M. Lamoureux, P. Briand, A. Girard, and G. Melin. Investigation of hot electrons in electron-cyclotron-resonance ion sources. *Journal of Applied Physics*, 76(5):2662–2670, 1994.
- [2] J. Benitez, C. Lyneis, L. Phair, D. Todd, and D. Xie. Dependence of the Bremsstrahlung Spectral Temperature in Minimum-B Electron Cyclotron Resonance Ion Sources. *IEEE Transactions on Plasma Science*, 45(7):1746–1754, 2017.
- [3] J. Y. Benitez, C. M. Lyneis, L. Phair, D. S. Todd, and D. Z. Xie. RECENT BREMSSTRAHLUNG MEASUREMENTS FROM THE SUPERCONDUCTING ELECTRON CYCLOTRON RESONANCE ION SOURCE VENUS. In *Proceeding of the 22nd International Workshop on Ion Sources*, pages 23–29, Busan, Korea, 2016.
- [4] V. A. Bernshtam, Yu V. Ralchenko, and Y. Maron. Empirical formula for cross section of direct electron-impact ionization of ions. *Journal of Physics B: Atomic, Molecular and Optical Physics*, 33(22):5025–5032, 2000.
- [5] J. A. Bittencourt. *Fundamentals of Plasma Physics*. Springer, New York, NY, New York, 2004.
- [6] P. Briand, R. Geller, and G. Melin. A newly designed ECR source for the lead injector of CERN, 9 1990.
- [7] Ian Brown. *The Physics and Technology of Ion Sources*. Wiley, 2004.
- [8] F. Cap, editor. *Waves and Instabilities in Plasmas*, volume 349 of *CISM International Centre for Mechanical Sciences*. Springer Vienna, Vienna, 1994.
- [9] Ferdinand F. Cap. *Handbook on Plasma Instabilities, Volume 1*. Elsevier, 1976.
- [10] Claudio Chiuderi and Marco Velli. *Basics of Plasma Astrophysics*. Springer-Verlag Mailand, 2015.
- [11] Brian P. Cluggish, Liangji Zhao, and Jin Soo Kim. Modeling of the stability of electron cyclotron resonance ion source plasmas. *Nuclear Instruments and Methods in Physics Research, Section A: Accelerators, Spectrometers, Detectors and Associated Equipment*, 631(1):111–120, 2011.
- [12] Rodney Coleman. *Stochastic Processes*. Springer Netherlands, Dordrecht, 1974.
- [13] G. Douysset, H. Khodja, A. Girard, and J. P. Briand. Highly charged ion densities and ion confinement properties in an electron-cyclotron-resonance ion source. *Physical Review E - Statistical Physics, Plasmas, Fluids, and Related Interdisciplinary Topics*, 61(3):3015–3022, 2000.

- [14] S. Gammino and G. Ciavola. ECR Ion Sources and Scaling Laws. *Proceedings of the 14th International Conference on Cyclotrons and their Applications, Cape Town, South Africa*, pages 337–380, 1996.
- [15] R. Geller. ECR source scaling concepts. In *Proceedings of the 1989 IEEE Particle Accelerator Conference*, pages 1088–1092, Chicago, IL, USA, 1989. IEEE.
- [16] R. Geller. ECRIS: the electron cyclotron resonance ion sources - (status). *Zeitschrift für Physik D Atoms, Molecules and Clusters*, 21(1 Supplement), 1991.
- [17] R. Geller. Electron cyclotron resonance sources: Historical review and future prospects (invited). *Review of Scientific Instruments*, 69(3):1302–1310, 1998.
- [18] R Geller. *Electron Cyclotron Resonance Ion Sources and ECR Plasmas*. Routledge, 12 2018.
- [19] A. Girard. Plasma diagnosis related to ion sources (invited). *Review of Scientific Instruments*, 63(4):2676–2682, 1992.
- [20] A. Girard, C. Perret, G. Melin, and C. Lécot. Modeling of electron-cyclotron-resonance ion source and scaling laws. *Review of Scientific Instruments*, 69(2):1100–1102, 1998.
- [21] R.J Goldston and P.H. Rutherford. *Introduction to Plasma Physics*. CRC Press, Boca Raton, 1st edition, 10 1995.
- [22] Gareth Guest. *Electron Cyclotron Heating of Plasmas*. Wiley, 2010.
- [23] P. G. Guest. The solid angle subtended by a cylinder. *Review of Scientific Instruments*, 32(2):164–165, 1961.
- [24] D. Hitz, A. Girard, G. Melin, S. Gammino, G. Ciavola, and L. Celona. Results and interpretation of high frequency experiments at 28 GHz in ECR ion sources, future prospects. *Review of Scientific Instruments*, 73(2):509, 2 2002.
- [25] I. Izotov, T. Kalvas, H. Koivisto, R. Kronholm, D. Mansfeld, V. Skalyga, and O. Tarvainen. Broadband microwave emission spectrum associated with kinetic instabilities in minimum-B ECR plasmas. *Physics of Plasmas*, 24(4), 2017.
- [26] I Izotov, O Tarvainen, D Mansfeld, V Skalyga, H Koivisto, T Kalvas, J Komppula, R Kronholm, and J Laulainen. Microwave emission related to cyclotron instabilities in a minimum-B electron cyclotron resonance ion source plasma. *Plasma Sources Science and Technology*, 24(4):045017, 7 2015.
- [27] I. Izotov, O. Tarvainen, V. Skalyga, D. Mansfeld, T. Kalvas, H. Koivisto, and R. Kronholm. Measurement of the energy distribution of electrons escaping minimum-B ECR plasmas. *Plasma Sources Science and Technology*, 27(2), 2018.
- [28] I. Izotov, O. Tarvainen, V. Skalyga, D. Mansfeld, H. Koivisto, R. Kronholm, V. Toivanen, and V. Mironov. Measurements of the energy distribution of electrons lost from the minimum B-field—The effect of instabilities and two-frequency heating. *Review of Scientific Instruments*, 91(1):013502, 1 2020.

- [29] F. Jaeger, A. J. Lichtenberg, and M. A. Lieberman. Theory of electron cyclotron resonance heating I. Short Time and Adiabatic Effects. *Plasma Physics*, 14:1073–1100, 1972.
- [30] S. Kasthurirangan, A. N. Agnihotri, C. A. Desai, and Lokesh C. Tribedi. Temperature diagnostics of ECR plasma by measurement of electron bremsstrahlung spectra. *Journal of Physics: Conference Series*, 388(PART 14), 2012.
- [31] L. Kenéz, S. Biri, J. Karácsony, A. Valek, T. Nakagawa, K. E. Stiebing, and V. Mironov. Diagnostic research of plasmas generated by a 14.5 GHz ECR ion source using Langmuir-probe. *Review of Scientific Instruments*, 73(2 II):617, 2002.
- [32] L. Kenéz, J. Karácsony, A. Kitagawa, M. Muramatsu, S. Biri, and A. Valek. Local plasma diagnostics research on Electron Cyclotron Resonance Ion Source. *Padeu*, 135:135–145, 2005.
- [33] Masanori Kidera, Michele Lamoureux, Vladimir Mironov, Takahide Nakagawa, and Grigori Shirkov. Correlation between the hot-electron dynamics and the afterglow currents in electron cyclotron resonance ion sources. *Review of Scientific Instruments*, 70(11):4234–4237, 1999.
- [34] Glenn F. Knoll and H. W. Kraner. *Radiation Detection and Measurement*, 1981.
- [35] Martin H. Kroll, Ken Emancipator, David Floering, and Daniel Tholen. An algorithm for finding the linear region in a nonlinear data set. *Computers in Biology and Medicine*, 29(5):289–301, 9 1999.
- [36] R. Kronholm, T. Kalvas, H. Koivisto, J. Laulainen, M. Marttinen, M. Sakildien, and O. Tervainen. Spectroscopic study of ion temperature in minimum-B ECRIS plasma. *Plasma Sources Science and Technology*, 28(7), 7 2019.
- [37] James W. LaBelle and Rudolf A. Treumann. *Geospace Electromagnetic Waves and Radiation*. Springer, 2006.
- [38] M. Lamoureux, A. Girard, R. Pras, P. Charles, H. Khodja, F. Bourg, J. P. Briand, and G. Melin. Evidence of low-frequency oscillations in heavy ion plasmas heated by electron cyclotron resonance. *Physics of Plasmas*, 3(12):4307–4309, 1996.
- [39] L Lamy, B Cecconi, P Zarka, P Canu, P Schippers, W S Kurth, R L Mutel, D A Gurnett, D Menietti, and P Louarn. Emission and propagation of Saturn kilometric radiation : Magnetoionic modes , beaming pattern , and polarization state. *Journal of Geophysical Research*, 116(X):1–16, 2011.
- [40] K. Langbein. Experimental investigation of the afterglow of the pulsed electron cyclotron resonance discharge. *Review of Scientific Instruments*, 67(3):1334–1336, 1996.
- [41] D. Leitner, J. Y. Benitez, C. M. Lyneis, D. S. Todd, T. Ropponen, J. Ropponen, H. Koivisto, and S. Gammino. Measurement of the high energy component of the x-ray spectra in the VENUS electron cyclotron resonance ion source. *Review of Scientific Instruments*, 79(3), 2008.

- [42] D. Leitner, C. M. Lyneis, S. R. Abbott, D. Collins, R. D. Dwinell, M. L. Galloway, M. Leitner, and D. S. Todd. Next generation ECR ion sources: First results of the superconducting 28 GHz ECRIS - VENUS. In *Nuclear Instruments and Methods in Physics Research, Section B: Beam Interactions with Materials and Atoms*, volume 235, pages 486–493, 7 2005.
- [43] M. A. Lieberman and A. J. Lichtenberg. Theory of electron cyclotron resonance heating. II. Long time and stochastic effects. *Plasma Physics*, 15(2):125–150, 1973.
- [44] Michael A. Lieberman and Allan J. Lichtenberg. *Principles of Plasma Discharges and Materials Processing: Second Edition*. Wiley, 2005.
- [45] Wolfgang Lotz. An empirical formula for the electron-impact ionization cross-section. *Zeitschrift für Physik*, 206(2):205–211, 1967.
- [46] C. M. Lyneis. SCALING LAWS IN ELECTRON CYCLOTRON RESONANCE ION SOURCES. *Review of Scientific Instruments*, pages 1–4, 2016.
- [47] D Mansfeld, I Izotov, V Skalyga, O Tarvainen, T Kalvas, H Koivisto, J Komppula, R Kronholm, and J Laulainen. Dynamic regimes of cyclotron instability in the afterglow mode of minimum-B electron cyclotron resonance ion source plasma. *Plasma Physics and Controlled Fusion*, 58(4):045019, 4 2016.
- [48] D. A. Mansfeld, A. V. Vodopyanov, M. D. Tokman, N. D. Kirukhin, D. I. Yasnov, and V. E. Semenov. Plasma losses from mirror trap, initiated by microwave radiation under electron cyclotron resonance conditions. *Plasma Physics and Controlled Fusion*, 60(11), 2018.
- [49] M. Marttinen, J. Angot, A. Annaluru, P. Jardin, T. Kalvas, H. Koivisto, S. Kosonen, R. Kronholm, L. Maunoury, O. Tarvainen, V. Toivanen, and P. Ujic. Estimating ion confinement times from beam current transients in conventional and charge breeder ECRIS. *Review of Scientific Instruments*, 91(1):013304, 1 2020.
- [50] D. Mascali, L. Celona, F. Maimone, J. Maeder, G. Castro, F. P. Romano, A. Musumarra, C. Altana, C. Caliri, G. Torrisci, L. Neri, S. Gammino, K. Tinschert, K. P. Spaedtke, J. Rossbach, R. Lang, and G. Ciavola. X-ray spectroscopy of warm and hot electron components in the CAPRICE source plasma at EIS testbench at GSI. *Review of Scientific Instruments*, 85(2):1–6, 2014.
- [51] L. Maunoury, L. Adoui, J. P. Grandin, F. Noury, B. A. Huber, E. Lamour, C. Prigent, J. P. Rozet, D. Vernhet, P. Leherissier, and J. Y. Pacquet. Afterglow mode and the new micropulsed beam mode applied to an electron cyclotron resonance ion source. *Review of Scientific Instruments*, 79(2):23–27, 2008.
- [52] G. Melin, F. Bourg, P. Briand, J. Debernardi, M. Delaunay, R. Geller, B. Jacquot, P. Ludwig, T. K. N’Guyen, L. Pin, M. Pontonnier, J. C. Rocco, and F. Zadworny. Some particular aspects of the physics of the ECR sources for multicharged ions. *Review of Scientific Instruments*, 61(1):236–238, 1990.

- [53] G. Melin, A. G. Drentje, A. Girard, and D. Hitz. Ion behavior and gas mixing in electron cyclotron resonance plasmas as sources of highly charged ions. *Journal of Applied Physics*, 86(9):4772–4779, 1999.
- [54] D. B. Melrose. Coherent emission mechanisms in astrophysical plasmas. *Reviews of Modern Plasma Physics*, 1(1):1–81, 2017.
- [55] D. B. Melrose and G. A. Dulk. ELECTRON-CYCLOTRON MASERS AS THE SOURCE OF CERTAIN SOLAR AND STELLAR RADIO BURSTS. *The Astrophysical Journal*, 259:844–858, 1982.
- [56] V Mironov, S Bogomolov, A Bondarchenko, A Efremov, and V Loginov. Numerical model of electron cyclotron resonance ion source. *Physical Review Special Topics - Accelerators and Beams*, 18(12):1–23, 2015.
- [57] V. Mironov, S. Bogomolov, A. Bondarchenko, A. Efremov, and V. Loginov. Some aspects of electron dynamics in electron cyclotron resonance ion sources. *Plasma Sources Science and Technology*, 26(7), 6 2017.
- [58] Vladimir Mironov, Sergey Bogomolov, Andrej Bondarchenko, Andrej Efremov, Vladimir Loginov, and Dmitrii Pugachev. Spatial distributions of plasma potential and density in electron cyclotron resonance ion source. *Plasma Sources Science and Technology*, 2019.
- [59] M Moisan. *Microwave Excited Plasmas, Plasma Technology*. Elsevier, 1992.
- [60] E. Naselli, D. Mascali, M. Mazzaglia, S. Biri, R. Rácz, J. Pálinkás, Z. Perduk, A. Galatá, G. Castro, L. Celona, S. Gammino, and G. Torrasi. Impact of two-close-frequency heating on ECR ion source plasma radio emission and stability. *Plasma Sources Science and Technology*, 28(8), 2019.
- [61] D. Neben, J. Fogleman, B. Isherwood, D. Leitner, G. Machicoane, S. Renteria, J. Stetson, and L. Tobos. X-ray investigation on the Superconducting Source for Ions (SuSI). In *23rd International Workshop on ECR Ion Sources*, volume 14. Institute of Physics Publishing, 2 2019.
- [62] Jonathan D. Noland. *Measurements of plasma bremsstrahlung and plasma energy density produced by electron cyclotron resonance ion source plasmas*. PhD thesis, University of California-Berkeley, 2011.
- [63] N. Omidi, C. S. Wu, and D A Gurnett. Generation of Auroral Kilometric and Z Mode Radiation by the Cyclotron Maser Mechanism. *Journal of Geophysical Research*, 89:883–895, 1984.
- [64] Alexander Piel. *Plasma physics: An introduction to laboratory, space, and fusion plasmas*. Springer-Verlag Berlin Heidelberg, 2010.
- [65] T Ropponen, O Tarvainen, I Izotov, J Noland, V Toivanen, G Machicoane, D Leitner, H Koivisto, T Kalvas, P Peura, P Jones, V Skalyga, and V Zorin. Studies of plasma breakdown and electron heating on a 14 GHz ECR ion source through measurement of plasma bremsstrahlung. *Plasma Sources Science and Technology*, 20(5):055007, 10 2011.



- [66] T Ropponen, O Tarvainen, P Jones, P Peura, T Kalvas, P Suominen, and H Koivisto. The effect of magnetic field strength on the time evolution of high energy bremsstrahlung radiation created by an electron cyclotron resonance ion source. *Nuclear Instruments and Methods in Physics Research A*, 600:525–533, 2009.
- [67] R. Z. Sagdeev and V. D. Shafranov. On the instability of a plasma with anisotropic distribution of velocities in a magnetic field. *Sov. Phys. JETP*, 12(1):130–132, 1961.
- [68] M. Sakildien, O. Tarvainen, R. Kronholm, I. Izotov, V. Skalyga, T. Kalvas, P. Jones, and H. Koivisto. Experimental evidence on microwave induced electron losses from ECRIS plasma. *Physics of Plasmas*, 25(6), 2018.
- [69] A. G. Shalashov, E. D. Gospodchikov, I. V. Izotov, D. A. Mansfeld, V. A. Skalyga, and O. Tarvainen. Control of electron-cyclotron instability driven by strong ECRH in open magnetic trap. *EPL (Europhysics Letters)*, 124(3):35001, 12 2018.
- [70] A. G. Shalashov, E. D. Gospodchikov, I. V. Izotov, D. A. Mansfeld, V. A. Skalyga, and O. Tarvainen. Observation of Poincaré-Andronov-Hopf Bifurcation in Cyclotron Maser Emission from a Magnetic Plasma Trap. *Physical Review Letters*, 120(15):155001, 2018.
- [71] A. G. Shalashov, M. E. Viktorov, D. A. Mansfeld, and S. V. Golubev. Kinetic instabilities in a mirror-confined plasma sustained by high-power microwave radiation. *Physics of Plasmas*, 24(3):1–14, 2017.
- [72] A. G. Shalashov, A. V. Vodopyanov, S. V. Golubev, A. G. Demekhov, V. G. Zorin, D. A. Mansfeld, and S. V. Razin. Maser based on cyclotron resonance in a decaying plasma. *JETP Letters*, 84(6):314–319, 11 2006.
- [73] Alexander G Shalashov, Egor D Gospodchikov, and Ivan Izotov. Electron-cyclotron heating and kinetic instabilities of a mirror-confined plasma: the quasilinear theory revised. *Plasma Physics and Controlled Fusion*, 2020.
- [74] Annette D. Shine. *Fitting Experimental Data to Straight Lines*, 2006.
- [75] V. Skalyga, I. Izotov, T. Kalvas, H. Koivisto, J. Komppula, R. Kronholm, J. Laulainen, D. Mansfeld, and O. Tarvainen. Suppression of cyclotron instability in Electron Cyclotron Resonance ion sources by two-frequency heating. *Physics of Plasmas*, 22(8), 2015.
- [76] P. Sortais. Pulsed ECR ion source using the afterglow mode (invited), 4 1992.
- [77] P Spädtke and Caprice Ecris. Investigation of pulsed mode operation with the frequency tuned CAPRICE ECRIS. *Review of Scientific Instruments*, 712(August 2015):10–13, 2016.
- [78] K. E. Stiebing, L. Schächter, and S. Dobrescu. The influence of the extraction voltage on the energetic electron population of an electron cyclotron resonance ion source plasma. *Review of Scientific Instruments*, 83(2):10–13, 2012.
- [79] L. Sun, H. W. Zhao, W. Lu, J. W. Guo, Y. Yang, H. Jia, L. Lu, and W. Wu. Review of highly charged ion production with ECR ion source and the future opportunities for HCI physics. *X-Ray Spectrometry*, 49(1):47–53, 2020.

- [80] D G Swanson. *Plasma Waves, 2nd Edition (Plasma Physics)*. Inst of Physics Pub, 2 edition, 2003.
- [81] O Tarvainen, I Izotov, D Mansfeld, V Skalyga, S Golubev, T Kalvas, H Koivisto, J Komppula, R Kronholm, J Laulainen, and V Toivanen. Beam current oscillations driven by cyclotron instabilities in a minimum-B electron cyclotron resonance ion source plasma. *Plasma Sources Science and Technology*, 23(2):025020, 4 2014.
- [82] O. Tarvainen, T. Kalvas, H. Koivisto, J. Komppula, R. Kronholm, J. Laulainen, I. Izotov, D. Mansfeld, and V. Skalyga. Kinetic instabilities in pulsed operation mode of a 14 GHz electron cyclotron resonance ion source. *Review of Scientific Instruments*, 87(2), 2016.
- [83] O. Tarvainen, T. Kalvas, H. Koivisto, J. Komppula, R. Kronholm, J. Laulainen, I. Izotov, D. Mansfeld, V. Skalyga, V. Toivanen, and G. Machicoane. Limitation of the ECRIS performance by kinetic plasma instabilities (invited). *Review of Scientific Instruments*, 87(2), 2016.
- [84] O. Tarvainen, T. Kalvas, H. Koivisto, R. Kronholm, M. Marttinen, M. Sakildien, V. Toivanen, I. Izotov, V. Skalyga, and J. Angot. Plasma diagnostic tools for ECR ion sources—What can we learn from these experiments for the next generation sources. *Review of Scientific Instruments*, 90(11):113321, 2019.
- [85] O. Tarvainen, R. Kronholm, T. Kalvas, H. Koivisto, I. Izotov, V. Skalyga, V. Toivanen, and L. Maunoury. The biased disc of an electron cyclotron resonance ion source as a probe of instability-induced electron and ion losses. *Review of Scientific Instruments*, 90(12), 12 2019.
- [86] O Tarvainen, T Ropponen, V Toivanen, T Kalvas, J Ärje, and H Koivisto. Diagnostics of plasma decay and afterglow transient of an electron cyclotron resonance ion source. *Plasma Sources Science and Technology*, 19(4):045027, 2010.
- [87] O. Tarvainen, V. Toivanen, J. Komppula, T. Kalvas, and H. Koivisto. Transverse distribution of beam current oscillations of a 14 GHz electron cyclotron resonance ion source. *Review of Scientific Instruments*, 85(2):6–9, 2014.
- [88] Olli Tarvainen. *Studies of electron cyclotron resonance ion source plasma physics*. PhD thesis, University of Jyväskylä, 2005.
- [89] Olli Tarvainen, Taneli Kalvas, and Jani Komppula. Pulsed Operation of ECR Ion Sources-Plasma Physics and Diagnostics. Number July, pages 4–6, 2011.
- [90] K. Tinschert, R. Iannucci, J. Bossler, and R. Lang. Experimental studies of the afterglow mode with xenon in a CAPRICE ECRIS. *Review of Scientific Instruments*, 75(5 PART II):1407–1409, 2004.
- [91] V. Y. Trakhtengerts and M. J. Rycroft. *Whistler and Alfvén Mode Cyclotron Masers in Space*. Cambridge University Press, 2008.

- [92] M. E. Viktorov, A. G. Shalashov, S. V. Golubev, E. D. Gospodchikov, D. A. Mansfeld, A. V. Vodopyanov, and V. V. Zaitsev. Kinetic instabilities in a mirror-confined plasma sustained by high-power microwave radiation. In *AIP Conference Proceedings*, volume 1771. American Institute of Physics Inc., 10 2016.
- [93] A. V. Vodopyanov, S. V. Golubev, A. G. Demekhov, V. G. Zorin, D. A. Mansfeld, S. V. Razin, and A. G. Shalashov. Observation of pulsed fast electron precipitations and the cyclotron generation mechanism of burst activity in a decaying ECR discharge plasma. *Journal of Experimental and Theoretical Physics*, 104(2):296–306, 4 2007.
- [94] R. M. Winglee. Interrelation between azimuthal bunching and semirelativistic maser cyclotron instabilities. *Plasma Physics*, 25(2):217–255, 1983.
- [95] Daniel Winklehner. *Ion Beam Extraction From Electron Cyclotron Resonance Ion*. PhD thesis, Michigan State University, 2013.
- [96] L. C. Woods. *Physics of Plasmas*. Wiley, 2003.
- [97] C. S. Wu. Kinetic cyclotron and synchrotron maser instabilities: Radio emission processes by direct amplification of radiation. *Space Science Reviews*, 41(3-4):215–298, 8 1985.
- [98] C. S. Wu and X. M. Qiu. Emissions of Second-Harmonic Auroral Kilometric Radiation. *Journal of Geophysical Research*, 88(A12):10072–10080, 1983.
- [99] P. A. Zavodszky, B. Arend, D. Cole, J. DeKamp, G. Machicoane, F. Marti, P. Miller, J. Moskalik, J. Ottarson, J. Vincent, and A. Zeller. Design of SuSI - Superconducting source for ions at NSCL/MSU - I. The magnet system. *AIP Conference Proceedings*, 749:131–134, 2005.
- [100] P. A. Zavodszky, B. Arend, D. Cole, J. Dekamp, G. MacHicoane, F. Marti, P. Miller, J. Moskalik, J. Ottarson, J. Vincent, and A. Zeller. Design of SuSI - Superconducting source for ions at NSCL/MSU - II. The conventional parts. In *Nuclear Instruments and Methods in Physics Research, Section B: Beam Interactions with Materials and Atoms*, volume 241, pages 959–964. North-Holland, 12 2005.
- [101] H. W. Zhao, L. T. Sun, J. W. Guo, W. H. Zhang, W. Lu, W. Wu, B. M. Wu, G. Sabbi, M. Juchno, A. Hafalia, E. Ravaioli, and D. Z. Xie. Superconducting ECR ion source: From 24-28 GHz SECRA to 45 GHz fourth generation ECR. *Review of Scientific Instruments*, 89(5), 5 2018.
- [102] H. Y. Zhao, H. W. Zhao, L. T. Sun, H. Wang, D. Z. Xie, B. H. Ma, X. Zh Zhang, X. X. Li, X. W. Ma, Y. H. Zhu, W. Lu, and Y. Shang. Effects of magnetic configuration on hot electrons in highly charged ECR plasma. *Plasma Sources Science and Technology*, 18(2), 2009.
- [103] G. Zschornack, M. Schmidt, and A. Thorn. Electron beam ion sources. *CAS-CERN Accelerator School: Ion Sources - Proceedings*, pages 165–201, 2013.